A REMOTE SENSING AND GIS-ENABLED ASSET MANAGEMENT SYSTEM (RS-GAMS) PHASE 2

Final Report

Contract Number: RITARS-11-H-GAT

Prepared by

Yichang (James) Tsai, Ph.D., P.E.

Zhaohua Wang, Ph.D., P.E.

Georgia Institute of Technology

Program Manager: Mr. Caesar Singh, USDOT

April 2014

DISCLAIMER

The views, opinions, findings, and conclusions reflected in this report are the responsibility of the authors only and do not represent the official policy or position of the USDOT, OST-R, or any State or other entity.

ACKNOWLEDGEMENTS

The work described in this report was supported by the U. S. Department of Transportation Office of the Assistant Secretary for Research and Technology (USDOT/OST-R). We would like to thank the technical advisory committee, including Mr. Butch Wlaschin, Mr. Thomas Van, Mr. Mark Swanlund, and Mr. Mike Moravec from Federal Highway Administration; Mr. Bouzid Choubane and Mr. Bruce Dietrich (retired) from Florida DOT; Ms. Angela Alexander, Mr. Gregory Mayo and Mr. Eric Pitts (retired) from Georgia DOT; Mr. Rick Miller from Kansas DOT; Dr. Judith B Corley-Lay from North Carolina DOT, for their valuable contributions to this project. The strong support provided by Georgia DOT, including Mr. Keith Golder, Mr. Gerald Ross (former Chief Engineer, retired), Mr. Russell McMurry, Ms. Georgene Geary, Mr. Timothy Dale Brantley, Ms. Jane Smith, Ms. Erany Robinson-Perry, Mr. Thomas Mims, Mr. Jim Leben, Mr. Terry Rutledge (retired), Mr. Ritchie Swindell and Mr. Rick Deaver (retired), is highly appreciated. We would like to thank SAGIS of Chatham County – Savannah Metropolitan Planning Commission and Fugro Roadware Inc for providing us with testing data. We would like to thank the following state DOTs and companies for their valuable inputs and technical supports, Connecticut DOT, Florida DOT, Kansas DOT, Louisiana DOTD, Mississippi DOT, Oklahoma DOT, South Carolina DOT, Texas DOT, Utah DOT, INO/Pavemetrics and Trimble Geo3D. We would like to thank the research team members, Dr. James Lai, Mr. Wouter Gulden, Dr. Anthony Yezzi, Ms. Yiching Wu, Dr. Vivek Kaul, Dr. Feng Li, Dr. Chengbo Ai, Mr. Zachary Lewis, Mr. Thibaut Dusanter, Mr. Chenglong Jiang, Mr. Zhengbo Li, and Mr. Jinqi Fang. Specially, we would like to thank Mr. Caesar Singh and Mr. Vasanth Ganesan for his assistance in managing this project.

Table of Content

Table of Figures

Table of Tables

Executive Summary

Under the U.S. Department of Transportation (DOT) Commercial Remote Sensing and Spatial Information (CRS&SI) Technology Initiative 2 of the Transportation Infrastructure Construction and Condition Assessment, an intelligent Remote Sensing and GIS-based Asset Management System (RS-GAMS) Phase 2 was developed and validated in this research project by integrating CRS&SI technology that can be operated non-destructively at highway speed to improve the inventory, condition assessment, and management of pavement and roadway assets including asphalt and concrete pavement distresses, pavement markings, and roadway geometric characteristics.

1. Research Focuses

To meet transportation agencies' urgent needs, six research focuses were determined at the beginning of this research project through the extensive discussion between the Georgia Tech research team and the Technical Advisory Committee (TAC), formed by nationwide experts.

- Research Focus #1: Automatic asphalt pavement crack classification
- Research Focus #2: Concrete pavement distress detection
- Research Focus #3: Pavement marking condition assessment
- Research Focus #4: Extraction of roadway geometric characteristics, including cross slope, horizontal curvature, and pavement width
- Research Focus #5: Two prototype GIS-based asset management and decision support systems for an concrete pavement condition evaluation and an roadway horizontal curve safety assessment
- Research Focus #6: Standard file exchange format for line laser imaging data

2. Research Outcome and Major Findings

To validate the improvement of inventory, condition assessment, and management of pavement and roadway assets using CRS&SI technologies, an intelligent sensing vehicle, the Georgia Tech Sensing Vehicle (GTSV), was developed by integrating the state-of-the-practice and commercially available sensing devices and technologies, including 3D line laser imaging digital cameras, mobile Light Detection and Ranging (LiDAR), Inertial Measurement Unit

(IMU), Global Positioning System (GPS), and Geographic Information Systems (GIS). The following list the major findings for each of six research focuses:

- **Research Focus #1: Automatic asphalt pavement crack classification**

  This research focus validated the performance of an automatic crack classification algorithm developed by PI previously, using 3D line laser imaging data (for clarity's sake, called pavement surface laser data hereafter). The algorithm is based on a multi-scale Crack Fundamental Element (CFE) model and uses the crack detection results, i.e. crack maps, as inputs, which have been validated in RS-GAMS Phase 1. The classification of two most commonly occurring cracks, load cracking and block cracking defined in the Georgia Department of Transportation's (GDOT) pavement distress survey manual, Pavement Condition Evaluation System (PACES), were implemented, tested, and validated. The promising results demonstrated that the algorithm is capable of transforming the raw sensing data and the detected crack maps into useful decision-support information, including crack types, severity levels, and extents.

  In the first test set, the selected pavement surface laser data (the pavement surface laser data is stored and compressed in 1,069 images; each image covers about 5-meter long and 4-meter wide of the roadway section) was reviewed by GDOT pavement engineers to establish the ground truth. Then, the ground truth was compared with the automatically classified results. Based on GDOT's defined distresses, the algorithm showed an accuracy of 92.2% on classifying load cracking in four severity levels and 98.1% on classifying block cracking in three severity levels. In the second test set, ten 100-ft test sections were selected on State Route (SR) 236, SR 275, and SR 67 in Georgia. In each test section, GDOT pavement engineers visually identify the crack types, severity levels, and extents in field, which was used as ground truth. Among ten test sections, four of them were surveyed by accurate measurements using a measuring wheel, while the other six sections were surveyed by visual estimation following GDOT's current survey practices. Then, comparison was made on deducts derived from the automatic crack classification and the field visual survey. For the wheel-measured sections, the average absolute difference of total deducts was 3.25 out of 100 (a pavement rating is between 0 and 100), and for the visually-estimated sections, the

average absolute difference was 5 out of 100. Both differences were within the error tolerance based on GDOT's current practice (5 out of 100).

The validation results show that the use of pavement surface laser data and the corresponding algorithm could improve the productivity and efficiency of collecting decision-support information needed in existing pavement management system. Moreover, the fine-grained sensing data also opened the opportunity to improve existing pavement management by adding more detailed decision-support information that cannot be acquired before though further research is needed to develop new applications.

- **Research Focus #2: Concrete pavement distress detection**

  This research focus validated the detection and measurements of various concrete pavement distresses, including cracking, faulting, spalling, and shoulder joint distress using pavement surface laser data. The validation results demonstrate the potential of using pavement surface laser data for automatically detecting distresses in concrete pavements. The test sites were selected on interstate highways I-16 and I-516.

  The validation of concrete pavement cracking detection using pavement surface laser data showed acceptable performance. The automatic crack detection results were compared to the manually digitized ground truth using a buffered Hausdorff scoring method that was developed in RS-GAMS Phase 1. The results showed that detection of cracks on I-516 (mainly longitudinal cracks) is accurate and robust; however, the detection of cracks on I-16 (mainly transverse cracks) is not as good as the one on I-516. The larger data acquisition interval along the driving direction, which was about 5 mm, might be the reason that some transverse cracks cannot be captured by pavement surface laser data. In comparison, the transverse laser data resolution is about 1 mm, which can better capture the longitudinal cracks. Limited to the laser data resolution, hairline cracks (thinner than 2 mm) were still challenging for automatic detection.

  The validation of concrete joint faulting measurement showed that it is very feasible to use pavement surface laser data for collecting faulting data at highway speed. Using the regression-based method, the automatic faulting measurements were consistent with

manually measured ground truth using the Georgia Faultmeter in both well-controlled lab test and the field test.

The accuracy of automatic spalling detection varied for different sizes of spalling. Spalling with widths greater than 90 mm can be successfully detected; the detection accuracy was reduced, but still acceptable for the ones between 50 and 90 mm wide, while it was hard to detect when the width was less than 50 mm. Though some small spallings were not successfully detected, they can be clearly observed on the laser data. Thus, the automatic detection algorithm could be further improved to handle such cases.

Since there is no dedicated application that is commercially available for shoulder joint distress detection, we explored the feasibility of using an automatic spalling detection algorithm to detect shoulder joint distress. The larger extent and depth of shoulder joint distress make them distinctive on laser range data and easier to detect. On the selected representative cases, the automatic detection results were visually consistent with field observation. However, it should be noted that due to the transverse coverage of the current pavement surface laser data (about 4 meters), the shoulder area might be missed when the vehicle wanders. In addition, a specific shoulder joint distress detection algorithm is needed to further ensure an accurate and robust detection.

- **Research Focus #3: Pavement marking condition assessment**

This research focus was to establish the correlation between the retroreflectivity measured by handheld retroreflectometer and the retro-intensity acquired from LiDAR point cloud. Establishing a reliable correlation is the key step for assessing pavement marking retroreflectivity conditions using a mobile LiDAR. In this preliminary study, thermoplastic and waterborne paint were selected, which are the most commonly used pavement marking materials. Test sites were selected on Ferst Drive, Hemphill Avenue, and 17th Street on/near the Georgia Tech campus.

It was discovered that the retro-intensity values acquired from mobile LiDAR are not sensitive to ambient temperatures, with an average standard deviation less than 0.0041. The

retro-intensity acquired from mobile LiDAR held good repeatability on the tested thermoplastic and waterborne materials with an average standard deviation of 0.0044.

There was an exponential correlation between retroreflectivity and retro-intensity with an R-square of 0.9525 for thermoplastic and 0.9267 for waterborne paint. The correlation between retroreflectivity and retro-intensity might be sensitive to different bead formulas of the pavement marking material. Separate correlation curves might be needed not only for different pavement marking material category, e.g. thermoplastic, waterborne, etc., but also for different bead formulas in the same material category. Based on the correlation results, a preliminary retro-intensity threshold corresponding to the minimum retroreflectivity (100 mcd/m^2/lux) defined in the MUTCD could be defined as 0.4263, with a 95% confidence interval ranging from 0.4035 to 0.4505 for thermoplastic and 0.3521, with a 95% confidence interval ranging from 0.2973 to 0.4264. Using the established correlations, a mobile LiDAR-based pavement marking retroreflectivity condition assessment method can be further developed.

- **Research Focus #4: Extraction of roadway geometric characteristics including cross slope, horizontal curvature, and pavement width**

  This research focus validated the accuracy, repeatability, and productivity of extracting roadway geometric characteristics, including pavement cross slopes, roadway horizontal curvatures, and pavement widths, using various sensing technologies, such as aerial photo, airborne LiDAR, mobile LiDAR, video log images, and GPS tracks. The measurement accuracy, repeatability, and productivity were evaluated for each pair of data type and technology.

  1) Cross Slope

     Mobile LiDAR is the only feasible technology for cross slope measurement. Using mobile LiDAR, the measurement achieved a desirable accuracy with a maximum difference of 0.28% cross slope (i.e. 0.17°) and an average difference less than 0.13% cross slope (i.e. 0.08°) on the tested sections with cross slopes between 1.9% and 7.2%. The acceptable accuracy is typically 0.2% (or 0.1°) during the construction quality

control. Repeatability assessment results showed the proposed method can achieve a good repeatability with the standard deviations within 0.05% (i.e. 0.03°) at 15 different benchmarked locations in three different runs. The acceptable repeatability is typically 0.2% during the construction quality control. A case study conducted on I-285 showed that the continuous cross slope measurement on a 3-mile section of roadway can be derived in less than 2 man-hours using the collected raw mobile LiDAR data. In summary, mobile LiDAR demonstrated to be very promising for conducting pavement cross slope measurements.

2) Horizontal Curvature

Five technologies, including mobile LiDAR, GPS tracks, video log images, airborne LiDAR, and aerial photos, were evaluated for roadway horizontal curve measurements. Mobile LiDAR was found to be the most accurate (-0.35%) and precise (±6.65%) method. The dense LiDAR points also provide a better chance for measuring different curve types, and identifying and measuring the curve transitions. Aerial photo can be used for large-scale roadway curvature measurement because of the large area coverage. However, its 0.5 US-survey-feet resolution and the resultant aliasing error is an issue in delineating markings. Airborne LiDAR cannot achieve acceptable measurement accuracy because the LiDAR point spacing was about 1.87 feet and the majority of tested roadway curvature offsets were less than 2 ft, which makes it difficult to accurately measure curvature. The video log Image technology can also measure the roadway curvature fairly accurately (5.2%) with a relatively lower precision (±13.15%). GPS Track was identified as the most efficient and productive method in this study, and it took about 62.5% less time than the next quickest technology. It provided good accuracy (-3.63%) and a precision (±10.76%), which is only next to mobile LiDAR technology. However, both the repeatability and the accuracy of the GPS track method relied on how close the data collection track is to the actual pavement lane. GPS data can be easily acquired, and the curve computation process is straightforward and can be fully automated. Thus, this method is very promising for highway agencies' practical use.

3) Pavement Width

Mobile LiDAR technology showed the best performance in pavement width measurement, in terms of accuracy (0.04% relative error), precision (±0.13%) and repeatability (0.1% variability). Mobile LiDAR technology, also, demonstrated good productivity in continuous pavement width measurement. Aerial photo and airborne LiDAR demonstrated relatively good accuracy and precision. However, the accuracy and precision were impacted by the difficulties in identifying the delineation of the road (i.e. starting and ending points for measurement) due to the limited data resolution, i.e. with an average density of 1.87 ft in the airborne LiDAR data used in this study and 0.5 US-survey-feet resolution in the aerial photo data used in this study. The effect of obstruction was also a factor that affects the measurement accuracy. Nevertheless, because both aerial photo and airborne LiDAR data have good area coverage in comparison to the limited roadway area captured by mobile LiDAR, they are feasible methods for conducting large-scale measurement with a less stringent accuracy requirement, e.g. for land use planning purposes. Video log image technology was fairly accurate (5.2%) and precise (±13.15%) for pavement width measurement. It also showed good repeatability (0.5% variability) in the repeatability assessment. Video log image technology also demonstrated the best productivity in measuring pavement width because it contains the best visual view to identify the measurement location and to conduct the measurement. However, the potential issue with this method is that the measurement accuracy relies on the accuracy of camera calibration, which requires rigorous computation and adjustment, which might be challenging for immediate use in transportation agencies. In addition, the coverage of the video log image is also limited. Therefore, multiple runs and multiple cameras will be needed for full coverage of different widths in both driving directions.

- **Research Focus #5: Two prototype GIS-based asset management and decision support systems for an concrete pavement condition evaluation and an roadway horizontal curve safety assessment**

  This research focus developed two prototype GIS-based applications to demonstrate the capabilities of using GIS as a platform to integrate different data sources and support various decision makings.

  The first prototype GIS application was to expedite concrete pavement condition evaluation. This application provided an adjustable visualization function that creates an accurate, instant, and comprehensive understanding of both overall roadway rating and the occurrences of a certain type of distress. Unlike the traditional survey method, which only has tabular data for project-level or segment-level pavement conditions, this application can accurately locate every single distress and provide slab-level spatial-referenced pavement distress images. These data provide all the detailed and necessary information to validate a maintenance decision, eliminating the need of additional field trips and greatly reducing the influence of subjectivity. Different data collected from different survey times (e.g. quarterly or annually) further provide an evolving image of the pavement condition, making effectiveness examination of treatment much easier and more efficient. In addition, the powerful search function makes distress data management and utilization much more flexible and user-friendly.

  The second prototype GIS application was to perform roadway horizontal curvature safety assessment. This application provides a convenient tool to help transportation agencies efficiently conduct roadway safety analysis. The roadway geometry data derived from different emerging sensing technologies can be conveniently imported to the developed application. The operators can flexibly input parameters based on engineering experience or official guidelines. More importantly, they can flexibly adjust the parameters under different analysis scenarios. The application was developed upon the GIS framework, which enables an immediate visualization of the analysis results. Additional GIS data, such as crash report data, can be seamlessly integrated with this application to generate more meaningful information for more in-depth safety analysis. In this study, horizontal curvature safety

assessment was used to demonstrate the capability of the developed application. With additional pavement geometry data, e.g. vertical curvature, grade, etc., the developed application can be immediately migrated to other safety elements that are important to different transportation agencies.

- **Research Focus #6: Standard file exchange format for line laser imaging data**

  This research focus suggested a standard File Exchange Format (FEF) for pavement surface laser data, including both 3D range and intensity data. Currently, it is difficult for a highway agency, who owns the line laser imaging data, to extract useful decision-support information because of the lack of a standard FEF. The data in a proprietary format can only be processed by the vendor who provides the data collection service. This largely limits the use of line laser imaging data because third party algorithms cannot be used for data extraction. This study suggested a standard FEF that can be implemented by vendors who provides data collection services. Thus, a highway agency will have the flexibility to use a third party for data processing. Also, data collected by different vendors can be easily combined and reused. This will significantly save agencies' cost and minimize the risk of not being able to use the collected data. In addition, interested third parties can focus on developing algorithms and applications for data processing and extraction without the restrictions of having to use a specific proprietary data format or developing their own hardware and data format. Although an initial attempt has been made to develop a standard FEF in this study to address this urgent need, a follow-up study is recommended to refine and implement the FEF by working closely with transportation agencies, manufacturers, and service providers who are developing and using line laser imaging data. To make the data quality consistent and adequate for highway agencies' different applications, which is provided from different vendors and at different times, a standard calibration procedure is also needed. In addition, a suitable data compression method is required along with the suggested FEF, which needs further study.

3. Recommendations for Future Research and Implementation

The following suggest the future research and implementation:

- With the promising results from the automatic asphalt pavement crack classification for load cracking and block cracking, it is recommended to extend the automatic classification to other types of distresses as defined in GDOT pavement distress manual. In addition, the algorithms can be easily extended to other crack survey protocols used by different state highway agencies because of the flexibility provided by the crack CFE model.

  The validated results of automatic cracking classification for load cracking and block cracking can be implemented in GDOT's pavement condition survey practice. Since these are the two major crack types in Georgia, it can dramatically save the field survey effort and improve the data quality and coverage. The Georgia Tech research team will work with GDOT to select large-scale roadways for testing. The results will be fed into GDOT's current pavement management system.

- The validation results for automatic concrete pavement faulting measurements showed very good consistency with manual measurements using a Georgia Faultmeter. A large-scale pilot study with a state DOT, e.g. GDOT, is suggested to automate the network-level faulting measurements. This can significantly improve the productivity, data accuracy, and data coverage.

- The concrete pavement crack detection shows promising results. However, it is difficult to detect hairline, transverse cracks due to the relatively coarser data resolution at the driving direction using the current line laser imaging device. Thus, to capture hairline cracks, the data capture frequency and resolution of a line laser imaging device needs to be further improved. In addition, to automate the crack evaluation for concrete pavements, automatic crack classification algorithms need to be developed, which can be based on the work we have done for asphalt pavements.

- New algorithms need to be developed because the automatic detection for concrete spalling doesn't work well on those with width less than 50 mm. In addition, new algorithms are needed for automatic shoulder joint distress detection.

- The pavement marking validation results indicate that pavement marking retroreflectivity conditions could be measured and evaluated using mobile LiDAR that can be operated at highway speed. However, the testing samples in this research project are limited. It is suggested that large-scale testing on more marking materials be conducted before it can be implemented.

- The validation results for roadway geometric characteristics data extraction can be used by state DOTs to select proper sensing technologies in considering data accuracy requirements and measurement productivity. Since horizontal curvatures and pavement cross slopes are important factors for roadway safety, a large-scale pilot study with a state DOT, e.g. GDOT, is suggested to automate the data collection procedures.

- A pilot study with a state DOT, e.g. GDOT, is suggested as a way to implement the two prototype GIS applications for concrete pavement condition evaluation and roadway horizontal curve safety assessment by integrating various large-scale data sources to support state highway agencies' decision making. The developed prototype GIS applications can also be useful for local transportation agencies (counties and cities) because of their limited resources to manage pavement condition data and conduct roadway safety analysis.

- With the urgent need of fully utilizing line laser imaging data for extracting useful decision-support information, a follow-up study is recommended to refine and implement the suggested standard FEF by closely working with selected transportation agencies, hardware manufacturers, and data collection service providers.

Chapter 1 Introduction

1. Background and Research Need

To propose technology that supports the application and validation of the U.S. Department of Transportation (DOT) Commercial Remote Sensing and Spatial Information (CRS&SI) technology Initiative 2 of the Transportation Infrastructure Construction and Condition Assessment, an intelligent Remote Sensing and GIS-based Asset Management System (RS-GAMS) was proposed and validated in this research project by integrating CRS&SI technology, which can be operated non-destructively at highway speed to improve the inventory, condition assessment, and management of roadway assets.

Figure 1-1 illustrates the architecture of the proposed RS-GAMS. An intelligent sensing vehicle, the Georgia Tech Sensing Vehicle (GTSV), was developed by integrating the state-of-the-practice and commercially available sensing devices and technologies, including 3D line laser imaging device, digital cameras, mobile Light Detection and Ranging (LiDAR), Inertial Measurement Unit (IMU), Global Positioning System (GPS), and Geographic Information Systems (GIS). Appendix I and II list the hardware specifications for the 3D line laser imaging system and mobile LiDAR system. As part of the comprehensive transportation asset management system, these CRS&SI technologies play an important role in collecting various transportation asset data, including traffic signs, pavement surface conditions, roadway characteristics, etc., which critically support data-driven decision-making. GIS is an excellent platform with which to integrate different data sources and provide convenient spatial data management functionalities. In the past, manual processing has been the major means of data collection; however, it is labor-intensive and time-consuming, and it also suffers from subjectivity and inaccuracy. As a result, the subsequent decision-making lacks reliability. With the advancement of CRS&SI technologies, the data collection process can be significantly improved with regard to its speed, comprehensiveness, accuracy, and reliability. However, the application of a new technology always lags behind its development due to the end users' concern regarding its usability and the risk resulting from the failure of significant investment. This technology gap can only be bridged by comprehensive testing and validation. This research project addresses this issue and aims to validate the applications of 3D line laser imaging

technology (for clarity's sake, the data collected by a 3D line laser imaging device is called pavement surface laser data, hereafter) and mobile Light Detection and Ranging (LiDAR) technology in assessing pavement surface distresses and roadway geometric characteristics. The first phase of this research project validated the automatic measurement of asphalt pavement rutting, automatic detection of asphalt pavement cracking, and automatic sign traffic sign data collection, as shown by the light grey blocks in Figure 1-1. The validation results in RS-GAMS Phase 1 can be found in the final report by Tsai and Wang (2013). This final report focuses on the validation results of RS-GAMS Phase 2. As shown in Figure 1-1, the dark grey blocks indicate the validated pavement distresses and roadway geometric characteristics (for asphalt pavement, the automatic classification of pavement cracks is also included in RS-GAMS Phase 2).

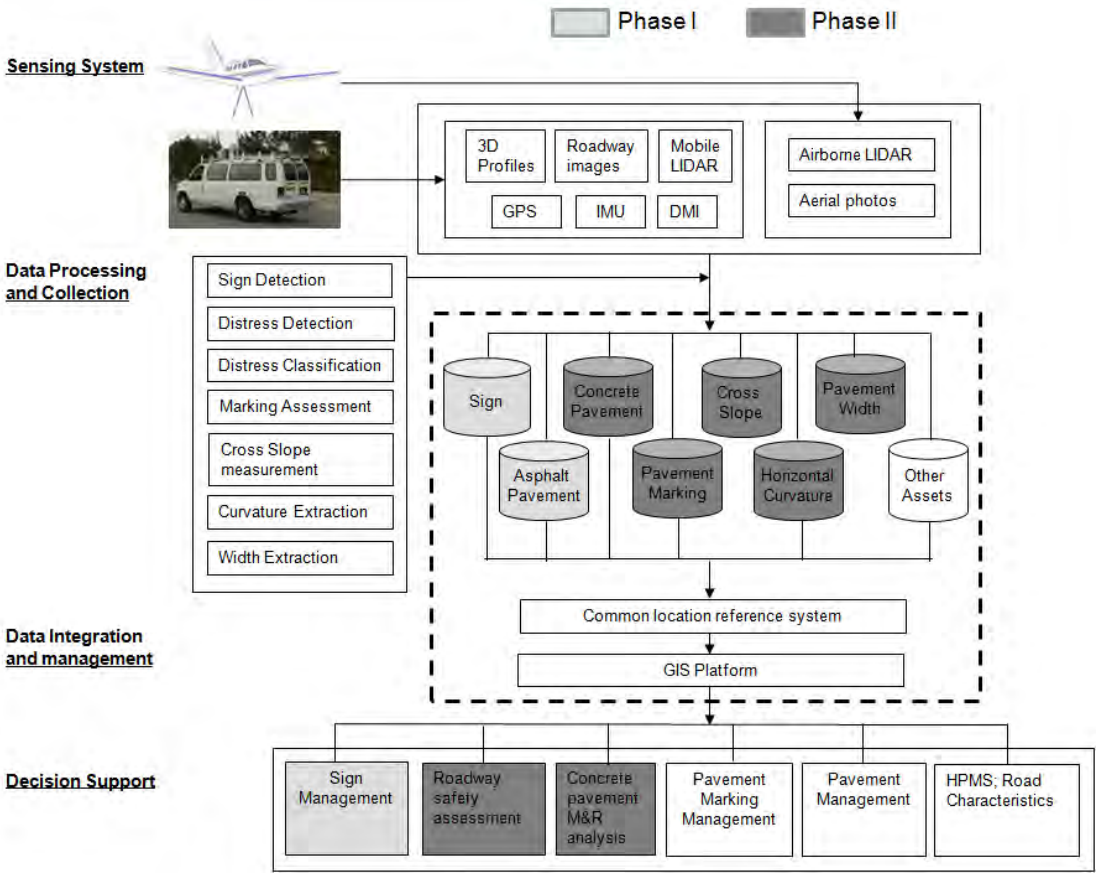

Figure 1-1 RS-GAMS architecture

The following are the challenges and research needs for inventory, condition assessment, and management of these roadway assets.

- **Pavement Asset**

  Pavement surface distress measurement is an essential part of a pavement management system (PMS) for determining cost-effective maintenance and rehabilitation strategies. A visual survey conducted by engineers in the field is still the most widely used means to inspect and evaluate pavement surface conditions, although such evaluation involves high degrees of subjectivity, hazardous exposure, and low production rates. Consequently, automated distress data collection is gaining wide popularity among transportation agencies. In the past two decades, many researchers have been developing pavement distress detection algorithms using 2D intensity-based images and, also, improving artificial illumination. However, it still remains a challenge to accurately and reliably detect and classify pavement distresses because of the inadequate pavement distress detection under various lighting conditions, contrasts, roadway environments, and weather conditions. In addition, these illumination systems are expensive and require routine replacement. The 3D line laser imaging technology has provided a different data acquisition mechanism, and it collects 3D pavement surface laser data (elevation) rather than the traditional 2D image data (intensity) that is sensitive to lighting conditions. This provides us a totally different opportunity to explore its capabilities of detecting and classifying pavement distresses. To validate the full potential of the emerging technologies on developing new transportation applications, it is desirable to use cutting-edge and commercialized products to minimize the limitations and uncertainty caused by the developing counterparts. Using the 3D line laser imaging technology, a comprehensive validation is needed to evaluate its capability of detecting and classifying these pavement distresses under different roadway environments (e.g. lighting, shadows, etc.) and different pavement conditions (e.g. crack severities ranging from fine to large). This validation will be indispensable for transportation agencies when they are seeking technologies to bring new capabilities to pavement distress detection and classification.

- **Roadway Asset**

  Pavement marking condition is critical to transportation safety. However, the manual survey method is very time consuming and infeasible for a network-level survey. Though the dedicated mobile survey method can improve the productivity, it is very costly. There is a need to explore a low-cost, mobile pavement marking condition assessment using mobile LiDAR technology.

  Collecting roadway geometric characteristics, including cross slope, roadway curvature, and pavement width, is important for transportation planning and roadway safety analysis. However, manual data collection for these roadway characteristics is very time consuming. This study explored the feasibility of measuring cross slope using LiDAR technologies. With emerging CRS&SI technologies, the resolution and accuracy of airborne LiDAR, GPS, and roadway images continue to increase and can be used to extract roadway curvature and pavement width. To provide valuable information for transportation agencies to make effective choices among different CRS&SI technologies for the applications with different desirable accuracy, there is a need to validate and compare them.

2. Research Approach and Focuses

Through discussion with the Technical Advisory committee (TAC), six research focuses were identified to address transportation agencies' urgent needs.

- **Research Focus #1: Automatic asphalt pavement crack classification**

  This research focus validates the performance of an automatic crack classification algorithm (previously developed by the PI) using pavement surface laser data. The algorithm is based on a multi-scale Crack Fundamental Element (CFE) model and uses the crack detection results, which have been comprehensively validated in RS-GAMS Phase 1, as inputs. The classification of two commonly occurring types of cracking, load cracking and block cracking, defined in the Georgia Department of Transportation's (GDOT) pavement distress survey manual, Pavement Condition Evaluation System (PACES), were implemented, tested, and validated.

- **Research Focus #2: Concrete pavement distress detection**

  This research focus validated the detection and measurements of various concrete pavement distresses, including cracking, faulting, spalling, and shoulder joint distress, using pavement surface laser data. The test sites were selected on interstate highways of I-16 and I-516.

- **Research Focus #3: Pavement marking condition assessment**

  This study focuses on evaluating the feasibility of using mobile LiDAR to perform pavement marking retroreflectivity condition assessment. Thermoplastic and waterborne paint, the most commonly used pavement marking materials, were selected to conduct the feasibility study. Test sites were selected on Ferst Drive, Hemphill Avenue, and 17th Street on/near the Georgia Tech campus.

- **Research Focus #4: Extraction of roadway geometric characteristics including cross slope, horizontal curvature, and pavement width**

  This research focus validates the roadway geometric characteristics data extraction, including pavement cross slopes, roadway horizontal curvatures, and pavement widths, using five sensing technologies, including aerial photo, airborne LiDAR, mobile LiDAR, video log images, and GPS tracks. The measurement accuracy, repeatability, and productivity were evaluated for each pair of data type and technology.

- **Research Focus #5: Two prototype GIS-based asset management and decision support systems for an concrete pavement condition evaluation and an roadway horizontal curve safety assessment**

  This research focus develops two prototype GIS-based applications to demonstrate the capabilities of using GIS as a platform to integrate different data sources to effectively support various decision-making processes.

- **Research Focus #6: Standard file exchange format for line laser imaging data**

  This research focus suggests a standard File Exchange Format (FEF) for pavement surface laser data, including both 3D range and intensity data. Thus, a highway agency will have the

flexibility to use a third party for data processing while the data can be provided by another vendor. Also, data collected by different vendors can be easily combined and reused. This will significantly save agencies' cost and minimize the risk of not being able to use the collected data.

3. Report Organization

This report is organized into ten chapters. Chapter 1 summarizes the research background, need, and approaches; Chapter 2 presents the validation results for asphalt pavement crack classification; Chapter 3 presents validation results for concrete pavement distress detection; Chapter 4 presents the feasibility study of pavement marking retroreflectivity condition assessment; Chapter 5 presents the extraction of roadway geometric characteristics including pavement cross slopes, roadway horizontal curvatures, and pavement widths; Chapter 6 introduces a prototype GIS-based expedited concrete pavement condition evaluation application; Chapter 7 introduces a prototype GIS-based expedited roadway safety assessment system; Chapter 8 suggests a standard FEF for pavement surface laser data; Chapter 9 discusses the outreach of the research results; and Chapter 10 summarizes the conclusions and makes recommendations for future research.

References

Tsai, Y. C. and Wang, Z. (2013). "A Remote Sensing And GIS-Enabled Asset Management System (RS-GAMS)." *Final Report*, Contract Number: DTOS59-10-H-0003, US Department of Transportation.

Chapter 2 Automatic Asphalt Pavement Crack Classification

This chapter presents the research results for validating the automatic crack classification for asphalt pavements, Research Focus #1.

1. Introduction

Pavement surface distress evaluation is an essential component of a pavement management system (PMS). Cracking, as one of the most common types of pavement distresses, is caused by constant overloading, asphalt aging, environmental impact, and improper structural design, etc. Progressive cracking can weaken pavement because it allows water and other foreign objects into the base and accelerates pavement deterioration. The proper treatment of pavement cracks at the optimal timing is important for cost-effective pavement maintenance. Many transportation agencies, including the GDOT, have invested major resources in their pavement condition survey and evaluation procedures to enhance their decision-making capabilities.

Traditionally, the collection of pavement crack data is usually done by visual inspection in the field. For example, in GDOT's practice, pavement surveyors manually identify the presence, types, and severity levels of cracking, and then estimate/measure and record the extent of each crack type and severity level. Such a task is dangerous, subjective, costly, time-consuming, and labor-intensive. Therefore, automatic pavement cracking evaluation is gaining attention among transportation agencies and researchers. To transform the manual practice into an automatic procedure, at least two steps should be included. Crack detection is the first step to identify the presence of pavement cracking from the collected pavement data and generate a crack map. Crack classification is the second step to automatically identify the types and severity levels from the detected crack map. Automatic crack detection using the emerging 3D line laser imaging technology has been validated in the RS-GAMS Phase 1 study. This study focuses on the validation of crack classification.

An automatic crack classification and quantification method has been previously developed by the PI following the GDOT PACES distress protocol. The pavement surface laser data can produce relatively more accurate crack map detection, and the objective of this research is to conduct a validation of the automatic crack classification and quantification using this input. This chapter is organized as follows. After an introduction in Section 1, Section 2 summarizes the

major findings through the literature review, including both current pavement distress protocols used in different federal and state transportation agencies and existing automatic crack classification algorithms. Section 3 presents the basic concept of the automatic crack classification and quantification method previously developed by the PI, followed by a comprehensive validation in Section 4. The GDOT PACES distress protocol is used as an example to demonstrate the performance of automatic asphalt crack classification. Section 5 presents an outreach study that applies the automatic crack classification and quantification method on the interstate highways, which are usually high-traffic-volume roadways and are challenging for the traditional manual survey; it visualizes the network-level pavement condition to support decision-making. In the end, Section 6 summarizes the major findings in this study.

2. Summary of Literature Review

The literature review in this chapter covers two aspects. First, the current pavement cracking survey practices from different federal and state transportation agencies are reviewed to better understand the objective of the automatic crack classification task and identify the similarities and differences between protocols. Then, the existing automatic crack classification algorithms are reviewed to understand the current status of automatic algorithm development and identify the gap between the current status and the desired crack classification objective. Appendixes III and IV present the content of the literature review in detail. The major findings are summarized as follows:

From the perspective of agency's current pavement distress protocols,

- **Complexity**: Transportation agencies usually have complicated and diverse crack definitions in their survey practice. The real-world distress protocols from transportation agencies usually involve human identification of complex crack patterns. Furthermore, for most protocols, multiple severity levels are defined under the same crack type, which also have an important impact on the pavement condition evaluation.
- **Subjectivity**: Though the detailed crack definitions are described in the protocols, the crack patterns on the real pavement are still diverse. Even for experienced human surveyors, different engineers may provide different crack survey results on the same

roadway section. An automatic crack classification and quantification method will overcome this issue and provide consistent results.

- **Diversity**: Different protocols are developed for different purposes. For example, the GDOT PACES protocol has a causal-based crack definition so that the crack survey results can directly contribute to their maintenance operations; the Long-term Pavement Performance (LTPP) protocol is a research grade data collection and focuses more on how to precisely record every single crack on the road. The data can be used for Mechanistic-Empirical Pavement Design Guide (MEPDG) calibration and validation. Different purposes lead to diverse crack definitions. The diversity between protocols makes it difficult to transform the automatic crack classification algorithm from one protocol to another.

From the perspective of existing automatic crack classification algorithms,

- **Preliminary outcomes**: In terms of classification, most of the existing studies provide the following crack type outcomes: longitudinal, transverse, diagonal, alligator, and block, etc. Such an outcome format simplified the classification problem but limited the real-world implementation. It is hard to establish the correlation between these preliminary outcomes and the actual crack definitions used by transportation agencies.
- **Limited crack characteristics**: Crack orientation and crack amount are two major characteristics that have been studied for automatic classification purposes. However, manual survey protocols require more characteristics, such as crack location, crack intersection, and possible polygon patterns.
- **No severity levels**: The classification of different crack severity levels is explored in the existing literature.
- **Lack of flexibility**: Most existing algorithms take the entire image as an input. The crack classification will be less effective when multiple crack types appear on the same image, and this also creates a significant challenge for accurate crack extent quantification.
- **Limited performance**: Most studies only validate their methods on a small set of pavement images. Some large-scale studies have shown that current automatic crack classification and quantification survey results usually have a poor correlation with manual survey results.

Overall, an automatic crack classification and quantification method still remains a challenge from the perspective of practical implementation. Targeting the gap between current status of automatic crack classification and real-world crack survey protocols, the following section will present a multi-scale crack representation approach for crack classification.

3. Multi-Scale Crack Representation for Crack Classification

Crack pattern, together with other crack properties, is crucial for differentiating crack types and severity levels in transportation agencies' pavement survey practices. The PI proposed a multi-scale CFE model in a previous study (Tsai & Jiang, 2012). This model topologically provides rich crack properties at three different scales (fundamental crack properties, aggregated crack properties, and clustered CFE geometrical properties) to support the development of an automatic crack classification method. It also standardizes crack performance measures for different transportation agencies and effectively deals with the diversity among different protocols. Figure 2-1 shows crack properties at three scales defined in the CFE model.

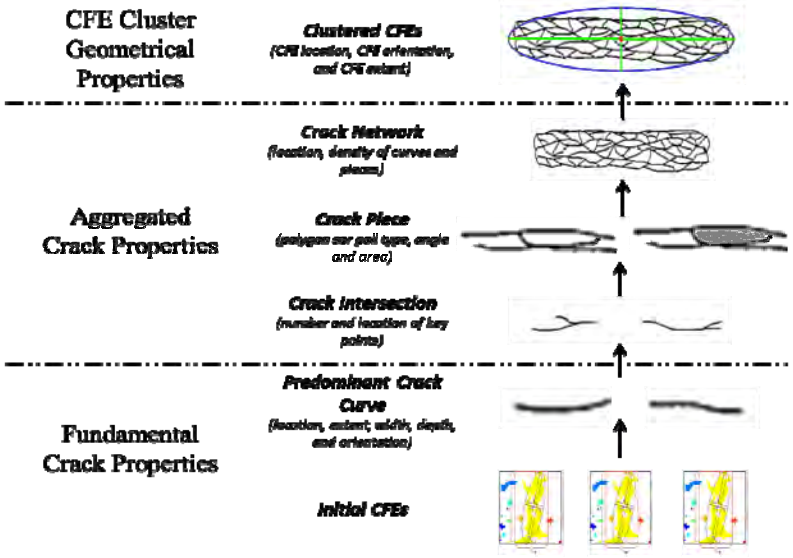

Figure 2-1 Multi-scale crack properties from CFE model (Tsai & Jiang, 2012)

The input for the multi-scale CFE model is the automated detected crack map. This crack map can be derived from either 2D or 3D data. Fundamental crack properties focus on each crack segment and describe the fundamental and physical properties of the cracks, including crack width, depth, length, etc.; aggregated crack properties focus more on crack patterns inside the

CFE and represent how cracks interact with each other, such as crack intersection, crack polygon, crack density, etc.; clustered CFE geometrical properties treat each CFE as a whole and describe its overall properties, including the CFE center, orientation, length, and width. From the bottom, the model represents the physical characteristics of pavement cracks; from the top, it tends to mimic the pavement engineers' manual evaluation procedure in the field (from the macro to the micro level observation). When experienced pavement engineers conduct a condition survey, they do not usually measure the crack width and depth first; instead, they first identify a group of cracks that should be clustered together as one element (CFE); then, they look at the crack pattern inside the CFE, and, finally, they measure the physical and fundamental crack properties. By clearly defining three scales of crack representation, the model can better incorporate both fundamental crack properties and human judgment. The method's features are explained in the following aspects:

- Consistency: The crack properties extracted through this model are independent from different pavement distress protocols. These crack properties, such as crack length, crack width, etc., are directly derived from the pavement data and detected crack map and are not influenced by agencies' protocols or survey practices. This consistency is critical as a standardized crack performance measure.
- Flexibility: These properties can be easily transformed between different protocols to develop a corresponding crack classification method through certain rules and criteria (as shown in Figure 2-2).

Based on this multi-scale crack representation concept, the PI further developed a crack classification and quantification method following the GDOT PACES distress protocol. The method itself doesn't require specific data format or crack detection algorithms, but the accurate crack detection using 3D pavement surface data is expected to provide better input.

4. Validation of the Automatic Crack Classification Method

4.1 Validation objective

The objective of this study is to validate the feasibility of automatic crack classification and quantification on asphalt pavements. To do so, we first validate the accuracy of automatic crack classification method on a large and diverse set of pavement images, and then compare the

results from the automatic crack classification and quantification with the field survey results conducted by experienced pavement engineers. The GDOT PACES distress protocol is selected as an example to conduct the validation. Load cracking and block cracking (in GDOT, transverse crack is also categorized as block cracking. For clarity's sake, we use block/transverse (B/T), hereafter), as two predominant asphalt pavement distresses in Georgia, are the focus of this The crack classification method can be easily extended to other crack-related distresses and protocols.

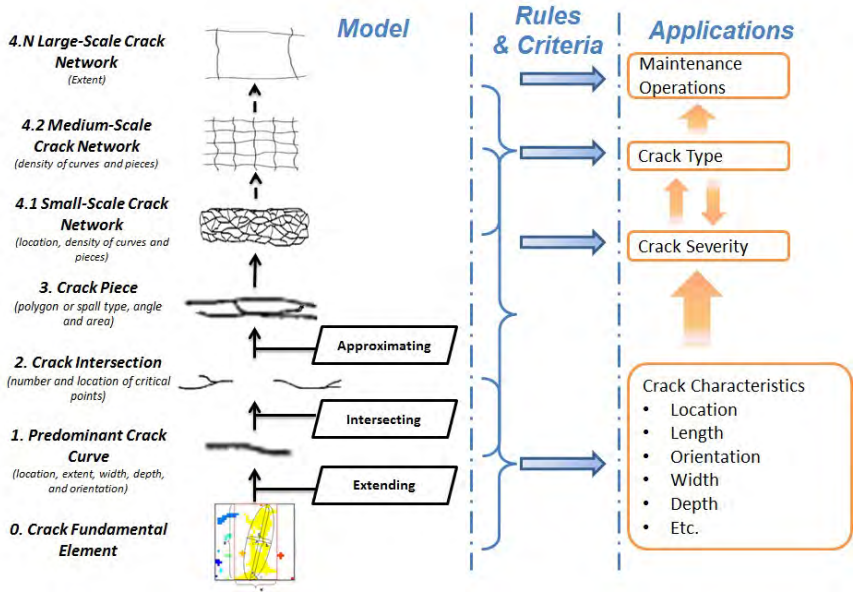

Figure 2-2 Crack classification using the extracted crack properties

4.2 Experimental design

Two series of experimental tests are conducted to fulfill the validation objective:

- An image-based validation test is conducted on State Route 236 / Lavista Road in Atlanta, Georgia to validate the accuracy of crack classification. With help from GDOT pavement engineers, each pavement image is visually reviewed, and the presence and severity level of load cracking and B/T cracking are manually labeled. In this test, we validate conduct an image-by-image comparison between the automatic crack classification results and manual labels.
- A site-based validation test is conducted to compare the results from automatic and manual field survey. It validates the accuracy of both crack classification and

quantification. Following GDOT's current pavement surface condition survey practice, ten 100-ft pavement sections are selected on SR 236, SR 275 and SR 67. Manual field surveys for load cracking and B/T cracking are conducted by GDOT liaison engineers. On the other hand, automatic crack evaluation also provides crack types, severity levels and extents on these selected sections. The deduct values caused by load cracking and B/T cracking are calculated and compared between automatic and manual crack survey.

In this study, the Laser Crack Measurement System (LCMS) is used to collect the 3D surface pavement data, and the crack detection is conducted using the analyzer software along with the system. The dimension of each pavement image is five-meter long in the driving direction and approximately four meters wide in the transverse direction. A large and diverse dataset is prepared to cover diverse crack characteristics.

- Crack type and severity levels: load cracking and B/T cracking are the focus of this test, and the experimental data cover all four severity levels for load cracking and three severity levels for B/T cracking. A total of 2,335 load cracking images are prepared, including 881 images with no load cracking, 1,145 images with Severity Level 1, 158 images with Severity Level 2, 136 images with Severity Level 3, and 15 images with Severity Level 4. A total of 1,224 B/T cracking images are prepared, including 97 images with no B/T cracking, 1006 images with Severity Level 1, 108 images with Severity Level 2, and 13 images with Severity Level 3. The crack type and severity level are labeled through manual review.
- Combination of multiple crack types: in the current manual field survey, the combination of multiple crack types mostly introduces the inconsistency into the survey results. A large portion of experimental data are pavement images that contains both load cracking and B/T cracking, in order to validate the performance of automatic crack classification on these cases.
- Crack location: the cracks are randomly located in the left wheel path, right wheel path, and non-wheel path regions in the experimental data. The correct extraction of crack location is the basis for load and B/T cracking classification.
- Crack pattern: as the severity level increases, the crack patterns in the experimental data changes gradually from single crack line to intersected crack networks. The capability of

interpreting complex and diverse crack patterns is another important aspect to be validated for the automatic crack classification.

The following subsections will present the validation tests and results in details.

4.3 Image-based validation

An image-based validation is first conducted on State Route 236 / Lavista Road in Atlanta, Georgia. The selected project, which has an excessive amount of load cracking and B/T cracking, starts from Milepost 0 (Atlanta city limit) to about Milepost 6.8 (I-285 Bridge). The experimental data includes 2,335 images for load cracking and 1,224 images for B/T cracking. The data from each crack type and severity level are randomly separated into two sets: 70% of the data are used for model training and calibration, while the rest, 30%, are used for testing.

Performance of load cracking classification

For load cracking, the training set consists of 619 images of no load cracking, 798 images of Severity Level 1, 108 images of Severity Level 2, 99 images of Severity Level 3, and 11 images of Severity Level 4. The algorithm performance on the test set is shown in Table 2-1.

Table 2-1 Performance of Load Cracking Classification

		Classified Severity Level						
		None	Level 1	Level 2	Level 3	Level 4	Total	Recall (%)
Actual Severity Level	None	247	15	0	0	0	262	94.3
	Level 1	10	317	20	0	0	347	91.4
	Level 2	0	6	42	2	0	50	84.0
	Level 3	0	0	2	35	0	37	94.6
	Level 4	0	0	0	0	4	4	100.0
	Total	257	338	64	37	4	700	
	Precision (%)	96.1	93.8	65.6	94.6	100.0		92.2

As shown in Table 2-1, a total of 700 test images are selected. The algorithm has overall high classification accuracy at about 92.2%. From the perspective of recall (i.e. the ratio of correctly classified cases to total actual cases), a larger portion of Severity Level 2 is not correctly classified compared to other severity levels. From the perspective of precision (i.e. the ratio of correctly classified cases to total classified cases), the classification for Severity Level 2 is quite low, which is mainly due to the clear difference between the sample sizes. Some representative

cases for load cracking and their automatic classification and quantification outcomes are shown in Figure 2-3.

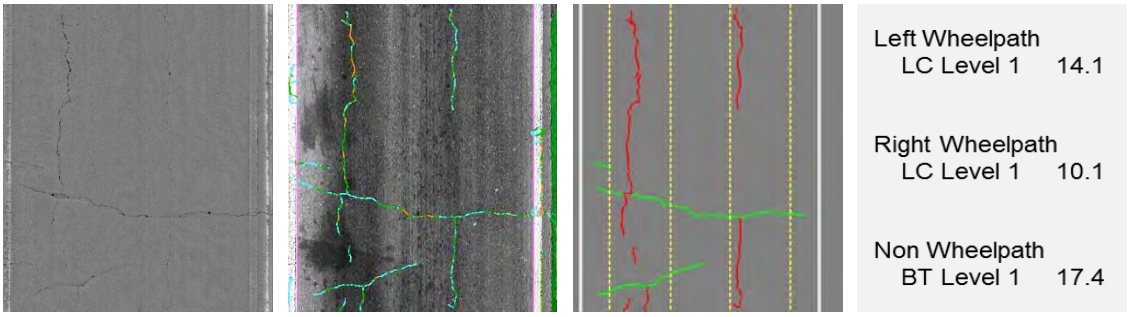

(a) Severity Level 1

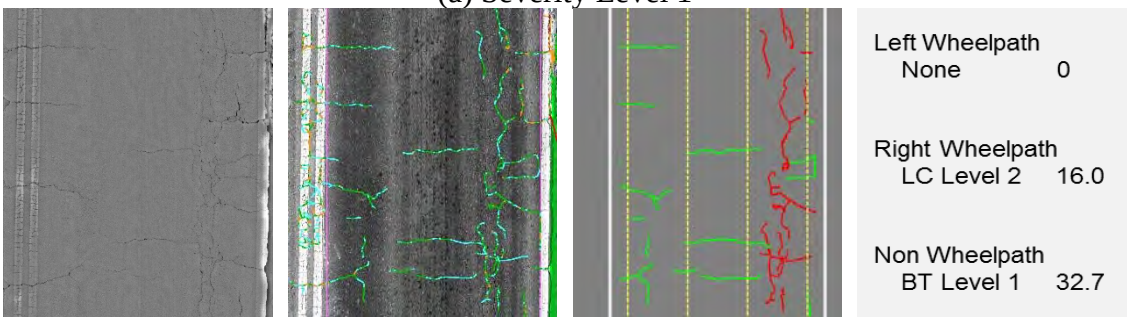

(b) Severity Level 2

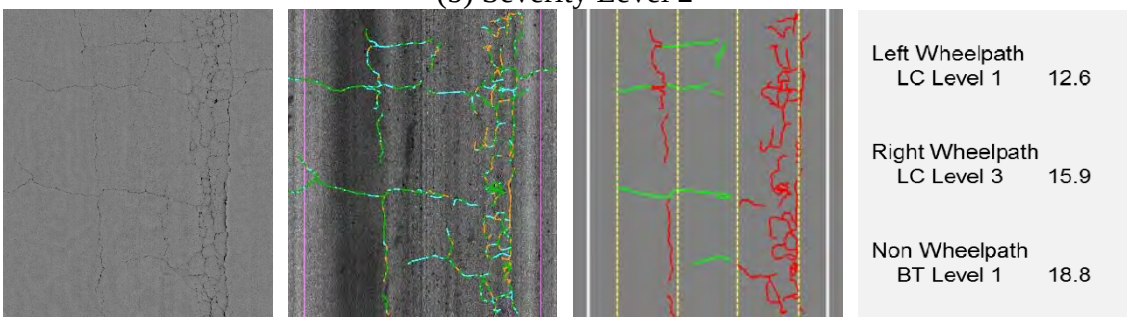

(c) Severity Level 3

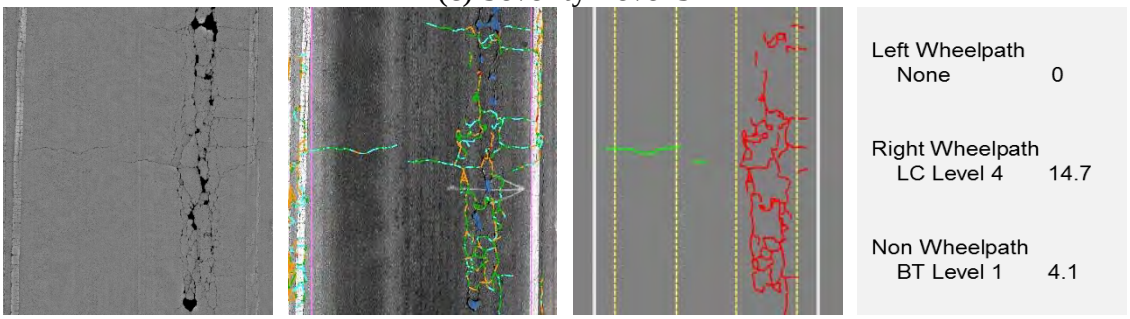

(d) Severity Level 4

Figure 2-3 Representative load cracking evaluation outcomes, from left to right: range image, crack map on intensity image, load cracking (red) and B/T cracking (green), and evaluation outcomes (unit: foot)

Performance of B/T cracking classification

For B/T cracking, the training set consists of 68 images of no B/T cracking, 703 images of Severity Level 1, 74 images of Severity Level 2, and 10 images of Severity Level 3. The algorithm performance on the test set is shown in Table 2-2.

Table 2-2 Performance of B/T Cracking Classification

		Classified Severity Level					
		None	Level 1	Level 2	Level 3	Total	Recall (%)
Actual Severity Level	None	27	2	0	0	29	93.1
	Level 1	1	298	4	0	303	98.3
	Level 2	0	0	31	3	34	91.2
	Level 3	0	0	0	3	3	100.0
	Total	28	300	35	6	369	
	Precision (%)	96.4	99.3	88.6	50.0		97.2

As shown in Table 2-2, a total of 369 test images are selected. The algorithm has, overall, high classification accuracy at about 97.2%. The results are also promising from the perspectives of both precision and recall. One possible reason is that the three target classes have quite distinctive differences on the crack properties. More data are still needed to further provide a more robust classification to Severity Levels 2 and 3. Some representative cases for B/T cracking and their automatic classification and quantification outcomes are shown in Figure 2-4.

4.4 Site-based validation

Section validations are further conducted to compare the results from automatic and manual crack surveys. Following GDOT's current crack survey practice, ten 100-ft pavement sections are selected on SR 236, SR 275 and SR 67. Manual field surveys for load cracking and B/T cracking are conducted. On the other hand, the automatic crack classification and quantification method provides crack types, severity levels and extents. The deduct values are calculated and compared between manual survey and automatic crack evaluation, and the results are presented as follows.

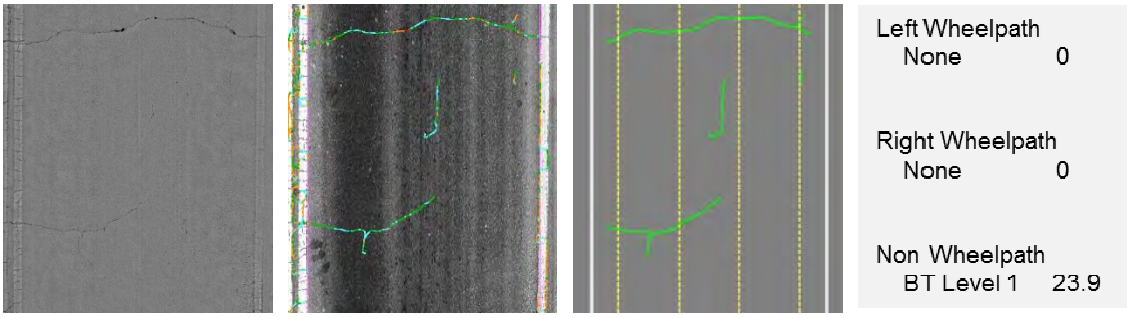

(a) Severity Level 1

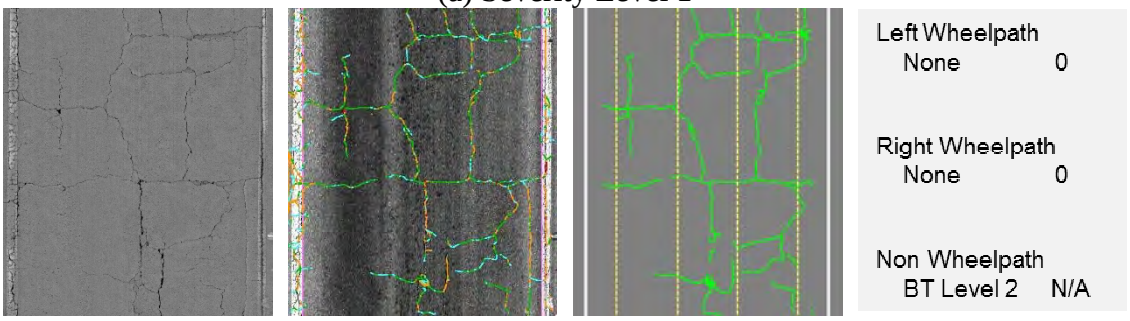

(b) Severity Level 2

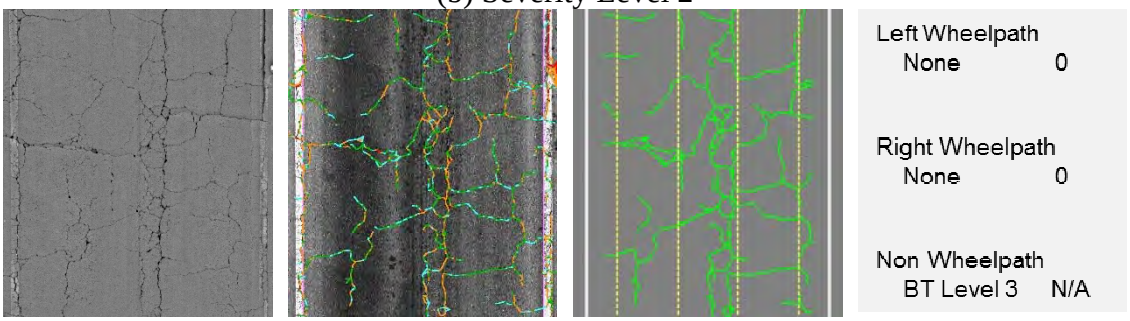

(c) Severity Level 3

Figure 2-4 Representative B/T cracking evaluation outcomes, from left to right: range image, crack map on intensity image, load cracking (red) and B/T cracking (green), and evaluation outcomes (unit: foot)

Validation on wheel-measured sections

On four selected sites, GDOT pavement engineers visually identify the crack types and severity levels in the field, and the crack extents are measured using a measuring wheel (which is time consuming) in order to reduce the potential bias through the manual survey. The experimental results are shown in Table 2-3. The columns on the left are field crack measurement results and their corresponding deducts, and the columns on the right are automatic results. Based on the experimental results, the overall deducts given by automatic crack evaluation are close to those in the field measurement and range image inspection. For the four selected sites, the average

absolute difference on overall deduct between automatic crack evaluation and wheel measurement is 3.25, which is within the error tolerance (5-10 deduct points) in GDOT's current survey practice. The differences are mainly caused by 1) load cracking Severity Level 1 is partially captured or detected, which leads to a lower deduct value in automatic evaluation results (e.g. SR 236 Site #3), and 2) a slight measurement difference on high severity levels (e.g. load cracking severity level 4 in SR 236 Site #2) results in a big difference on the deduct points. Both reasons will be further illustrated in the following subsection.

Table 2-3 Section Validation with Wheel Measurement

(a) SR 236 Site #1

	Wheel Measurement		**Automatic Evaluation**	
	Extent(%)	Deduct	Extent(%)	Deduct
Load Lvl 1	56	15	48	15
B/T Lvl 1	100	18	100	18
Overall		33		33

(b) SR 236 Site #2

	Wheel Measurement		**Automatic Evaluation**	
	Extent(%)	Deduct	Extent(%)	Deduct
Load Lvl 1	30	10	25	9
Load Lvl 2	7	9	7	9
Load Lvl 4	11	29	7	22
B/T Lvl 1	99	18	100	18
Overall		47		40

(c) SR 236 Site #3

	Wheel Measurement		**Automatic Evaluation**	
	Extent(%)	Deduct	Extent(%)	Deduct
Load Lvl 1	41	13	27	9
Load Lvl 2	2	2	0	0
B/T Lvl 1	100	18	100	18
Overall		31		27

(d) SR 275 Site #1

	Wheel Measurement		Automatic Evaluation	
	Extent(%)	Deduct	Extent(%)	Deduct
Load Lvl 1	71	15	47	15
Load Lvl 3	9	19	8	17
B/T Lvl 1	78	18	80	18
Overall		37		35

Validation on visually-estimated sections

Beside the four sites where crack extents are measured in detail using a measuring wheel, six other sites are also evaluated in this study. On these sites, GDOT pavement engineers visually identify the crack types and severity levels, and visually estimate the crack extents in the field (following GDOT's current practices). The experimental results are shown in 4.5 Limitations of the crack classification and quantification

Through the validation, the major issues of crack classification and quantification using 3D pavement data can be categorized as follows:

System resolution of current 3D line laser imaging technology

The resolution of the 3D line laser imaging system that has been used in this study is 1 mm on the transverse direction and 5 mm on driving direction. Our previous study shows that the system has the capability to capture cracks wider than 2 mm, but only has limited performance when dealing with cracks around 1mm wide (hairline cracks). Most hairline cracks are only partially captured or are completely missing on the range image (as shown in Figure 2-5), which leads to certain differences between automatic evaluation outcomes and manual survey results.

Table 2-4. On most sites, the overall deducts given by automatic crack evaluation are still close to those in the field estimation and range image inspection. For SR 275 Sites #2 and #3, the hairline cracks in the field are not captured or only partially captured by the 3D line laser imaging system, which significantly impacts the overall deduct. For these six sites, the average absolute difference on overall deduct between automatic crack evaluation and visual estimation is 5 out of 100, which is within the error tolerance of GDOT’s current survey practice.

4.5 Limitations of the crack classification and quantification

Through the validation, the major issues of crack classification and quantification using 3D pavement data can be categorized as follows:

System resolution of current 3D line laser imaging technology

The resolution of the 3D line laser imaging system that has been used in this study is 1 mm on the transverse direction and 5 mm on driving direction. Our previous study shows that the system has the capability to capture cracks wider than 2 mm, but only has limited performance when dealing with cracks around 1mm wide (hairline cracks). Most hairline cracks are only partially captured or are completely missing on the range image (as shown in Figure 2-5), which leads to certain differences between automatic evaluation outcomes and manual survey results.

Table 2-4 Section Validation with Visual Estimation

(a) SR 275 Site #2

	Visual Estimation		**Automatic Evaluation**	
	Extent(%)	Deduct	Extent(%)	Deduct
Load Lvl 1	90	15	0	0
B/T Lvl 1	10	4	0	0
Overall		19		0

(b) SR 275 Site #3

	Visual Estimation		**Automatic Evaluation**	
	Extent(%)	Deduct	Extent(%)	Deduct
Load Lvl 1	12	7	0	0
B/T Lvl 1	30	7	25	6
Overall		14		6

(c) SR 275 Site #4

	Visual Estimation		**Automatic Evaluation**	
	Extent(%)	Deduct	Extent(%)	Deduct
Load Lvl 1	20	8	14	7
B/T Lvl 1	60	11	45	9
Overall		19		16

(d) SR 275 Site #5

	Visual Estimation		Automatic Evaluation	
	Extent(%)	Deduct	Extent(%)	Deduct
Load Lvl 1	100	15	57	15
B/T Lvl 1	60	11	57	11
Overall		26		26

(e) SR 67 Site #1

	Visual Estimation		Automatic Evaluation	
	Extent(%)	Deduct	Extent(%)	Deduct
Load Lvl 1	100	15	51	15
B/T Lvl 1	100	18	81	18
Overall		33		33

(f) SR 67 Site #2

	Visual Estimation		Automatic Evaluation	
	Extent(%)	Deduct	Extent(%)	Deduct
Load Lvl 1	70	15	88	15
Load Lvl 2	15	15	0	0
B/T Lvl 1	20	6	15	5
Overall		21		21

Figure 2-5 Limitation of current technology on hairline cracking (images from SR236 Site #3)

Limitation of automatic crack detection

Furthermore, the automatic crack detection algorithm cannot be guaranteed to provide a precise crack map on every image. As shown in Figure 2-6, some cracks are only partially detected, and the pavement areas with clear double crack lines are, also, detected as only a single crack line. The limitation of automatic crack detection also impacts the performance of the subsequent crack classification and measurement.

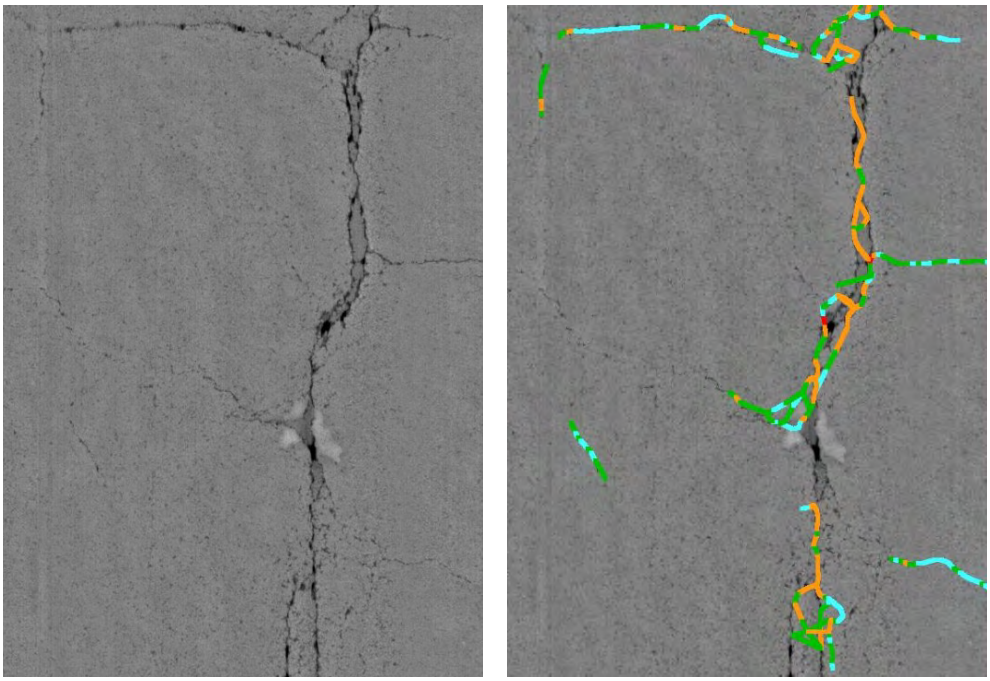

(a) Range image (b) Detected crack map

Figure 2-6 Limitation of crack detection algorithms (images from SR236 Site #2)

Measurement biases through crack quantification

In this study, each wheelpath is assumed to contain only one load cracking severity level; we intentionally choose the predominant load cracking severity level when multiple severity levels happen in the same wheelpath. As shown in Figure 2-7(a), although a short segment of load cracking Severity Level 2 is identified on the bottom of the image, the whole wheelpath is still measured and recorded as Severity Level 1. Similarly, the short segment of load cracking at Severity Level 4 in Figure 2-7(b) is disregarded, which might have a larger impact on the deduct calculation, since high severity levels usually correspond to a much higher deduct value. However, since this automatic crack evaluation is conducted with 100-percent coverage, such biases are assumed to counterbalance each other, and, therefore, they don't have a significant impact on the overall condition assessment.

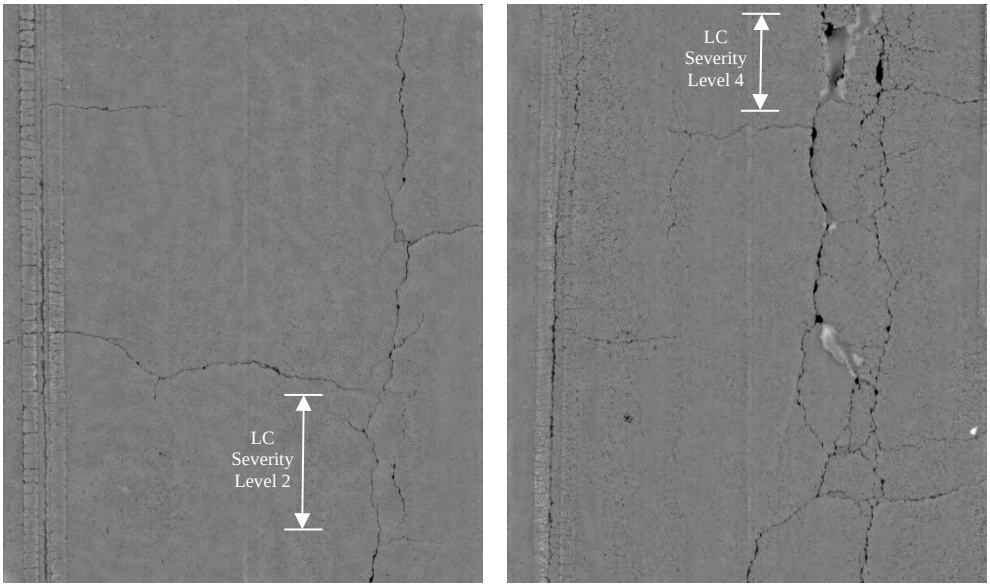

(a) SR236 Site #3 (b) SR236 Site #2

Figure 2-7 Assumptions of crack quantification in this study

5. Case Study on Interstate Highway I-85

We have demonstrated the performance of crack classification and quantification through a series of image-based and site-based field validation tests in previous sections. This section presents an outreach study by applying it on the interstate highways, which are usually high-traffic-volume roads and are challenging for traditional manual surveys. The selected test site is I-85 southbound between Exit 104 and Exit 85 (about 19 miles). According to the information provided by GDOT, the road segment inside the I-285 perimeter is in poor condition and will be resurfaced soon.

The pavement data is collected on the test site, and the crack classification and quantification is conducted automatically. Figure 2-8 shows some representative samples and the corresponding automatic crack evaluation outcomes. Due to the high traffic volume, it is difficult to conduct a field manual survey to establish the ground truth; therefore, the video-log images from front and back camera are provided for comparison purposes.

Front Camera

Back Camera

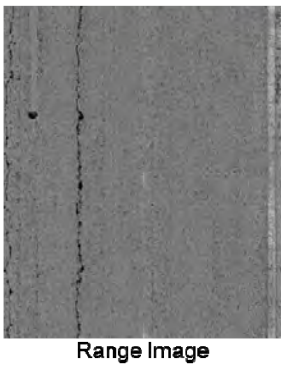

Range Image

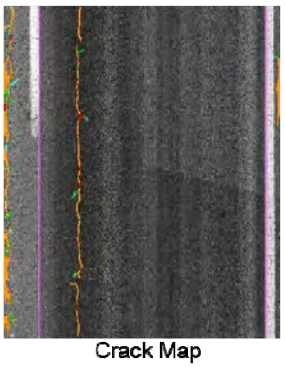

Crack Map

Left Wheelpath	
LC Level 1	15.9
Right Wheelpath	
None	0
Non Wheelpath	
None	0

Evaluation Outcomes

(a) Load cracking

Front Camera

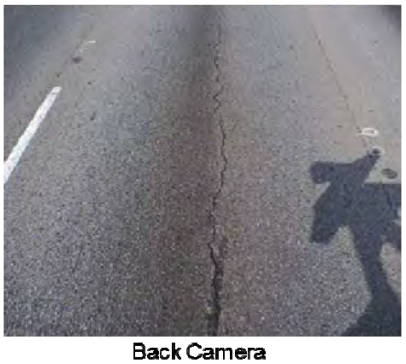

Back Camera

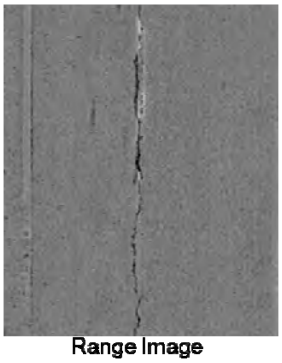

Range Image

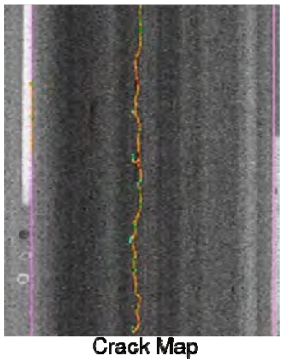

Crack Map

Left Wheelpath	
None	0
Right Wheelpath	
None	0
Non Wheelpath	
BT Level 1	18.8

Evaluation Outcomes

(b) B/T cracking

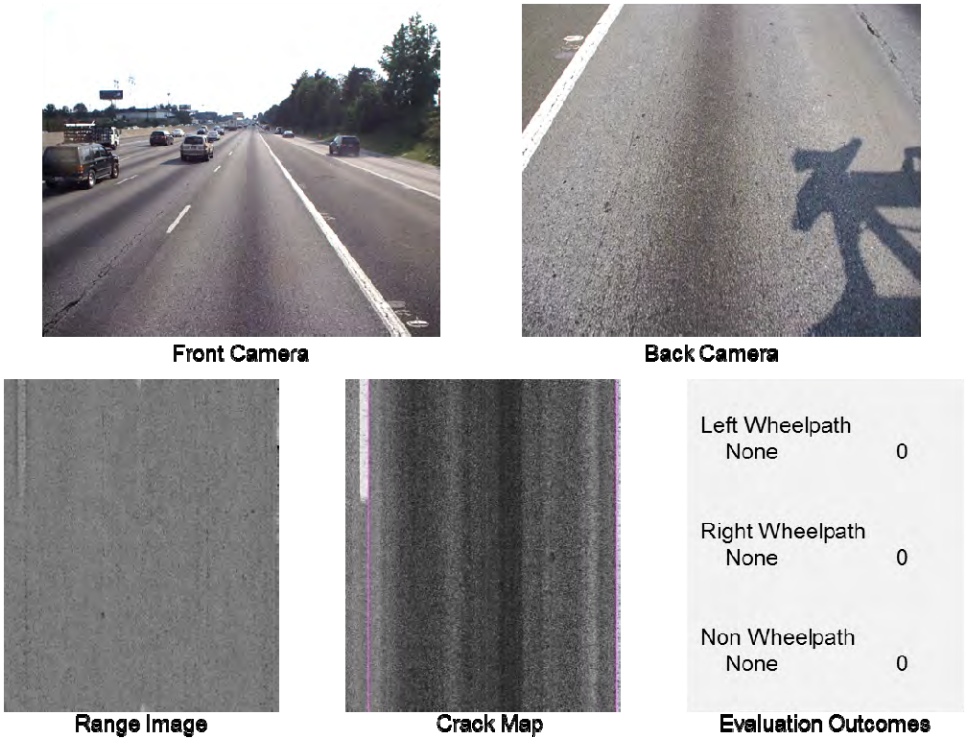

(c) Good pavement

Figure 2-8 Representative samples on the selected interstate test site

Based on the automatic crack evaluation outcomes, the deduct distribution of load and B/T cracking can be generated and visualized on a GIS map (as shown in Figure 2-9). The pavement condition inside the I-285 perimeter is clearly worse than that of outside I-285. The automatic crack evaluation using 3D pavement data is promising for transforming the sensing data and detected crack map into decision support information; it is especially beneficial on the high-volume-traffic roads, such as interstate highways, where traditional manual surveys are difficult to conduct.

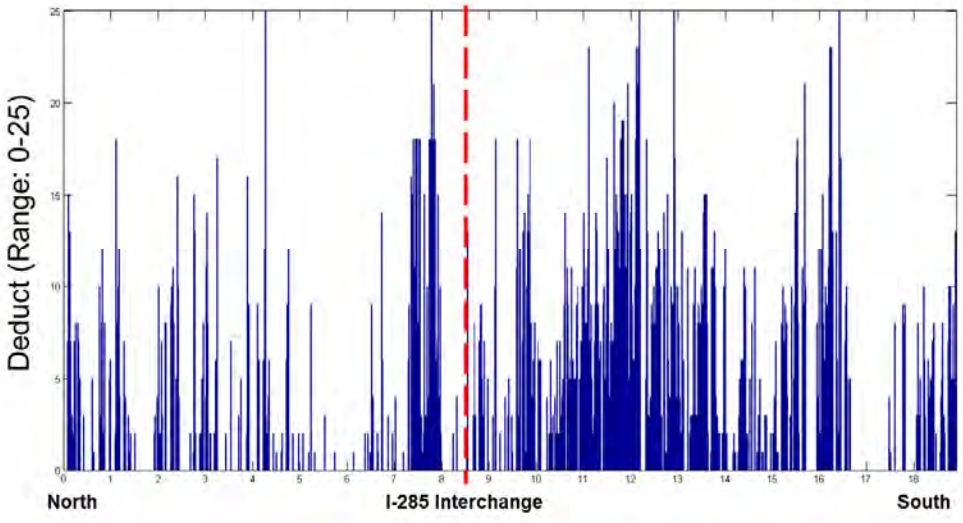

(a) Deduct distribution

(b) GIS visualization

Figure 2-9 Overall crack condition on the selected interstate test site

6. Summary

The emerging 3D line laser imaging technology has demonstrated its great potential on pavement condition survey. Automatic crack detection using the 3D pavement surface data has been validated to provide more accurate crack map. With the detailed preservation of crack characteristics, it is expected to better support the automatic crack classification and

quantification. This study validates the performance of a previously developed crack classification and quantification method. The major findings are summarized as follows:

First, automatic crack classification and quantification is feasible on asphalt pavements. In this study, we validate crack classification and quantification following GDOT COPACES distress protocol. Through the validate tests, the automatic method has demonstrated high accuracy of classifying load cracking, B/T cracking and their severity levels, and the crack quantification results are close to manual field survey conducted by experienced GDOT liaison engineers.

- An image-based validation is first conducted to validate the accuracy of crack classification. Actual pavement data are collected, manually reviewed, and labeled by GDOT pavement engineers to establish the ground truth. The automatic crack classification method shows an accuracy of 92.2% on classifying load cracking and its severity levels and 97.2% on classifying B/T cracking and its severity levels.
- A site-based validation is then conducted to compare the results from automatic and manual crack survey. Ten different 100-ft. sections are selected on SR236, SR275, and SR67 following GDOT's current crack survey practice. For the four wheel-measured sections, the average absolute difference between automatic crack classification and quantification results and manual survey results is 3.25 out of 100, and for the six visually-estimated sections, the average absolute difference is 5 out of 100. Both differences are within the error tolerance of GDOT's current survey practices.

Second, the automatic crack classification provides most robust classification results on low severity level cracks. The classification accuracy of load cracking and B/T cracking Severity Level 1 is constantly over 90% with the largest portion of experimental data. The load cracking and B/T cracking on interstate highways in Georgia are mostly at Severity Level 1. The automatic crack classification and quantification method is very promising to be implemented on interstate highways at this stage.

Third, the automatic crack classification and quantification, especially for quantification, is influenced by the capability of data acquisition system and crack detection algorithm.

- Through the site-based validation, it is observed that for the sections where manual survey results are significantly different from the automatic results, most of the cracks are hairline cracks. The resolution of the 3D line laser imaging system that has been used in this study is 1 mm on the transverse direction and 5 mm on driving direction. Its performance with hairline cracks (about 1mm wide) is less robust.
- The performance of transverse crack quantification is fair. The data acquisition interval at driving direction is 5mm to collect data at highway speed. Under this interval, some transverse crack may be only partially detected, so their extents are underestimated through the crack quantification. With the current system, the vehicle needs to drive at the speed of less than 20km per hour to collect 3D pavement surface data at 1mm interval.

For future research, additional experimental data should be added, especially for the high severity level cracks, to further improve the classification accuracy on these cases. Besides load cracking and B/T cracking, other crack-related distresses, such as edge cracking, reflective cracking, etc., should be incorporated as well. The classification of these cracks may involve historical and structural data of the pavements.

For the outreach of this study, we will first test the automatic crack classification and quantification on Interstate 285 near Atlanta, and then extend to the entire interstate highway system in Georgia. Since interstate highways are usually challenging for field survey due to the high traffic volume, the automatic survey results will be a good complement to GDOT's current pavement survey practice. At the next stage, these methods will be further tested and implemented on the state routes in Georgia. The method can also be extended to classify and quantify cracks for different distress protocols, e.g. FDOT's flexible pavement survey.

Beyond crack classification, the concept of multi-scale crack representation using Crack Fundamental Element can be extended to developed national consistent crack measures to meet the need of MAP-21. State DOTs have invested major resources to collect and maintain their legacy data over decades for pavement management, and are not willing to change their distress protocol. This concept provides the opportunity to flexibly transform between their own distress protocols and national consistent measures. In addition, 3D pavement surface data, automatic crack detection algorithms, and multi-scale crack representation from the Crack Fundamental

Element (CFE) model can be used to develop next-generation pavement preservation planning tools, such as sensor-based, intelligent crack sealing planning tool.

References

Tsai, Y., Jiang C. (2012). “Crack Detection Using High-resolution 3D Line Laser Imaging Technology”, 7th RILEM International Conference on Cracking in Pavements, Delft, Netherlands, June 20, 2012.

Chapter 3 Validation of Concrete Pavement Distress Detection

1. Introduction

Pavement surface distress measurement is an essential part of a pavement management system (PMS) for determining cost-effective maintenance and rehabilitation strategies. Visual surveys conducted by engineers in the field are still the most widely used means to inspect and evaluate pavements, although such evaluations involve high degrees of subjectivity, hazardous exposure, and low production rates. Consequently, automated distress identification is gaining wide popularity among transportation agencies.

For the past two decades, using a 2D intensity-based imaging system has been the main way most state departments of transportation have collected data. The intensity-based data acquisition method makes it sensitive to lighting effects. In general, because of the intensity-based data acquisition method, the performance of distress detection algorithms is severely hampered in the presence of shadows, lighting effects, non-uniform crack widths, and poor intensity contrast between cracks and surrounding pavement surfaces. The challenge persists in spite of all the research work that has been carried out to improve image acquisition techniques by minimizing the lighting defects (Kaul et al., 2010). However, it is difficult to achieve consistent crack detection under different ambient lighting conditions when using natural light for illumination (Xu, 2005). Some illumination devices, such as LED lighting, are used to provide constant lighting that prevents the impact of shadows (Xu, 2005; Xu, 2007). However, the beam width of the LED lighting is 0.5 inch, which is not thin enough to provide sufficient depth resolution. The shallow cracks and/or thin cracks, which have low intensity contrast with surrounding pavement, are sometimes difficult to detect. Again, many algorithms are able to perform well only in an image data set which has images that are not too different from each other. Otherwise, manual inputs are required to adjust the input parameters so that the algorithms can perform reasonably. Although 3D stereovision has been studied recently, it is not operational. Therefore, full automation of pavement distress detection has remained a challenge, especially for accurate and reliable detection (Kaul et al., 2010).

2. Introduction of 3D Line Laser Imaging System

Line laser imaging technology includes measuring the range of an object using the projected lighting and the triangulation computation. The advent of recent sensor and information technologies has dramatically improved the performance of line laser imaging technology and makes it feasible for real-world applications, including the support of detecting cracks and other types of pavement distresses. Detailed pavement surface laser data can now be collected at highway speed with adequate resolutions in x, y, and z dimensions. This has gained great attention from researchers, industries, and transportation agencies in recent years. The line laser imaging technology for pavement crack detection and rutting measurement has, for the first time, been comprehensively validated in the lab and in the field in 2010 through a research project entitled "Remote Sensing and GIS-enabled Asset Management System (RS-GAMS)", sponsored by the USDOT/OST-R Commercial Remote Sensing and Spatial Information (CRS&SI) Technologies program.

This 3D line laser imaging system is different from the 2D intensity-based imaging system. First, the 3D line laser imaging system is not sensitive to lighting effects when measuring the range (i.e. elevation). Noises, like oil stains and poor intensity contrast, will not interfere with the segmentation algorithms using the acquired range data. As long as there is a distinguishable elevation difference between a crack and its surrounding background, the segmentation algorithm is able to capture the crack. Increased attention has been drawn to the development of this pavement surface laser data acquisition system and its potential application. Researchers from Texas (Li et al., 2010) have developed a research version of the 3D laser system and have demonstrated the system's capability, but the developed system is still in the research stage and has low system performance. The low-resolution data collected from such a system (e.g., it collects only 200 profiles per second and has only 2 mm crack depth resolution) limits the system's capability. In addition, it cannot be operated at highway speed.

LCMS is one of the commercially available 3D line laser imaging systems (Laurent et al., 2008). It employs high-speed cameras, custom optics, and laser line projectors to acquire 2D intensity images and high resolution 3D profiles of road surfaces that allow for automatic detection of cracks and the evaluation of macro-texture and other road surface features. Designed for both day and nighttime operation in all types of lighting conditions, the system is immune to sun and

shadows and is capable of measuring pavement types ranging from concrete to dark asphalt. This system can be operated at speeds of up to 100 km/h on roads as wide as 4 meters and collect 5,600 profiles per second (100 km/h for collecting transverse profiles at an interval less than 5 mm). The depth resolution can be up to 0.5 mm.

This system can produce data with much better granularity, and, thus, it has a great potential to better detect pavement distresses. In the previous study, the capability of pavement surface laser data on asphalt pavement distress detection, especially on cracking and rutting, has been demonstrated. This chapter will comprehensively validate the capability of pavement surface laser data for conducting automatic concrete pavement distress detection, including cracking, faulting, spalling, and shoulder joint distress. This chapter is organized as follows. After the literature review and introduction to the 3D line laser imaging system in Sections 1 and 2, the following four sections will present the comprehensive validation on automatic concrete distress detection using pavement surface laser data, including cracking in Section 3, faulting in Section 4, spalling in Section 5, and shoulder joint distress in Section 6. Section 7 will summarize the major findings in this study.

3. Validation of Automatic Concrete Pavement Crack Detection

Automatic crack detection can be conducted based on pavement surface laser data, and its performance on asphalt pavement has been validated in a previous study. Compared to asphalt pavement, crack detection on concrete pavement has some unique challenges: first, transverse joints on Jointed Plain Concrete Pavement (JPCP) may impact the performance of automatic crack detection, especially for the joints with poor conditions; second, parallel grooves (transverse or longitudinal) on diamond-grooved concrete surfaces may lead to potential false positive crack detection. The section will quantitatively validate the accuracy of automatic cracking detection on concrete pavement. In addition, some representative cases, including hairline cracks, misdetection as joints, and false positive detection caused by pavement damage, will be presented regarding the potential issue of concrete pavement crack detection.

3.1 Experimental data

The experimental data of the validation test were collected on interstate highways I-16 and I-516 near Savannah, Georgia. Both highways are concrete pavement on the selected test sites (as shown in Figure 3-1).

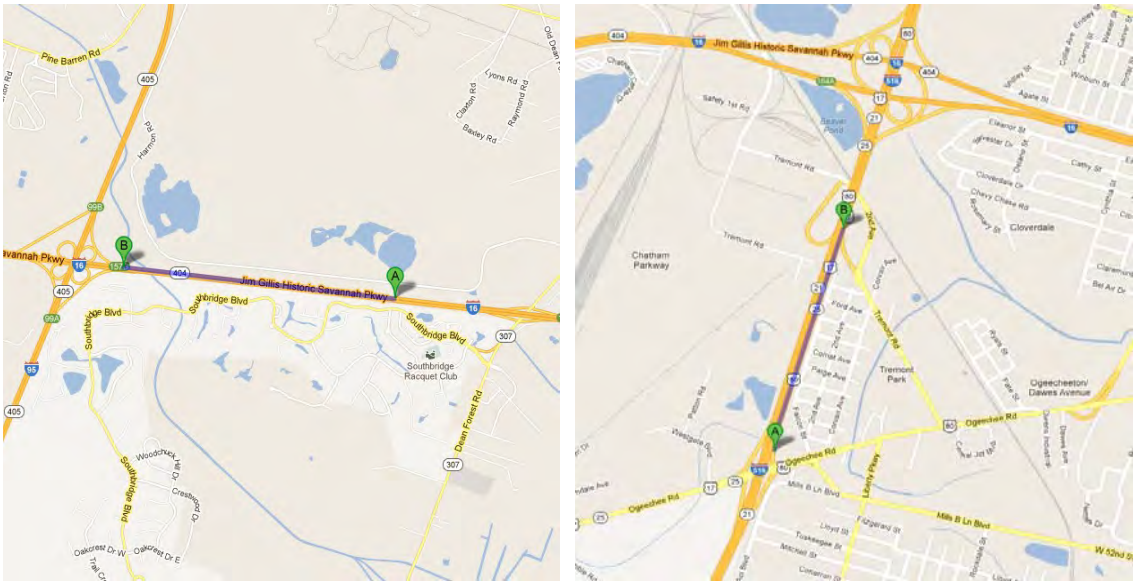

(a) I-16 test site (b) I-516 test site

Figure 3-1 Selected test sites on concrete crack detection

On the I-16 test site, we selected a total of 27 slabs westbound from MP159 to MP157; this roadway has representative cracking patterns, most of which are transverse cracking / broken slabs. Each of these slabs is marked with a unique ID for future reference (as shown in Figure 3-2), and the distresses on these slabs are drawn roughly for comparison purposes. On the I-516 test site, we selected a total of 15 slabs northbound from MP3 to MP4. Similarly, each of these slabs was marked with a unique ID. Digital photos of the selected testing sites were taken from the road shoulder to track the detailed distress condition and provided certain reference through the validation.

Figure 3-2 Manually labeling the selected concrete slab for crack detection validation

3.2 Experimental design

The following procedures are conducted to quantitatively evaluate the performance of automatic crack detection on concrete pavement:

- First, the ground truth was manually digitized and extracted from the pavement surface laser data. The data was presented in the form of a range image (Figure 3-3(a)). Based on the visual inspection of a range image, the cracking positions were manually digitized and converted to a binary ground truth crack map (Figure 3-3(b)).
- Then, the crack map results were generated using an automatic crack detection algorithm. The crack map can be overlaid on an intensity image or a range image (Figure 3-3(c)), and different colors of the detected crack line represent different crack widths. There are two typical ways to convert data into a binary crack map:
  - The first way is to manually digitize the intensity or range image with a crack map overlay (similar to ground truth establishing procedure).
  - The second way is to interpret the XML file as the results of distress detection and reconstruct a binary crack map (Figure 3-3(d)).
- Finally, the two binary crack maps were compared – ground truth and automatic detection. The buffered Hausdorff scoring method was employed to conduct an objective and quantitative evaluation.

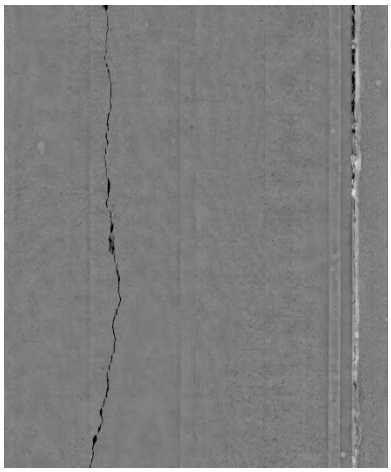

(a) Range Image

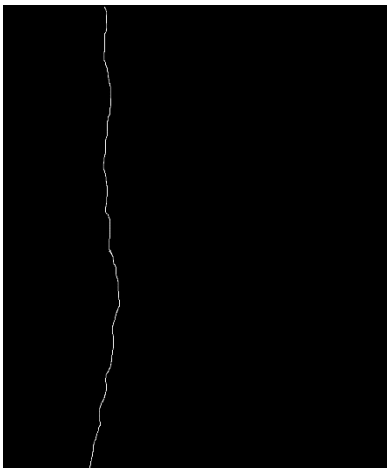

(b) Manually Digitized Ground Truth

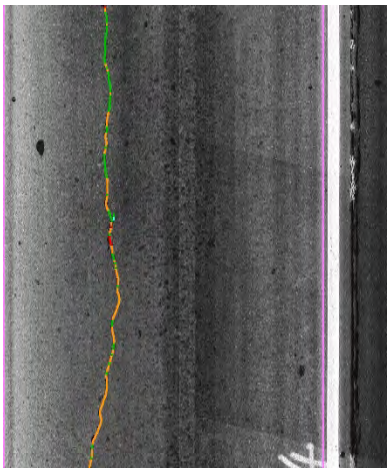

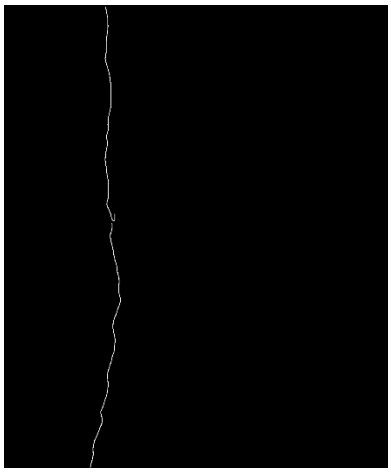

(c) Automatic Crack Detection (d) Binary Automatic Crack Detection

Figure 3-3 Illustration of evaluation procedure

3.2 Introduction on buffered Hausdorff scoring method

The buffered Hausdorff scoring method was proposed in our previous study to evaluate the performance of asphalt crack detection (Kaul et. al., 2010; Tsai et. al., 2010). It incorporates the strengths of both mean square error and Hausdorff distance by modifying the Hausdorff distance metric. The Hausdorff distance is among the most popular distance measures and measures the distance between two curves; it is a metric. It has been extensively used in literature (Beauchemin et al., 1998; Wang, 2002). For any two sets of points $A = a_1, a_2, ..., a_n$ and $B = b_1, b_2, ..., b_m$,

$$H(A, B) = \max(h(A, B), h(B, A))$$

Where

$$h(A,B) = \max_{a \in A} \min_{b \in B} \|a - b\|$$

$h(A,B)$ is the greatest of all the small distances from points of A to B and is the greatest of all the small distances from points of B to A. Figure 3-4 illustrates this distance measurement effectively.

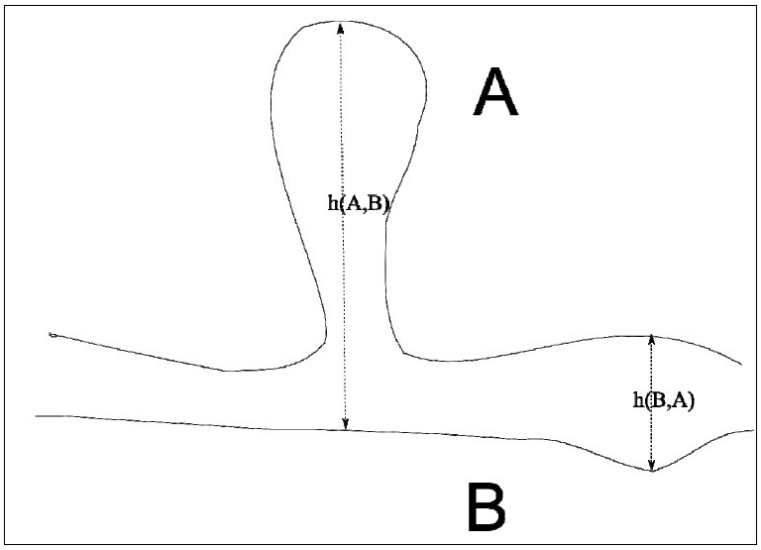

Figure 3-4 Illustration of Hausdorff distance

The value of the Hausdorff distance is large, even if one crack pixel in the segmented image is far from the ground truth image crack pixels. Seeing this limitation of the Hausdorff distance metric, a new metric was developed that does not suffer from the defects of the Hausdorff distance. The intuitive development of this measure is described next. A better distance measure than the Hausdorff distance is the modified Hausdorff distance given by $MH(A,B)$:

$$MH(A,B) = \max(h_1(A,B), h_1(B,A))$$

Where

$$h_1(A,B) = \frac{1}{m} \sum_{a \in A} \min_{b \in B} \|a - b\|$$

After initially using the modified Hausdorff distance measure for our image comparison, we felt that there was one more possible improvement. Once a crack pixel in the automatically segmented image falls substantially away from the closest pixel in the ground truth image, it no longer makes sense to heavily penalize this distance. Wrong detections beyond a certain distance should be penalized equally. This leads to a new distance measure, the buffered Hausdorff distance measure given by $BH(A,B)$.

$$BH(A,B) = \max(h_2(A,B), h_2(B,A))$$

Where

$$h_2(A,B) = \frac{1}{m}\sum_{a\in A} \underset{L}{sat} \min_{b\in B} \|a-b\|$$

Here, $\underset{L}{sat}$ indicates that when the distance of the crack pixel to the closest crack pixel in the other image exceeds a saturation value L, we use a constant value of L for the distance. The buffer L was chosen to be 50 in this validation, which fits the selected image resolution of 1,040x1,250 based on our previous sensitivity study. Figure 3-5 illustrates the buffered Hausdorff distance measure. The sample values of the buffered distance have a very intuitive meaning, too. The buffered distance can be interpreted as the average Euclidean distance between the crack pixels in the ground truth image and the segmented images. To compare other scoring methods with this buffered distance, a scaled scoring measure was derived as given below:

$$\text{Buffered distance score} = 100 - \frac{BH(A,B)}{L}\times 100$$

The buffered distance effectively measures the performance of the segmentation methods and generates a score that corresponds with the qualitative performance of visual inspection. Using the buffered Hausdorff scoring method, the experimental results on I-516 and I-16 test sites are presented in the following subsections.

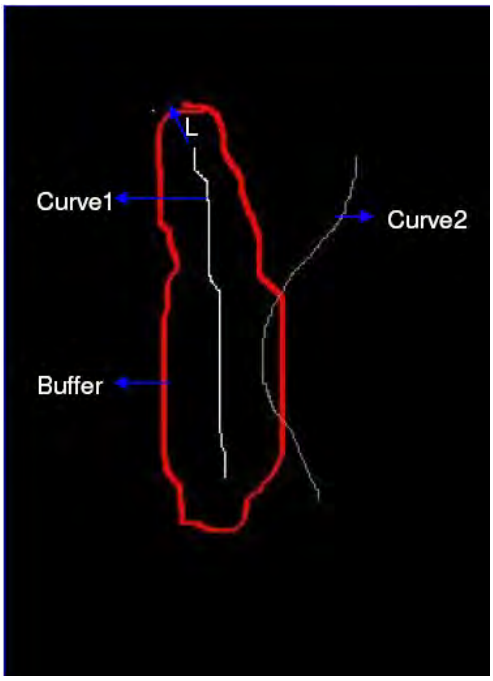

Figure 3-5 Illustration of Buffered Hausdorff distance measure

3.3 Validation on I-516 test site

This subsection presents the experimental results on I-516. The majority of cracks on this test site are longitudinal cracking. A total of 15 slabs with longitudinal cracking were selected. Since the normal length of the slab is larger than the collected pavement image in the driving direction, some slabs were divided into two images in the experimental test, where the consecutive image is represented with the same ID and a single quote (e.g. Slab #1').

Figure 3-6 and Figure 3-7 are two examples demonstrating the performance of automatic crack detection on this test site. Figure 3-6 shows longitudinal cracking on a concrete pavement with normal crack width and no spalling. Figure 3-6 (a) and (b) shows the intensity and range images collected from the 3D laser line imaging system. Figure 3-6 (c) shows automatic crack detection results; it can be observed that, besides the cracks, the longitudinal and transverse joints for this JPCP are also extracted, which are labeled as straight blue lines. Figure 3-6 (d) shows the ground truth, which is manually digitized from the range image, and Figure 3-6 (e) shows the binary crack map generated from the automatic detection results. Figure 3-6 (f) is a digital photo taken from the road shoulder on this specific slab. Based on visual evaluation, the crack detection results are very close to the manually digitized ground truth. The buffered Hausdorff scoring

method also gives a high score of 96.59 on this image, which indicates an accurate detection. Also, the transverse and longitudinal joints are successfully differentiated from the cracks. Similarly, Figure 3-7 shows longitudinal cracking with a large crack width and some spalling. The automatic crack detection shows an accurate outcome, as well, in this case.

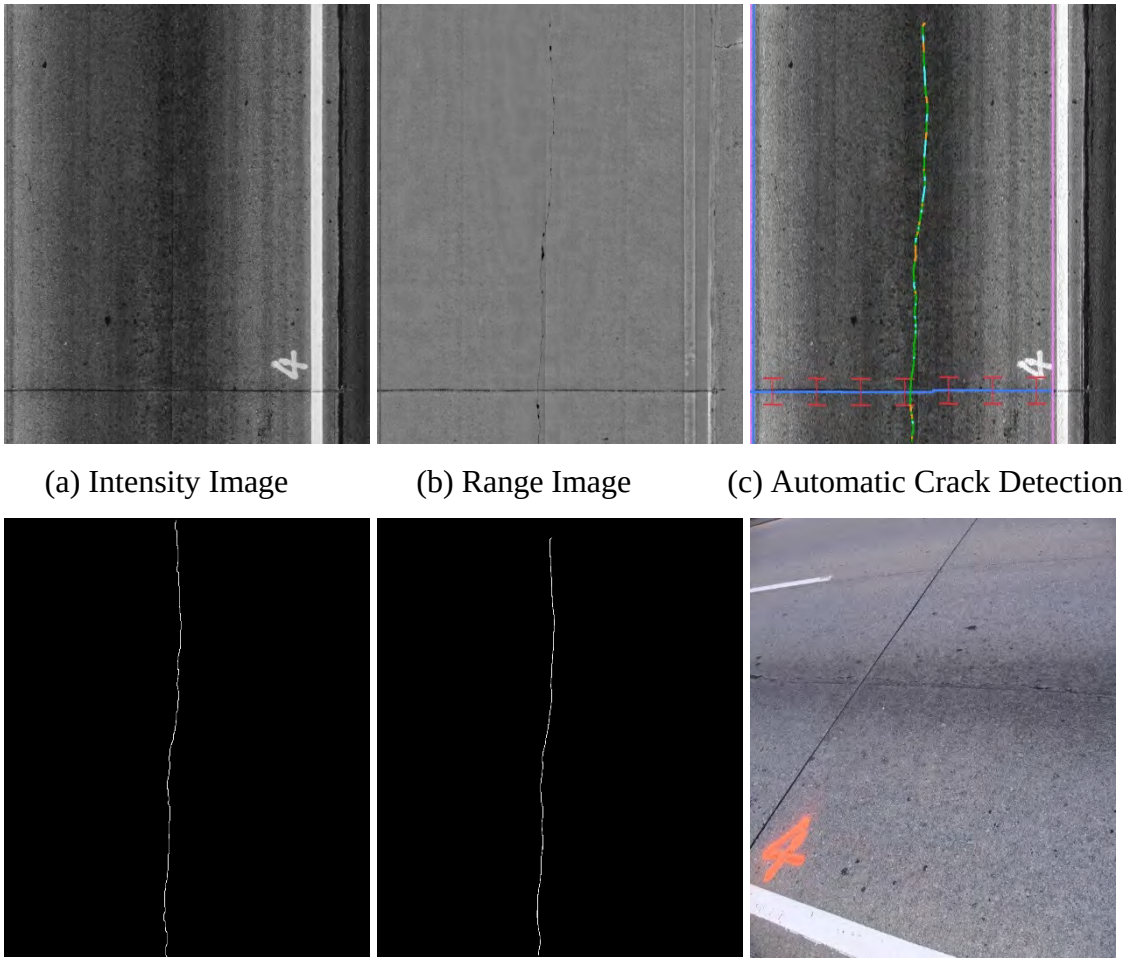

(a) Intensity Image (b) Range Image (c) Automatic Crack Detection

(d) Ground Truth I Binary Detection Results (f) Field Photo

Figure 3-6 Crack detection on Slab #4 on I-516 test site (Score: 96.5859)

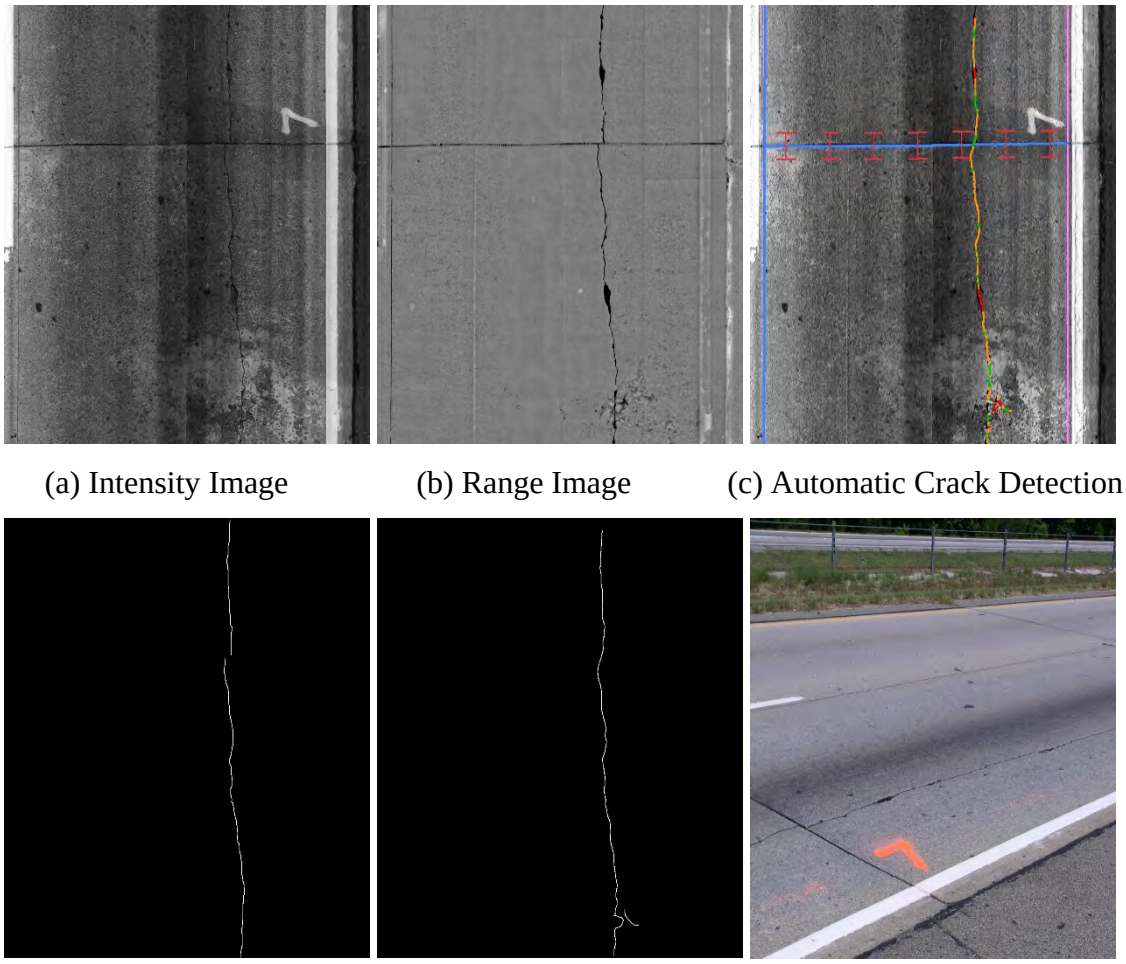

(a) Intensity Image (b) Range Image (c) Automatic Crack Detection

(d) Ground Truth (e) Binary Detection Results (f) Field Photo

Figure 3-7 Crack detection on Slab #7 on I-516 test site (Score: 93.4601)

The overall performance on this test site is summarized in Table 3-1. The automatic crack detection using pavement surface laser data shows accurate and robust detection results on most of the images, having an overall average score of 85.89. The cases with poor performance are mainly caused by misclassification between cracks and construction joints, which will be further explained in the following subsections.

Table 3-1 Performance Evaluation of Crack Detection on I-516 Test Site

Slab ID	Description	Score
1	Longitudinal cracking, wide with spalling	97.4526
1'	Longitudinal cracking, normal width	95.167
2	Longitudinal cracking, normal width	97.595
3	Longitudinal cracking, wide with spalling	98.0972
3'	Longitudinal cracking, wide with spalling	98.6694
4	Longitudinal cracking, normal width	96.5859
4'	Longitudinal cracking, normal width	81.3702
5	Longitudinal cracking, normal width	93.2204
6	Longitudinal cracking, normal width	89.6559
7	Longitudinal cracking, wide with spalling	93.4601
7'	Longitudinal cracking, wide with spalling	41.8065
8	Longitudinal cracking, wide with spalling	86.8667
8'	Longitudinal cracking, wide with spalling	46.8266
9	Longitudinal cracking, wide with spalling	90.9242
9'	Longitudinal cracking, wide with spalling	97.2637
10	Longitudinal cracking, wide with spalling	96.8542
11	Longitudinal cracking, normal width	78.0038
11'	Longitudinal and transverse cracking, normal width	63.1563
12	Longitudinal cracking, wide with spalling	87.9587
13	Longitudinal cracking, wide with spalling	54.7187
14	Longitudinal cracking, wide with spalling	96.9098
15	Longitudinal cracking, wide with spalling	95.0416
15'	Longitudinal cracking, normal width	97.8843
AVG	**Average Score on the I-516 site**	**85.8908**

3.4 Validation on I-16 test site

This subsection presents the experimental results on I-16. The majority of the cracks on this test site are transverse cracking / broken slab. A total of 27 slabs were selected. Similarly, some slabs are divided into two images through the data collection, where the consecutive image is represented with the same ID and a single quote (e.g. Slab #C1').

Figure 3-8 and Figure 3-9 are two examples that demonstrate the performance of automatic crack detection on this test site. Figure 3-8 shows transverse cracking on concrete pavement with normal crack width and slight spalling. Based on visual evaluation, the crack detection results are close to the manually digitized ground truth. The buffered Hausdorff scoring method also gives a

high score of 90.45 on this image, which indicates accurate detection. Similarly, Figure 3-9 is a broken slab with a large crack width and severe spalling. This introduces some uncertainty into the crack detection, since some spalling is large enough to be detected separately as spalling (as shown in the blue area on the image). Based on visual inspection, the overall pattern of detected cracks are similar to the one in the ground truth, although some false positives and false negatives are observed. The buffered Hausdorff score on this image is 85.41.

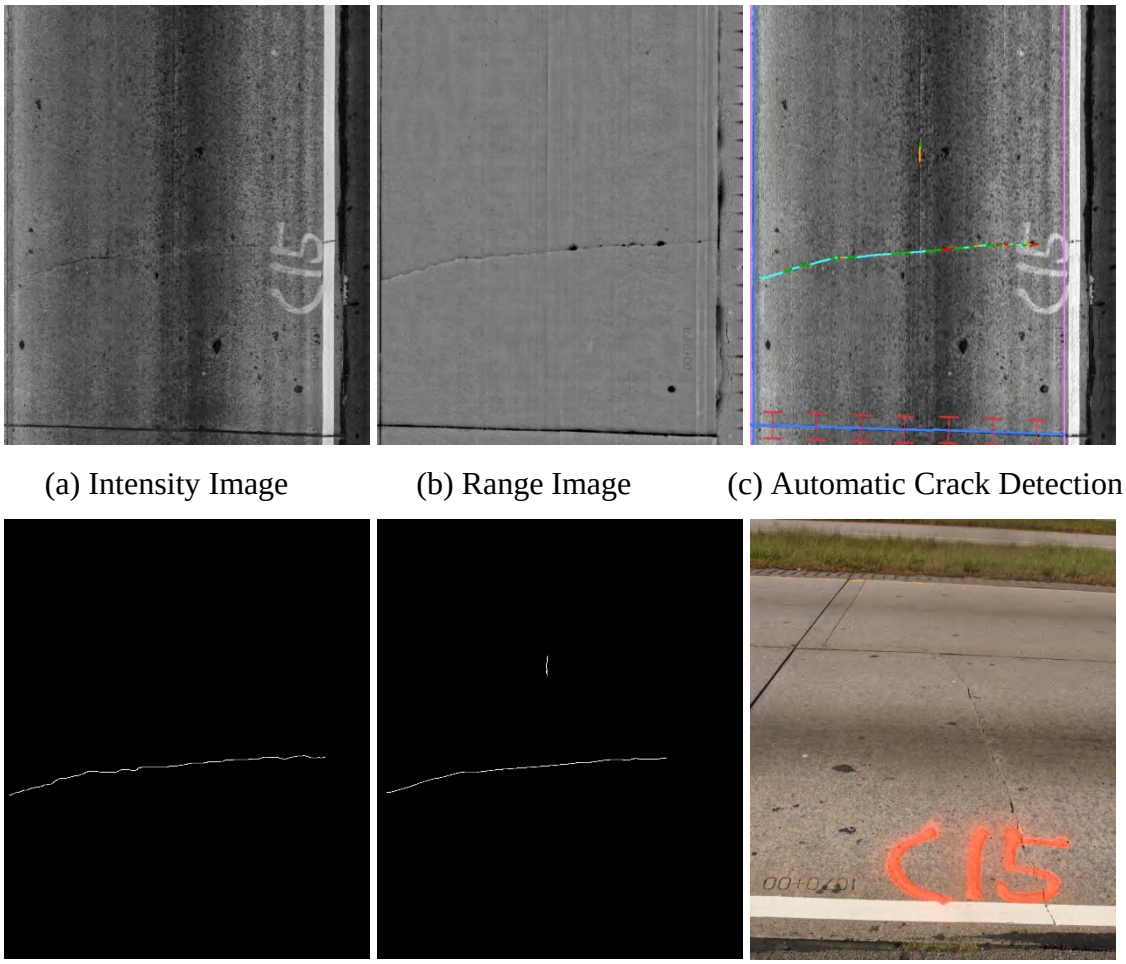

(a) Intensity Image (b) Range Image (c) Automatic Crack Detection

(d) Ground Truth (e) Binary Detection Results (f) Field Photo

Figure 3-8 Crack detection on Slab #C15 on I-16 test site (Score: 90.4512)

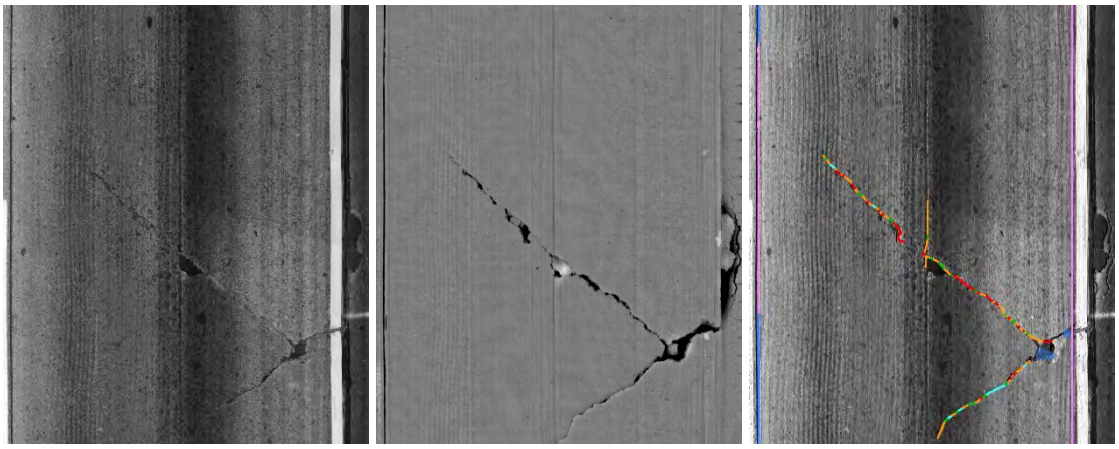

(a) Intensity Image (b) Range Image (c) Automatic Crack Detection

(d) Ground Truth (e) Binary Detection Results (f) Field Photo

Figure 3-9 Crack detection on slab #C1' on I-16 test site (Score: 85.4087)

The overall performance on this test site is summarized in Table 3-2. The performance of automatic crack detection on this site is not as good as on the I-516 test site, having an overall average score of 64.95. This is probably due to three reasons: 1) compared to longitudinal cracking, transverse cracking has a higher probability of being misclassified as construction joints; 2) many hairline cracks are observed on this site, which are difficult for the current system to detect due to the resolution limit; and 3) many severe spallings along the cracks interfere with the crack detection performance. More details on these failed / poor-performance cases are presented in the following subsection.

Table 3-2 Performance Evaluation of Crack Detection on I-16 Test Site

Slab ID	Description	Score
C1	Transverse cracking, normal width	75.3972
C1'	Broken slab, wide with spalling	85.4087
C2	Transverse cracking, normal width	59.8938
C3	Transverse cracking, normal width	84.6954
C4	Broken slab, wide with spalling	54.3036
C8	Broken slab, wide with spalling	47.1257
C10	Transverse cracking, normal width	89.279
C12	Transverse cracking, hairline	46.8648
C13	Replaced slab, hairline cracking	39.5158
C14	Broken slab, wide with spalling	50.5526
C15	Transverse cracking, normal width	90.4512
C16	Transverse cracking, normal width	47.7935
C17	Transverse cracking, hairline	45.1996
C18	Transverse cracking, normal width	92.6896
C20	Broken slab, wide with spalling	54.871
C22	Replaced slab, hairline cracking	59.9153
C24	Replaced slab, longitudinal cracking	37.121
C26	Longitudinal cracking, wide with spalling	94.0759
C27	Longitudinal cracking, wide with spalling	78.9262
AVG	**Average Score on the I-16 site**	**64.9516**

3.5 Potential issues of concrete pavement crack detection

Through the performance evaluation of automatic crack detection on concrete pavement, several major issues are identified, including hairline cracks, misdetection as joints, and false positives caused by pavement damage. Each of these issues is discussed below with a representative example to analyze the potential cause and future solution.

Hairline cracks

Similar to asphalt pavement, hairline cracks on concrete pavement also form a major challenge for crack detection. The data acquisition interval of the current 3D line laser imaging system is 1 mm in the transverse direction and 5 mm in the driving direction. In this experimental test, it wasn't practical to manually measure the crack width on the test site due to the heavy traffic on

the interstate highway. Based on our previous experience on asphalt pavement, cracks with widths below 2 mm are difficult to detect. Figure 3-10 shows a representative case of hairline cracking. The middle part of the transverse crack on the image is hairline. It can be seen that that portion is too thin to be observed, even from the high-resolution digital photos taken from the shoulder. The automatic detection can only extract part of the entire crack line in this case, which leads to a poor buffered Hausdorff score. The hairline cracking issue is better observed on I-16 test site, resulting in an overall, relatively low score on that site; also, the larger data acquisition interval in the driving direction makes it more difficult to capture transverse hairline cracking.

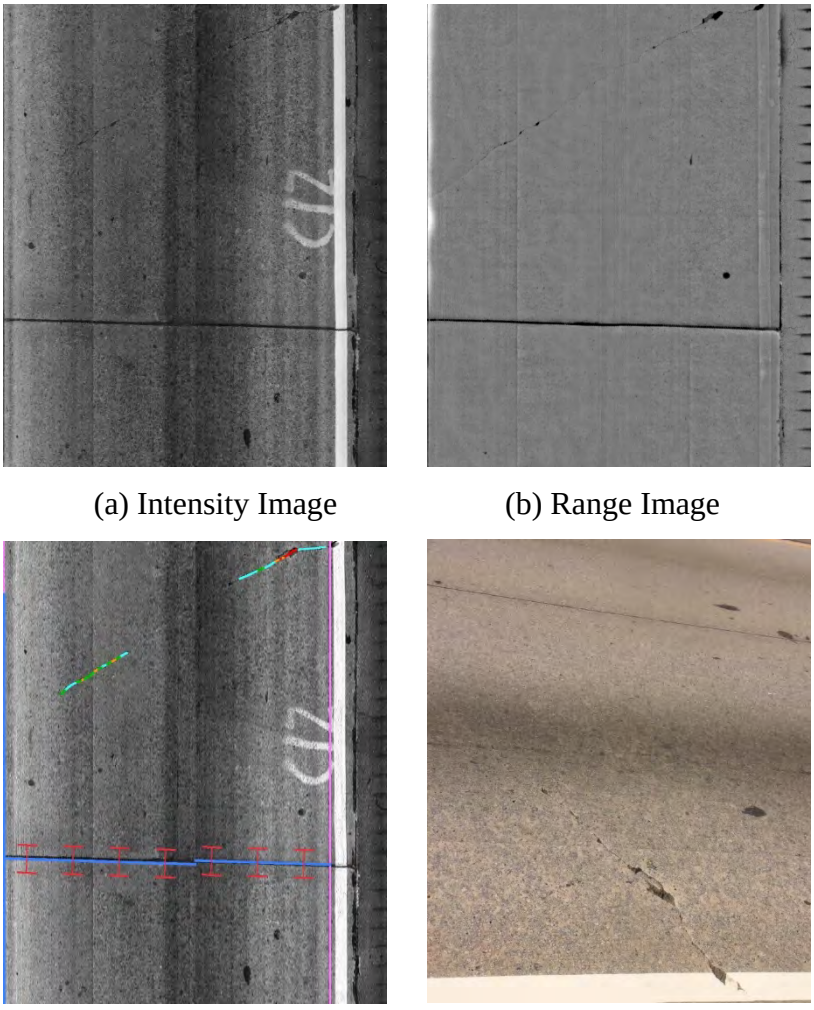

(a) Intensity Image (b) Range Image

(c) Automatic Crack Detection (d) Field Photo

Figure 3-10 Crack detection on hairline cracking

Misclassification as Joints

For concrete pavement, especially for joint plain concrete pavement, automatic crack detection needs to be conducted together with joint detection. Concrete joints have very similar appearance and characteristics with cracks; without a separate joint detection, most of the joints will be captured as concrete cracking, as well. Although the joint detection algorithm performs relatively accurately (presented in the faulting measurement validation section), conducting joint detection simultaneously with crack detection introduces the potential risk that some cracks may be misclassified as joints at the first stage.

Through the experimental tests, several such cases are observed for both transverse cracking and longitudinal cracking. Figure 3-11 shows an example of transverse cracking; the left side of the crack is detected successfully, while the right side is misclassified as a joint. Figure 3-12 shows an example of longitudinal cracking; the top side of the crack is detected successfully, while the bottom side is misclassified as a joint. Based on the experimental results, these false detection cases usually happen under the following two situations: 1) cracks appear to be approximate straight lines and 2) some spalling occurs along the crack and interfere with the crack detection.

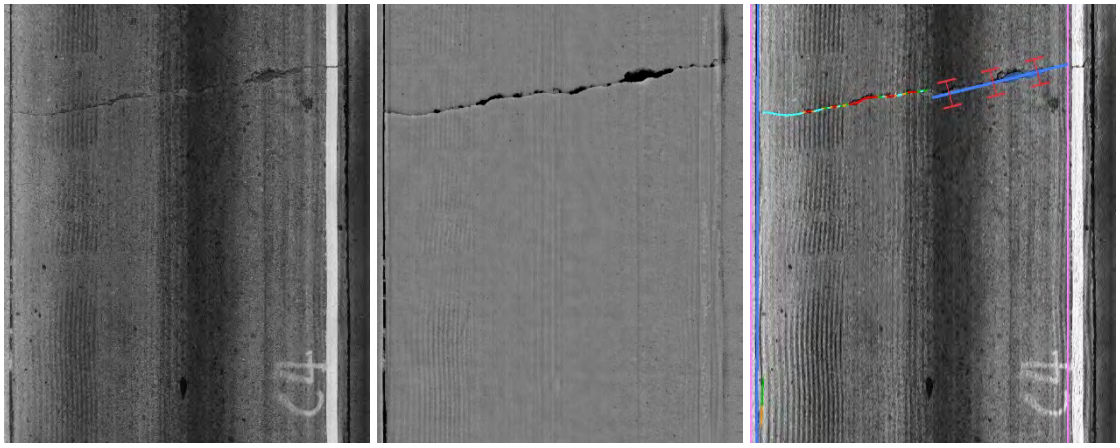

(a) Intensity Image (b) Range Image (c) Automatic Detection Results

Figure 3-11 Misclassification of transverse cracking as concrete joint

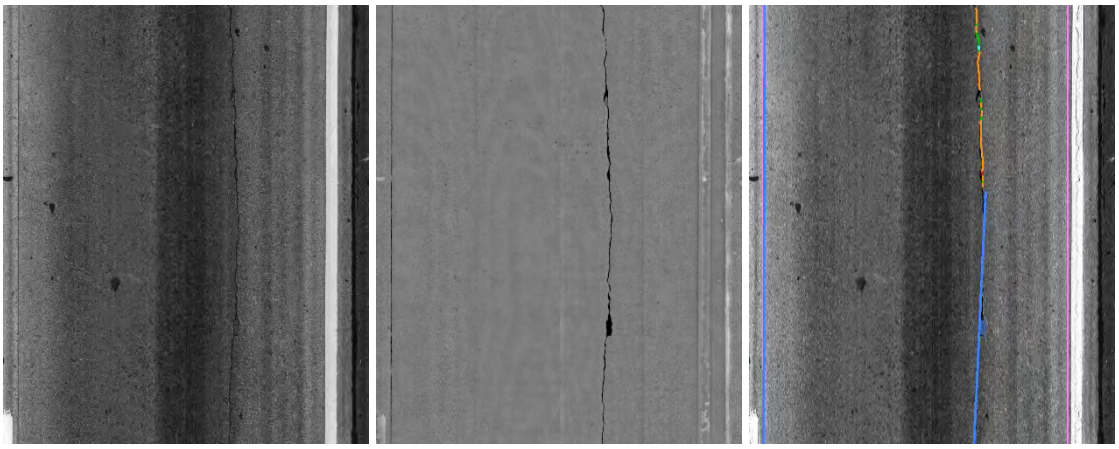

(a) Intensity Image (b) Range Image (c) Automatic Detection Results

Figure 3-12 Misclassification of longitudinal cracking as concrete joint

To remove these false detections, the following additional criteria can be considered as a follow-up step after crack and joint detection. First, the location of detected joints is evaluated, especially for longitudinal joints. If a longitudinal joint is located in the middle of the lane, there is a high probability that it is a false joint detection. Second, the connectivity between joints and neighboring cracks is evaluated. If a joint is directly connected to cracks, either longitudinal or transverse, it may be a false joint detection, as well. These further modifications will improve the crack and joint detection accuracy in future implementation.

False Positive Detection

Similar to asphalt pavement, false positive detections still exist in concrete pavement. This is mainly due to the data acquisition mechanism of the 3D line laser imaging system. Since pavement surface laser data is purely based on the elevation of pavement surface, any pavement damage that result in an elevation change will lead to potential risk on crack detection. One example is shown in Figure 3-13. We can observe a clear straight dent along the driving direction on the range image (Figure 3-13(b)), whose appearance is quite similar to cracks; automatic crack detection also extracts those out as cracking (Figure 3-13(c)). However, this dent is most likely to be caused by a flat tire of heavy trucks**,** which is a false positive detection in this case.

These false positives are the issue that we have to face under the 3D data acquisition mechanism. To further remove these, the characteristics of these false detections need to be studied and

classified, and then a specific filter can then be designed to remove them either at the data preprocessing stage or during the post processing of the detection results.

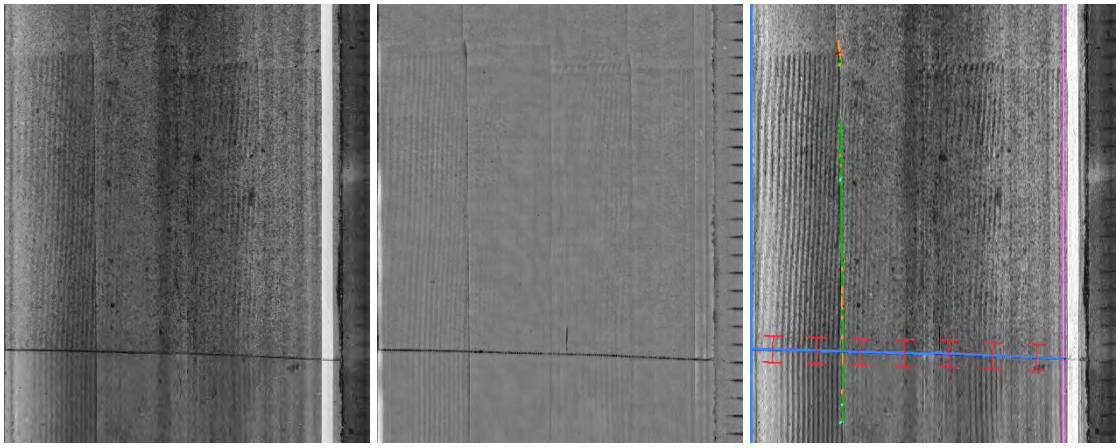

(a) Intensity Image (b) Range Image (c) Automatic Detection Results

Figure 3-13 Example of false positive detection

3.6 Summary

For automatic concrete pavement crack detection using a 3D line laser imaging system, the major findings are summarized as follows:

First, the 3D line laser imaging system shows overall acceptable performance for automatic crack detection on concrete pavement. Two test sites were selected on interstate highways I-516 and I-16 to quantitative evaluate the crack detection performance. Automatic crack detection results were compared with the manually digitized ground truth using the buffered Hausdorff scoring method. The automatic crack detection shows quite accurate and robust results on the I-516 test site, which mainly consists of longitudinal cracking. The crack detection performance on I-16 test site was not as good; this is mainly due to the fair amount of hairline cracking and interference due to severe spalling and joint detection. Through the discussion of false detection cases in this chapter, there is still the potential to further improve the performance of these cases. In summary, from the crack evaluation perspective, the emerging 3D line laser imaging system demonstrates its capability to support further automatic concrete pavement condition evaluation.

Second, hairline cracks are still quite challenging for automatic detection. The data acquisition interval of the current 3D line laser imaging system (1 mm in the transverse direction and 5 mm in the driving direction) makes it difficult to detect hairline cracks thinner than 2 mm. Also, the

fact that there are more false negatives detected in transverse cracking can be explained by the large data acquisition interval in the driving direction.

Third, as on asphalt pavement, pavement damage caused by flat tires or trucks still has an impact on crack detection on concrete pavement. A dent on pavement has a very similar appearance as cracking and may lead to a false positive detection. The characteristics of these pavement damages need to be studied and classified, and a specific filter can then be designed to remove them, either at data preprocessing stage or during the post processing of the detection results.

4. Validation of Concrete Pavement Faulting Measurement

Faulting is the differential vertical displacement of the slab edge across a transverse joint caused by inadequate load transfer, differential deflection at the joint, inadequate base support, or sub-base erosion (Jung et al., 2008). The difference in elevation affects vehicle ride quality, accelerates vehicle damage, and leads to distresses, such as corner breaks and blowups; thus, faulting has a major effect on vehicle operation costs and pavement life-cycle costs (FHWA, 2006). Faulting is an important performance indicator for jointed concrete pavements and the criteria for pavement restoration decisions.

Faulting has traditionally been collected by manual methods. The Georgia Faultmeter, designed by GDOT, is one of the most popular hand-held devices for performing faulting measurement and is used by many state highway agencies, including GDOT (2004) and the Minnesota Department of Transportation (MnDOT) (Burnham, 2003). In this method, a surveyor finds a gap in traffic and sets the faultmeter at a single spot along a designated joint to measure faulting. GDOT requires the meter to be set approximately 15 cm (6 in) from the pavement edge marking in the outside lane. The surveyor pushes the button to acquire a faulting measurement and records it manually. This manual operation is labor-intensive, time-consuming, costly, and dangerous to workers and drivers. It also limits the faulting measurement to only the sampled joints, not all of the joints. GDOT conducts faulting measurement on every eighth joint (GDOT, 2004). Therefore, alternative methods for effectively and safely collecting faulting data are much needed. In addition, state highway agencies are now required to collect faulting data under the new Highway Performance Monitoring System (HPMS) reassessment (OHIP & FHWA 2008). This strongly motivates state DOTs to look for cost-effective means to collect faulting data.

Recently, some state highway agencies, such as the Florida Department of Transportation (FDOT) and the Mississippi Department of Transportation (MDOT), have collected faulting data using single laser profile data that were collected for the IRI (MaGhee, 2004; Nazef et al., 2009). With the single profile data, it is important to have an adequate sampling interval to locate the joint. Nazef et al. reported that a 1.7 cm (0.68 in) sampling interval yields a 95% joint detection rate using the algorithm developed by the FDOT. The chance of missing joints increases as the sampling interval increases.

With the advance of sensing technology, the 3D line laser imaging technique creates the potential to use not one single profile but the entire pavement surface to measure the faulting across concrete joints. Figure 3-14 illustrates the basic principle of capturing line laser data along the joints while the vehicle is driving at highway speed, and Figure 3-15 gives an example of the collected pavement surface laser data at the location of a concrete joint. It can be observed that the elevation change of the pavement surface is clearly captured by the laser data, which makes it possible to develop automatic faulting measurement algorithms.

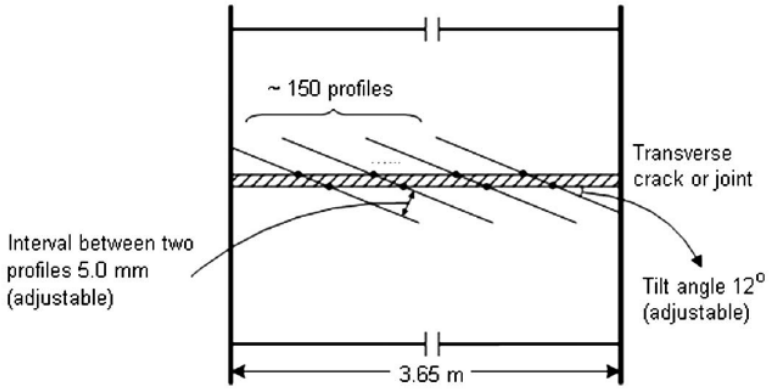

Figure 3-14 Illustration of the alignment of the 3D continuous laser profiles

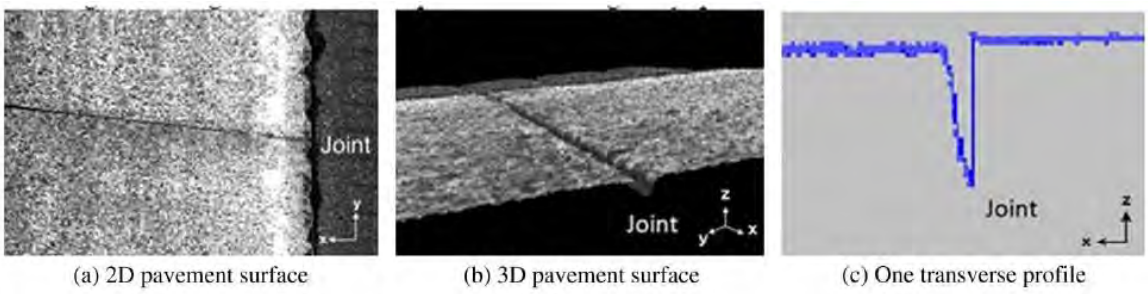

(a) 2D pavement surface (b) 3D pavement surface (c) One transverse profile

Figure 3-15 Example of pavement surface laser data for faulting measurement

To validate the capability of using the pavement surface laser data on faulting measurement and to examine the performance of corresponding automatic faulting measuring methods, a comprehensive validation test was conducted in our research. Using the same pavement surface laser data, two different methods are evaluated in this section, including a regression-based faulting measurement (Tsai, et al., 2012) and the concrete joint module provided in the commercial software. The test results, analysis, and major findings are presented in this report to provide an overall performance evaluation and, also, to make suggestions for future improvement.

4.1 Validation using the regression-based faulting detection method

For the regression-based method, a controlled in-lab experimental test was first conducted to examine the detection accuracy of the method; then, a field test was conducted on I-16 to evaluate the accuracy and the feasibility of operating the integrated sensing system at highway speeds.

Controlled In-lab Experimental Result and Analysis

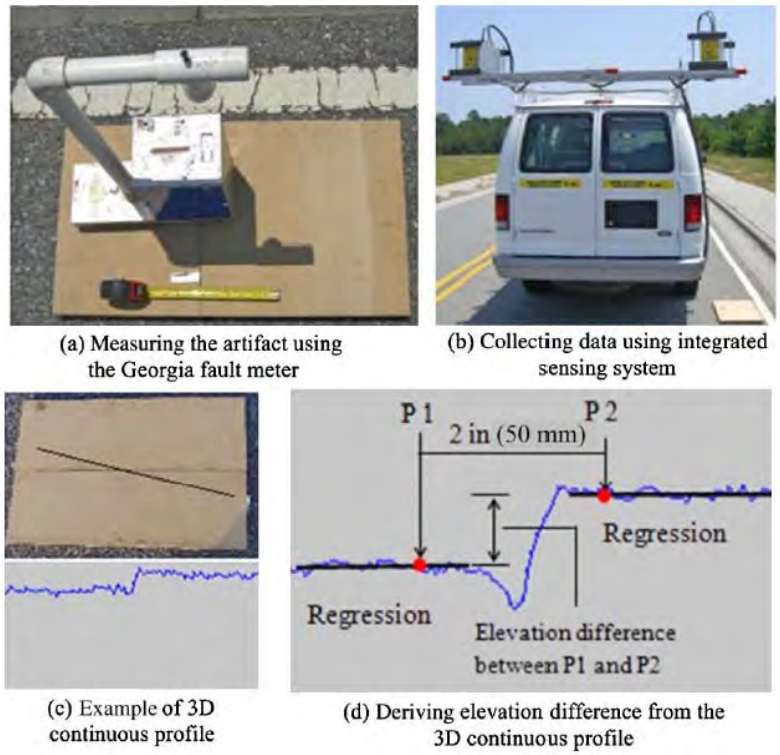

(a) Measuring the artifact using the Georgia fault meter

(b) Collecting data using integrated sensing system

(c) Example of 3D continuous profile

(d) Deriving elevation difference from the 3D continuous profile

Figure 3-16 Controlled test

In-lab tests were designed to test the regression-based method with the faulting in different ranges in a well-controlled environment, as it is difficult to locate a testing section of an appropriate length that can cover a full range of faulting. The artifacts, made of two wood panels creating two flat surfaces with known elevation differences, were used to create the elevation differences ranging from 0.8 to 15 mm (1/32 to 19/32 in). The purpose was to mimic the range of faulting measured by the Georgia Faultmeter. The artifacts were set level on a fairly flat road on the Georgia Tech campus to ensure a consistent elevation difference between any two points on the two panels. The known elevation differences were also confirmed using the Georgia Faultmeter on the test site, as shown in Figure 3-16. The integrated sensing system was then used to collect the pavement surface laser data with a 1mm (0.04 in) resolution in the transverse direction and a 5mm (0.2 in) interval between two profiles in the travel direction at low speed, as shown in Figure 3-16(b). With a 12° tilt angle, approximately 15 profiles were collected along the 38 cm (15 in) wide wood panel. Figure 3-16(c) shows one of the 3D continuous pavement profiles that can be used to derive the elevation difference. The elevations of the two flat surfaces can be established by applying regression to the points representing the surface, as shown in Figure 3-16(d). Following the footprint of the Georgia Faultmeter, the elevations of two measurement points (P1 and P2 in Figure 3-16(d)), separated by 50 mm (2 in.), were estimated using the regression lines, and then the elevation difference could be calculated.

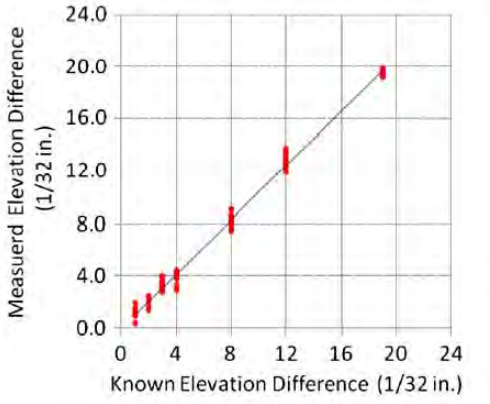

Figure 3-17 Known & derived elevation differences

The accuracy of the derived elevation differences was then evaluated by comparing the derived and the known elevation differences. Figure 3-17 shows the derived elevation differences were close to the known elevation differences with a small variation. The comparison results in Table

3-3 show that the average absolute differences are within 1 mm (0.04 in), and the variances among different profiles were fairly small (less than 1 mm) and consistent across various elevation differences. The regression-based method slightly overestimated the elevation differences. The 0.8 mm (1/32 in) elevation difference may not be detected reliably because of the 0.5 mm resolution in the vertical direction. The results of the controlled field tests have demonstrated that the regression-based method can achieve an accuracy of less than 1 mm with small variances among different profiles.

Table 3-3 Summary Result of Elevation Statistics

Known elevation difference (in.)	Known elevation difference (mm)	Sample size	Mean (mm)	Average difference (mm)	Average absolute difference (mm)	Standard deviation (mm)	Coefficient of variance
1/32	0.8	20	1.0	0.2	0.2	0.3	0.27
2/32	1.6	6	1.6	0.0	0.3	0.3	0.21
3/32	2.4	19	2.7	0.3	0.3	0.3	0.12
4/32	3.2	13	3.1	−0.1	0.3	0.4	0.13
8/32	6.4	15	6.5	0.1	0.3	0.4	0.06
12/32	9.5	20	10.1	0.6	0.6	0.4	0.04
19/32	15.1	20	15.5	0.4	0.4	0.2	0.01

Field Experimental Result and Analysis

Field tests were also conducted on I-16 to evaluate the accuracy and repeatability of the regression-based method and the feasibility of operating the integrated sensing system at highway speeds. A 450-ft test section covering 15 joints on eastbound I-16 between milepost 154 and 155 was selected because of the sampled faulting reported on the section by GDOT's engineers. The slabs are 9 m (30 ft) long and 3.65 m (12 ft) wide. The 15 slabs were first labeled and marked with a sequential number and a point where the faulting was measured on the basis of GDOT's faulting measurement practice (GDOT, 2004). The marked point was approximately 15 cm (6 in) from the pavement edge marking. The faulting was measured three times at each joint to establish the ground truth. The integrated sensing system was then used to collect faulting data at two different highway speeds, 100 and 80 km/h (62.5 and 50 mph). The joint can be captured by the profile with 1 mm (0.04 in) resolution in the transverse direction. Three runs were repeated at each speed to evaluate the repeatability of derived faulting measurements and the feasibility of operating the integrated sensing system at highway speeds. The 3D continuous pavement profile data at the marked point where the faulting was measured by the Georgia

Faultmeter was identified manually, and faulting was derived on the basis of the selected profile data using the same method described in the controlled field test section.

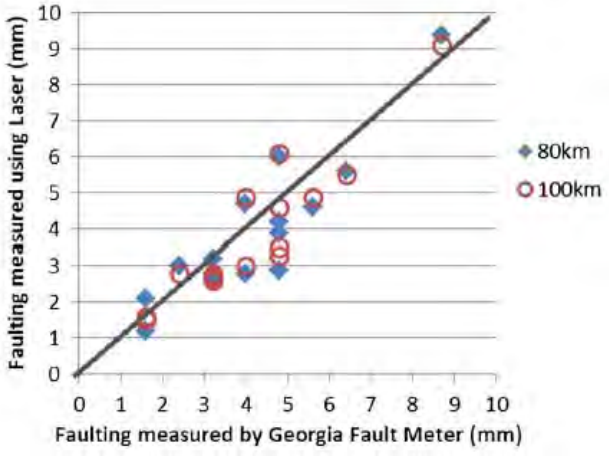

Figure 3-18 Measured vs. derived faulting measurements

Faulting measurements of the 15 joints derived from the 3D continuous pavement profile data were compared with those measured using the Georgia Faultmeter to evaluate the accuracy and repeatability of the regression-based method at highway speed. Figure 3-18 shows that the derived faulting measurements are fairly close to the ones measured using the Georgia Faultmeter, with a maximum difference of less than 2 mm. Table 3-4 summarizes the derived faulting measurements on the 15 joints collected on I-16 at different speeds. The derived faulting measurements range from 1.2 to 9.4 mm (0.05 to 0.37 in), and 13 out of 15 joints have a difference of less than 1 mm; the largest difference is 1.9 mm.

Table 3-4 Statistics of Derived Faulting Measurement on 15 Slabs by Speeds

Slab	Georgia fault meter (mm)	80 km/h Mean (mm)	80 km/h Difference (mm)	80 km/h Standard deviation (mm)	100 km/h Mean (mm)	100 km/h Difference (mm)	100 km/h Standard deviation (mm)	80–100 Mean difference (mm)
1	4.8	3.9	−0.9	0.2	4.6	−0.2	0.3	−0.6
2	1.6	1.2	−0.4	0.3	1.6	0.0	0.2	−0.5
3	1.6	2.1	0.5	0.5	1.5	−0.1	0.3	0.6
4	4.8	6.0	1.2	0.3	6.1	1.3	0.9	−0.1
5	4.8	4.2	−0.6	0.1	3.3	−1.5	0.1	0.9
6	5.6	4.6	−1.0	0.1	4.9	−0.7	0.3	−0.3
7	6.4	5.6	−0.8	0.4	5.5	−0.9	0.1	0.1
8	3.2	2.6	−0.6	0.6	2.7	−0.5	0.2	−0.1
9	3.2	2.8	−0.4	0.8	2.8	−0.4	0.4	0.0
10	3.2	3.2	0.0	0.4	2.6	−0.6	0.3	0.5
11	4.0	4.7	0.7	0.4	4.9	0.9	0.3	−0.2
12	4.0	2.8	−1.2	0.6	3.0	−1.0	0.3	−0.2
13	2.4	3.0	0.6	0.9	2.8	0.4	0.1	0.1
14	4.8	2.9	−1.9	0.6	3.5	−1.3	0.8	−0.5
15	8.7	9.4	0.7	0.5	9.1	0.4	0.1	0.3

The repeatability of the derived faulting measurements collected in three runs at each speed was evaluated next. Figure 3-19 and Figure 3-20 show the derived faulting measurements from three runs at 80 and 100 km/h, respectively. As shown in Figure 3-19 and Figure 3-20, there is no significant difference among the different runs. The standard deviations are within 1 mm, as shown in Table 3-4. The maximum differences among three runs were also reviewed. For the data collected at 100 km/h, 13 out of 15 joints (87%) have a maximum difference of less than 1 mm (0.04 in.). Results indicate that the derived faulting measurements can achieve a desirable repeatability among different runs at the same speed. Finally, the derived faulting measurements were compared at different speeds. Figure 3-21 shows the derived faulting measurements are fairly close at different speeds, and no significant difference or bias can be observed. The differences are within 1 mm (0.04 in), as shown in Table 3-4. On the basis of these analyses, the proposed method can achieve a desirable repeatability among different runs and at different speeds, and it is feasible to operate the integrated sensing system at highway speed (e.g., 100 km/h) for collecting faulting data.

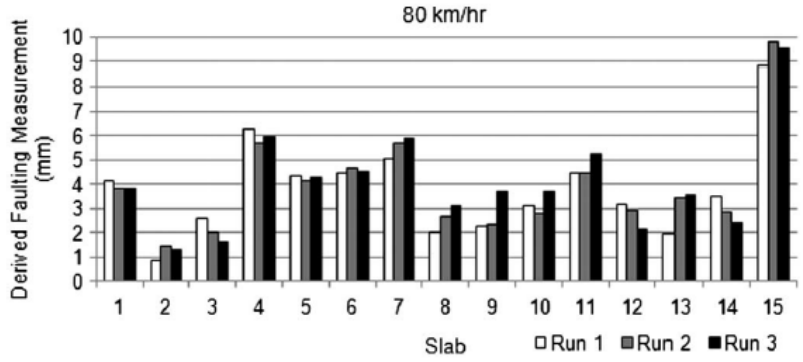

Figure 3-19 Derived faulting measurements at 80 km/h

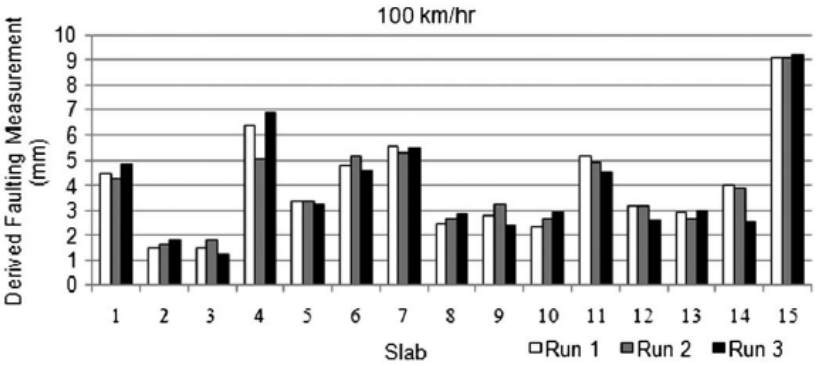

Figure 3-20 Derived faulting measurements at 100 km/h

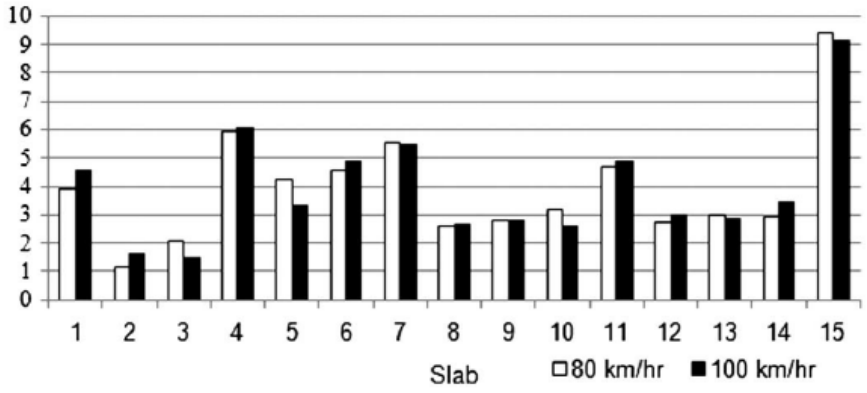

Figure 3-21 Comparison of faulting measurements at different speeds

On the basis of lab tests and field tests conducted on I-16, the preliminary results have demonstrated that it is feasible to collect faulting data with desirable accuracy and repeatability when using the 3D continuous profiles acquired by the integrated sensing system at highway speeds.

4.2 Validation using the concrete joint module in the commercial software

Transverse Joint Detection Module Test

To test the accuracy of the software for detecting transverse joints, we conducted a validation test on a dataset of 941 images. An example of the expected detection result is shown as Figure 3-22.

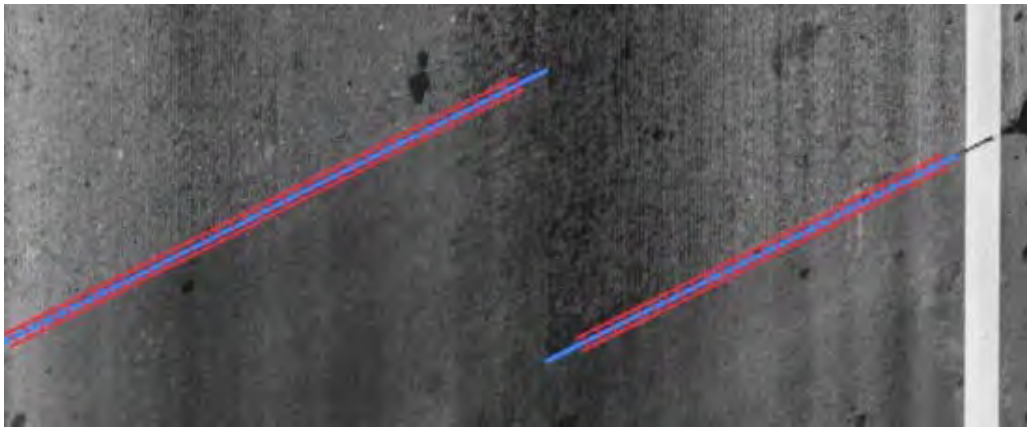

Figure 3-22 Example of correctly detected cases

The blue lines in the image indicate the location of the joint, while the red bars indicate the measuring points for faulting; the information will be utilized in the next section. It can be seen

that for the expected outcome, the correct detection needs to be on both sides of the road, and the length of the detected lines (the blue ones) should match the actual transverse joint length.

Within these images, 5 images with transverse joints were not detected correctly (Type II error); in 4 images, other distresses, such as cracks, are mistakenly detected as joints (Type I error). Considering both Type I and Type II errors, the joint detection module still achieved an accuracy of 99.5%.

To find the reasons for the incorrect detection, we further examined the error cases. Four false-positive cases were big transverse cracks sharing the typical characteristics of joints (shown in Figure 3-23):

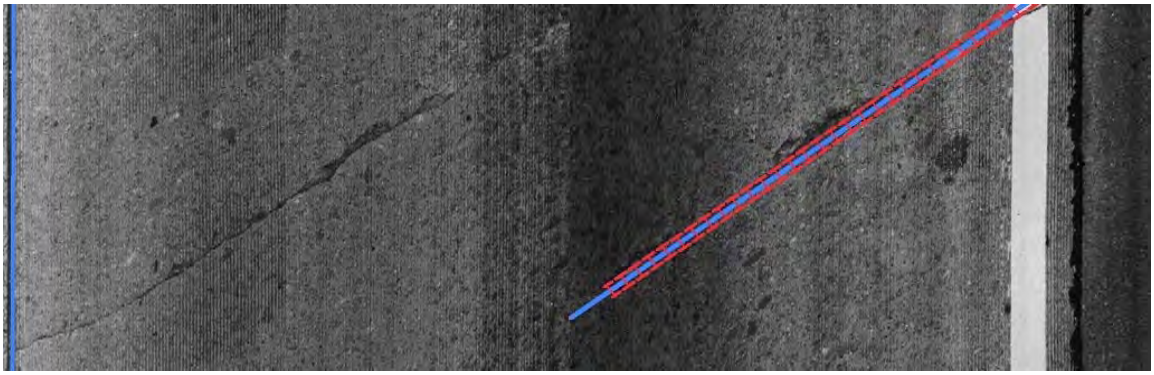

Figure 3-23 Example of false-positive cases

This type of case is, naturally, difficult to eliminate because these cracks have almost all the unique characteristic of joints. However, it is very rare for the crack to maintain a consistent width and straightness in both sides of the pavements. So, unlike transverse joints, normally these cases would only occur in one side of the pavement. As a result, it is easy to find them by comparing the detection results with the other side of the pavement.

Five false-negative cases have the detection results only on one side, as shown in Figure 3-24:

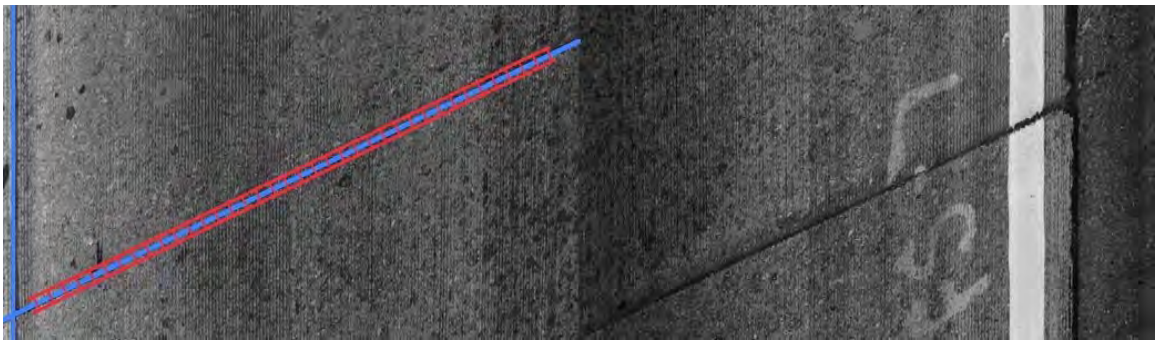

Figure 3-24 Example of false-negative cases

Most of these cases contain joints with a portion outside the image, which may cause problems for the detection. However, it is not common for the false-negative cases to occur on both sides. By examining the detection result on the other side of the pavement, the impact of false-positive cases can be much reduced.

Some other special cases were also tested. There are 5 images containing joints with asphalt patches (Figure 3-25), and all such cases are detected correctly, which indicates patching may not influence the detection process.

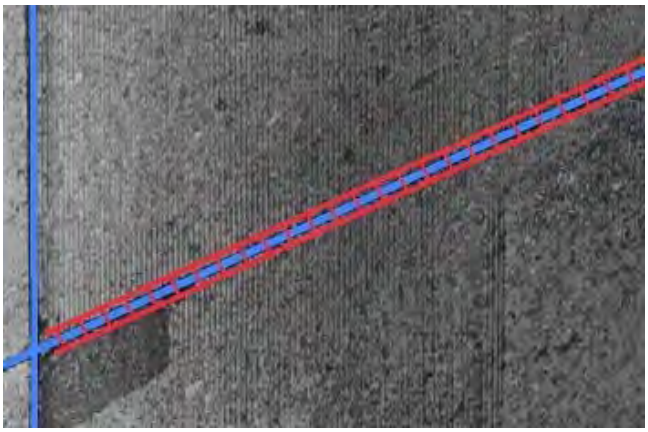

Figure 3-25 Example of joints with patch

Faulting Measuring Module Test

Data Collection and Ground Truth Establishment

For faulting measurement, we collected data on a section of I-16. The location is shown in the map in Figure 3-26. Field measurement was conducted to establish the ground truth for this

validation test. Three places on the route were selected for manual ground-truth data collection; each of the three places contained 10 continuous concrete slabs. One place is around EB MP159 (Site #1), and the other two spots are on WB MP159 (Site #2) and MP156 (Site #3). All those joints measure are marked with color painting. The Georgia Faultmeter, which has already been introduced in the literature review, was used as the measuring tool, as shown in Figure 3-27.

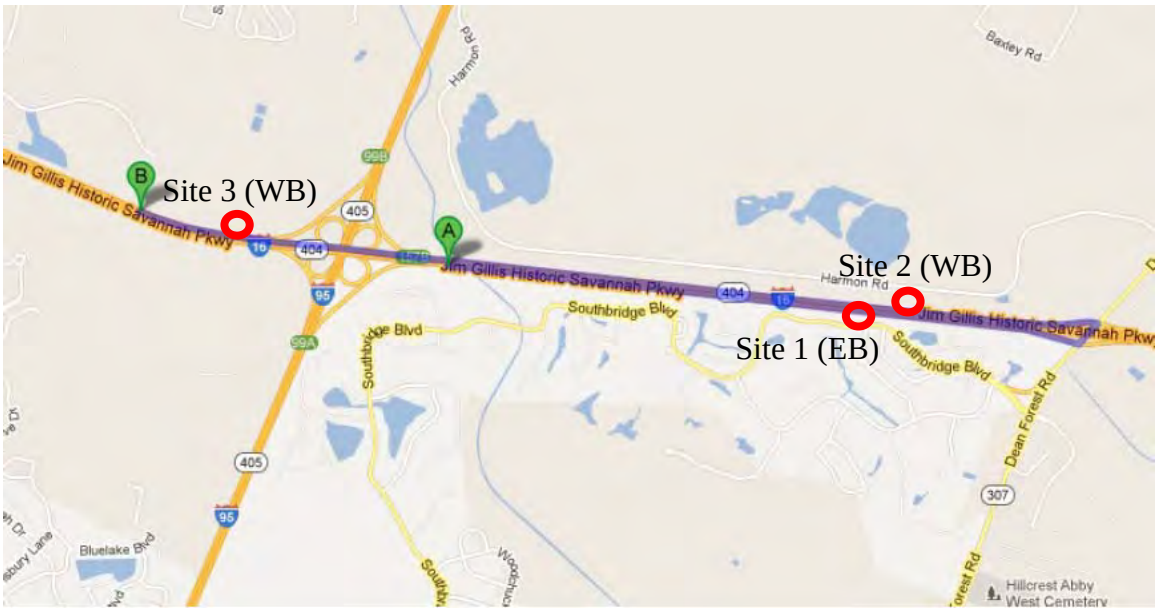

Figure 3-26 Locations of data collection

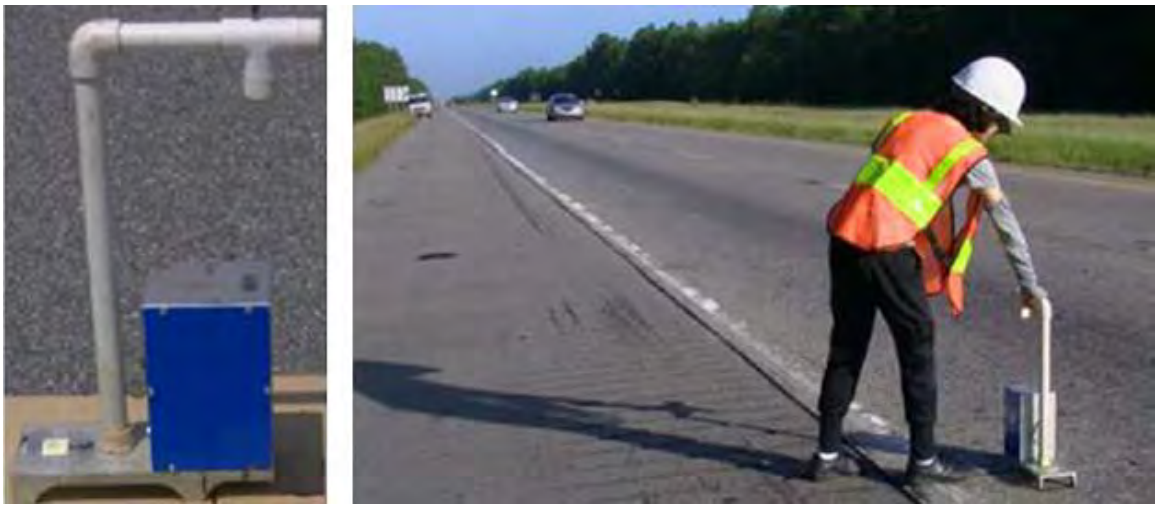

Figure 3-27 *Left*: Georgia Faultmeter; *Right*: Manual measurement on the roadway

To reduce random errors, multiple runs were conducted for the same pavement section. The marked measuring location example is shown in Figure 3-28, with the white dot painted on the joint indicating the measuring point:

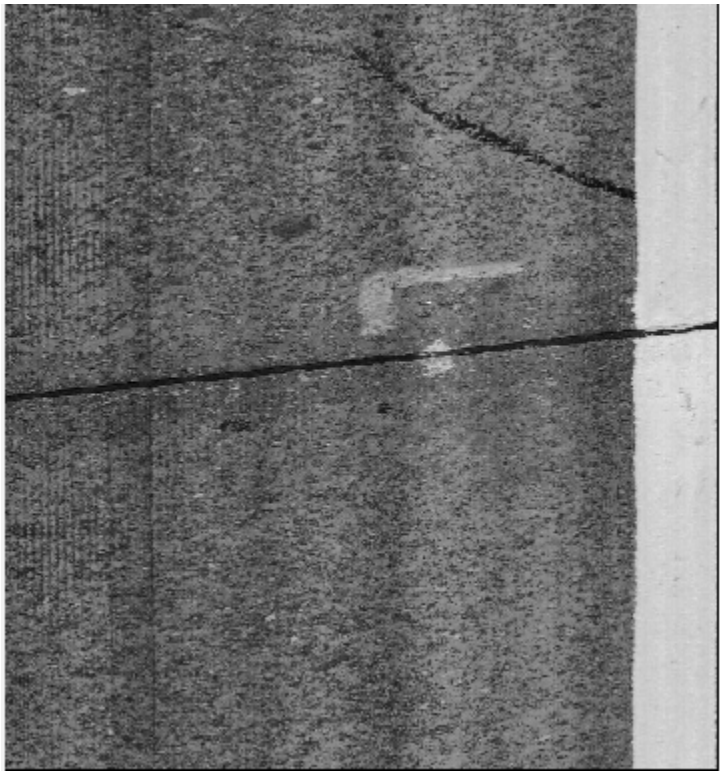

Figure 3-28 Marked measuring point in pavement surface laser data

Testing Results

The tests consisted of several major steps. First, a proper configuration was needed for the software to achieve good performance. In this test, we added a further averaging procedure, which calculated the average detected elevation differences among all points within the marked area to reduce possible random errors. After that, a comprehensive analysis and interpretation of the final result were made to arrive at the conclusion.

a) Parameter Configuration

The faulting detection module of the software has several adjustable parameters, which would influence the detection performance. The most important parameters are illustrated in Figure 3-29:

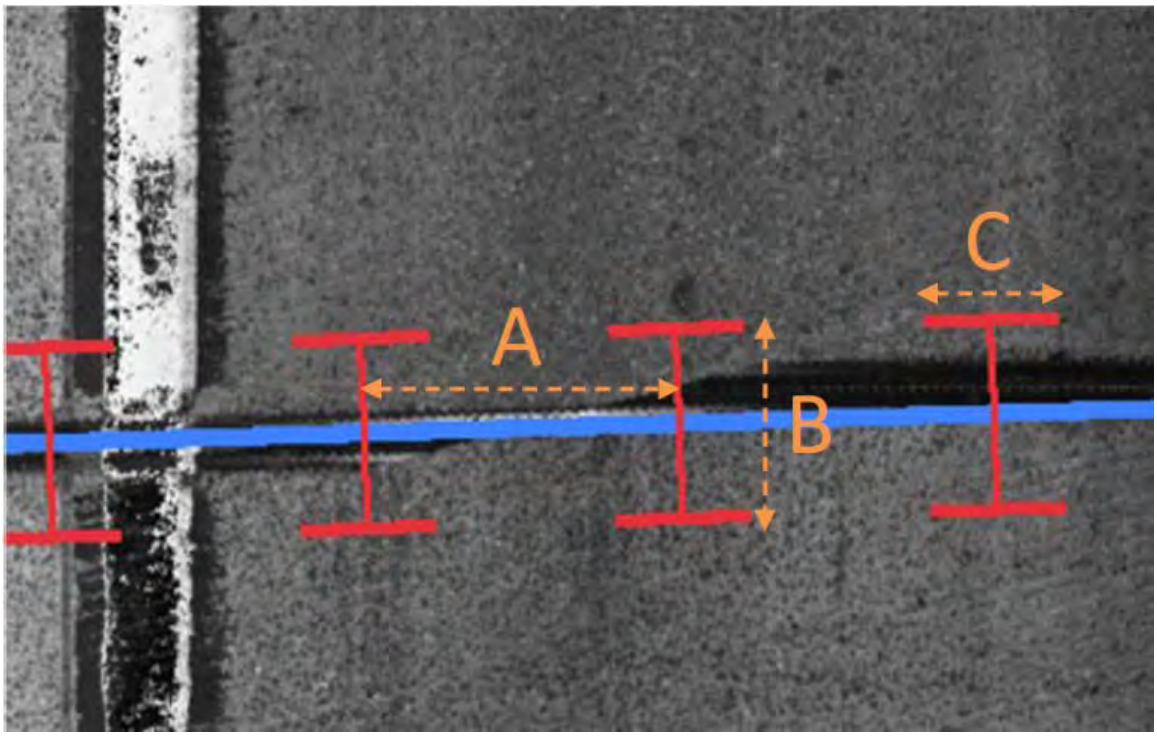

Figure 3-29 Faulting measurement parameters

The mechanism of the detection module obtains the elevations of both ends of the red bars in Figure 3-29, and then compares their differences in elevation. A is the distance between consecutive measuring points along the joint; B is the distance between two measuring ends; and C is the averaging window length. Our averaging program requires the distance A to be 1 mm, which will be elaborated upon later. As the averaging process would be done in the next step, we set the averaging window size, which is the distance C in Figure 3-29, as 1 mm, too. So, the only variable left adjustable is the distance B. To find out the optimal value of distance B, we tried multiple settings, including 50 mm, 100 mm, 200 mm, and 300 mm. The test results are discussed below:

b) Initial Result Averaging

As is shown in Figure 3-28, the measuring point is actually an area in the image, so to increase the precision, we set the distance A to a very small value (1 mm) and programmed to get the average evaluation difference within the area as the final outcome. Normally, there will be nearly 40 points within the marked area. We first find these points by the X coordinate range (horizontal), and then extract them from the XML file generated by the software.

c) Result Analysis

The final result after the averaging process is discussed in this section. From the test results, we calculated the mean and standard deviation values of the error, which is defined as the absolute difference between the software-measured value and the ground truth for different settings. We also calculated the 95% confidence upper limit of the error for every setting - basically this means the error has a probability of 95% lying below this limit.

The Site 1 data has the largest error, with more than 2 mm at 95% of the upper limit for all the settings; in the other two sites, this value can be controlled within 2 mm for some settings. However, even for Site 1, the average error value is only slightly higher than 1 mm; in the other two sites, the average errors are both below 1 mm. In reality, the faulting cases we have interests in normally have elevation differences larger than 5 mm, so a mean error of approximately 1 mm and maximum of 2 mm variance for small portion cases is acceptable. Through performance comparison among different settings of B distance, it can be seen that the 50 mm setting has the worst accuracy with the highest mean and deviation values of error in all three sites; the other three groups are much better. The performance of 100 mm, 200 mm, and 300 mm are slightly different. At Site 1 and Site 2, 100 mm has the best performance, while 300 mm has the worst, approximately 1 mm and 0.5 mm lower in the 95% upper limit, respectively; in Site 3, the 300 mm setting performs the best, while 100mm performs the worst, yet is only 0.3 mm lower in the 95% upper limit. So, 100 mm has overall slightly better performance than 300 mm. Meanwhile, the 200 mm setting has consistently good performance, which can also be a recommended setting.

Table 3-5 Test Result for Site 1 (Error = |Measured Value – Ground Truth|)

Site 1	Field Test(Ground Truth)				LCMS Results			
Sample number	Round1	Round2	Round3	Average / mm	50mm	100mm	200mm	300mm
1	0.79	0.79	2.38	1.32	0.23	0.49	1.07	2.23
2	3.18	1.59	1.59	2.12	0.41	0.54	-0.03	0.41
3	2.38	2.38	3.18	2.65	-1.62	0.62	1.51	0.21
4	2.38	3.18	3.97	3.18	0.61	1.65	2.61	2.33
5	1.59	0.79	1.59	1.32	0.83	0.48	2.40	1.00
6	2.38	3.18	3.18	2.91	5.34	1.83	1.70	2.05
7	1.59	1.59	0.79	1.32	-1.43	0.40	0.63	0.94
8	5.56	5.56	4.76	5.29	2.48	4.18	3.23	2.55
9	3.97	3.97	4.76	4.23	0.72	2.20	1.19	1.23
10	1.59	1.59	1.59	1.59	-0.11	0.74	1.09	1.02
Extra	3.18	3.18	1.59	2.65	0.86	1.30	2.37	2.56
Error Mean	/				2.28	1.29	1.18	1.26
Error Std dev.	/				1.03	0.43	0.85	0.99
95% Conf. Upper Limit	/				4.29	2.13	2.85	3.20

Table 3-6 Test Result for Site 2 (Error = |Measured Value – Ground Truth|)

Site 2	Field Test(Ground Truth)				LCMS Results			
Sample number	Round 1	Round 2	Round 3	Average / mm	50mm	100mm	200mm	300mm
1	11.11	11.11	11.91	11.38	/	/	/	/
2	0.79	0.79	0.79	0.79	0.49	-0.021	1.438	1.057
3	4.76	4.76	5.56	5.03	6.28	4.718	4.088	3.708
4	3.97	3.18	3.18	3.44	8.06	3.588	5.491	5.464
5	7.14	6.35	5.56	6.35	2.29	7.087	7.204	8.107
6	3.18	3.18	3.18	3.18	0.047	1.54	2.776	2.7
7	3.97	3.18	2.38	3.18	10.69	2.123	3.521	4.457
8	3.18	3.18	3.18	3.18	1.46	2.645	2.669	3.648
9	5.56	5.56	5.56	5.56	2.4	4.734	4.917	4.709
10	9.53	9.53	9.53	9.53	7.27	10.826	10.013	9.154
Error Mean	/				3.11	0.82	0.76	0.98
Error Std dev.	/				2.02	0.44	0.49	0.61
95% Conf. Upper Limit	/				7.06387	1.6815	1.7269	2.1686

Table 3-7 Test Result for Site 3 (Error = |Measured Value – Ground Truth|)

Site 3	Field Test(Ground Truth)				LCMS Results			
Sample number	Round1	Round2	Round3	Average / mm	50mm	100mm	200mm	300mm
1	5.56	5.56	5.56	5.56	6.005	4.481	3.838	4.138
2	7.14	7.94	7.94	7.67	5.398	8.745	8.216	7.284
3	3.97	3.97	3.97	3.97	5.598	3.718	4.42	4.19
4	3.97	3.97	3.97	3.97	/	/	/	/
5	7.14	7.94	7.94	7.67	6.686	7.988	8.016	7.564
6	3.97	3.97	3.97	3.97	5.684	5.275	4.443	3.45
7	4.76	3.97	4.76	4.50	1.88	4.837	5.018	5.738
8	5.56	6.35	6.35	6.09	6.307	7.854	7.239	5.749
9	4.76	3.18	3.97	3.97	4.449	4.642	4.707	4.844
10	6.35	7.14	6.35	6.61	/	/	/	/
Error Mean	/				1.30	0.85	0.74	0.64
Error Std dev.	/				0.84	0.51	0.44	0.45
95% Conf. Upper Limit	/				2.94047	1.8517	1.5989	1.5282

And Figure 3-30, Figure 3-31and Figure 3-32 visualize the detection results. It's fairly clear that the 100 mm, 200 mm and 300 mm settings all outperform the 50 mm one.

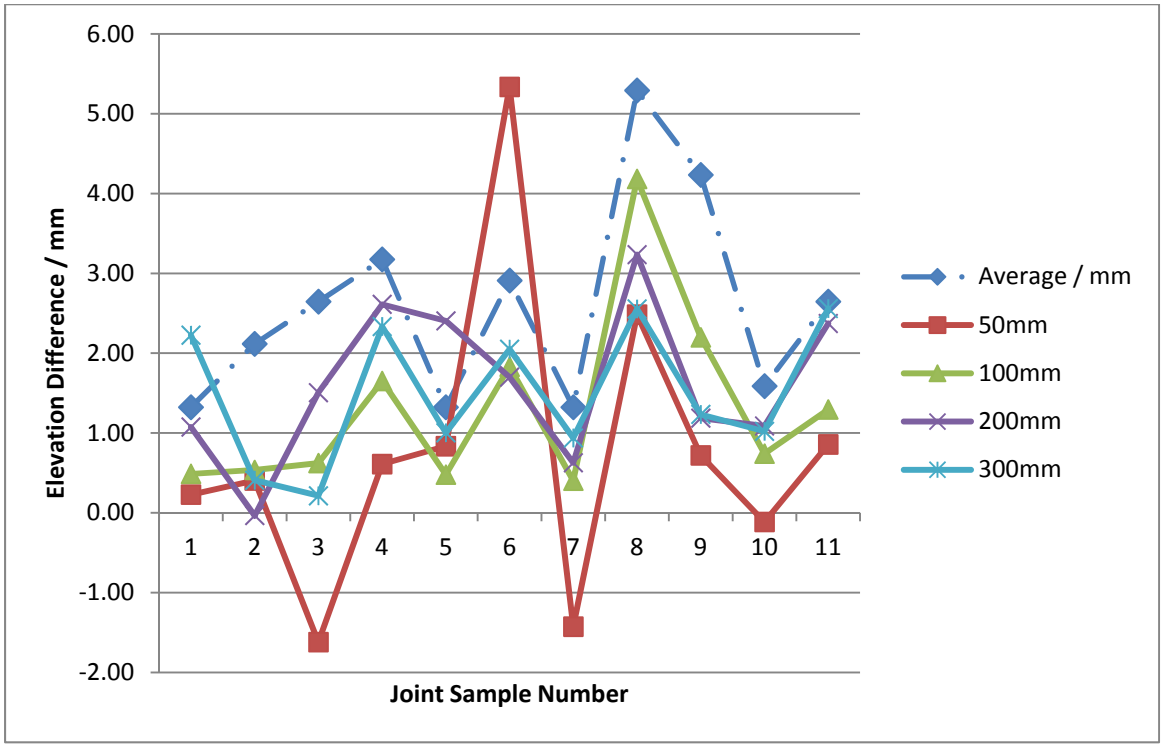

Figure 3-30 Site 1 result

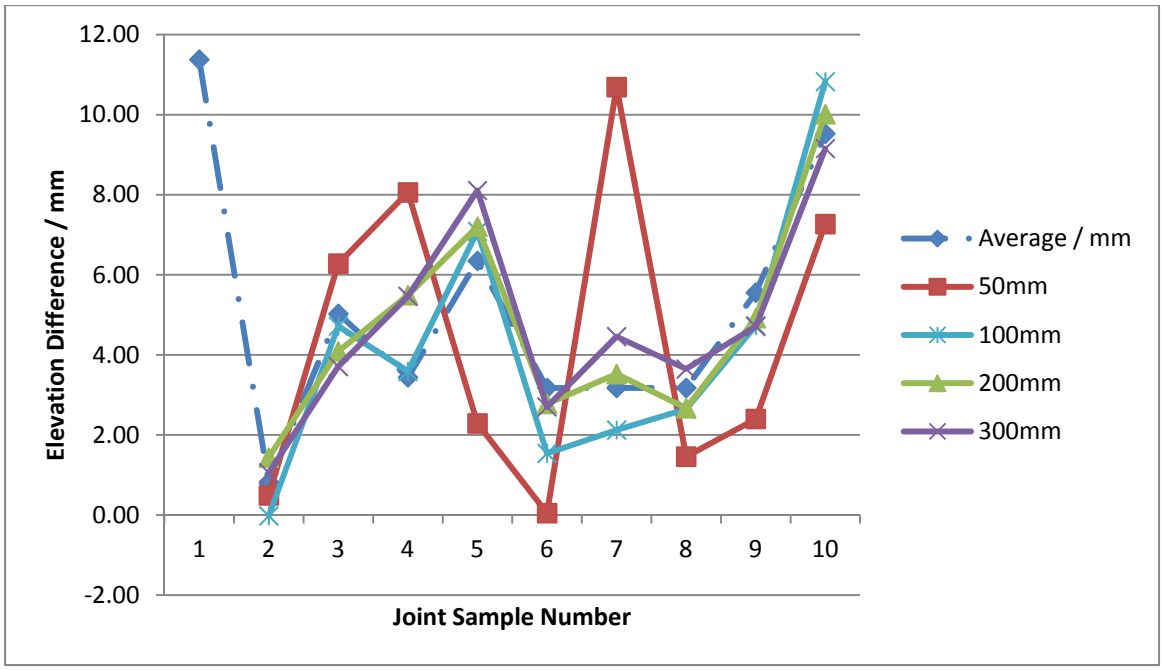

Figure 3-31 Site 2 result

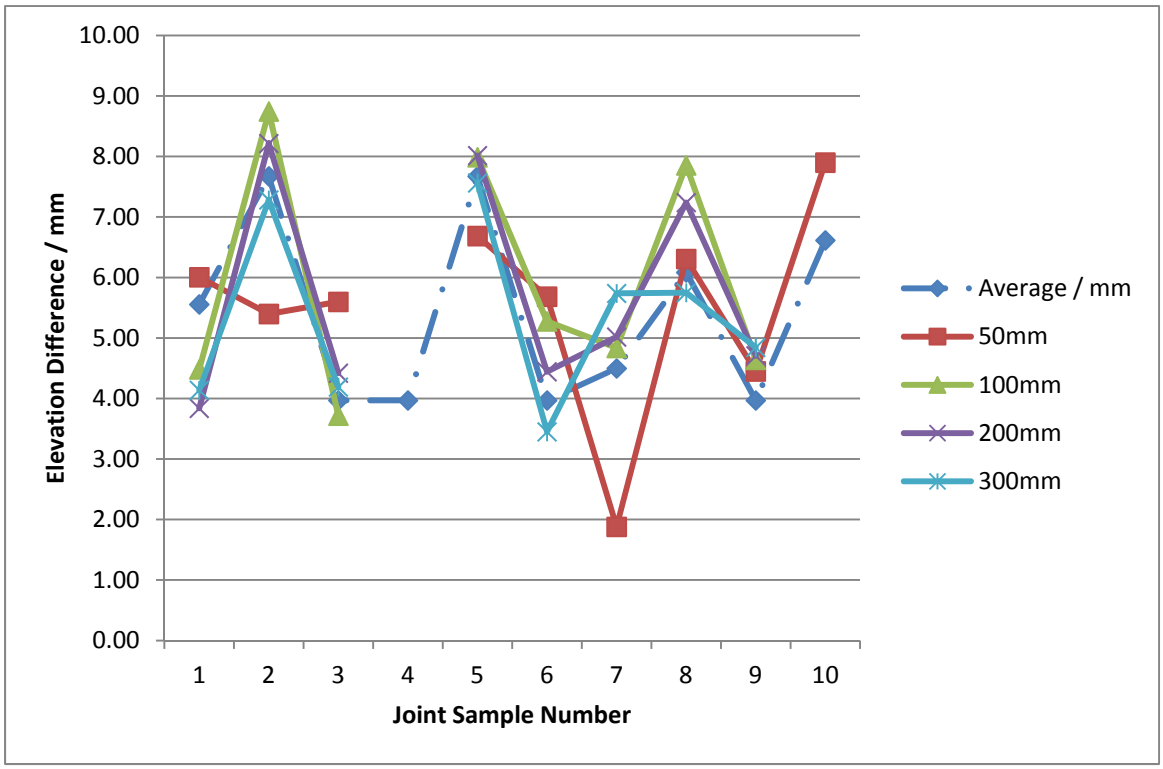

Figure 3-32 Site 3 result

In this test, most cases have been successfully measured, yet three cases in which joints have been successfully detected failed to provide faulting measurement information. Results with the symbol '/' indicate failure to provide faulting information. Most of these problems occurred in joints with a portion outside the image and with a marked location close to the image edge, as shown in Figure 3-33.

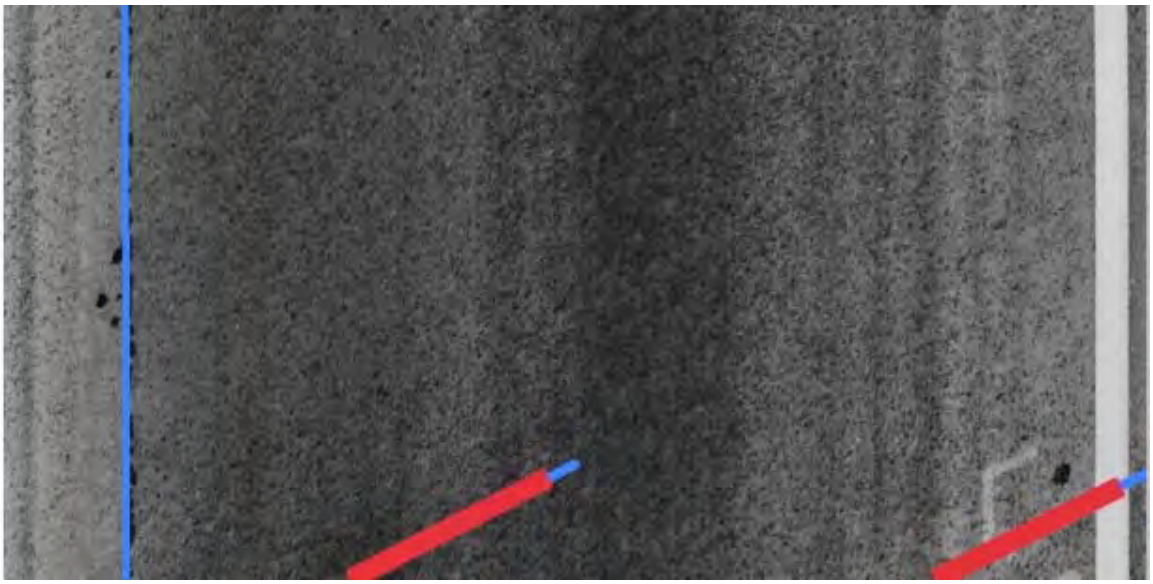

Figure 3-33 Example of joints with excluded part

In conclusion, with proper settings, the pavement surface laser data along with the faulting detection software can measure the elevation difference across transverse joints with an average error of approximately 1 mm, and less than 1 mm variance in most cases; the 95% error limits can be controlled within 2 mm in two of three sites tested, and slightly over 2 mm in the third site. Per the requirement of the project needs, the accuracy provided is acceptable. According to the testing results, the recommended setting of the distance between two measuring points can be either 100 mm or 200 mm. If possible, multiple tests using different settings are also recommended to reduce false detection cases.

4.3 Summary

To validate if the 3D pavement surface data acquired by the new technology could provide sufficient accuracy, two detection methods are tested in the study. For the regression-based detection method, both controlled in-lab tests and field tests were conducted for performance

evaluation. The controlled test shows less than 0.6 mm mean error with small variances in multiple cases; the field test, which collects data at highway speed, also shows less than a 1.5 mm mean error with a standard deviation smaller than 1 mm at 80 km/h and 100 km/h. So, though the speed of data collecting can affect detection accuracy, the variation is not significant and won't affect the consequent analysis.

For the built-in faulting detection software module test, in which the data-collecting vehicle drove at approximately 96.6 km/h (60 mile/h), different software configurations were tested to achieve the optimal accuracy. It was found that with 100 mm or 200 mm as the measuring distance setting, the average error can be controlled around 1 mm with less than 1 mm variance. Future research could focus on improving handling missed cases where joints are not completely inside the images.

Judging from these validation test results, it is concluded that with the proper detection algorithm and software configuration, collecting faulting data by using the integrated sensing system at highway speeds to collect 3D continuous profile data is feasible and produces data with desirable accuracy and repeatability. Though the regression-based method and the built-in software occasionally produce incorrectly detected cases, the overall detection accuracy is acceptable, and through post-processing, it is easy to reduce the impact of such cases.

5. Validation of Concrete Pavement Spalling Detection

Spalling is a common type of concrete pavement distress that usually occurs along the construction joints between concrete slabs. According to the LTPP's definition, spalling refers to cracking, breaking, chipping, or fraying of slab edges within 0.3 m from the face of transverse joints. GDOT defines spalling as the deterioration of concrete at the joint, which usually starts with the breaking or flaking off of the concrete at the joint; as they worsen, raveling and pop-outs occur (as shown in Figure 3-34). Due to its random spatial distribution pattern on the concrete pavement, it is difficult to design a sampling strategy for manual spalling survey. Therefore, automatic spalling detection will help improve the cost-effectiveness of concrete pavement maintenance and enhance roadway safety.

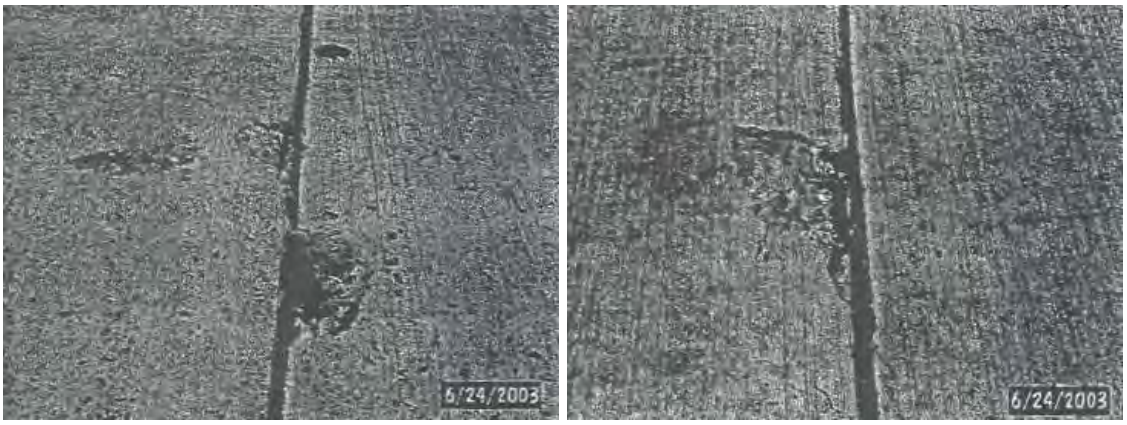

Figure 3-34 Example of spalling at concrete joint (GDOT 2003)

With the advance of sensing technology, an automatic spalling detection method can now be developed using 3D laser pavement data. The section will validate the accuracy of automatic spalling detection on concrete pavement. In addition, some representative false negative cases (e.g. asphalt-filled spalling and small/shallow spalling) and false positive cases (e.g. crack spalling, shoulder-joint distress, and concrete coring) will be presented to reveal the potential issue of concrete pavement spalling detection.

5.1 Experimental data

The experimental data of the validation test were collected on interstate highways I-16 and I-516 near Savannah, Georgia. Both highways are concrete pavement on the selected test sites (as shown in Figure 3-35).

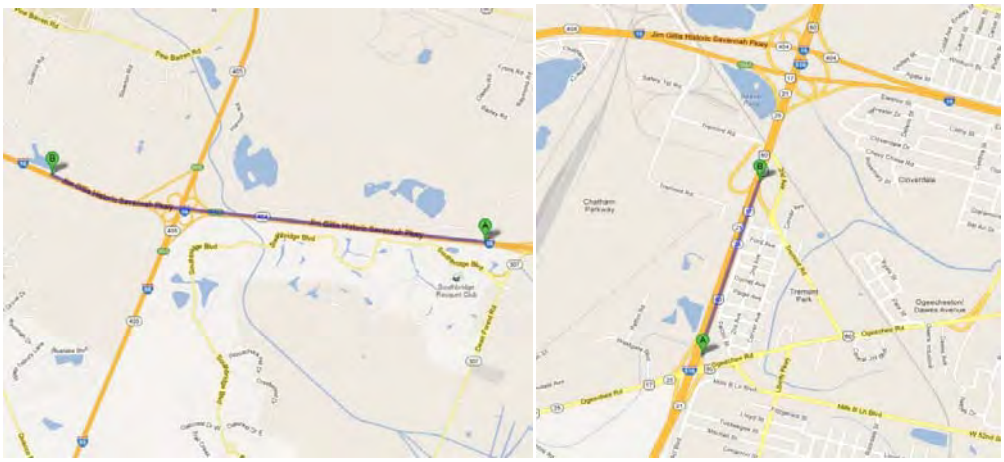

(a) I-16 test site (b) I-516 test site

Figure 3-35 Selected test sites on concrete spalling detection

5.2 Experimental design

The following procedures were conducted to evaluate the performance of automatic spalling detection on concrete pavement:

- First, the ground truth was established by manually reviewing the collected pavement surface laser data and identifying the location of spalling. Since the distribution of spalling is sparse on actual concrete pavement, it is not practical to manually record the ground truth along the road. However, spalling has a distinctive elevation change on concrete pavement, and a 3D range image is sufficient to support the ground truth established for validation purposes (as shown in Figure 3-36(a)). Based on the visual review of collected range images from the entire test site, the spalling location is manually identified.
- Then, the automatic spalling detection algorithm is applied. The spalling detection results can be overlaid on an intensity image or range image (Figure 3-36(b)).
- Finally, the ground truth and automatic detection results are compared. The numbers of correctly-detected/missed spalling are counted to calculate the overall detection precision.

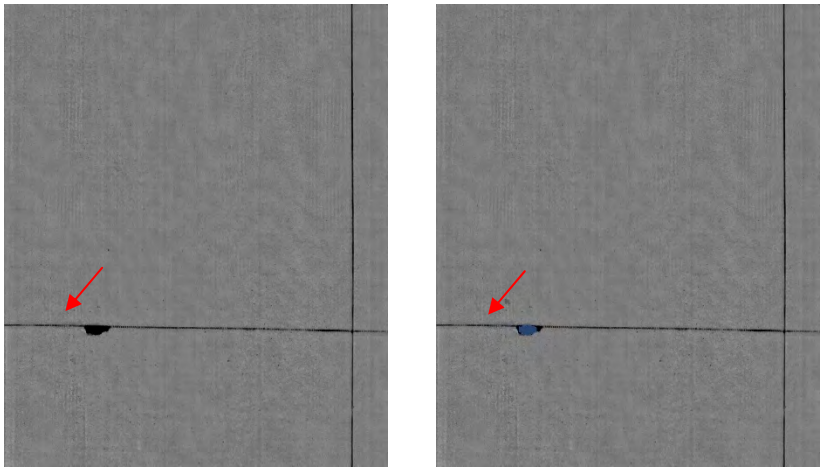

(a) Ground Truth (b) Automatic Spalling Detection Result

Figure 3-36 Illustration of spalling evaluation procedure

5.3 Validation on I-516 and I-16 test sites

Based on the manual review, a total of 86 spalling locations were identified on the selected test sites. Of these, 65 spallings were correctly detected, while 21 spalling locations were missed by the automatic detection algorithm, which provides a detection precision of 75.6%. Some representative cases are presented below.

Correct Detection Cases

Figure 3-37 shows three representative examples of correctly detected spalling. It can be observed that the location and shape of spalling do not have a significant impact on the performance of the automatic spalling detection algorithm. The automatic detection can also extract multiple spalling locations from the same pavement image.

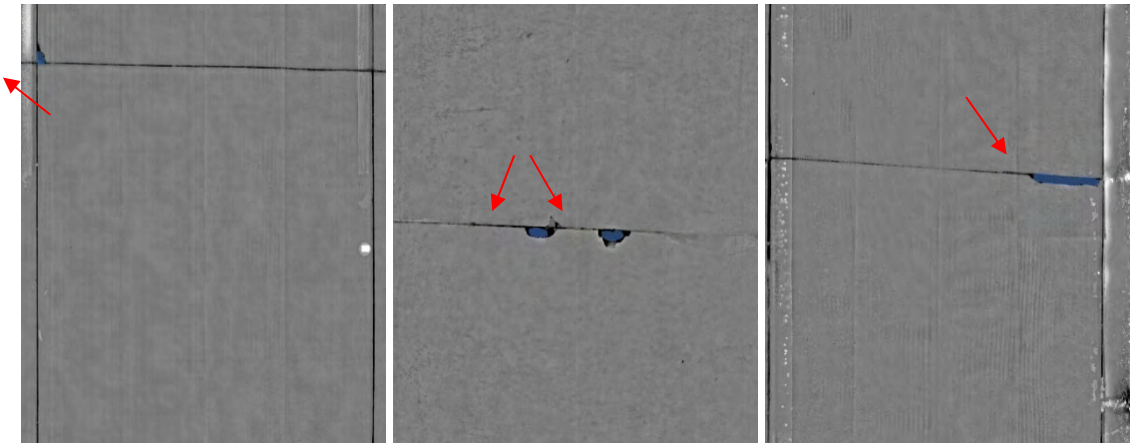

(a) Lane Line (b) Middle (c) Edge Line

Figure 3-37 Examples of correctly detected spalling

False Negative Cases

After a careful review of the 21 spalling locations that were missed by the automatic detection algorithm, these false negative cases can generally be classified into two different types:

- Undersized spalling: as shown in Figure 3-38(a), the size of the spalling is too small to be captured by the automatic detection algorithm. Besides the area, the depth of the spalling is another factor that may influence detection performance. In some cases, the spalling is too shallow and not distinct enough on the range image. The minimum size of spalling to be detected can be adjusted as a parameter in the automatic algorithm; however, a lower limit that is too small may introduce additional false positives into the spalling detection. On the other hand, GDOT only requires recording spalling sites whose areas are larger than 1.5’’x6’’. Through a rough measurement on the range image, the length of the spalling in Figure 3-38(a) is about 2.4 inches (around 60mm), which does not have to be recorded.

- Asphalt-patched spalling: as shown in Figure 3-38(b), some spalling sites have already been patched with asphalt in previous maintenance. Although some asphalt patches may not be in good condition, they still reduce the distinctiveness of spalling on concrete pavement and introduce the potential for false positives in spalling detection.

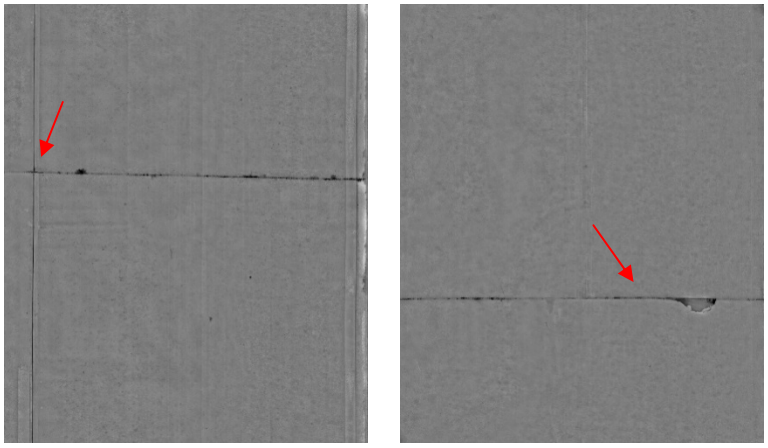

(a) Undersized Spalling (b) Asphalt-patched Spalling

Figure 3-38 Examples of false negative cases of spalling detection

False Positive Cases

Based on the review of the spalling detection results on the entire test site, some false positive cases are also identified. These cases can generally be classified into three different types:

- Spalling on severe cracking / broken slab: As mentioned in the previous section, spalling can also occur along both transverse and longitudinal cracking on concrete pavement, which usually indicates a high severity level of cracking. The spalling detection algorithm itself cannot differentiate spalling along joints or along cracks and, therefore, introduces some false positive cases through the validation test (as shown in Figure 3-39 (a)). Since we have already validated the joint detection algorithm on concrete pavement, these false positives can easily be removed as a follow-up step after spalling detection by comparing the location of detected spalling and joints.
- Shoulder-joint distress: This type of distress is caused by vertical movement in concrete slabs; it usually happens on the shoulder area right after a transverse joint. It has some characteristics similar to spalling and is also extracted by the spalling detection algorithm (as shown in Figure 3-39(b)). Although these results are false positive for spalling detection, it

does reveal the possibility of using the spalling detection algorithm to detect and measure this type of shoulder-joint distress. More details will be presented in the next section. Similarly, false positives can easily be removed by comparing the location of detected spalling and transverse joints.

- Coring: The quality control of concrete construction usually requires core drilling on the concrete surface. The deep coring has significant elevation changes and, therefore, is captured as false positives in some cases (as shown in Figure 3-39(c)). These false positives can also be removed based on location information.

Overall, although quite a few false positive cases are observed through the validation test, almost all of them can be eliminated by comparison with the detected joint location; therefore, these false positive cases should not have a significant influence on the real-world implementation of the automatic spalling detection algorithm.

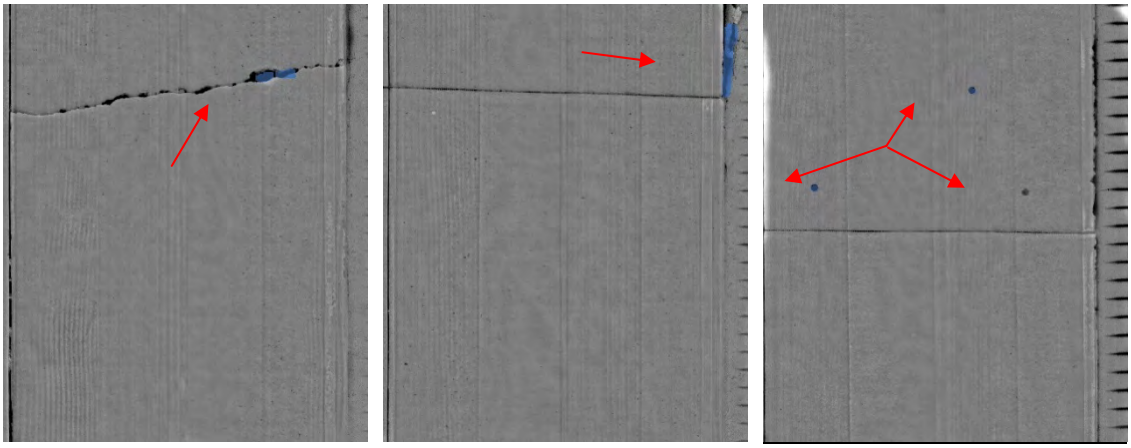

(a) Cracking (b) Shoulder-Joint Distress (c) Coring

Figure 3-39 Examples of false positive cases of spalling detection

Detection Accuracy vs. Spalling Size

To find the relationship between the spalling size and detection accuracy, we compared the missed cases and the correctly detected cases in terms of spalling size. According to the definition in the LTPP manual, we treat the distance from the furthest edge of the spalling to the joint as the spalling size. So, for longitudinal spallings, the size is in the transverse direction, and for transverse spallings, it is in the longitudinal direction. An example is shown in Figure 3-40 (a). In some cases, the spalling is located in the intersection between longitudinal and transverse

joints; we use the longer distance to either joint in two directions as the spalling size, shown as Figure 3-40 (b).

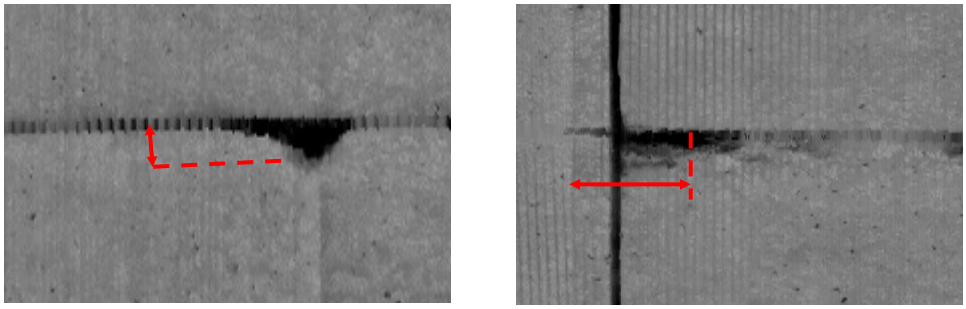

(a) Spalling on a single joint (b) Spalling in the intersection

Figure 3-40 Examples of spalling size measurement

The detection results are reorganized according to the measured spalling size, and the obtained frequency for each size group is shown in Figure 3-41 and Table 3-8. It can be seen that the software can hardly detect spalling sizes smaller than 50 mm; the software can detect some spalling sizes larger than 50 mm but smaller than 90 mm, but the accuracy is not very good (59%); for spalling sizes larger than 90 mm, the detection accuracy becomes much better (90%). One of the reasons for these results could be that the software module was originally designed for pothole detection; though the spalling has characteristics similar to potholes, spalling tends to be much smaller. So, the pothole detection module may have some internal filtering mechanism that eliminates small candidates and reduce computation time, which won't affect pothole detection but could cause false negative spallings. To examine such an assumption, we developed our own detection algorithm, which successfully detected most of the cases missed by the software module and using the same dataset. The test indicates that the 3D data have the capability to provide desired accuracy for spalling detection, and in cases of small-sized spallings, future algorithm modification may help improve the detection accuracy.

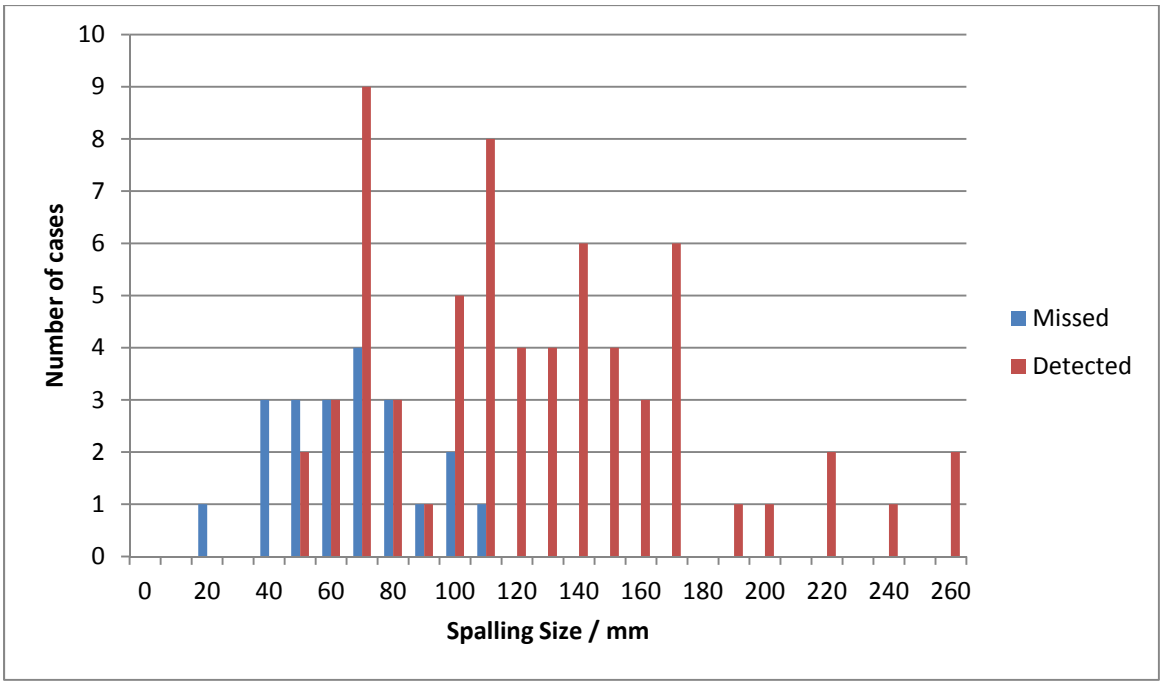

Figure 3-41 Frequency vs. spalling size

Table 3-8 Software Detection Accuracy for Different Spalling Sizes

Spalling size / mm	≤50	50-90	>90	Total
Missed cases	7	11	3	21
Detected cases	2	16	47	65
Accuracy	22%	59%	90%	76%

5.4 Summary

For automatic concrete pavement spalling detection using a 3D line laser imaging system, the major findings are summarized as follows:

First, the 3D line laser imaging system shows overall acceptable performance for automatic spalling detection on concrete pavement. Two test sites were selected on interstate highways I-516 and I-16 to evaluate the spalling detection performance. The ground truth was established by manually reviewing the collected range images. The automatic spalling detection shows accurate results: 65 out of 86 spalling locations were detected, which provides a detection precision of 75.6%. The spalling detection is also robust to different spalling locations and shapes.

Second, two types of representative false negative cases are observed, including undersized spalling and asphalt-patched spalling. Undersized spalling may not influence the detection performance in real-world implementation, since GDOT's current manual survey practice already has a minimum requirement for the size of spalling to be recorded. Asphalt-patched spalling is expected to impact the detection accuracy; however, the percentage of this type of cases is minor in the selected test sites.

Third, false positive detections are also observed through the review of the experimental results, including three major types: crack spalling, shoulder-joint distress, and coring. Most of these false positives can be removed by comparing their locations with detected transverse joints.

Fourth, the detection accuracy of the built-in spalling detection software varies for spalling locations with different sizes. Spalling less than 50 mm wide can hardly be detected; between 50 and 90 mm wide, the detection accuracy is better but not satisfactory; for spalling locations more than 90 mm, the accuracy becomes quite good. Such results may due to the internal filtering mechanism of the algorithm to reduce computation time. Our own detection algorithm has successfully detected most cases missed by the software, indicating the capability of the data to provide the desired accuracy.

6. Validation of Concrete Pavement Shoulder Joint Distress Detection

Shoulder joint distress is another type of concrete pavement distress that occurs along the pavement shoulder. GDOT defines shoulder joint distresses as the depression in the shoulder is caused by the vertical movement in the concrete slabs under load, which may cause material to be pumped out at the joint (as shown in Figure 3-42) . Since this distress takes the form of large spalling locations along the roadway edge, this section will explore the possibility of an automatic spalling detection algorithm that can identify the location and extent of shoulder joint distresses using 3D pavement data.

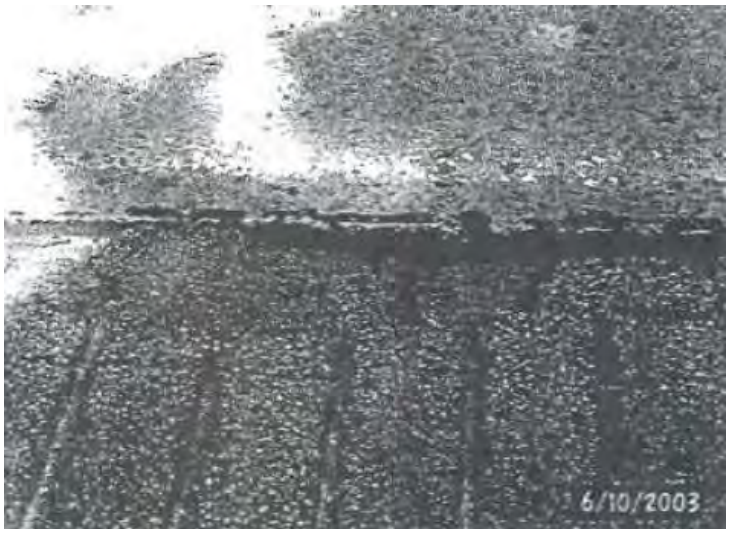

Figure 3-42 Example of shoulder joint distress (GDOT 2003)

6.1 Experimental data

The experimental data of the validation test were collected on interstate highway I-16 near Savannah, Georgia, with concrete pavement on the selected test site (as shown in Figure 3-43).

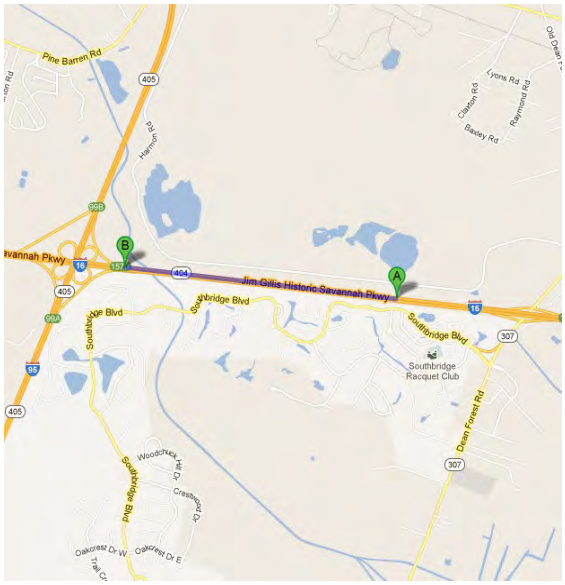

Figure 3-43 Selected I-16 test site on concrete shoulder joint distress detection

6.2 Experimental design

Unlike for cracking, faulting, and spalling, it is difficult to provide a quantitative ground truth for shoulder joint distresses due to their continuity and large extent. Therefore, we manually selected several slabs on the test site. Each of these slabs was marked with a unique ID, and the shoulder joint distresses along these slabs were roughly drawn on a distress map for comparison purposes.

Digital photos of the selected slabs were taken from the road shoulder to track the detailed distress conditions and provide certain references through the validation. Then, the automatic spalling detection algorithm was applied on these slabs to see if it could capture the location and extent of shoulder joint distresses. The detection results were visually compared to photos and distress maps taken from the field survey.

6.3 Validation on I-16 test site

Figure 3-44 to Figure 3-47 show the experimental results of four representative cases. Images (a) and (b) show the intensity and range images of the selected location; Image (c) shows the detected shoulder joint distress (blue area); and Image (d) shows the digital photo at the same location. Based on the experimental results, it can be observed that although it is difficult to identify them in intensity images, shoulder joint distresses appear quite distinctively in range images. Having characteristics similar to spalling (elevation drop), their larger extents and areas actually simplify the automatic detection. Based on visual judgment, the detection results are basically consistent with field observations, including distress maps and digital photos.

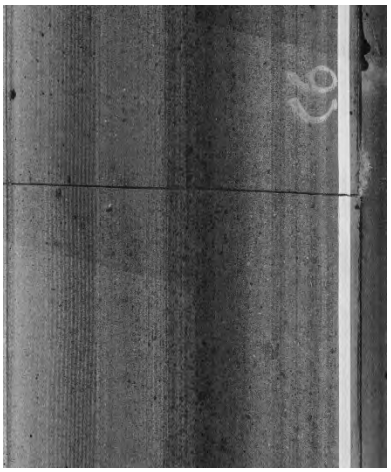

(a) Intensity Image

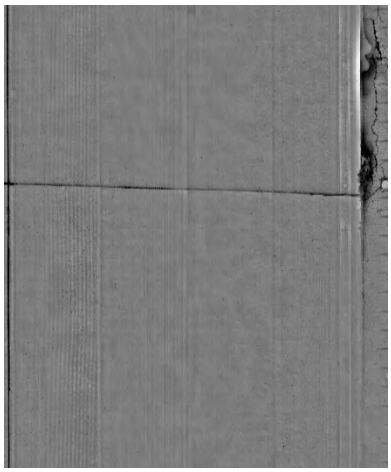

(b) Range Image

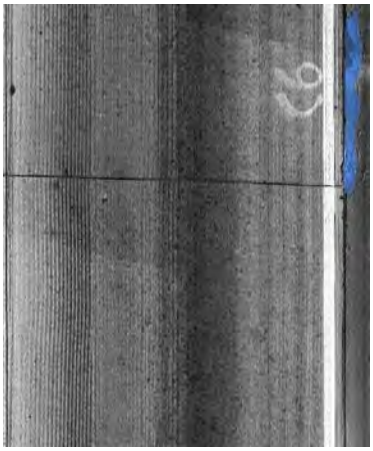


(c) Automatic Distress Detection (d) Field Photo

Figure 3-44 Shoulder-joint distress detection on Slab #C6

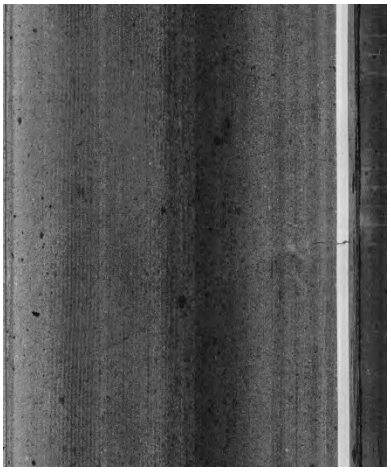
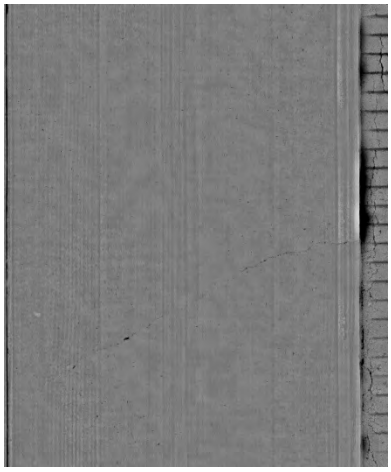

(a) Intensity Image (b) Range Image

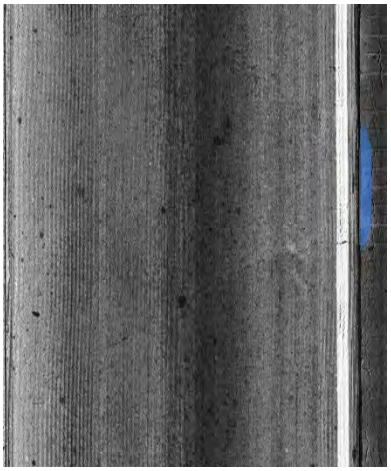


(c) Automatic Distress Detection (d) Field Photo

Figure 3-45 Shoulder-joint distress detection on Slab #C6'

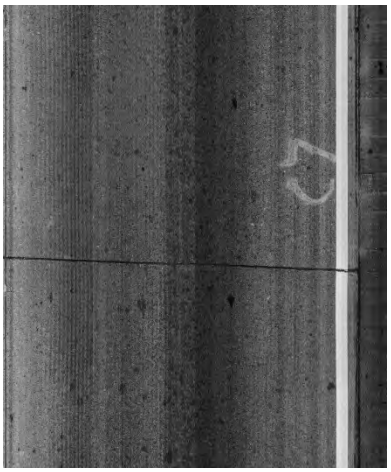

(a) Intensity Image

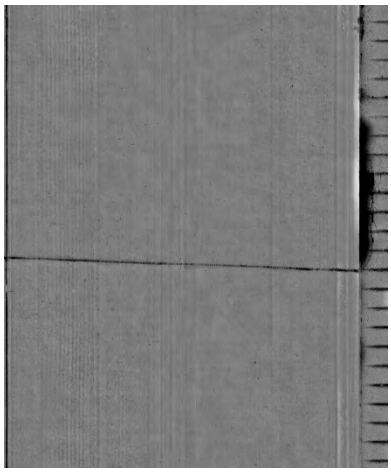

(b) Range Image

(c) Automatic Distress Detection

(d) Field Photo

Figure 3-46 Shoulder-joint distress detection on Slab #C7

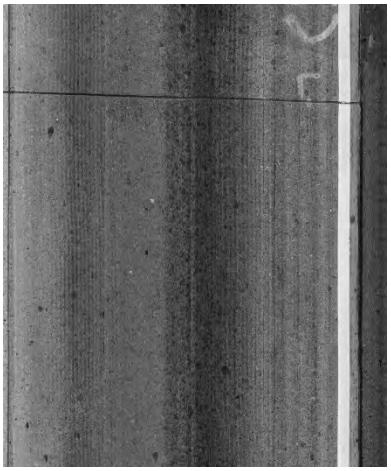

(a) Intensity Image

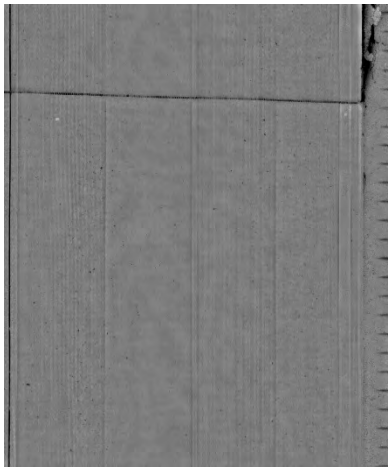

(b) Range Image

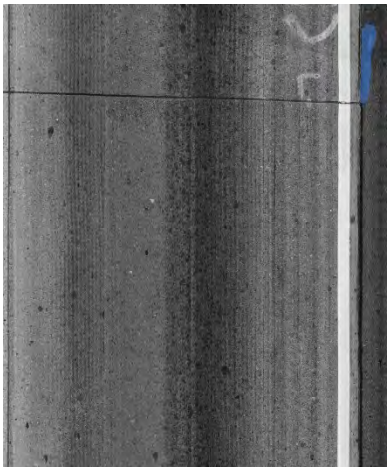

(c) Automatic Distress Detection (d) Field Photo

Figure 3-47 Shoulder-joint distress detection on Slab #C9

6.4 Summary

For automatic concrete pavement shoulder joint distress detection using a 3D line laser imaging system, the major findings are summarized as follows:

First, the 3D line laser imaging system has shown potential to capture the shoulder joint distresses. Because of the distinctive elevation change of such distresses on the pavement shoulder, they can also be automatically identified following principles similar to spalling detection. The experimental results on the test sites are visually consistent with field observation. Furthermore, the automatic detection results are associated with the quantitative area and depth of the distress, which provides an objective and consistent way of making severity level judgments and extent reporting.

Second, it should be noted that due to the transverse coverage of the current 3D line laser imaging system (about 4 meters), it is not guaranteed that the shoulder area will be captured while the vehicle is driving in the outside lane. Therefore, if this specific type of distress is targeted, it is suggested that data collection along the edge line be conducted; in this case, users should be aware that a narrow strip near the lane line might not be captured by the system.

Third, current shoulder joint distress detection is conducted using the automatic spalling detection algorithm, since both distresses share some similar characteristics. However, it is still suggested that a separate detection algorithm be developed to: 1) narrow the region of interest to

the shoulder area to speed up the detection process and reduce the number of potential false positives and 2) deal with significant shoulder drop-off.

7. Summary

The emerging 3D line laser imaging technology has demonstrated its great potential to accomplish automatic distress detection on concrete pavement. A series of comprehensive validation tests were conducted on selected test sites on interstate highways I-16 and I-516. Four different types of concrete pavement distresses were validated, and the major findings are summarized as follows:

For concrete cracking, the 3D line laser imaging system shows overall acceptable performance when performing automatic crack detection. Automatic crack detection results were compared with manually digitized ground truth data through a buffered Hausdorff scoring method. The automatic crack detection shows quite accurate and robust results on longitudinal cracks on I-516 site; however, the crack detection performance on transverse cracks on I-16 site was not as good. The false negative detection on transverse cracking can be explained by the larger data acquisition interval in the driving direction. As in asphalt pavement, the hairline cracks (thinner than 2 mm) are still challenging for automatic detection. Also, severe spalling and joint detection impact the crack detection performance, but only in a limited number of cases.

For concrete faulting, it is feasible to collect faulting measurement at highway speed using a 3D line laser imaging system. Using the regression-based method, the automatic faulting measurements are quite consistent with manually measured ground truths using the Georgia Faultmeter in both controlled lab test and field test. With proper parameter configuration, the concrete joint module in the commercial software can also provide acceptable faulting measurement results.

For concrete spalling, the automatic detection accuracy using the commercial software varies for different sizes. Spalling with widths larger than 90 mm can be successfully detected; between 50 and 90 mm wide, the detection accuracy drops but is still acceptable; spallings locations less than 50 mm wide can hardly be detected. Undersized spalling and asphalt-patched spalling are two common types of false negatives. Although some small spalling locations were not successfully detected, they can be clearly observed on a range image. Therefore, it is believed that there is

still room to further improve the automatic spalling detection algorithm. Some false positives were observed in the experimental test, including crack spalling, shoulder-joint distress, and coring. Most of these false positives can easily be removed by comparing their locations with detected transverse joints.

For shoulder joint distresses, this study explores the feasibility of using the automatic spalling detection algorithm on shoulder joint distress detection. The larger extent and depth of shoulder joint distresses make them quite distinctive in range images and relatively straightforward to detect. On the selected representative cases, the automatic detection results are visually consistent with field observations (including distress map and digital photos). However, it should be noted that, due to the transverse coverage of the current 3D line laser imaging system (about 4 meters), it is not guaranteed that the shoulder area will be captured while the vehicle is driving in the outside lane. Also, developing a specific shoulder joint distress detection algorithm to further ensure accurate and robust detection is recommended.

References

Ahmed, M. F. M., and Haas. C. T. (2010). "The Potential of Low Cost Close Range Photogrammetry Towards Unified Automatic Pavement Distress Surveying." *Transportation Research Board Annual Meeting,* Washington, D. C.

Alekseychuk, O. (2006). "Detection of Crack-Like Indications in Digital Radiography by Global Optimisation of a Probabilistic Estimation Function." PhD Thesis, BAM-Dissertationsreihe, Band 18.

EI-Korchi, T., Gennert, M. A., Ward M. O., Wittels. N. (1991). "Lighting Design for Automated Pavement Surface Distress Evaluation." *Transportation Research Record:Journal of the Transportation Research Board*, 1311, 144-148.

Hou, Z., Wang K. C. P., Gong. W. (2007). "Experimentation of 3d Pavement Imaging through Stereovision." *Proc., International Conference on Transportation Engineering*, 376-381.

Kaul, V., Tsai Y., Mersereau. R. M. (2010). "A Quantitative Performance Evaluation of Pavement Distress Segmentation Algorithms." *Transportation Research Record: Journal of the Transportation Research Board*, 2153, 106-113.

Laurent, J., Lefebvre D., Samson. E. (2008). “Development of a New 3D Transverse Laser Profiling System for the Automatic Measurement of Road Cracks.” *SURF 2008.*

Lee, H., and Kim. J. (2006). “Analysis of Errors in Ground Truth Indicators for Evaluating the Accuracy of Automated Pavement Surface Image Collection and Analysis System for Asset Management.” *Journal of ASTM International*, 3(5), 1-15.

Li, Q., Yao, M., Yao X., Xu. B. (2010). “A Real-Time 3d Scanning System for Pavement Distortion Inspection.” *Measurement Science and Technology*, 21(1), 1-8.

McGhee, K. H. (2004). “Automated Pavement Distress Collection Techniques: A Synthesis of Highway Practice.” *NCHRP Synthesis 334,* Washington, D.C.

Nazef, A., Mraz, A., Gunaratne M., Choubane. B. (206). “Experimental Evaluation of a Pavement Imaging System: Florida Department of Transportation's Multipurpose Survey Vehicle.” *Transportation Research Record: Journal of the Transportation Research Board*, 1974, 97-106.

Raman, M., Hossain, M., Miller, R., Cumberledge, G., Lee, H., Kang. K., (2004). “Assessment of Image-Based data Collection and the AASHTO Provisional Standard for Cracking on Asphalt-Surfaced Pavements.” *Transportation Research Record: Journal of Transportation Research Board*, 1889, 166-125.

Tsai, Y., Kaul, V., Mersereau, R. M. (2010). “A Critical Assessment of Pavement Distress Segmentation Methods Performance Evaluation of Pavement Distress Segmentation Methods.” *Journal of Transportation Engineering*, 136 (1), 11-19.

Wang, K. C. P. (2000). “Designs and Implementations of Automated Systems for Pavement Surface Distress Survey.” *Journal of Infrastructure Systems*, 6(1), 24-32.

Wang, K. C. P., and Gong. W. (2002). “Real-Time Automated Survey of Pavement Surface Distress.” *Proc., International Conference on Applications of Advanced Technologies in Transportation Engineering*, 465-472.

Wang, K. C. P., and Tee. W. (2002). “Understanding of Pavement Profiling and Validation of an Implementation.” *Proc., International Conference on Traffic and Transportation Studies*, 817-824.

Wang, K. C. P. (2004). “Challenges and Feasibility for Comprehensive Automated Survey of Pavement Conditions.” *Proc., International Conference on Applications of Advanced Technologies in Transportation Engineering*, 531-536.

Wang, K. C. P., and Gong. W. (2005). “Real-Time Automated Survey System of Pavement Cracking in Parallel Environment.” *Journal of Infrastructure Systems*, 11(3), 154-164.

Wang, K. C. P., Gong W., Hou. Z. (2008). “Automated Cracking Survey”. *Proc., RILEM International Conference on Cracking in Pavements*, 881-889.

Xu, B. (2005). “Artificial Lighting for the Automated Pavement Distress Rating System.” Austin, TX.

Xu, B. (2007). “Summary of Implementation of an Artificial Lighting System for Automated Visual Distress Rating System.” Austin, TX.

Chapter 4 Feasibility Study of Pavement Marking Retroreflectivity Condition Assessment Using Mobile LIDAR

1. Introduction

Pavement marking is one of the most important traffic control devices and is closely related to highway safety. It provides critical delineation information for road users. Pavement marking retroreflectivity is the most important feature of pavement marking to maintain its vital functionality during nighttime. FHWA has proposed a set of requirements as a mandate for the minimum pavement marking retroreflectivity and defined them in the Manual on Uniform Traffic Control Devices (MUTCD, 2009). Public transportation agencies, including state DOTs, must design and implement their programs for pavement marking management to maintain retroreflectivity at or above the minimum level.

Traditionally, two manual methods are commonly used by public transportation agencies to collect pavement marking retroreflectivity condition data: nighttime inspection and retroreflectometer measurement. For nighttime inspection, a windshield survey is carried out during nighttime by field engineers driving along the roadways and recording the road sections with poor retroreflectivity. Although nighttime inspection can be conducted at driving speed, the condition assessment results are subjective and inconsistent. A retroreflectometer measurement is conducted by making sampled retroreflectometer readings along the roadway. Although retroreflectometer readings can be consistent, as defined by the American Society for Testing and Materials (ASTM), field engineers need to conduct the measurement while being physically on the road. Such an operation is not only labor-intensive and time-consuming, but, more importantly, may be dangerous because engineers will be exposed to traffic. Therefore, there is a need for a safe and cost-effective pavement marking retroreflectivity condition assessment method that produces reliable and consistent results so that public transportation agencies can implement effective pavement marking management plans.

In recent years, many emerging sensing technologies have become technically mature and commercially available, e.g. computer vision, mobile LiDAR, scanning laser profiler, etc. It is important to explore feasible technologies and technology applications that can support a mobile pavement marking retroreflectivity condition assessment. Because a LiDAR system uses a

principle similar to the one a retroreflectometer uses to measure retroreflectivity and because USDOT RS-GAMS Phase 1 has demonstrated the potential for applying LiDAR technology to the condition assessment of traffic sign retroreflectivity, a LiDAR system holds the potential to be applied to pavement marking condition assessment. Therefore, the objective of this study is to explore the feasibility of measuring pavement marking retroreflectivity condition using LiDAR technology.

Section 1 presents the background and identifies the objective of this study. Section 2 presents a literature review regarding the current pavement marking retroreflectivity condition practice and the previous studies on mobile assessment. Section 3 presents the research method. Section 4 presents the experimental test and the preliminary results. Section 5 presents the findings and provides recommendations for future research.

2. Literature Review

2.1. The significance of pavement marking

Pavement markings are beneficial to drivers for their significance in keeping drivers on track and ensuring driving safety by conveying continuous information of “the intended travel path for short-range operations and the roadway alignment for long-range delineation” to drivers (Carlson et al., 2009). Recognizing the significance of pavement marking on driving safety, traffic agencies invest millions of dollars in maintaining the quality of pavement marking in the United States each year. Retroreflectivity is a widely accepted performance measure of pavement markings. To maintain the retroreflectivity of pavement marking at a serviceable level within a reasonable budget, researchers have devoted many efforts to set up minimum criteria for pavement marking retroreflectivity. Based on these research findings, FHWA has published minimum criteria of retroreflectivity through the new MUTCD and has required that all public traffic agencies design their own programs to maintain the retroreflectivity of pavement markings at or above the minimum level.

Engineers have been evaluating the effect of pavement marking on the improvement of driving safety ever since the 1940s. Most studies have concluded that pavement markings do improve driver/roadway safety. Centerlines, for example, as a major pavement longitudinal marking, have been proven effective in keeping drivers from shifting from the road's centerline to the right side

of the road, as well as motivating them to drive, remarkably, slower (Taragin, 1947). As for edge lines, a before-and-after study in Connecticut has proven that the presence of edge lines can reduce accidents. Besides, centerlines also have some influence on slowing driving speed (Williston, 1960). A similar study (Basile, 1962) in Kansas has observed a reduction in fatalities on two-lane, rural highways but no significant changes in the total number of injuries with the presence of edge pavement markings. However, these very early studies all adopted the simplest research methods, and no details of the research processes are available. These methods have limitations; for example, they cannot exclude the impact of other factors, such as weather, on roadway safety. Apparently, these studies failed to consider the differences in the retroreflectivity conditions of pavement markings in their analysis. A more recent experimental study (Tsyganov et al., 2006) adopted a before-and-after study approach to quantifying the effect of edge lines on improving safety on the rural two-lane highways in Texas. In the study, a statistical crash analysis found that "edge-line treatments on rural two-lane roadways may reduce accident frequency up to 26% and the highest safety impacts occur on curved segments of roadways with lane widths of 9 to 10 ft." In addition, the researchers also conducted stationary traffic observation and driving tests under different circumstances. However, an increase in speed by an average of 5 mph, or 9%, on both straight and curved highway segments, instead of a speed drop, has been observed in the tests. Even though there are some conflicts about the impact of the pavement marking on the driving speed, these studies all agree with the conclusion that the presence of pavement markings improves roadway safety, especially when the pavement marking conditions are particularly poor. Smadi et al. (2008) studied the crash records and established spatial correlations with the pavement marking retroreflectivity using data from the entire Iowa primary road system. Although the results from the entire dataset didn't show that lower pavement marking retroreflectivity correlates to a higher crash rate, the results with only lower retroreflectivity ($\leq$ 200 mcd/m^2/lux) indicates a statistical significant negative correlation with the crash rate (i.e. when the pavement marking retroreflectivity is lower than 200 mcd/m^2/lux, crash rates increase as the pavement marking retroreflectivity decreases).

2.2. Research on the minimum retroreflectivity level

Research has shown that pavement marking will work effectively as long as the pavement marking meets minimum criteria, but there is no proof that shows higher retroreflectivity would

improve roadway safety. Therefore, it's necessary to determine the minimum level of acceptable retroreflectivity. In the 1990s, FHWA sponsored the development of a computer model named Computer-Aided Road-Marking Visibility Evaluator (CARVE) to establish a set of criteria for minimum level of retroreflectivity based on the posted speed limits and the presence of retroreflective raised pavement markers. Then, FHWA included the research results as part of an internal report and recommended criteria for minimum retroreflectivity. Many other institutes and DOTs have, also, developed general recommendations for the minimum criteria of retroreflectivity. Although these recommendations vary, they all ranged from 90 to 130 $mcd/m^2/lux$ (Debaillon et al., 2008). With the application of new materials and technologies in pavement markings, these criteria are no longer applicable. The University of Iowa improved the CARVE to the Target Visibility Predictor in order to keep pace with new pavement marking technology. A study (Debaillon et al., 2008) adopted this new system and incorporated many new inputs to establish updated criteria. In this research, the researchers also included pavement surface type (e.g. asphalt or concrete) and vehicle type (passenger or freight). From this study emerged a set of minimum pavement marking retroreflectivity recommendations for typical conditions on U.S. highways. However, this research only employs a deterministic model (i.e. TarVIP) based on illumination physics and vehicle/roadway geometry. None of the results were validated using actual field retroreflectivity measurements or drivers' perception. Therefore, further research is necessary to validate the results. Recently, the new MUTCD has published a recommendation for minimum retroreflectivity but does not require forceful implementation because of the budget concerns of DOTs.

The presence of pavement markings is essential for driving safety, and it is significant that the pavement marking should be at or above a minimum level (i.e., at least visible to the drivers). When retroreflectivity is low, driving risk can increase significantly. In order to maintain the visibility of pavement markings or keep the retroreflectivity above the minimum criteria, methods for quantitative measurement of retroreflectivity are needed by transportation agencies for pavement marking management. The following section reviews different retroreflectivity measurement methods.

2.3. Retroreflectivity measurement methods

2.3.1. Visual Inspection

Visual inspection is a measurement practice in which evaluators stand by the roadside or drive along the road to visually rate the condition of pavement marking retroreflectivity. Choosing to drive along the road could be a very efficient method that imposes little impact on the traffic. In addition, visual inspection is also very inexpensive because no special devices are needed, and only two engineers are needed for the whole evaluation process, one for driving and one for evaluating. However, human eyes are not reliable because when they encounter different background contrasts, the brightness of an object will look very different. Thus, one evaluator's rating results usually differ from another's because of expertise, experience, and subjectivity. Research conducted by the Texas Department of Transportation (TxDOT) (Benz et al., 2009) tried to correlate the visual inspection results with data collected by a handheld retroreflectometer and found that there was a correlation between the average rating of several evaluators (8 different evaluators in the research) but the correlation was sometimes inconsistent. However, when individual ratings were analyzed, significant biases from the handheld retroreflectometer readings appeared; even training seems to be ineffective in improving accuracy. Factors, other than retroreflectivity, including facing angle, lighting condition, etc., may also impact the visual condition assessment (FHWA, 2007). In conclusion, even though visual inspection has advantages, it has the drawback of being qualitative and subjective and, therefore, cannot be used as a standardized method.

2.3.2. Handheld Retroreflectometer

Using handheld retroreflectometers provides a method for quantitative measurement of pavement marking retroreflectivity. A handheld retroreflectometer could be placed on a pavement marking and readings of the pavement marking retroreflectivity at each spot can be taken. Standard procedures are available for conducting measurement with a handheld retroreflectometer, and the operation can be handled with little training. With the standard operation, both the repeatability and reproductivity can be controlled. The price of a handheld retroreflectometer is usually $12,000 to $25,000 per unit depending on the model, but it is much less expensive than a mobile device ($80,000 without the van) (Benz et al., 2009), which will be discussed later. However, there are disadvantages to using a handheld retroreflectometer. The measurement operation may

require lane closures and may cause unsafe situations because the operators are exposed to Most importantly, a large number of samples can be expensive to acquire and process. Since measurement of retroreflectivity with a handheld retroreflectometer is a standard operation, a brief introduction of available ASTM standards is provided in the following sections.

ASTM E1710-11 has proposed standard procedures for retroreflectivity measurement under dry conditions with a portable retroreflectometer at standard "30 meter geometry" (Figure 4-1). In addition, this standard has also described a standard configuration of the retroreflectometer that all the following products should follow.

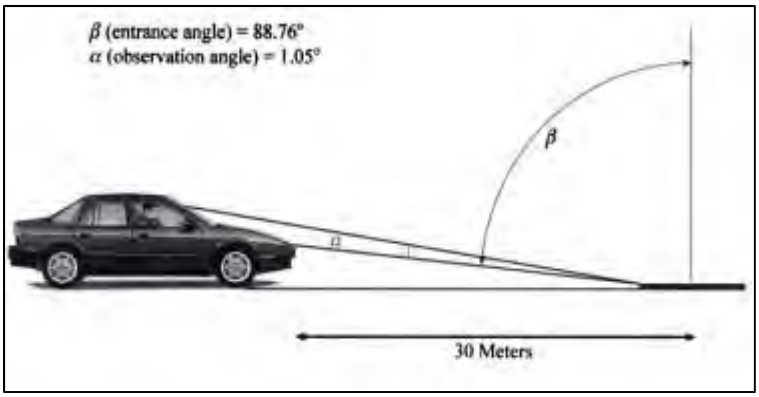

Figure 4-1 Standard geometry (Bernstein. 2000)

ASTM E2176-08, on the other hand has provided standard procedures for retroreflectivity measurement under continuous wetting conditions with a retroreflectometer. This condition simulates the raining scenario (Figure 4-2).

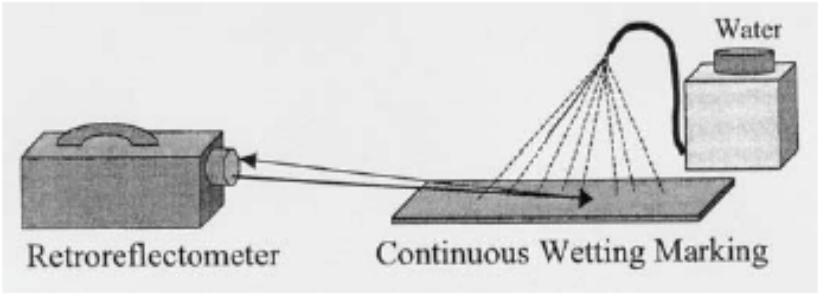

Figure 4-2 Illustration of the continuous wetting measurement (ASTM E2176)

ASTM E2177-11 is available as standard procedures (i.e. wet recovery) for measuring retroreflectivity under wet condition, which is similar to the scenario in which there is a rain before measurement (Figure 4-3). However, it was claimed that this method does not necessarily

reflect the condition of pavement marking after a rain. A portable or mobile retroreflectometer could be used but should comply with the requirements for the apparatus described in ASTM E1710-11.

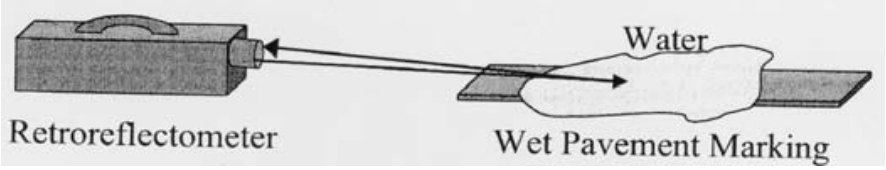

Figure 4-3 Illustration of wet condition (ASTM E2177)

Data collected following these standard procedures usually have good repeatability and reproductivity in practice. However, these standards have only described the application of a handheld retroreflectometer. Although a mobile retroreflectometer is also mentioned in ASTM E2177-11, it is not described in detail. In the following section, a few available mobile methods will be discussed.

2.3.3. Mobile Retroreflectometer

Using a mobile retroreflectometer provides a means and a method for network-level data collection. Usually, a mobile retroreflectometer system consists of a van, a mobile retroreflectometer, and a computer system for data storage. Retroreflectometers have some very attractive advantages. Mobile retroreflectometers are able to collect network-level data, and they can be operated at highway speed and do not disrupt the traffic. However, the cost of a mobile retroreflectometer is about four times that of a handheld retroreflectometer. Besides, the mobile retroreflectometers require more training and maintenance. In addition, the readings of retroreflectometers can be inconsistent for many reasons. For example, a study (Benz et al., 2009) found that the mobile retroreflectometer is very sensitive to two factors and could cause inconsistent data. The sensitivity analysis found that distance from the pavement marking to the sensors and position across the measurement window have most significant impact on the mobile retroreflectivity measurement. Unlike the handheld retroreflectometer, no standard operating procedures are available for mobile retroreflectometers. Thus, false calibration and operation can result in very inconsistent data and, ultimately, raise concerns about mobile retroreflectometers among the state DOTs.

LaserLux, as an example of mobile retroreflectometer available for DOTs since the 1990s, has been evaluated by the TxDOT (Benz et al., 2009). It was proven that many factors, such as measuring geometry, temperature, and pavement profile, had significant influence on the accuracy of the collected data. Even though there was a motion compensation system incorporated into the LaserLux, the errors still could not be removed. Similarly, other currently available mobile retroreflectometers all either have problems in accuracy or need a complex set-up and calibration process (Lee, 2011). The National Cooperative Highway Research Program (NCHRP) Innovations Deserving Exploratory Analysis (IDEA) program (Lee, 2011) has recently proposed an advanced system to measure the marking retroreflectivity at highway speed. The system under research has a tracking system to keep the measurement geometry automatically and a calibration system to simplify the process for calibration. Researchers claim that experimental tests have shown the accuracy of the system, but it still needs further evaluation and validation in field.

Currently available mobile retroreflectometers are still not fully validated for implementation; thus, evaluation and improvement efforts are still ongoing. Besides, it's also worthwhile to explore the potential application of emerging technologies.

2.4. The LiDAR technology

Light Detection And Ranging (LiDAR) is an optical remote sensing technology that can measure the distance to or other properties of a target by illuminating the target with light, often using pulses from a laser (Cracknell et al., 1991). The retro-value in LiDAR is the percentage of the redirected energy from the target, divided by the emitted energy from LiDAR. The principle is consistent with FHWA's definition of retroreflectivity. The LiDAR vehicle has been used to collect pavement inventory data and not designed for retroreflectivity measurement on purpose, but since it applies a similar principle as a retroreflectometer, it would be promising to study the feasibility of measuring pavement marking retroreflectivity using LiDAR technology.

2.5. Summary

Pavement marking plays an important role in driving safety. The retroreflectivity condition is identified as the most important condition for pavement marking and draws major concerns from public transportation agencies because poor retroreflectivity has been proven to be strongly

correlated with nighttime crash rates, especially under undesirable conditions, such as a rainy night. Traditionally, state DOTs conduct manual condition assessment using visual inspection and handheld retroreflectometers. Evaluation by visual inspection is subjective and usually inconsistent. Assessment by handheld retroreflectometer is usually accurate and consistent with proper operation. However, it is so labor-intensive and time-consuming that it cannot fulfill the need for a continuous condition assessment covering the full network. It may, also, require extra resources for traffic control, and it may expose field engineers to open traffic. A good alternative is the mobile retroreflectometer, but available devices, such as the LaserLux, require a very complex process of calibration before each data collection. Any improper operation or setup could cause faulty data to be collected. In addition, many factors have proven to significantly impact the accuracy and consistency of mobile retroreflectometers. There is still a need to explore alternative mobile pavement marking retroreflectivity condition assessment methods. As the LiDAR system has already been used for traffic sign inventory and retroreflectivity condition assessment by utilizing the retro-intensity value that can measure the ratio of light redirected from an object to the light emitted from the laser, an alternative mobile method is possible for pavement marking retroreflectivity condition assessment.

3. Research Method

The objective of this study is to evaluate the feasibility of conducting pavement marking retroreflectivity condition assessment using LiDAR technology by establishing the preliminary correlation between the retroreflectivity readings measured by handheld retroreflectometers and the LiDAR retro-intensity values. The proposed research method is composed of four steps: test site selection, data collection, data preprocessing, and data analysis. Figure 4-4 shows the detailed procedures of this research.

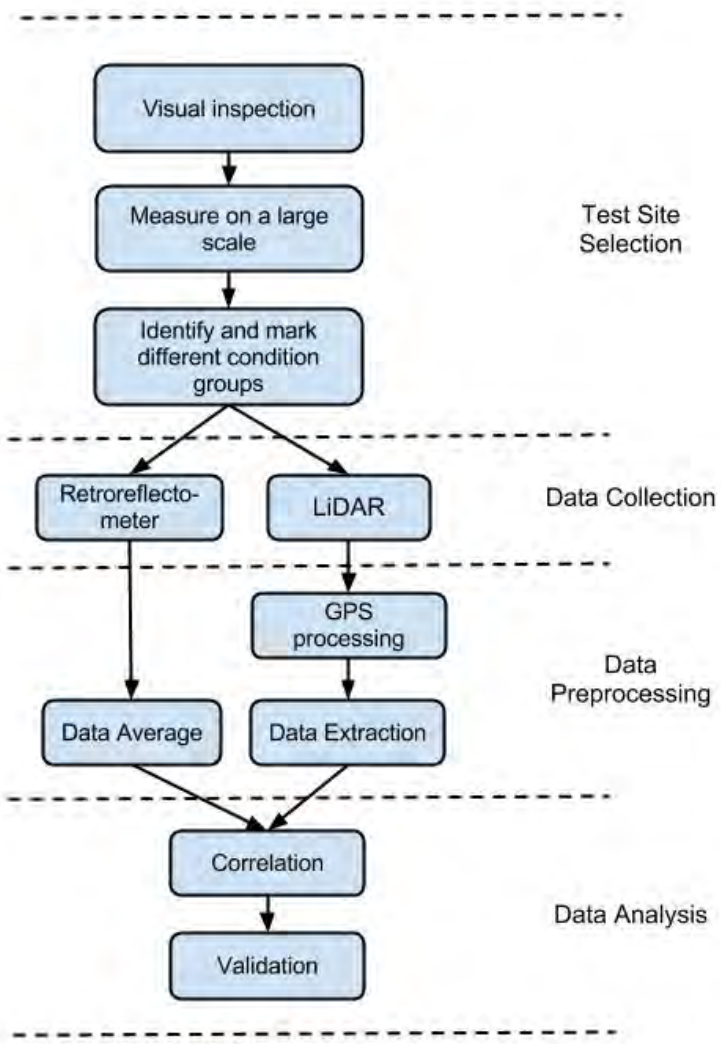

Figure 4-4 Flowchart of establishing correlation retroreflectivity and retro-intensity

- Test site selection: To establish a reliable correlation, the pavement marking retroreflectivity data should consist of complete coverage of different conditions. Thermoplastic was selected as the focused material in this study, as it is popularly used on state routes and interstates in Georgia and many other states. To include the complete coverage of different conditions, a visual inspection during nighttime was first conducted to purposely include the road sections containing different retroreflectivity conditions. Second, a preliminary retroreflectivity measurement using handheld retroreflectometer (at large measurement interval, e.g. 50 ft.) was conducted to further narrow down the road sections with different conditions. Third, detailed retroreflectivity measurements

using a retroreflectometer (at small measurement intervals, e.g. 1 ft.) were conducted to collect the comprehensive pavement marking condition within each candidate section.

- Data collection: To fully cover the selected road sections, three runs of LiDAR data were collected using GTSV. The three runs of data were also used to assess the repeatability of the measurement. The corresponding retroreflectivity measurement using a retroreflectometer was also conducted right after the LiDAR data collection.
- Data preprocessing: The retroreflectometer readings are first averaged to obtain the retroreflectivity of each sample spot. The GPS of the LiDAR data are first post-processed to obtain a higher GPS accuracy and then the retro-intensity from the LiDAR data are extracted manually using Trimble Analyst Software.
- Data analysis: Once both retroreflectivity readings and the corresponding retro-intensity values are collected, the correlation can be established based on their spatial association. The detailed procedures are discussed in the experimental test section.

4. Experimental Tests

Prior test results show that retroreflectivity of pavement markings consisting of various materials behaves differently. This research focuses mainly on thermoplastic and waterborne paint, the most popular pavement marking materials. After obtaining the LiDAR retro-intensity data and the retroreflectivity measured at the same field locations, we conducted a regression analysis to explore the correlation between the LiDAR retro-intensity values and the retroreflectivity. With the correlation, critical values that differentiate acceptable pavement markings from unacceptable ones will be established for retro-intensity and used for the assessment of the pavement marking condition.

4.1. Data collection

Data collection that covers retroreflectivity conditions from extremely bad to brand new involves the selection of a test site using the visual inspection method. Through this method, Ferst Drive between State Street and Techwood Drive on the Georgia Tech campus was selected for thermoplastic pavement marking test. Hemphill Avenue and 17th Street were selected for a waterborne paint pavement marking test. To examine the detailed trend on the selected test sections, preliminary retroreflectivity measurements were conducted using a *StripeMaster II*

handheld retroreflectometer to get an idea of the distribution of retroreflectivity at the selected sites. Based on the trend, more detailed test sections were selected so that the retroreflectivity conditions were distributed evenly from bad to brand new. For thermoplastic and waterborne paint pavement markings, details about the test section selection are introduced as follows:

4.1.1. Thermoplastic

Thermoplastic pavement markings on Ferst Drive between State Street and Techwood Drive on the Georgia Tech, Atlanta campus were installed by Georgia Tech facility management personnel. The thermoplastic pavement markings are of various conditions because of uneven aging and deterioration rates. Figure 4-5 shows the trend of the retroreflectivity along the selected road segment.

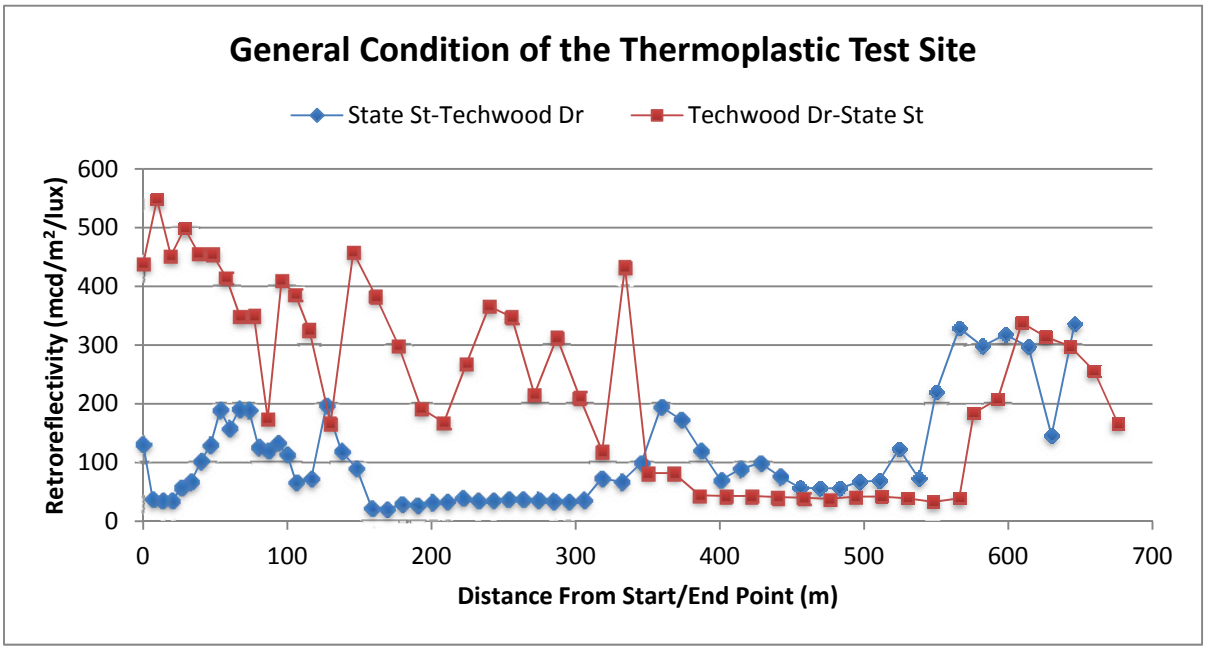

Figure 4-5 The pavement marking retroreflectivity condition on the Ferst Dr. on Georgia Tech campus

It can be observed that the selected thermoplastic test site consists of varying retroreflectivity conditions ranging from 30 mcd/m^2/lux to more than 600 mcd/m^2/lux. Based on the information of the general condition in Figure 4-5, twelve test locations were selected and covered different ranges of retroreflectivity. Each condition group was 10-ft in the longitudinal direction and contained 10 samples spaced one foot apart. To establish a reliable correlation, the

retroreflectivity condition within each 1-ft section was maintained homogeneously. The detailed range for each condition group is shown in Table 4-1.

Table 4-1 Retroreflectivity of Thermoplastic Test Sections

Range (mcd/m^2/lux)	No. of Test Sections
0-50	3,10
50-100	1,4,5
100-200	2
200-300	7,12
300-400	6,11
400-500	9
500-600	10

The exact locations of different condition groups were spray painted on the pavement to ensure that the location measurement from different times or from different sensors were consistent. After marking the samples in the field shown in Figure 4-6, the retroreflectivity for each sample was collected three times with a handheld retroreflectometer, complying with the ASTM E1710-11 standard, and then the entire test site was surveyed using the GTSV for three runs.

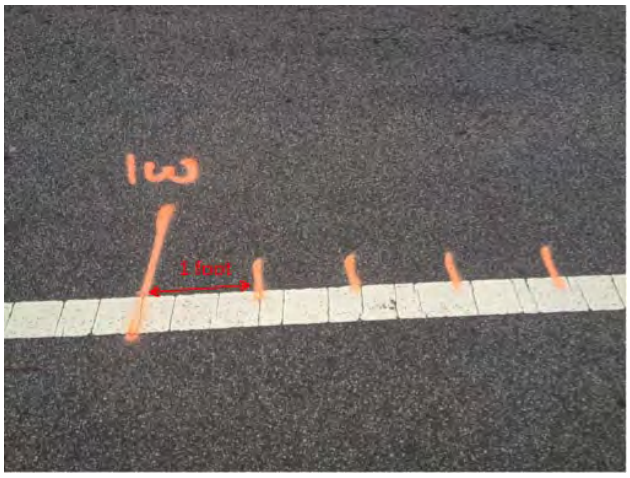

Figure 4-6 An example of the selected thermoplastic test section

4.1.2. Waterborne Paint

Hemphill Avenue and 17th Street, shown in Figure 4-7, were identified as test sites for the road segments that were installed with waterborne paint markings under various conditions. We used an approach similar to the approach we used to determine the test sections for thermoplastic. We first conducted a preliminary rough measurement of the pavement markings. Figure 4-8 shows the results.

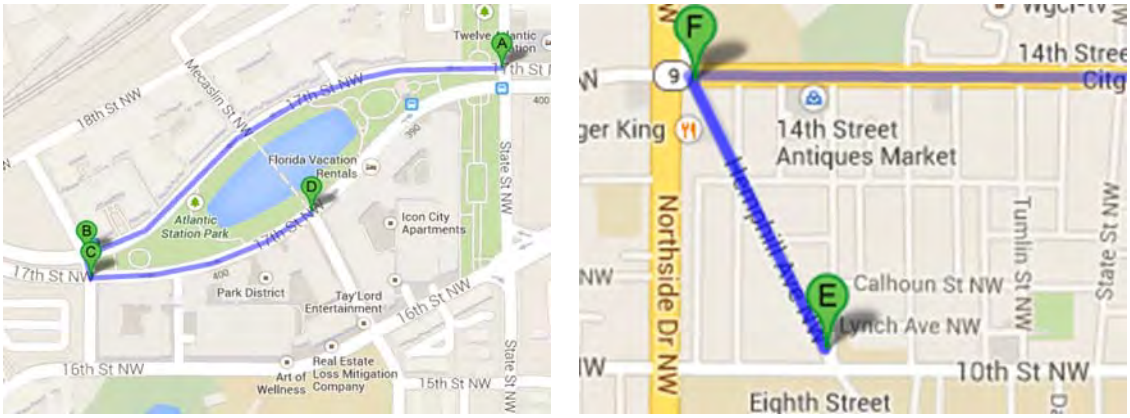

Figure 4-7 Test sites of waterborne paint markings

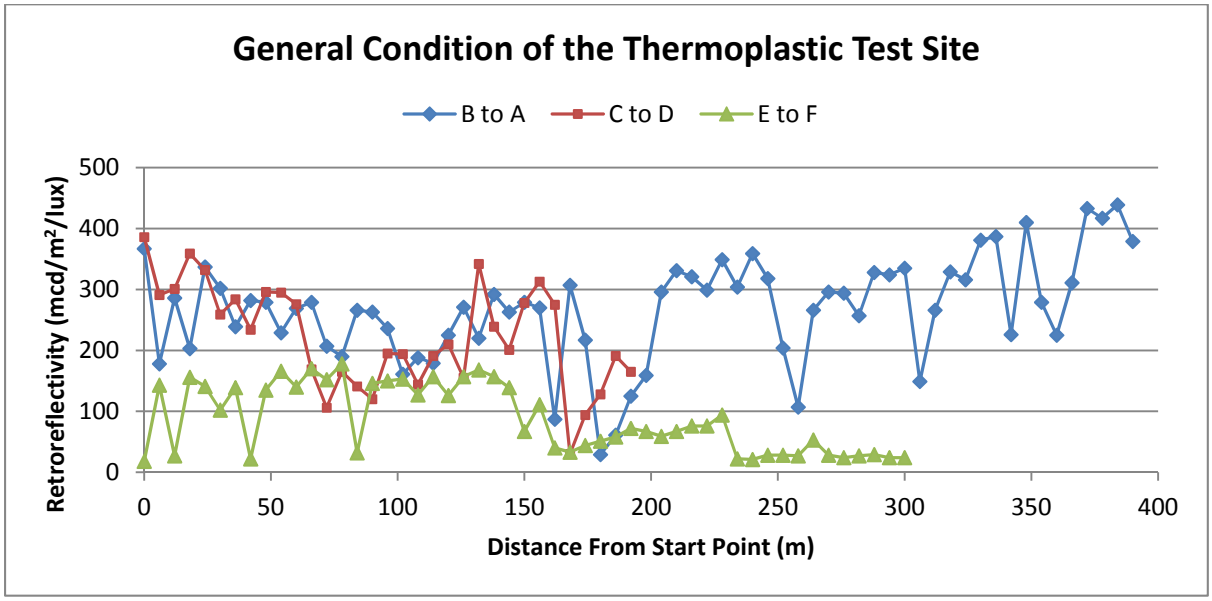

Figure 4-8 The pavement marking retroreflectivity condition on Hemphill Avenue and 17th Street

It can be observed that the selected test sites contain pavement markings with various conditions from 0 to 450 mcd/m^2/lux. Based on the trends on the road segments, 16 test sections were selected; eight sections were on Hemphill Avenue, and eight sections were on 17th Street. The markings that were selected on Hemphill Avenue are indicated by dash lines, and each dash line is segmented into samples foot apart. On 17th Street, the test sections are also sampled one foot apart with 10 samples in each section. Table 4-2 shows the detailed distribution of conditions of the test sections.

Table 4-2 Retroreflectivity of Thermoplastic Test Sections

Range (mcd/m^2/lux)	No. of Test Sections
0-50	1, 2
50-100	3, 4, 7 ,8
100-150	5, 6, 11
150-250	12, 13
250-350	9,10,14,15
>350	16

4.2. Data Extraction

Trimble Trident 3D Analyst software was used to extract the data. All the samples were extracted into a Geographic Information System (GIS) layer through the video log images that were synchronized with the mobile LIDAR, shown as the green line in Figure 4-9. Then, the layer was mapped onto the calibrated LiDAR point-cloud, shown in Figure 4-10. At each sample location, retro-intensity values of the LiDAR points were manually extracted, shown in Figure 4-10. As the LiDAR device used in this study (i.e. Riegl LMS-Q120i) can acquire 10000 points per second, at least three retro-intensity values could be obtained to associate with each sample section (i.e. 1-ft section in the longitudinal direction). For example, the yellow rectangle shown in Figure 4-11 represents the actual 1-foot test section. Although there are ten LiDAR points cast over this section, only the middle point fully cast on the pavement marking can be used for establishing correlation(the highlighted point in red circles shown in Figure 4-11). Consequently, for each 1-foot section, approximately three retro-intensity values are associated. For the points that partially cast over the pavement marking section, the retro-intensity values might not reflect the true retroreflectivity condition because the energy was redirected by both the pavement and pavement marking.

Figure 4-9 Create a new layer to locate sample site in the video log image

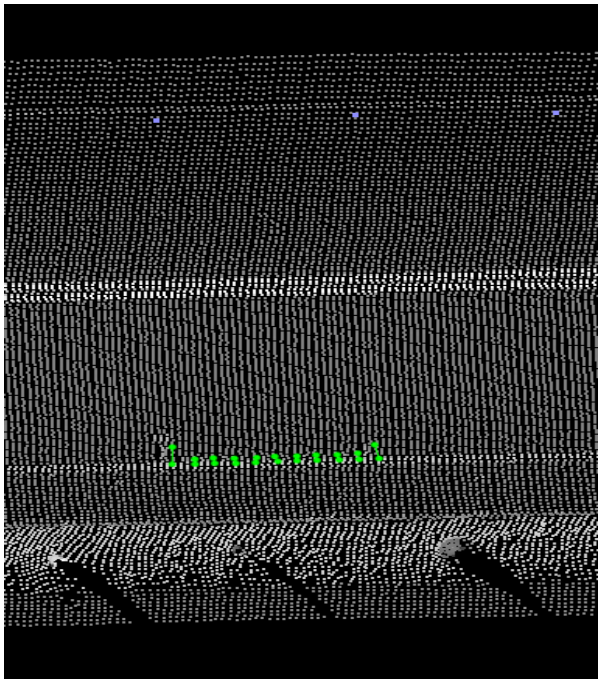

Figure 4-10 The new layer mapped onto the point-cloud

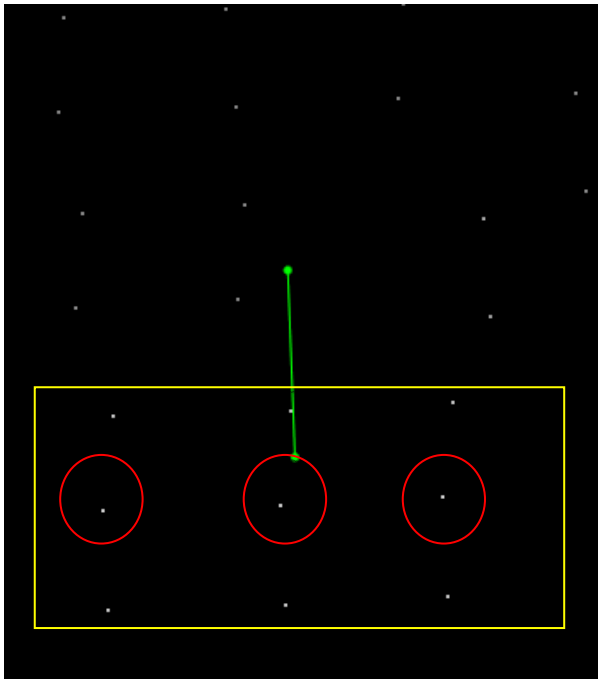

Figure 4-11 Selected points included in the analysis

4.3. Data Analysis

4.3.1. Handheld Retroreflectometer Measurement

To show the general condition of the pavement markings in each test section, Figure 4-12 and Figure 4-13 illustrate the average retroreflectivity and standard deviations. Figure 4-12 shows that thermoplastic sections with average retroreflectivity above 200 mcd/m^2/lux, where the standard deviations at the sections with high retroreflectivity, are significantly larger than the standard deviations of the sections with low retroreflectivity. One possible explanation for the large standard deviation is because of various traffic, weather, and sunshine conditions; the condition of the pavement marking deteriorates at a dynamic rate at different locations, so the condition of the pavement markings is not uniform across the 10-foot test section. However, when the retroreflectivity of the pavement marking is below 100, the condition of the entire section is uniformly below the standard.

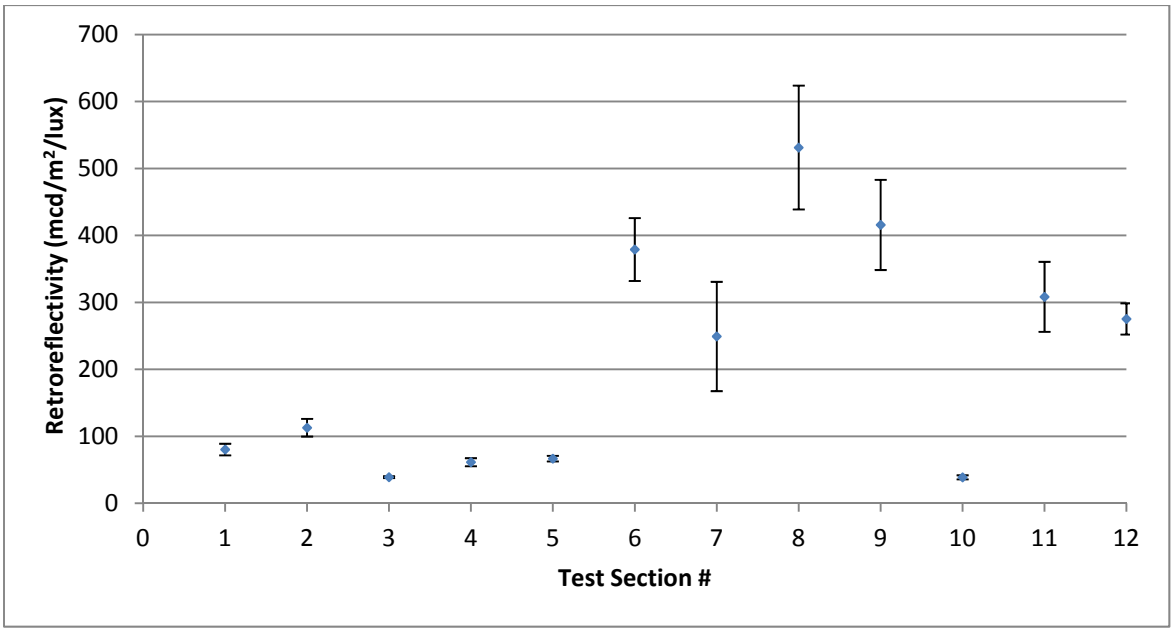

Figure 4-12 Average retroreflectivity on test sections thermoplastic markings

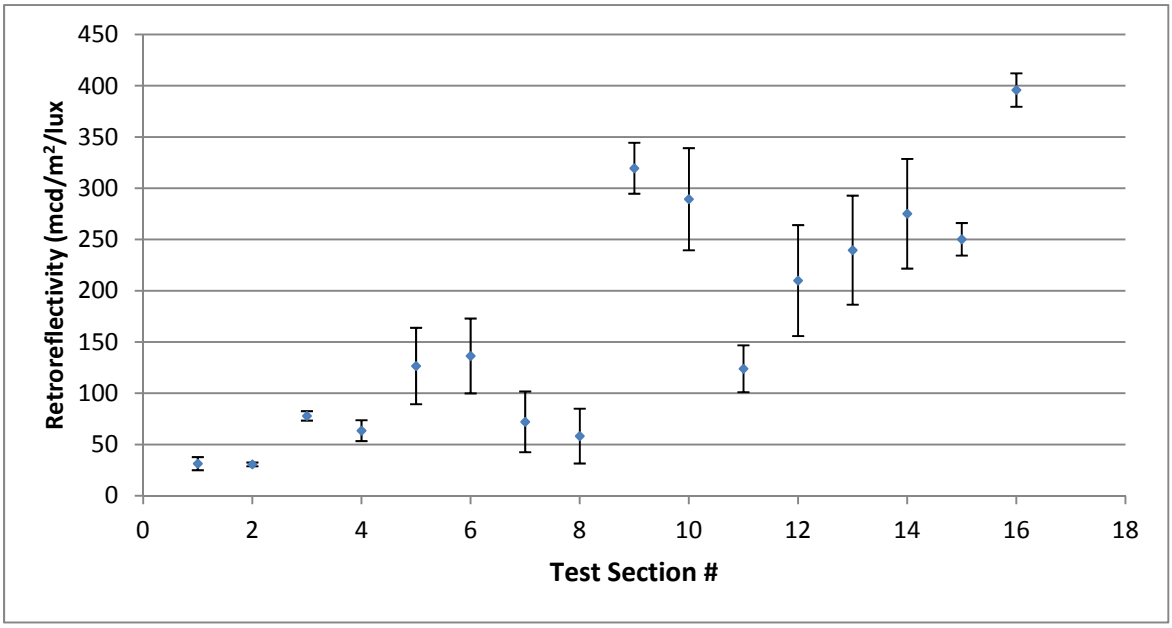

Figure 4-13 Average retroreflectivity on test sections waterborne paint markings

From Figure 4-13, it can be determined that waterborne paint shows much lower retroreflectivity than thermoplastic because even the retroreflectivity of the new waterborne paint is only around 400 mcd/m^2/lux. In addition, a similar trend can also be observed for waterborne paint; that is, the retroreflectivity above 200 mcd/m^2/lux shows the largest variation.

4.3.2. LiDAR Measurements

Repeatability

To assess the pavement marking condition consistently, the LiDAR system should be able to measure retro-intensity with good repeatability. To evaluate repeatability, we plotted the retro-intensity values of all of the thermoplastic test sections for the three runs in Figure 4-14.

The three runs overlapped quite well except for some of the sections with large variations, such as Sections 2 and 7. Closer examination reveals that the three runs have a maximum standard deviation of 0.0154 and an average standard deviation of 0.0044, which still holds a good repeatability over all the sections. The retro-intensity of three runs for waterborne paint shows similar results.

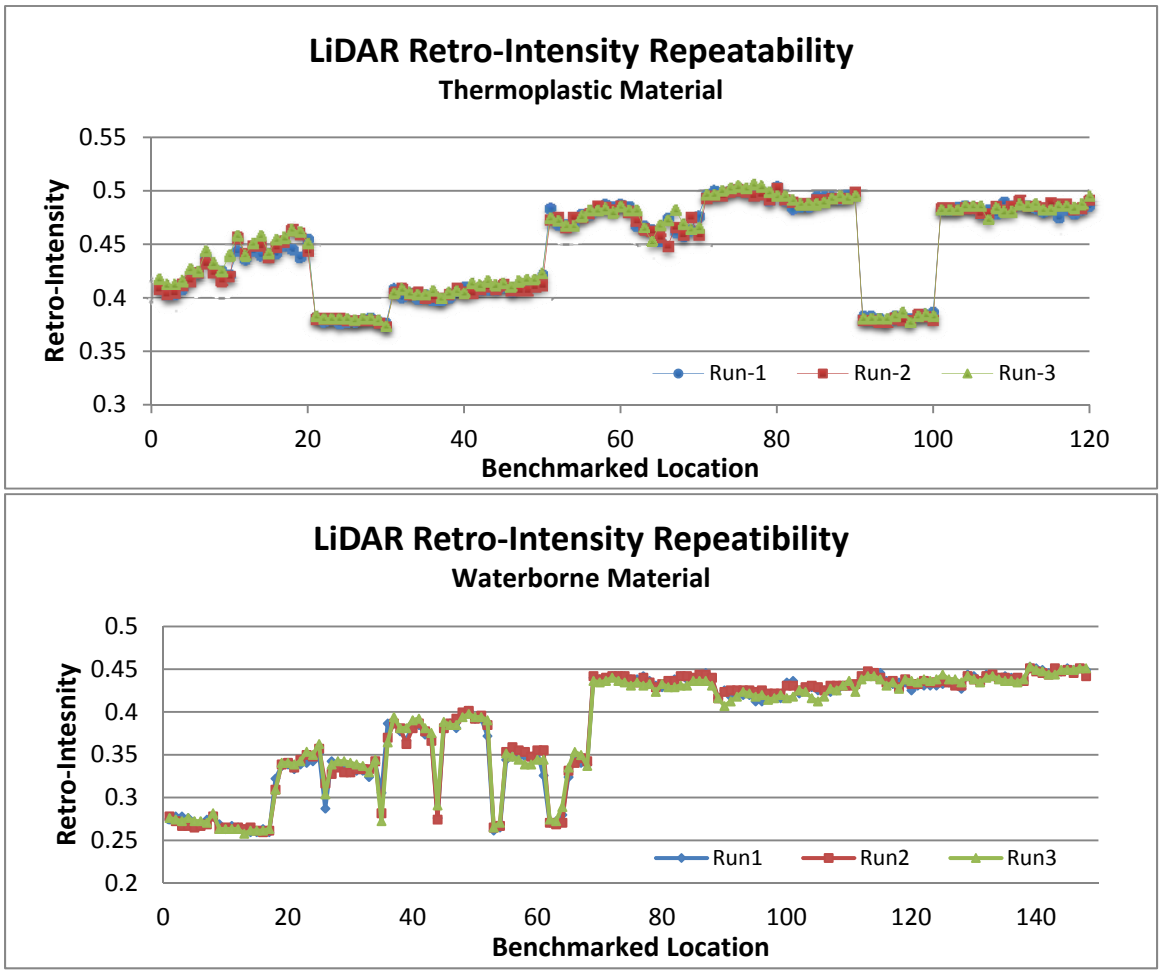

Figure 4-14 LiDAR retro-intensity repeatability

Sensitivity to Temperature

To assess the sensitivity of the LiDAR retro-intensity values to the temperature, a field test was conducted on I-16, which is near the Georgia Tech, Savannah campus. The ambient temperature was collected at each hour for six consecutive hours (i.e. 9:00am – 3:00pm). Two locations with different retro-intensity values were selected to measure the LiDAR retro-intensity values, including a pavement marking section with high retro-intensity value and a concrete pavement surface section with low retro-intensity. Figure 4-15 shows the results of the sensitivity. Both the pavement marking section (with high retro-intensity values) and the non-pavement marking section (with low retro-intensity values) show only a small variance (0.0041 and 0.0039 respectively) as the temperature changed between 88.3°F to 119.5°F.

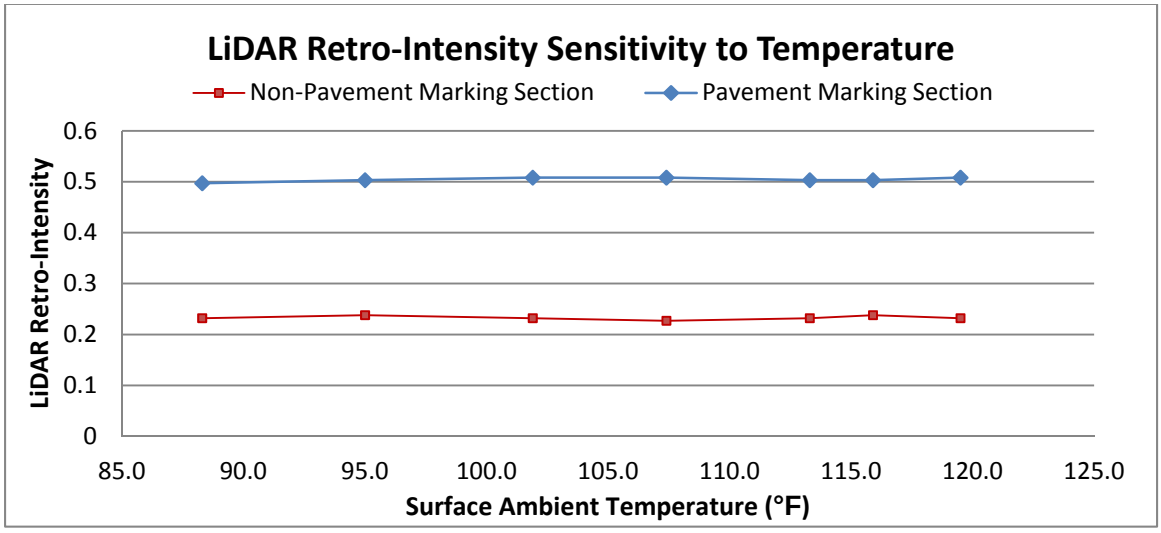

Figure 4-15 LiDAR retro-intensity sensitivity to ambient temperature

Based on the results derived from the sensitivity study, unlike the mobile pavement marking retroreflectivity measurement device, the LiDAR retro-intensity values are not sensitive to the ambient temperature. For example, the Florida Department of Transportation reported that "*changes in temperature were observed to have a significant impact on measured retroreflectivity (using LaserLux)*" (Fletcher et al., 2007). The insensitivity to temperature is a very important feature of the mobile LiDAR for establishing a reliable correlation between the retro-intensity and retroreflectivity in the following sections. It is also critical to ensure that the

LiDAR-based pavement marking retroreflectivity condition assessment can produce a consistent outcome under different temperature conditions in practice once the correlation is established.

4.3.3. Correlation Establishment

Figure 4-16 (a) to (d) shows the collected retroreflectivity and retro-intensity data for thermoplastic and waterborne paint materials. It can be determined that the retro-intensity values correlate with retroreflectivity well from condition group to condition group. Within the test sections, especially those with large retroreflectivity (over 200 mcd/m^2/lux), the retroreflectometer readings show a bigger variation due to the randomness of individual measurements at each single location, while the LiDAR retro-intensity readings are continuously measured using the GTSV and shows more consistent values with smaller variations.

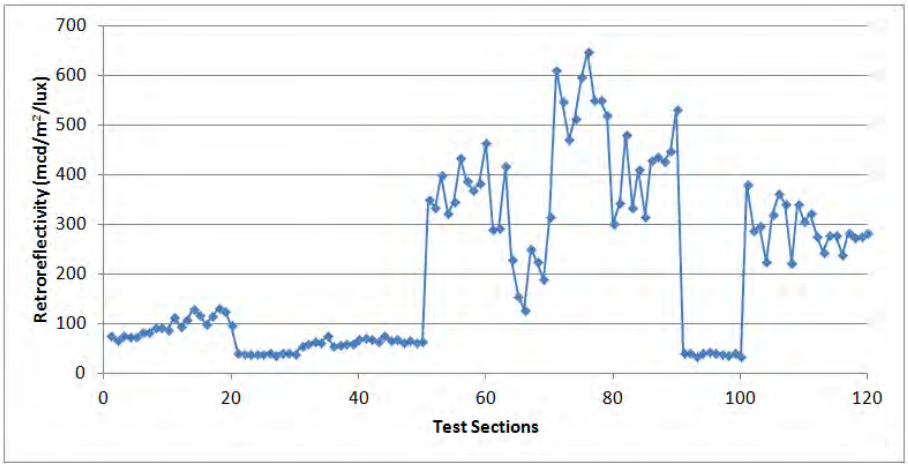

(a) Retroreflectivity for thermoplastic

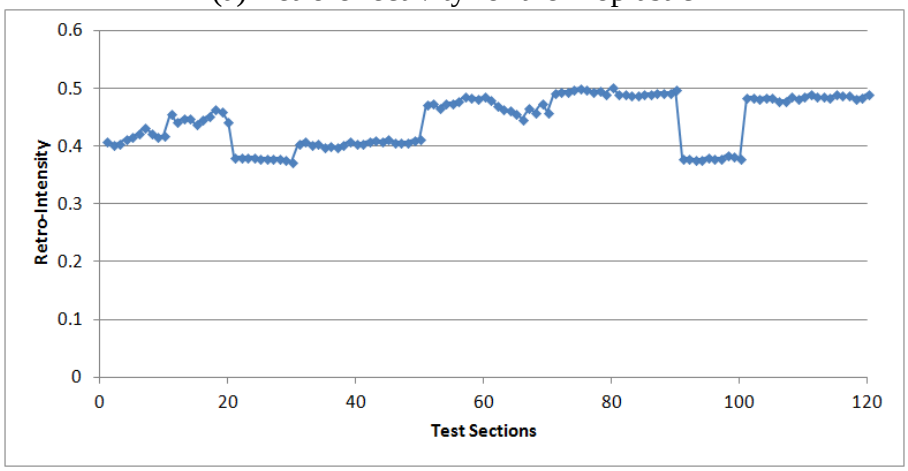

(b) Retro-intensity for thermoplastic

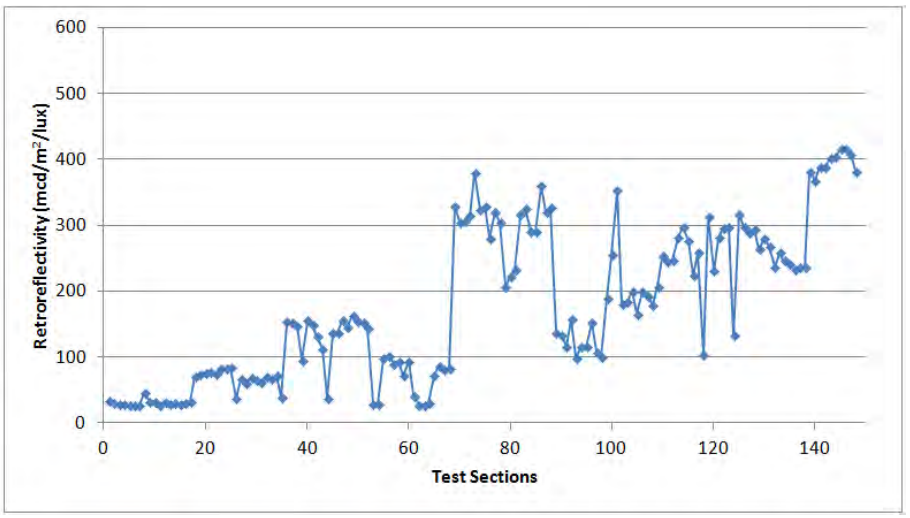

(c) Retroreflectivity for waterborne paint

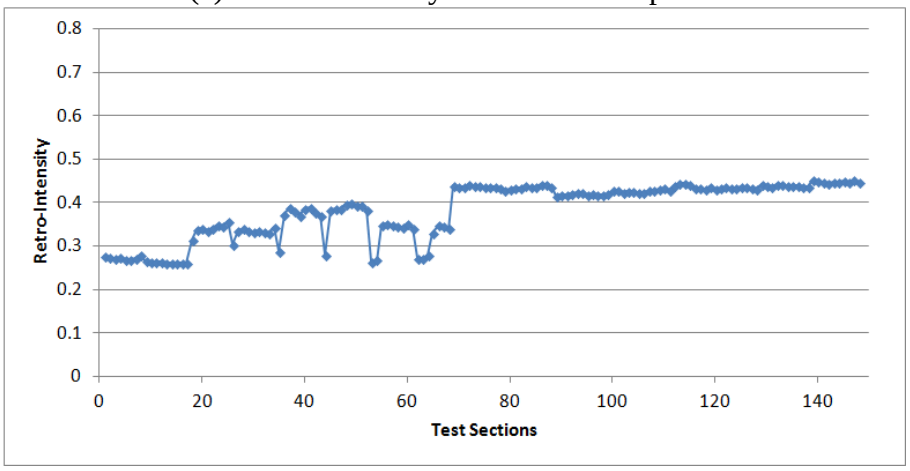

(b) Retro-intensity for waterborne paint

Figure 4-16 Retroreflectivity and retro-intensity for thermoplastic and waterborne paint materials

Regression using exponential function was conducted with data from the 12 thermoplastic test sections and 16 waterborne paint test sections. The results of the regression analysis are shown in Figure 4-17 and Figure 4-18. These results do not indicate any deterministic models between the retroreflectivity and the retro-intensity values from LiDAR, although high R^2 values are observed, which indicates strong correlations.

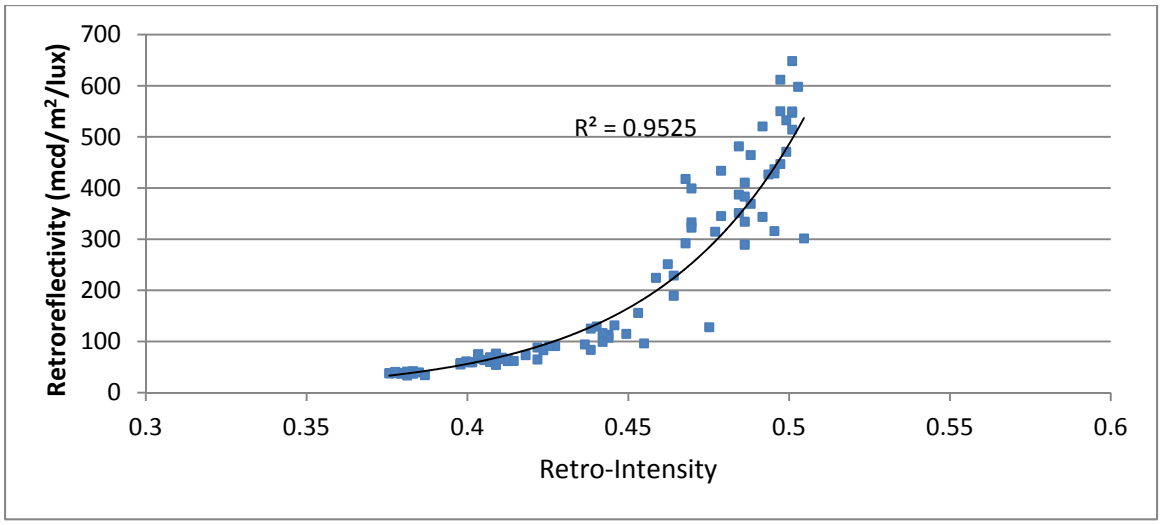

Figure 4-17 Correlation between retroreflectivity and LiDAR retro-intensity of thermoplastic material

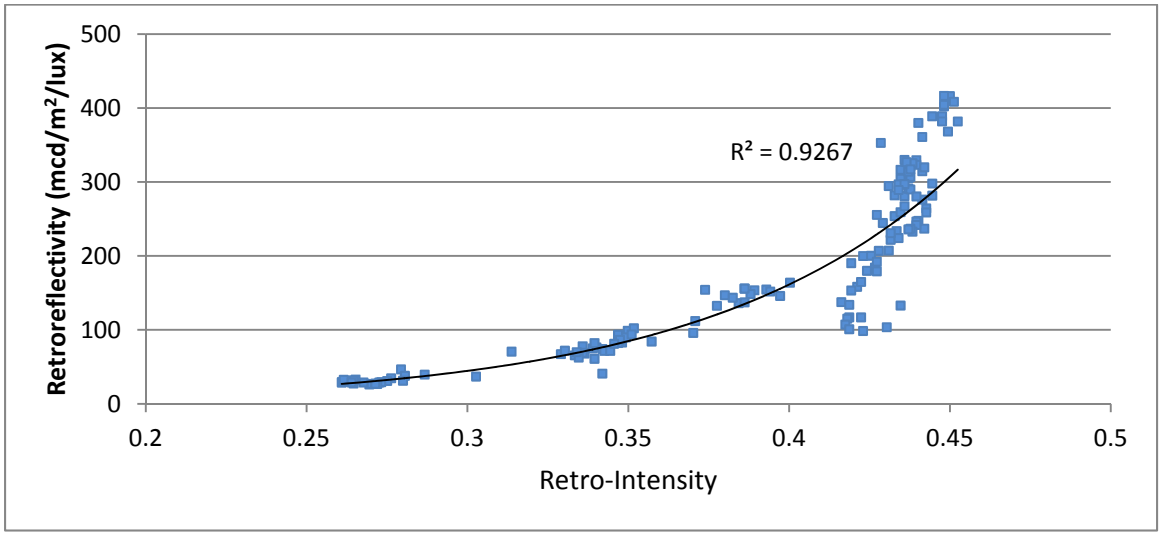

Figure 4-18 Correlation between retroreflectivity and retro-intensity of waterborne paint material

Figure 4-17 and Figure 4-18 show clear exponential relationships between the handheld retroreflectometer measurement and the LiDAR retro-intensity values for both thermoplastic and waterborne paint materials. The R-squares are as high as 0.9525 and 0.9267, respectively. Even though the R-square for the waterborne paint is as high as 0.9267, the middle-ranged test sections (150-250 mcd/m^2/lux for waterborne paint) shows an obvious deviation from the general trend. Instead of lump summing all the samples to form a single correlation, further

investigations were conducted to study the cause of such a deviation. Figure 4-19 shows the deviation of the two selected locations for waterborne material; the blue color represents the data collected on the Hemphill Street, whereas the red color represents the data collected on the 17th Street. Although both locations have waterborne paint-based pavement markings, it is suspected that the different bead formula (i.e. bead shape and diameter distribution) could have an impact of the correlation results.

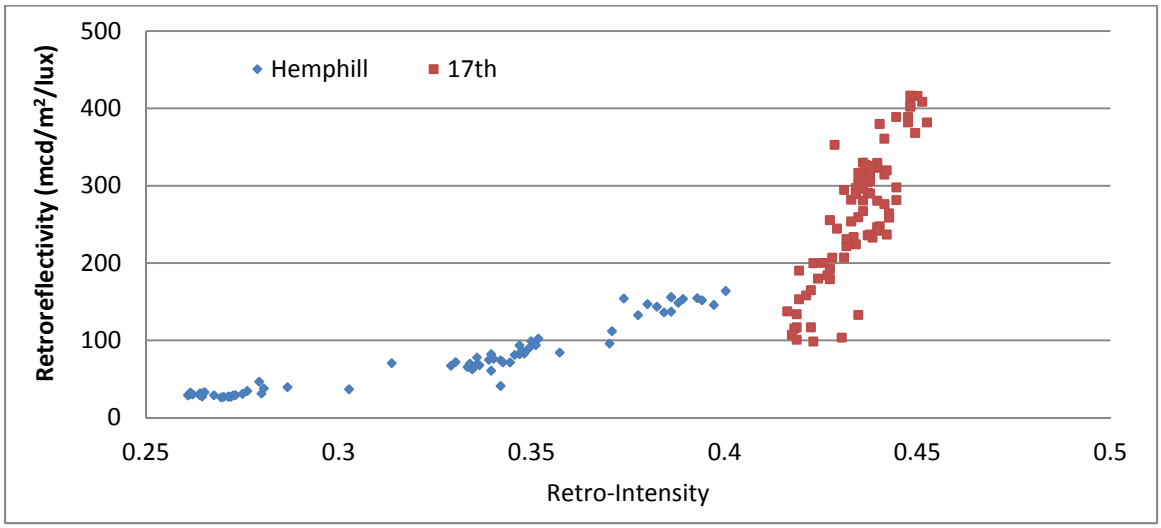

Figure 4-19 Different retro-intensity responses from different road sections

The test sections on Hemphill Street and 17th Street were revisited to capture the microscopic images of the pavement markings. Figure 4-20 shows two examples of the bead observed on Hemphill Street and 17th Street, respectively. There is some bead formula difference observed in both of the sections. Based on the observation of the microscopic images, it is suspected that Hemphill Street used Type I bead only, while 17th Street used Type I and Type IV bead mix with a 4:1 or 3:1 ratio. The roundness of the Type IV glass beads collected on 17th Street is better than then ones on Hemphill Street. In addition, the glass bead density treated on 17th Street is much higher than Hemphill Street, which is a good explanation of the general retroreflectivity differences. There is a need to further investigate the impact of different bead formulas to establish the correlation between the retro-intensity values from mobile LiDAR and the retroreflectivity from the retroreflectometer.

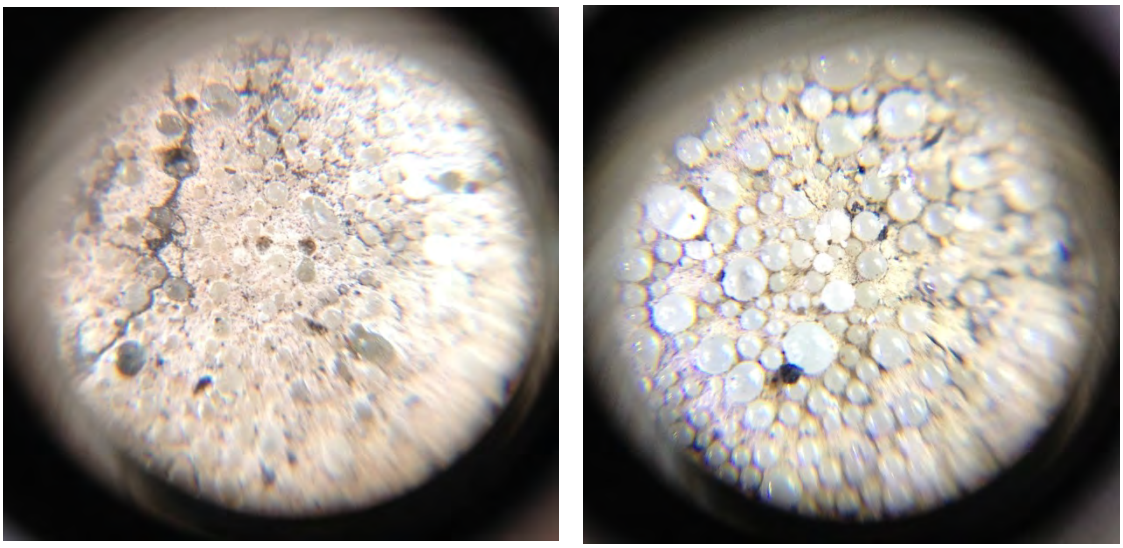

(a) (b)

Figure 4-20 Observation of the microscopic glass beads on a) Hemphill Ave. and b) 17th Street

Although the derived correlations still require further validation, these correlations are promising for developing an automated pavement marking retroreflectivity condition assessment in the future. For example, assuming the derived correlation curve between the LiDAR retro-intensity and retroreflectivity were validated, if the critical value of retroreflectivity is 100mcd/m^2/lux for separating pavement marking retroreflectivity condition, one can conduct the condition assessment of pavement marking using the corresponding critical retro-intensity value. The detailed analysis results in Table 4-3 show that if the experimental tests are performed on thermoplastic independently many times, 95% of the mean retro-intensity will fall in between 0.4035 to 0.4505 when the mean retroreflectivity for a sample spot is 100mcd/m^2/lux. If the experimental tests are conducted on waterborne paint, the 95% confidence interval will be 0.2973 to 0.4264 with a mean retro intensity of 0.3561 for the retroreflectivity of 100mcd/m^2/lux. These critical retro-intensity values can be used to determine the threshold separating good pavement markings from poor ones.

Table 4-3 Critical Retro-intensity Value

Material	Retroreflectivity	Retro-Intensity	Confidence Level	Confidence Interval	
Thermoplastic	100mcd/m^2/lux	0.4263	95%	0.4035	0.4505
Waterborne paint	100mcd/m^2/lux	0.3561	95%	0.2973	0.4264

5. Conclusions and Recommendations

This study focuses on exploring the feasibility of conducting a pavement marking retroreflectivity condition assessment using LiDAR technology by establishing the correlation between the retroreflectivity values measured by handheld retroreflectometer and the retro-intensity value acquired from a LiDAR point cloud. In this study, as the most commonly used materials of DOT maintained highway and local roads, thermoplastic and waterborne paint were used to establish the correlation. The same procedure can be followed for establishing the correlation with other pavement marking materials. For thermoplastic, Ferst Drive on the Georgia Tech campus was selected as the test site to conduct the data collection; it consisted of 12 10-foot test sections and 120 individual 1-foot testing sample sections. The retroreflectivity from the selected thermoplastic test sections ranged from around 30mcd/m^2/lux to about 600mcd/m^2/lux and covers the typical range for thermoplastic material from newly built to completely deteriorate. For waterborne paint, Hemphill Avenue and 17th Street were selected as the test site for data collection. On Hemphill Avenue, eight dash lines and on 17th Street, eight 10-foot test sections were measured with the *StripeMaster II* Retroreflectometer. The retroreflectivity from the selected waterborne paint test sections ranged from around 30mcd/m^2/lux to about 400mcd/m^2/lux. The following summarizes the findings of this study:

- It is discovered that the retro-intensity values acquired from mobile LiDAR are not sensitive to ambient temperatures, having an average standard deviation of less than 0.0041. The retro-intensity acquired from mobile LiDAR has good repeatability on the tested thermoplastic and waterborne materials with an average standard deviation of 0.0044.
- It is discovered that there is an exponential correlation between retroreflectivity and retro-intensity with an R-square of 0.9525 for thermoplastic and 0.9267 for waterborne paint.
- It is discovered that the correlation between retroreflectivity and retro-intensity might be sensitive to different bead formulas of the pavement marking material. Separate correlation curves might be needed not only for different pavement marking material category, e.g. thermoplastic, waterborne, etc., but also needed for different bead formulas under the same material category, e.g. different bead formulas, etc.
- Based on the correlation results, the preliminary retro-intensity threshold corresponding to the minimum retroreflectivity (100mcd/m^2/lux) defined in the MUTCD can be determined as

0.4263, with a 95% confidence interval ranging from 0.4035 to 0.4505 for thermoplastic and 0.3521, with a 95% confidence interval ranging from 0.2973 to 0.4264. Using the established correlations, a mobile LiDAR-based pavement marking retroreflectivity condition assessment method can be further developed.

To achieve such a mobile method, the following recommendations for future research are suggested:

1) To validate the preliminary results using additional data collected with different bead formulas.
2) To validate the established correlations for thermoplastic and waterborne pavement markings with additional data collected by both the GTSV and a retroreflectometer.
3) To extend the experimental test to other pavement markings materials (e.g., tape, polyuria) following similar procedures proposed in this study.
4) To validate the critical retro-intensity values that correspond to the minimum pavement marking retroreflectivity standards required by the MUTCD and transportation agencies by comparing with both a handheld retroreflectometer and night-time visual inspection.
5) To develop an automatic method for extracting pavement marking retro-intensity data from the LiDAR point cloud to streamline the condition assessment as proposed in this study.

References

Bahar, G., Masliah, M., Erwin, T., Tan, E., and Hauer, E. (2006). “Pavement Marking Materials and Markers: Real-World Relationship between Retroreflectivity and Safety over Time.” NCHRP Web Document, Vol. 92, 206p.

Basile, A. J. (1962). “Effect of Pavement Edge Markings on Traffic Accidents in Kansas.” Highway Research Board Bulletin.

Benz, R.J., Pike, A.M., Kuchangi, S.P., and Brackett, Q. (2009). “Serviceable Pavement Marking Retroreflectivity Levels: Technical Report.” Texas Transportation Institute, Texas Department of Transportation, Federal Highway Administration, 150p.

Bernstein, R. (2000). "Summary of Evaluation Findings for 30-Meter Handheld and Mobile Pavement Marking Retroreflectometer." Highway Innovative Technology Evaluation Center (HITEC), Washington, DC USA.

Carlson, P.J., Park, E.S., and Andersen, C. K. (2009). “Benefits of pavement markings: a renewed perspective based on recent and ongoing research.” Transportation Research Record: Journal of the Transportation Research Board, Vol. 2107, pp. 59-68.

Cracknell, A.P., and Hayes, L. (1991). “Introduction to remote sensing.” CRC press.

Debaillon, C., Carlson, P.J., Hawkins, H.G., He, Y., Schnell, T., and Aktan, F. (2008). “Review and Development of Recommended Minimum Pavement Marking Retroreflectivity Levels.” Transportation Research Record: Journal of the Transportation Research Board, Vol. 2055, pp. 71-77.

Fletcher, J., Philpott, A., Choubane, B., and Holzschuher, C. (2007). “Characterization and Mitigation of Temperature Sensitivity within Mobile Retroreflectometer Unit.” Transportation Research Record: Journal of the Transportation Research Board, Vol. 2015, pp. 91-102.

Harrigan, E.T. (2006). “Pavement Marking Materials and Markers: Testing the Relationship between Retroreflectivity and Safety.” NCHRP Research Results Digest, Vol. 305, 6p.

Holzschuher, C., and Philpott, A. (2006). “Mobile Retroreflectivity Unit (MRU) Surveying of Maintenance Rating Program (MRP) Sites”. Florida Department of Transportation, State Materials Office.

Lee, T. (2011). “Advanced Methods for Mobile Retroreflectivity Measurement of Pavement Marking.” NCHRP-IDEA Program Project Final Report, 19p.

Smadi, O., Souleyrette, R.R., Ormand, D., and Hawkins, N.R. (2008). “Pavement Marking Retroreflectivity: Analysis of Safety Effectiveness.” Transportation Research Record: Journal of the Transportation Research Board, Vol. 2056, pp. 17-24.

Taragin, A. (1947). “The Effect on Driver Behavior on Center Lines on Two-Lane Roads.” Highway Research Board Proceedings.

Tsyganov, A.R., Machemehl, R.R., Warrenchuk, N. M., and Wang, Y. (2006). “Before-After Comparison of Edge Line Effects on Rural Two-Lane Highway.” University of Texas, Austin, Texas Department of Transportation, Federal Highway Administration.

Williston, R. M. (1960). “Effect of Pavement Edge Markings on Operator Behavior.” Highway Research Board Bulletin.

Chapter 5 Measurements of Roadway Geometric Characteristics Using Emerging Sensing Technologies

1. Introduction

Roadway geometric characteristics play a critical role in both operational quality and safety. The data collection of roadway geometric characteristics is essential for carrying out effective activities by transportation agencies throughout the lifecycle of a roadway, e.g. construction quality assurance and quality control (QA/QC) for newly built roads, safety adequacy assessment for in-service roads, etc. It is important for transportation agencies to obtain reliable roadway geometric characteristic data. Traditionally, manual data collection has been used by transportation agencies. However, such manual processes are labor-intensive and time-consuming because field engineers need to be physically on the road to conduct measurements. In addition, such manual processes can be dangerous, e.g. on high-speed roadways, and may require extensive resources, e.g. traffic control. There is a need for a cost-effective and reliable roadway geometric characteristics data collection.

In recent decades, emerging sensing technologies have become practically mature and commercially available. There are opportunities to utilize these technologies for carrying out a cost-effective and reliable data collection for roadway geometric characteristics. The objective of this study is to critically assess the accuracy of different sensing technologies and identify their applicability to different roadway geometric characteristic data collections. In this study, five popular emerging sensing technologies, including aerial photo, airborne LiDAR, mobile LiDAR, video log image, and global positioning system (GPS) track, and three important roadway geometric characteristics, including pavement width, horizontal curvature and cross slopes, are assessed. Horizontal curvature and cross slope are identified as the most important safety-related roadway geometric characteristics. Therefore, this study focuses on these two characteristics. In addition, since pavement width, as an auxiliary characteristic, is often measured with these two safety-related characteristics, it is also included in this study. The detailed objectives of this study are listed as below:

- To quantitatively assess the accuracy and repeatability;
- To quantitatively measure the productivity;

- To identify the challenges and opportunities;
- To suggest feasibility/applicability for different practical needs.

Section 1 presents the background and identifies the objectives of this study. Section 2 presents the assessment method. Section 3 presents the experimental test using the actual data from different roadways. Section 4 summarizes the findings of this study and provides recommendations for future research.

2. Assessment Method

The objective of this section is to present the detailed assessment method carried out in this study. Accuracy, productivity and repeatability are the three measurements used in this study. Accuracy is defined as the absolute difference between the ground truth and the actual measurement from different sensing technologies. The productivity is defined as the total processing time from the beginning of data processing to the final measurement delivery. Repeatability is defined as the measurement consistency (i.e. measurement variance) using different runs of data at different times but under similar environmental condition. Table 5-1 lists the detailed assessment items that have been carried out in this study for each technology:

Table 5-1 List of the Detailed Assessment Items

	Pavement Width			Horizontal Curvature			Cross Slope		
	Acc.	Pro.	Rep.	Acc.	Pro.	Rep.	Acc.	Pro.	Rep.
Aerial Image	x	x	-	x	x	-	-	-	-
Airborne LiDAR	x	x	-	x	x	-	-	-	-
Mobile LiDAR	x	x	X	x	x	x	x	x	x
Video Log Image	x	x	X	x	x	x	-	-	-
GPS Track	-	-	-	x	x	-	-	-	-

- Pavement width: The accuracy and productivity were assessed using aerial images, airborne LiDAR, mobile LiDAR and video log image. GPS track is excluded for this task, as it is obviously not applicable. Repeatability was assessed using only mobile LiDAR and video log image because additional datasets containing different runs were acquired using GTSV.
- Horizontal curvature: The accuracy and productivity were assessed using all five technologies. Repeatability was assessed using only mobile LiDAR and video log images because additional datasets containing different runs were acquired using the GTSV.

- Cross slope: The accuracy, productivity, and repeatability were assessed using only mobile LiDAR. The other four technologies were obviously not applicable for this task, which requires high accuracy. Airborne LiDAR has been attempted for cross slope measurement in previous studies, but the accuracy was not satisfied for most of the applications (Souleyrette et al., 2003).

In the following subsections, the assessment data, ground truth measurements, and the detailed extraction methods for each roadway geometric characteristic are presented.

2.1. Assessment data selection

To comprehensively assess different technologies, three testing sites were selected to cover representative ranges of the focused characteristics, including the Georgia Tech Savannah campus, Jimmy Deloach Parkway, and Pooler Parkway. Figure 5-1 shows the location of the testing sites.

Figure 5-1 Layout of the assessment data in this study

Data was then collected for the five technologies that cover the selected testing sites. These data, namely aerial photo, airborne LiDAR data, mobile LiDAR data, video log image, and GPS track, are described as follows:

- Aerial photo: The aerial photo data was acquired in 2009 by Sanborn Map Company for Chatham County, Georgia, for the Metropolitan Planning Commission. The data has a spatial resolution of 0.5 foot in both the x and y directions. Figure 5-2 shows a sample aerial photo used in this study.

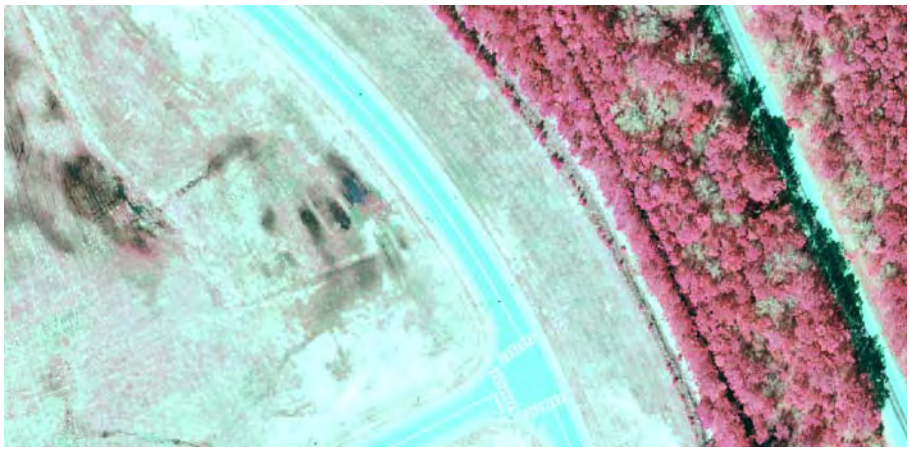

Figure 5-2 Aerial photo data sample used in this study

- Airborne LiDAR: The airborne LiDAR data was acquired in the spring, 2009, by Sanborn Map Company for Chatham County, Georgia, for the Metropolitan Planning Commission. The data has a spatial resolution of 0.78 ft in the vertical direction and 2 ft in both the x and y directions. Figure 5-3 shows a sample airborne LiDAR point cloud used in this study.

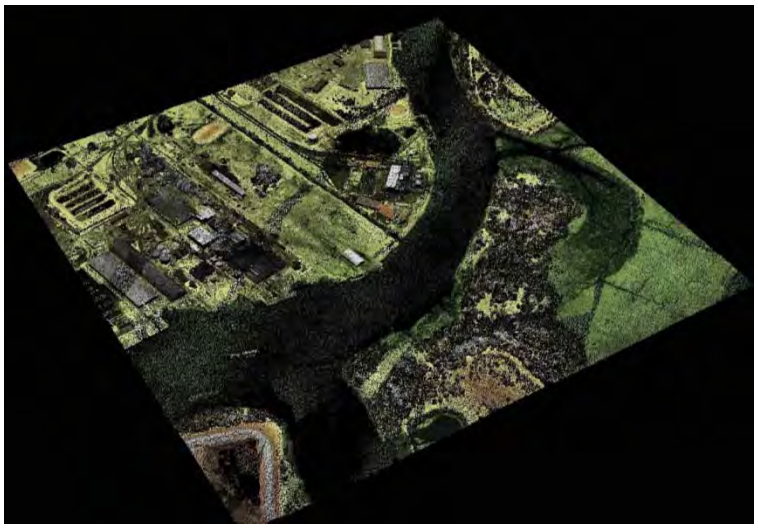

Figure 5-3 Airborne LiDAR data sample used in this study

Mobile LiDAR: The mobile LiDAR data was acquired using the GTSV. The LiDAR model used in the GTSV (i.e. Riegl LMS-Q120i) has a point acquisition frequency of 10,000 Hz and a measurement error of 2 cm. As the vehicle is operating at 60 mph, the longitudinal resolution of the data is approximately 1 ft, and the transversal resolution is less than 3 in. Figure 5-4 shows a sample mobile LiDAR point cloud used in this study.

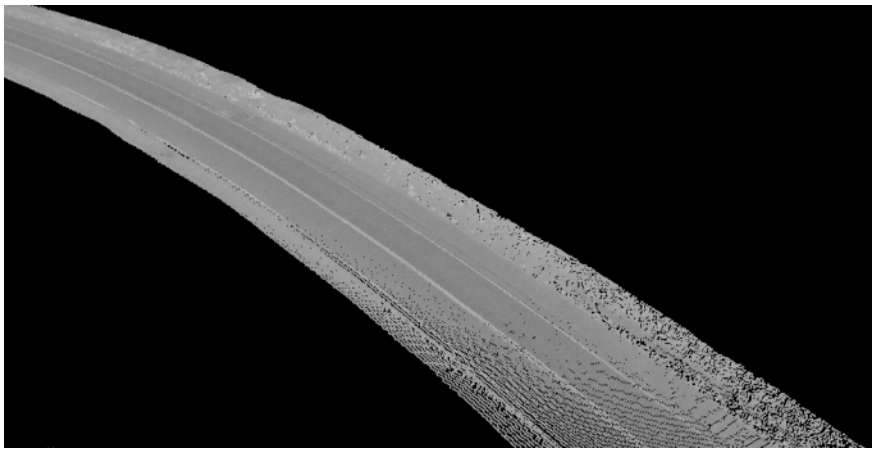

Figure 5-4 Mobile LiDAR data sample used in this study

- Video log Image: The video log image data was acquired using the GTSV. The image data was captured using calibrated cameras (i.e. PTGrey GRAS-50S5c) in the GTSV and which have a resolution of 2,448x2,048. Figure 5-5 shows a sample video log image used in this study.

Figure 5-5 Video log image data sample used in this study

- GPS track: The GPS track data was acquired using the GTSV. The GPS data collected was acquired at a 100Hz frequency, which is corrected using continuously operating reference station (CORS) data from the National Geographic Survey (NGS) and post processed using an inertial measurement unit (IMU) and a distance measurement instrument (DMI) from Applanix solutions. The positional accuracy after the post processing is 5cm in z direction and 3cm in x and y directions when the satellite reception is ideal, while the positional accuracy can consistently be fewer than 10cm in three directions under any typical satellite reception condition. Figure 5-6 shows a sample GPS track used in this study.

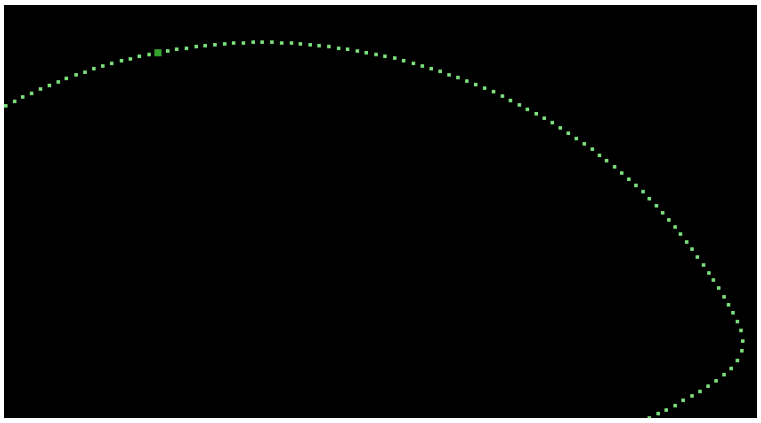

Figure 5-6 GPS data sample used in this study

2.2. Ground truth measurement

The ground truth measurements, i.e. pavement width, horizontal curvature and cross slope, were collected at the locations shown in Figure 5-1. For each ground truth location, the average of multiple measurements was taken.

Pavement Width: A tape measure was employed to conduct the measurement. The data collection locations are distributed on the Georgia Tech Savannah campus, Jimmy Deloach Parkway, and Pooler Parkway, consisting of 17 ground truth measurements. Figure 5-7 shows an image of how the pavement width measurement was carried out on the Georgia Tech Savannah campus.

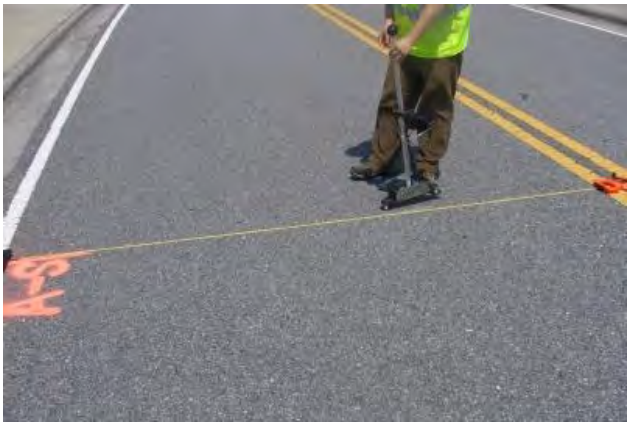

Figure 5-7 Ground truth measurement using tape for pavement width

Horizontal curvature: The chord-offset measurement (Carlson *et al.*, 2005; Ibraheem & Hammodat, 2011) was employed to calculate the horizontal curvature. Using a 100-ft long tape measure, the offset between the arc and the mid-point of the chord was measured. Using the equation $R=L^2/8m+m/2$, the radius of the curve, where L is the chord length and m was the offset. The chord and offset measurement method was chosen for ground truth measurement, as well as the subsequent sensing data measurement, to provide a consistent comparison among the collected data from different data sources. The data collection locations were distributed on the Georgia Tech Savannah campus, Jimmy Deloach Parkway, and Industrial Park, consisting of 29 ground truth measurements. Figure 5-8 shows an image of how the chord-offset measurement was carried out on Jimmy Deloach Parkway.

Figure 5-8 Ground truth measurement using chord-offset method for horizontal curvature

Cross slope: The 4-foot digital level was employed to measure the cross slope, which is also typically used by most of transportation agencies (FDOT, 2008; TxDOT, 2004). The data collection locations were distributed on the Georgia Tech Savannah campus, Jimmy Deloach Parkway, and Pooler Parkway, consisting of 15 ground truth measurements. In addition, to verify the reliability of the digital level on cross slope measurement, a dipstick profiler was employed. Figure 5-9 shows two images of how the cross slope measurement was carried out using digital level and dipstick on the Georgia Tech Savannah campus.

Figure 5-9 Ground truth measurement using digital level and dipstick for cross slope

2.3. Roadway geometric characteristic assessment methods

The measurement derived from each sensing technology was carried out with the help of commercial software, including Quick Terrain Modeler, ERDAS IMAGINE, Trident Analyst, and ArcGIS. Though the relevant software often differs for visualization and measurement for each kind of sensing technology data, the methodology was the same to ensure a fair assessment. The principle of how each type of roadway geometric characteristic was assessed from different data sources was followed.

Pavement width: The width measurement for the sensing data was done in the following steps:

- Identify ground truth points (denoting pavement edge markers) in the data.
- Use linear metric tools to find the width by measuring from the inside edge of the pavement edge marker up to the outside edge of the middle pavement marker (W3 in Figure 5-10).
- Select 2 points at 2-ft intervals on each side of the initial point on the pavement edge marker (W1, W2 and W4, W5 in Figure 5-10) and measure the width similarly.
- Average the 5 values to come up with the representative width of that location.

- Compare the set of ground truth values with the set of values measured for the specific sensing technology using a paired t-Test. A paired t-Test assesses whether two sets of observations input into the test are statistically different or similar. It also gives the tendency of the difference between the sets of observations. Based on the data obtained by the t-Test, the relative error measure was computed and a confidence interval for 95% confidence was constructed about the mean of the deviation between the sets of observations.

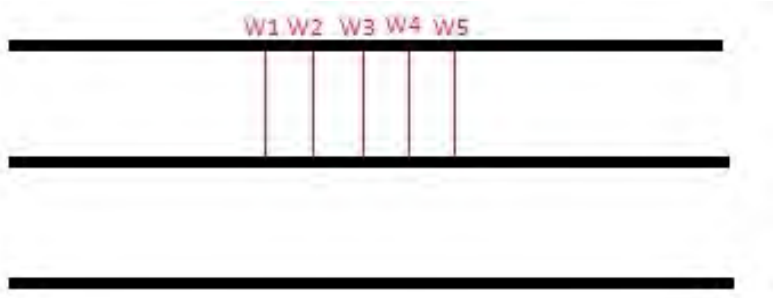

Figure 5-10 Averaging adjacent measurements for pavement width

Horizontal curvature: The curvature measurement for each sensing technology was carried out in the following steps:

- Identify chords used for ground truth measurements using their start and end coordinates given, in the data.
- Use linear measurement tools to find the chord (C3 in Figure 5-11), and then draw the offset to the nearer edge of the pavement edge marker from the middle of the chord.
- Select 2 points on each side of the chord starting point and joining point at 2-ft intervals, join the corresponding point to draw the new chord (C1, C2 and C4, C5 in Figure 5-11), and measure the offset similarly.
- Average the 5 values (O1, O2, O3, O4 and O5) and compare them with the ground truth.
- Compare the set of ground truth values with the set of values measured for the specific sensing technology using a paired t-Test. Obtain the relative error parameter and the 95% confidence interval about the mean difference, as mentioned previously for width measurements.

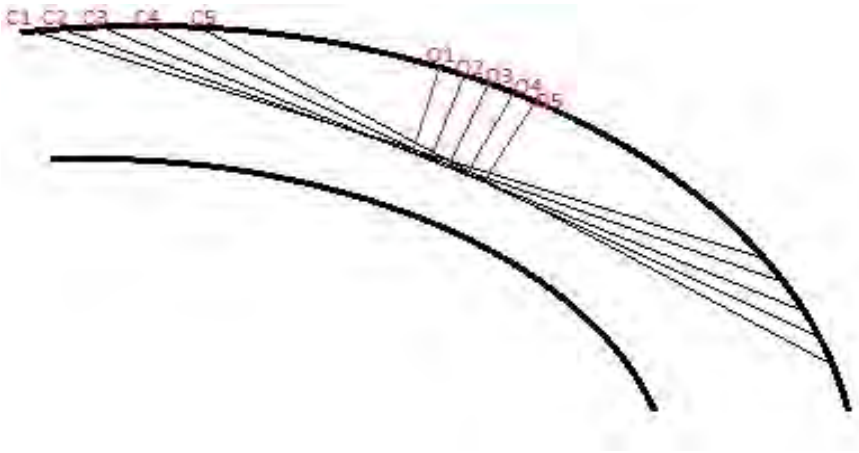

Figure 5-11 Averaging adjacent measurements for horizontal curvature

Cross slope: The cross slope measurement for each sensing technology was carried out in the same manner as pavement width.

3. Preliminary Assessment Results

This subsection presents the assessment results using different sensing technologies in the measurement of the three roadway geometric characteristics. Three types of quantitative assessment are carried out in this subsection, including accuracy and precision assessment, repeatability assessment, and productivity assessment.

3.1. Accuracy and precision assessment

The accuracy and precision assessment of the data measured from each sensing technology was carried out with the paired t-test. The output of the test gave a central tendency of the error of the data measured from a specific technology. Additionally, based on the variance of the measurement data, an interval was constructed with 95% confidence for the sensing technology measurements, which is representative of the precision of the measurements carried out for that sensing technology. These parameters were plotted on a relative error graph, which is the one for the width measurements. For cross slope, since only mobile LiDAR technology was used, the absolute difference was used instead of a paired t-test so that the error could be compared with the required accuracy using digital level, i.e. 0.1°.

Width: The output of the paired t-test and the interval constructed is given in the Figure 5-12 along with the measures tabulated in Table 5-2. By observing Figure 5-12, it can be interpreted

that all the technologies have a relative error measure of <2.5%. This leads to an error of being within ±0.3 feet for a 12-foot lane width, which is within the accuracy requirement of ±1 feet, according to the Highway Performance Monitoring System.

Of the technologies evaluated, mobile LiDAR performed best with an average relative error of 0.04%. It is also most precise of all the sensing technologies evaluated with a precision of ± 0.13%. This means, for a 12-foot lane width, there is 95% probability that the mobile LiDAR will give an error within -0.01 ft to +0.02 ft. This can be corroborated by the scatter plot of the ground truth measurements and the measured width data in Figure 5-13. Next in accuracy is the airborne LiDAR technology, which has an error of 0.6% but is much more imprecise at ± 0.84%.

The aerial photo technology has the least accuracy for width measurements, having a relative error of -2.13%. This also has the tendency to underestimate the width measure, such as giving a width measure always less than the true value. This can also be observed in the scatter plot in Figure 5-13. A possible reason for this is that the aerial photo is only a 2-D representation without any depth information, whereas the true width measured is the distance between lane markers in the three dimensions. However, adjusting for known cross-slope values yields an improvement of 0.13%. Another reason may be due to the uncertainty posed by the 0.5 feet resolution of the data.

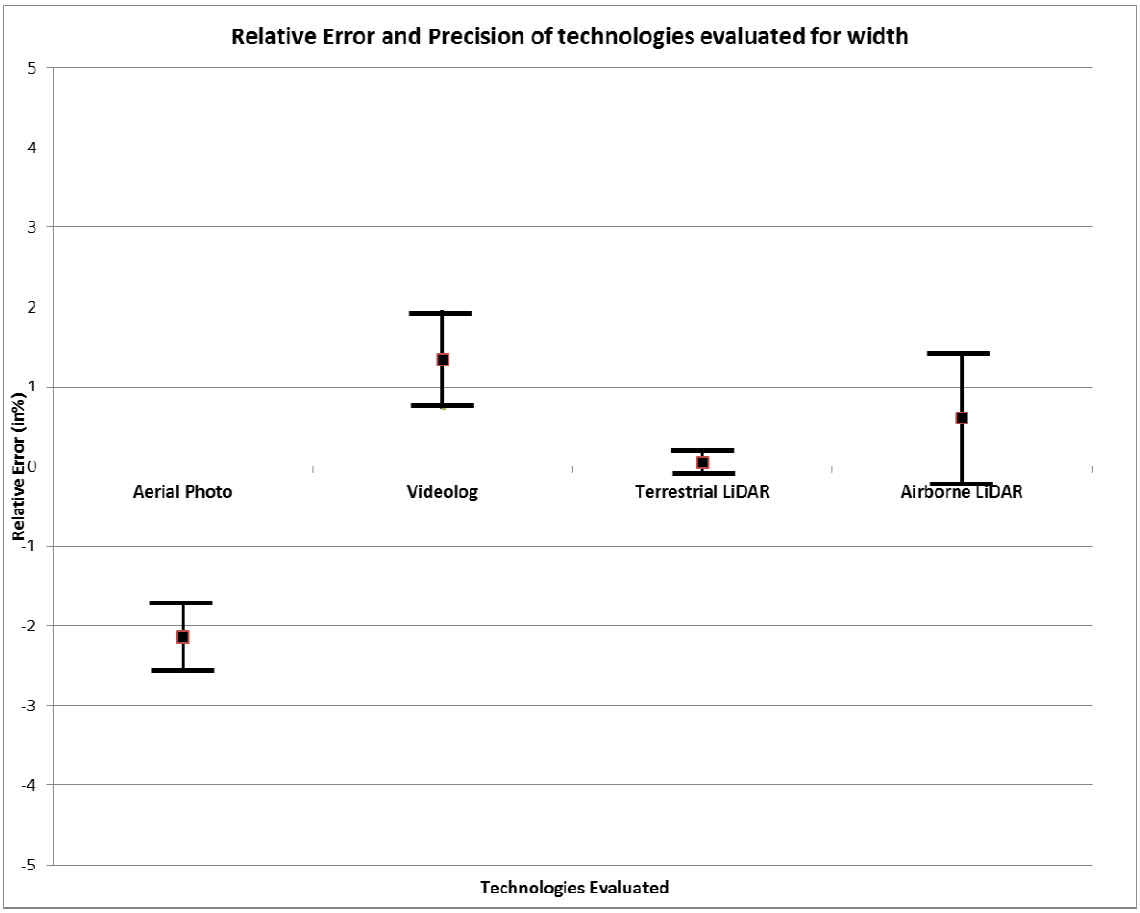

Figure 5-12 Relative error and 95% confidence interval plot for each sensing technology evaluated for width measurements.

Table 5-2 The Mean Percentage of Error and the Interval Constructed for Each Sensing Technology.

	Aerial Photo	Airborne LiDAR	Mobile LiDAR	Video log
Error	-2.13%	0.6%	0.04%	1.34%
Precision	± 0.44%	± 0.84%	± 0.13%	± 0.62%

The video log image technology has the tendency to overestimate the width measure. This can be confirmed by observing the scatter plot of the ground truth and the widths measured, as seen in Figure 5-13. This phenomenon can be due to two factors. One is the changing spatial resolution in the video log image due to the projection system's being a perspective projection system. This means that locations on the roadway farther from the image acquisition point will have less spatial resolution than those locations that are nearer.

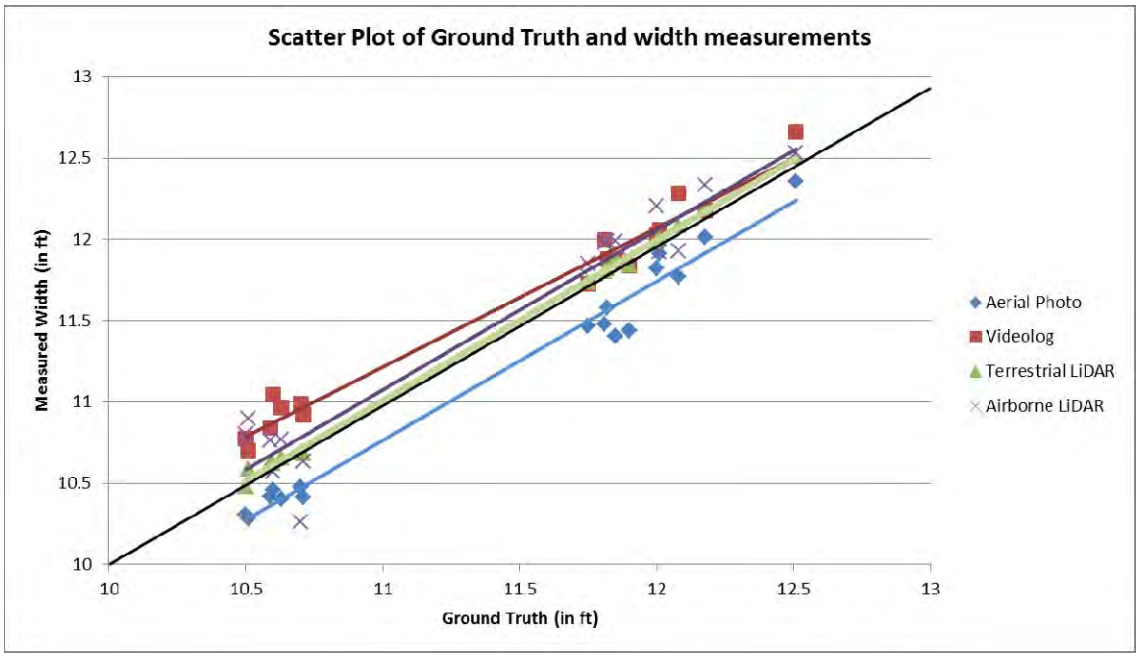

Figure 5-13 Scatter plot of ground truth measurements and widths measured

Curvature: The output of the paired t-test for curvature measurements and the interval constructed is given in the Figure 5-14, along with the measures tabulated in the Table 5-3. By observing Figure 5-14 and the corresponding table, it can be interpreted that all the technologies with the exception of the airborne LiDAR technology give a relative error measure of < 8%. This leads to an error of being within ±80 feet for a road section with radius of curvature of 1000 feet.

The airborne LiDAR technology gives a very high relative error measure of -51.72% and a very low precision of ±37.98%. This is due to the low point density of 2 feet, which is unfit to measure the curvature using the chord offset method. In this method, the offset often comes out to be less than 2 feet for chord lengths of 100 feet. Thus, it is very difficult to interpolate, even manually, those measurements.

Of the technologies evaluated, mobile LiDAR again performs best with an average relative error of 0.35%. It is, also, the most precise of all the sensing technologies evaluated with a precision of ±6.65%. This means, for a road section with radius of curvature of 1,000 ft, there is 95% probability that the mobile LiDAR will give an error within -70 ft to +63 ft.

Next in terms of accuracy is the GPS track technology. It gives the second-best relative error measure with -3.63%, and with a precision of ± 10.76%, it gives a slightly better precision than the video log and aerial photo technologies.

Video log technology has an error of 5.2%, but, in terms of precision, it gives a range of ±13.15%. The aerial photo is also capable of giving comparable accuracy, with an average relative error of 7.87%, with a relatively better precision of ±11.58%.

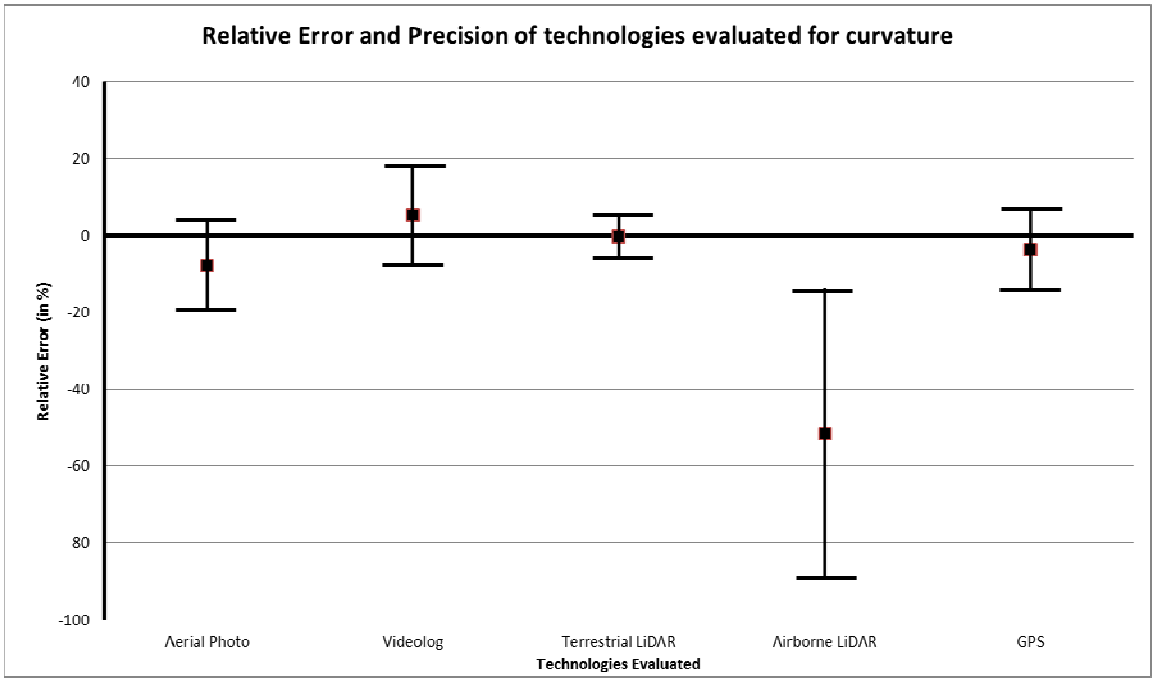

Figure 5-14 Relative error and 95% confidence interval plot for each sensing technology evaluated for curvature measurements.

Table 5-3 The Mean Percentage of Error and the Interval Constructed for Each Sensing Technology.

	Aerial Photo	Airborne LiDAR	Mobile LiDAR	Video log	GPS
Error	-7.78%	-51.72%	-0.35%	5.2%	-3.63%
Precision	± 11.58%	± 37.98%	± 6.65%	± 13.15%	± 10.76%

From the scatter plot of the ground truth measurements and the measured curvature data in Figure 5-15, the trend line of mobile LiDAR (green) and of video log data points (light brown) can be observed to follow closely the true value line (black). This can lead to a false

interpretation that both the technologies have similar capabilities to deliver the desired accuracy. However, by observing the color-coded data points in Figure 5-15, it can be deduced that the mobile LiDAR points are closer to the trend line and, thus, are more precise. This is not the case for the video log data points.

Another observation that can be made from the scatter plot is that for road sections with low curvatures, all the technologies (except airborne LiDAR) give measurements closer to the true value than for higher curvatures. Thus, the variances of the observations increase with increasing curvature.

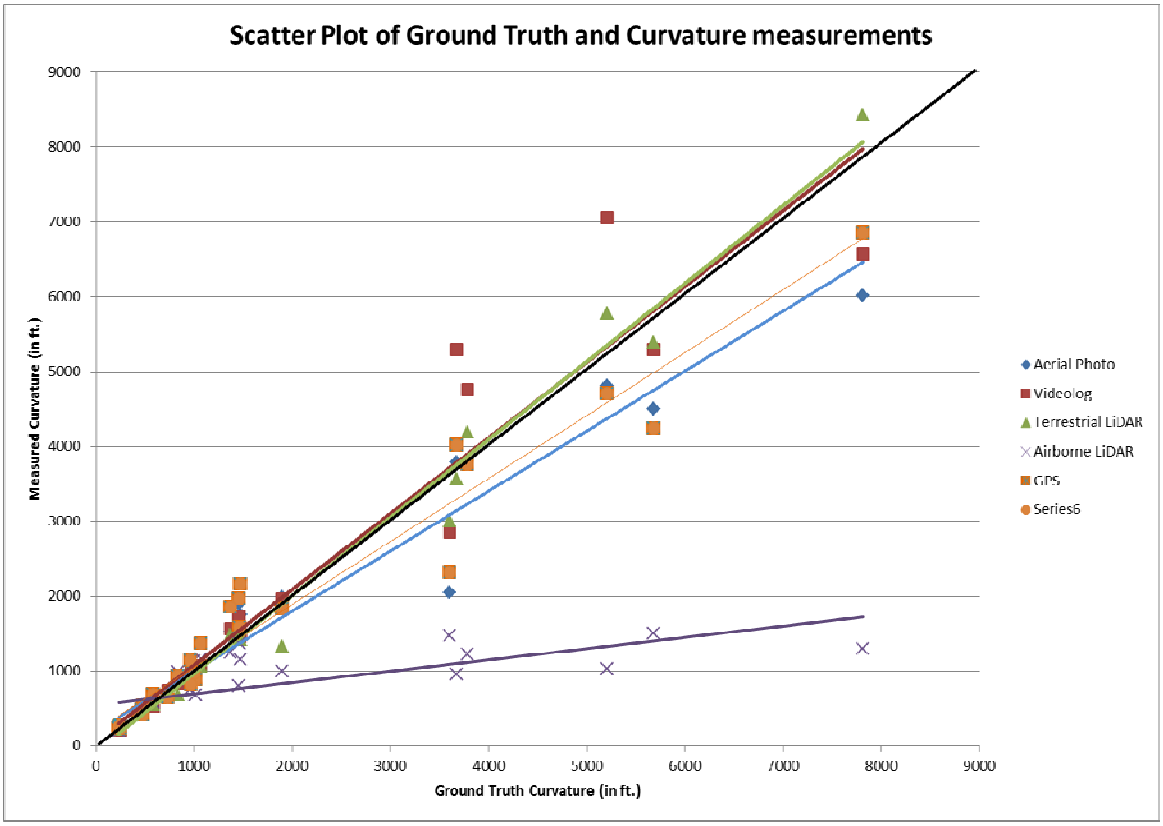

Figure 5-15 Scatter plot of ground truth measurements and measured radius

Cross slope: The cross slope measurements at the 15 benchmarked locations derived from the proposed method were compared to those measured using a digital level with 0.1° accuracy. At each benchmarked location, the ground truth was measured twice, and the measurements were averaged. Table 5-4 shows that the derived measurements are very close to the ones measured using the digital level; there is a maximum difference of 0.28% cross slope (i.e. 0.17°) and an

average difference less than 0.13% cross slope (i.e. 0.08°). No bias is observed from the results. From the results, it is identified that the derived cross slope measurements achieves a desirable accuracy, considering the instrumentation accuracy for the digital level°, which is used by many transportation agencies, is only 0.1 (Wang, 2010).

Table 5-4 Assessment Results of the Cross Slope Measurement Accuracy

	Ground Truth (%)	Proposed Method		Absolute Difference (%)	Relative Difference (%)
		Mean (%)	STDev (%)		
GT Savannah campus	2.18%	2.06%	0.02%	0.13%	5.77%
	2.09%	2.07%	0.02%	0.02%	1.02%
	1.92%	2.04%	0.02%	-0.12%	-6.08%
	2.18%	1.89%	0.02%	0.30%	13.52%
	2.53%	2.39%	0.03%	0.14%	5.48%
Jimmy Deloach Parkway	5.68%	5.92%	0.02%	-0.24%	-4.20%
	5.42%	5.37%	0.03%	0.04%	0.81%
	5.68%	5.44%	0.02%	0.23%	4.14%
	5.33%	5.03%	0.05%	0.29%	5.50%
	5.94%	5.78%	0.03%	0.16%	2.76%
Pooler Parkway	7.17%	7.16%	0.04%	0.01%	0.17%
	6.82%	6.75%	0.02%	0.07%	0.96%
	7.34%	7.46%	0.03%	-0.12%	-1.61%
	6.99%	6.84%	0.02%	0.16%	2.23%
	7.17%	7.24%	0.03%	-0.07%	-1.04%

3.2. Repeatability assessment

The results of the repeatability analysis for width and curvature measurements are given in the Table 5-5. Both the technologies evaluated for repeatability demonstrated quite low variance. The variance was expressed in terms of the percentage of the mean of the observations for the same location across multiple runs. Therefore, the percentage measures mean that, for example, a 12-foot lane width the variability due to repeatability will be ±0.06 feet for video log technology and ±0.012 feet for mobile LiDAR. Similarly, for the curvature measurements, a road with radius of curvature of 1000 feet will have a variability of ±8 feet for video log images and ±9 feet for mobile LiDAR.

We can observe that mobile LiDAR shows a lower variance than the video log technology for the width measurements, while for the curvature measurements, the measures of variance are almost similar.

Table 5-5 Repeatability Measures

Geometric Parameters	Video log	Mobile LiDAR
Width	0.5%	0.1%
Curvature	0.8%	0.9%

A separate test was conducted to assess the repeatability of cross slope measurement using mobile LiDAR. The repeatability of the measurements at the 15 benchmarked locations was also studied by conducting the data collection in three different runs. Figure 5-16 shows derived cross slope measurements from the three runs. As shown in Figure 5-16 and Table 5-5, there is no significant difference observed among the different runs. The standard deviations are within 0.05% (i.e. 0.03°) at all benchmarked locations. The results show that the derived cross slope measurements using the proposed method are consistent and repeatable in different runs.

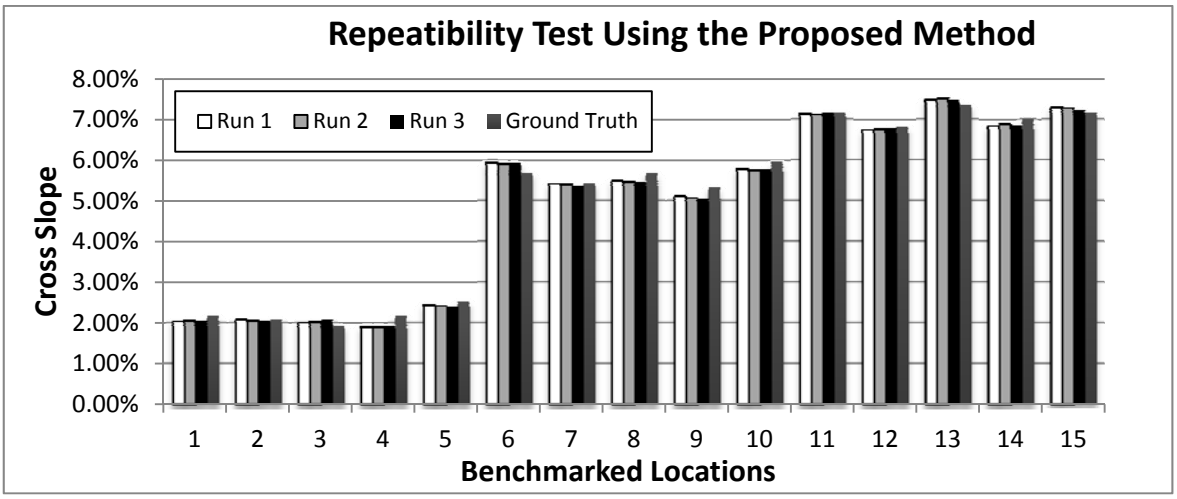

Figure 5-16 Assessment results of the cross slope measurement repeatability.

3.3. Productivity assessment

The productivity assessment for width measurements in Figure 5-17 shows that the video log image technology is the quickest to evaluate the width, followed by the mobile LiDAR technology. The airborne LiDAR technology and the aerial photo technology take considerably more time to complete the width measurements. This productivity measure correlates with the resolution of the data and, thus, the ease of identifying the measurement points in the data for measurement.

The productivity assessment for curvature measurements in Figure 5-18 also demonstrates that the GPS track technology is the most efficient and productive technology as far as time taken to measure is concerned. It takes about 62.5% less time than the next quickest technology. Video log image technology is the next quickest to evaluate curvature, followed by the mobile LiDAR technology. The airborne LiDAR technology and the aerial photo technology, again, are time-consuming to complete the width measurements. The measurement of curvature takes longer than the width measurement due to the need to measure both the chord and the offset five times for each observation.

Figure 5-17 Time taken per mile measure for all the sensing technologies evaluated for width measurements.

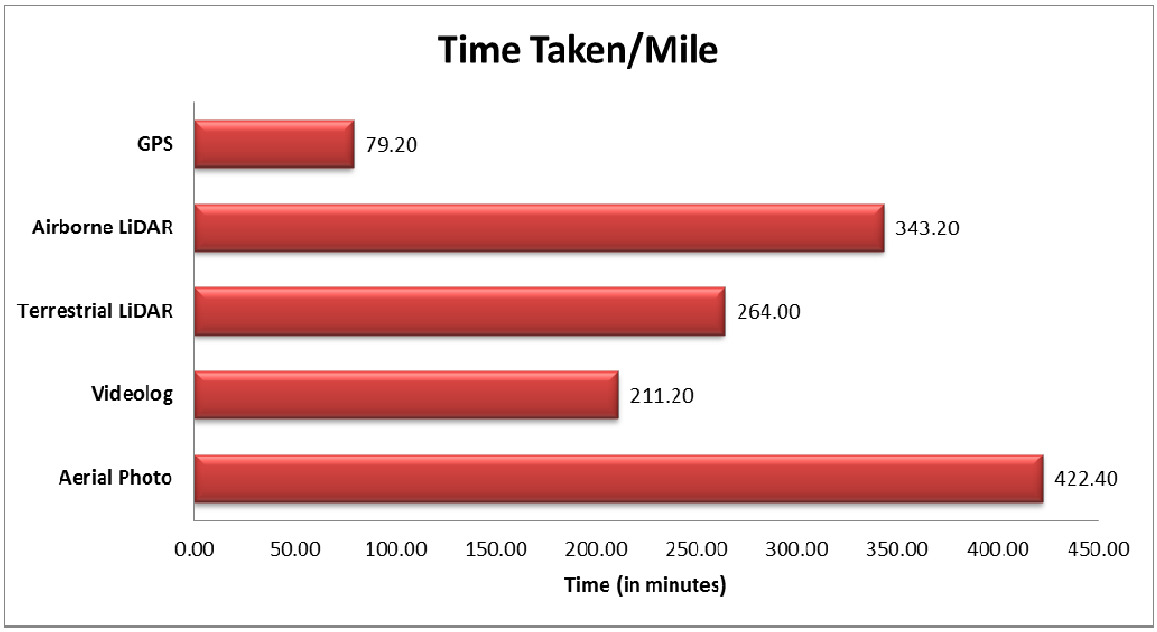

Figure 5-18 Time taken per mile measure for all the sensing technologies evaluated for curvature measurements.

The productivity assessment for cross slope measurement was conducted through a case study on I-285. The test demonstrated that the proposed method has the capability to conduct network-level analysis efficiently. The GIS-based cross slope measurement map of the 3-mile section of roadway that was studied can be derived in less than 2 man hours using the collected raw LiDAR data.

4. Findings and Recommendations

In this section, the conclusions drawn from the roadway characteristics work done are consolidated based on the understanding of the data, agency needs, and results of the validation.

4.1. Findings

4.1.1. Pavement Width

For pavement width extraction, all the sensing technologies evaluated measure the pavement width within the acceptable limit of accuracy (±1 foot).

- Mobile LiDAR technology shows the best performance in pavement width measurement in terms of accuracy (0.04% relative error), precision (±0.13%), and repeatability (0.1%

variability). Mobile LiDAR technology also demonstrates a good productivity in continuously condition pavement width measurement.

- Aerial photo and airborne LiDAR also demonstrate relatively good accuracy and precision. However, the accuracy and precision are impacted by the challenges in identifying the delineation of the road (i.e. starting and ending points for measurement) due to the limited data resolution, i.e. with the average density of 1.87 feet in the airborne LiDAR data used in this study and US-survey-feet resolution in the aerial photo data used in this study. The additional errors, compared with mobile LiDAR technology are also prone to aliasing error, and there is also the effect of obstructions. Nevertheless, both aerial photo and airborne LiDAR data have good coverage of the targeting area rather than the limited roadway area captured in mobile LiDAR technology; it is a feasible to use aerial photo and airborne LiDAR to conduct large scale measurement with a less stringent accuracy requirement, e.g. purposed land-use planning.
- Video log Image technology is fairly accurate (5.2%) and precise (±13.15%) for pavement width measurement. It also shows good repeatability (0.5% variability) in the repeatability assessment. Video log image technology also demonstrated the best productivity in extracting pavement width because it contains the best visual view to identify the measurement location and to conduct the measurement. However, the potential issue with this system is that the measurement accuracy relies on the accuracy of camera calibration, which requires rigorous computation and adjustment that might be challenging for immediate use in transportation agencies without appropriate training. In addition, the coverage of the video log image is also limited. Therefore, multiple runs and multiple cameras will be needed for a full coverage of different widths in both driving directions.

4.1.2. Horizontal Curvature

For the roadway horizontal curvature extraction exercise, all methods can be accurate (within 8% relative error) except airborne LiDAR (-51.72% relative error).

- Of all the technologies evaluated, mobile LiDAR was found to be the most accurate (-0.35%) and precise (±6.65%). Also, the continuous data with high density provides a better chance of not only measuring different curve types, but also identifying and measuring the curve transitions.

- Aerial photo can be used for large scale road curvature measurement because of the large coverage area of the data. However, as with the width measurement, its 0.5 US-survey-feet resolution and the resultant aliasing error is an issue in delineating markers.
- The failure of airborne LiDAR data used to extract curvature accurately can be attributed to its coarse resolution (1.87 feet)/ point spacing. The fact that the majority of offsets measured are less than 2 feet aggravate the shortcoming of this method.
- The video log Image technology can also measure the roadway curvature fairly accurately (5.2%) and with a relatively lower precision (±13.15%). However, there are limitations identified in video log Image technology.
- GPS Track is identified as the most efficient and productive method among other methods in this study, as it takes about 62.5% less time than the next quickest technology. It gives a good accuracy (-3.63%) and a precision (±10.76%), which is next only to mobile LiDAR technology. The whole process can be fully automated. However, there are two limitations identified for GPS track:
    - Both the repeatability and the accuracy of the method rely on how close the data collection track is to the actual pavement lane. Lane changing and vehicle maneuvering can have extensive impacts on the measurement accuracy. In addition, the accuracy also relies on the frequency and accuracy of the GPS acquisition. Although many transportation agencies collect GPS data, since the frequency and accuracy of the GPS devices in these agencies may not be comparable to the ones used in this study, the final curvature measurement could be less accurate.
    - The method still needs auxiliary data as a visual aid (i.e. video log image, GIS map, etc.) to localize the road section for analysis.

4.1.3. Cross slope

Using mobile LiDAR, the accuracy can achieves a desirable measurement with a maximum difference of 0.28% cross slope (i.e. 0.17°) and an average difference less than 0.13% cross slope (i.e. 0.08°) on the tested sections with cross slopes ranging between 1.9% and 7.2%. The acceptable accuracy is typically 0.2% (or 0.1°) during the construction quality control (FDOT, 2008). Repeatability assessment results show the proposed method can achieve good repeatability with the standard deviations within 0.05% (i.e. 0.03°) at 15 different benchmarked

locations in three different runs. The acceptable repeatability is typically 0.2% during the construction quality control. A case study conducted on I-285 shows that the continuous cross slope measurement on a 3-mile section of roadway can be derived in less than 2 man hours using the collected raw LiDAR data.

4.2. Recommendations

- Mobile LiDAR is identified as the most accurate and repeatable technology for measuring pavement width, horizontal curvature, and cross slope. It also demonstrated very good productivity in processing these geometric features using commercially available software. With the high accuracy, mobile LiDAR has the potential to be used in applications that require high accuracy, e.g. construction QA/QC. However, the initial investment and the needs for heavy data storage and processing capacity might hinder an immediate popularization of the technology in transportation agencies' practices.
- At the constraints of budget and manpower, GPS Track and video log Image technology are more feasible for use in a local agency to conduct curvature measurement for single horizontal curves. From the assessment result, these technologies can still provide a reasonable accuracy. Moreover, the light-weight processing requirement and fast processing speed make these technologies more feasible for quicker application in transportation agencies' practices. However, considering the accuracy from these technologies, applications that have less accuracy requirement, e.g. safety assessment, can be implemented first by incorporating these technologies.
- Aerial photo and airborne LiDAR technologies also demonstrated certain capabilities in extracting the three focused geometric characteristics. However, the results of the accuracy and precision of these technologies from this study do not warrant an immediate utilization in transportation agencies' practice. However, it is identified that the accuracy is highly dependent on the resolution and density of the data. Improved performance is expected if transportation agencies are able to collected aerial photo and airborne LiDAR data with higher resolution and density.
- Manual methods are used in this study to extract roadway geometry characteristics from different technologies and to conduct the assessment. There is a need to develop individual automated algorithms/methods to facilitate the process using different technologies. This

study reveals that transportation agencies can benefit from the assessed sensing technologies. They will potentially gain more benefits from these sensing technologies by incorporating automated algorithms/methods into their practices.

References

Carlson, P., Burris, M., Black, K., and Rose, E. (2005). “Comparison of Radius-Estimating Techniques for Horizontal Curves.” Transportation Research Record: Journal of the Transportation Research Board, 1918(-1), 76-83.

FDOT. (2008). “Section 330: Hot Bituminous Mixtures - General Construction Requirement.”

TxDOT. (2004). “Texas Department of Transportation Special Specification 5622 - Cross Slope Control.”

Hiremagalur, J., K. Yen, T. Lasky, and B. Ravani. (2009). “Testing and Performance Evaluation of Fixed Mobile Three-Dimensional Laser Scanning Systems for Highway Applications.” Transportation Research Record: Journal of the Transportation Research Board, Vol. 2098, No. 1, pp. 29-40.

Ibraheem, A. T., and Hammodat, W. W. (2011). “Review and Modeling the Methods of Radius-Estimating Techniques for Horizontal Curves.” ARPN Journal of Engineering and Applied Sciences, 6(12).

Souleyrette, R., Hallmark, S., Pattnaik, S., O'Brien, M., and Veneziano, D. (2003). “Grade and Cross Slope Estimation from LIDAR-based Surface Models.” University Transportation Centers Project MTC-2001-02 and CTRE Management Project 01-98.

Wang, D. (2010). “Cross Slope - Revised Specification Highlights.” State Construction Office, Tallahassee, Florida.

Chapter 6 Concrete Pavement Condition Evaluation – A Prototype GIS Application

1. Introduction

Pavement distress is one of the most critical pavement conditions affecting roadway maintenance and driving experience. With a proper monitoring system, the data of deterioration rates and extent, along with the areas needing maintenance, could be collected. Such data is of critical importance when establishing schedules for repair, estimating contract quantities, and determining the effectiveness of rehabilitation procedures. As a result, critical distresses could be discovered at early stages so that maintenance costs can be reduced to the minimum amount.

In GDOT, concrete pavement distress data are collected and managed by survey crews periodically using the Concrete Pavement Condition Survey Instruction Manual (CPACES). The data collected includes counting each distress type in different severities and providing some other text description for special notes.

Such a manual approach has proven effective, but it still suffers from several problems in both data collection and management processes. As for the data collection, a manual survey takes a long time and can be highly labor-intensive. Though guidelines have been made to define the classification of distresses, the manual data collecting process still involves high subjectivity generated from the differences in the surveyors' experience and expertise.

For the management, the data collected misses some key information, which could result weaker support for maintenance decisions. First, the survey records usually contain only mile-level count numbers without the exact location information or images of individual distresses, making them very difficult to validate and causing redundant work. For example, when a road section is rated below the criterion for slab replacement, the repairers must make additional field trips to locate the aimed distresses. Temporal comparison is also affected, as even the same number of cracks within a mile may occur in completely different areas, so that the true treatment effectiveness cannot be told. In addition, as the records accumulate in time, searching becomes more troublesome and less efficient.

Because of all the aforementioned problems, an intelligent, automatic pavement distress data collection and management tool providing highly detailed analysis is greatly needed.

Therefore, the tool should use information technology to analyze and visualize highly detailed pavement distress data; this would provide comprehensive management capacity to support roadway maintenance decisions.

The first part of this report introduces the problems in traditional manual pavement distress data collection and management systems, which explains the need for a new automatic and more comprehensive management tool. The second part introduces the key functions and the necessary preparation for the new pavement distress management application we have developed. The third part demonstrates use of the data collected from a 5-mile road section on I-16 to illustrate the application's workflow. The last part summarizes the benefits and future potential of this application.

2. Development of the GIS-Based Concrete Pavement Condition Evaluation Application

2.1. Identified needs

Roadway maintenance normally involves large amounts of financing and labor costs, which are limited resources that should only go to projects with high priority. Detailed, multi-level visualization of the distress conditions of a large roadway network provides an instant, accurate, and comprehensive impression of the potential problem locations and severity information, which helps to set project priorities and support maintenance decisions.

2.2. Data preparation and software environment set up

To use this application, some necessary preparation needs to be done first. The raw data collected needs to be processed and organized into geo-databases, and the ArcMap environment also needs to be correctly set up for the application to function properly.

2.2.1. Data Preparation

The pavement distress data are collected using 3D line laser imaging device and GPS. For each concrete slab, a pavement image file, along with an XML file storing information of distress

types, crack length, width and depth, joint location, faulting measures, and pothole properties will be provided. Based on this information, another classification algorithm is used to fine tune it into CPACES-defined distress types. Both the raw data and the processed classification information need to be stored for the application to use. A geo-database file needs to be created to accommodate the format requirement of the application. Each road section has its own table in the database; a row in each table stores all the distress information and GPS coordinates of a concrete slab and, also, provides a polyline symbol representing it on the map.

2.2.2. ArcMap Setting up

First, the user needs to establish a folder connection to the geo-database created above. For each road section table in the database, a same-name layer needs to be created for visualization. If the setup is correctly done, the user would be able to see the GPS tracks on the base map.

2.3. Key functions

2.3.1. Overall pavement condition inspection

The application provides two query methods for overall pavement condition visualization, as shown in Figure 6-1.

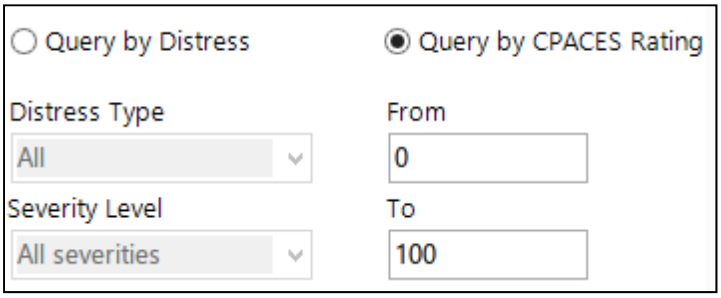

Figure 6-1 Two query methods for overall pavement condition visualization

The first method is defined by the Concrete Pavement Condition Survey Instruction Manual (CPACES), which is used by GDOT and could provide historic data for comparison. CPACES defines a rating system that corresponds to the number of occurrences of a certain distress type within a mile to a deduction value and then subtracts 100 by the total deduction to generate the final score. There are 5 major distresses defined in CPACES for concrete pavement: longitudinal crack, broken slab, faulting, shoulder distress, and spalling. A deduction table is also given to

help calculate the total deduction. The query result in this application will be presented as a colored map in ArcMap, with each mile-long section in a uniform color indicating its CPACES score level.

The second method is based on the information of individual distresses. The user could choose to view all types of distresses or just a single one, as shown in Figure 6-2. In addition, the severity option is also available to include all severities or only the ones beyond a desired level.

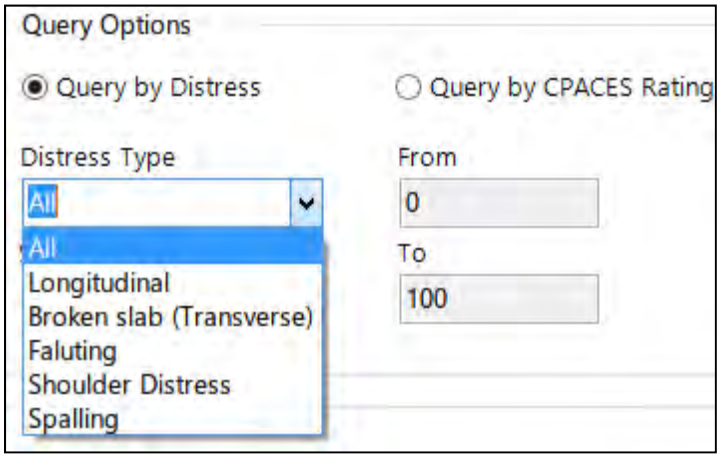

Figure 6-2 Supported concrete distress types

The query result will also be illustrated as a colored map, except the color unit section is much smaller with the length of a concrete slab. The location of each occurrence would be marked out, and the detailed distress information can be obtained by checking the property of the small sections.

2.3.2. Slab-level distress inspection

In slab-level distress inspection module, the user will be able to locate individual distresses qualified by intended filtering rules, such as certain distress types and severity levels. Search results will be listed to allow interaction and shown on the map. High definition pavement images of the distresses can also be obtained easily for validation.

2.3.3. Visualization Customization

The application also provides options for visualization customization. A user could choose survey date to inspect data collected in different times, which provides a good way to monitor

the changes of pavement distress conditions at the slab level. For the colored maps, the application provides many options, like user-defined colors that make it convenient to avoid complex situations in which using the same set colors for closely distributed roads could cause confusion.

3. Case Study: I-16

In this experimental test, we used the data collected from a 5-mile section on I-16. The data was processed and organized into a geo-database file. One of the data tables for the I-16 Eastbound road section is shown in Figure 6-3.

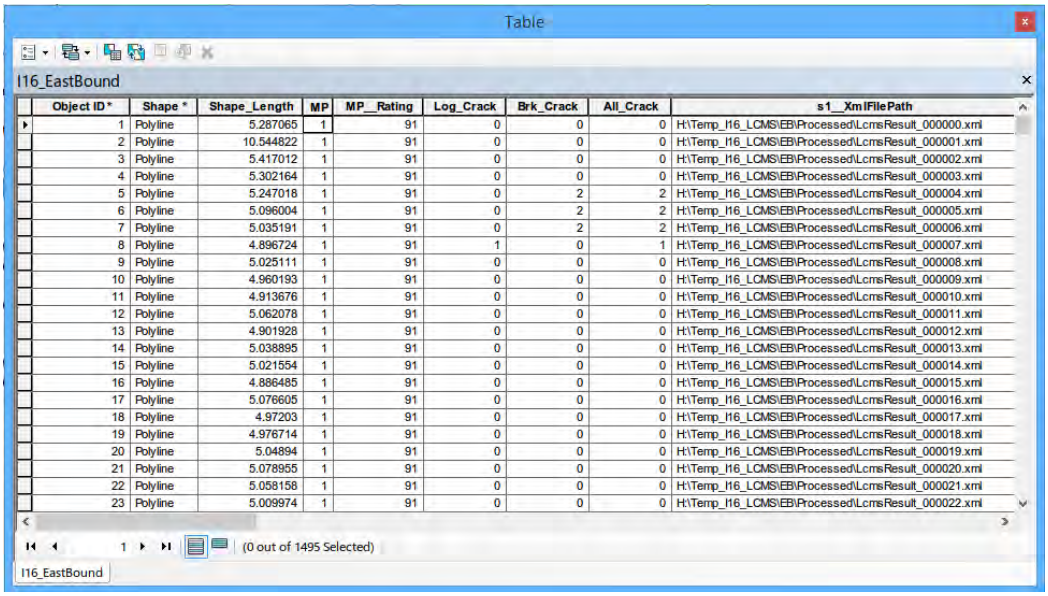

Object ID *	Shape *	Shape_Length	MP	MP__Rating	Log_Crack	Brk_Crack	All_Crack	s1__XmlFilePath
1	Polyline	5.287065	1	91	0	0	0	H:\Temp_I16_LCMS\EB\Processed\LcmsResult_000000.xml
2	Polyline	10.544822	1	91	0	0	0	H:\Temp_I16_LCMS\EB\Processed\LcmsResult_000001.xml
3	Polyline	5.417012	1	91	0	0	0	H:\Temp_I16_LCMS\EB\Processed\LcmsResult_000002.xml
4	Polyline	5.302164	1	91	0	0	0	H:\Temp_I16_LCMS\EB\Processed\LcmsResult_000003.xml
5	Polyline	5.247018	1	91	0	2	2	H:\Temp_I16_LCMS\EB\Processed\LcmsResult_000004.xml
6	Polyline	5.096004	1	91	0	2	2	H:\Temp_I16_LCMS\EB\Processed\LcmsResult_000005.xml
7	Polyline	5.035191	1	91	0	2	2	H:\Temp_I16_LCMS\EB\Processed\LcmsResult_000006.xml
8	Polyline	4.896724	1	91	1	0	1	H:\Temp_I16_LCMS\EB\Processed\LcmsResult_000007.xml
9	Polyline	5.025111	1	91	0	0	0	H:\Temp_I16_LCMS\EB\Processed\LcmsResult_000008.xml
10	Polyline	4.960193	1	91	0	0	0	H:\Temp_I16_LCMS\EB\Processed\LcmsResult_000009.xml
11	Polyline	4.913676	1	91	0	0	0	H:\Temp_I16_LCMS\EB\Processed\LcmsResult_000010.xml
12	Polyline	5.062078	1	91	0	0	0	H:\Temp_I16_LCMS\EB\Processed\LcmsResult_000011.xml
13	Polyline	4.901928	1	91	0	0	0	H:\Temp_I16_LCMS\EB\Processed\LcmsResult_000012.xml
14	Polyline	5.038895	1	91	0	0	0	H:\Temp_I16_LCMS\EB\Processed\LcmsResult_000013.xml
15	Polyline	5.021554	1	91	0	0	0	H:\Temp_I16_LCMS\EB\Processed\LcmsResult_000014.xml
16	Polyline	4.886485	1	91	0	0	0	H:\Temp_I16_LCMS\EB\Processed\LcmsResult_000015.xml
17	Polyline	5.076605	1	91	0	0	0	H:\Temp_I16_LCMS\EB\Processed\LcmsResult_000016.xml
18	Polyline	4.97203	1	91	0	0	0	H:\Temp_I16_LCMS\EB\Processed\LcmsResult_000017.xml
19	Polyline	4.976714	1	91	0	0	0	H:\Temp_I16_LCMS\EB\Processed\LcmsResult_000018.xml
20	Polyline	5.04894	1	91	0	0	0	H:\Temp_I16_LCMS\EB\Processed\LcmsResult_000019.xml
21	Polyline	5.078955	1	91	0	0	0	H:\Temp_I16_LCMS\EB\Processed\LcmsResult_000020.xml
22	Polyline	5.058158	1	91	0	0	0	H:\Temp_I16_LCMS\EB\Processed\LcmsResult_000021.xml
23	Polyline	5.009974	1	91	0	0	0	H:\Temp_I16_LCMS\EB\Processed\LcmsResult_000022.xml

Figure 6-3 I-16 Eastbound data table

Each row in this table represents a concrete slab that is shown as a polyline symbol on the map. Each column in this table represents a kind of distress property or related image file and XML file location.

After adding a folder connection and creating layers in ArcMap, as mentioned above, the user can click the button on the ArcMap toolbar to start the application. The application interface is shown in Figure 6-4.

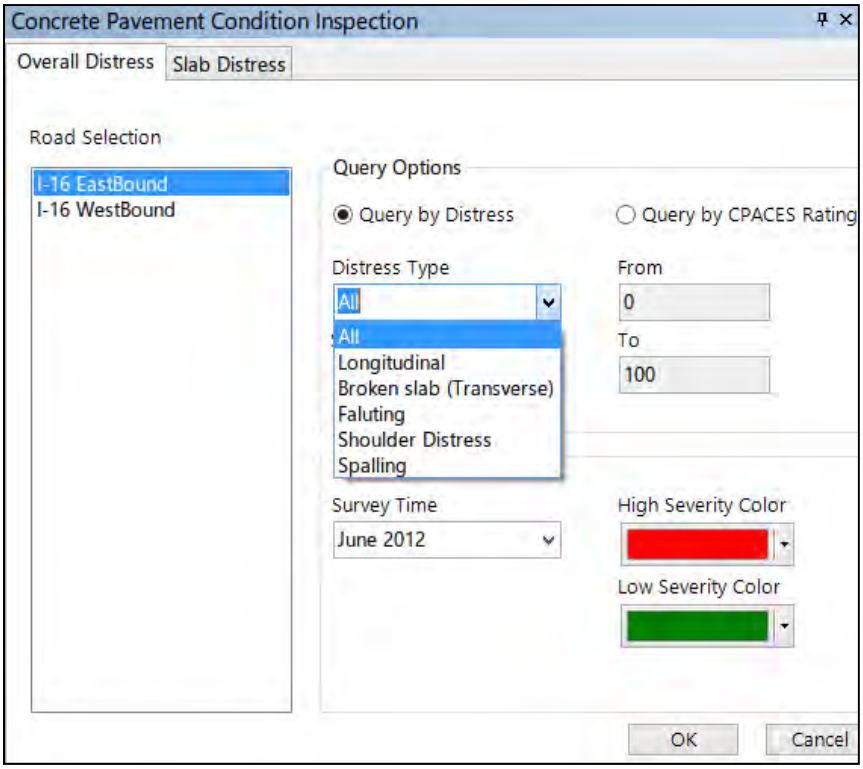

Figure 6-4 Application user interface

The road names are already loaded into the left-side box. The user could click either item to select one road or select both to show them together. In the "Query options" area, the user could choose to query by the mile-based CPACES rating or by individual crack information. If the CPACES rating option is selected for both roads, the result is shown in Figure 6-5.

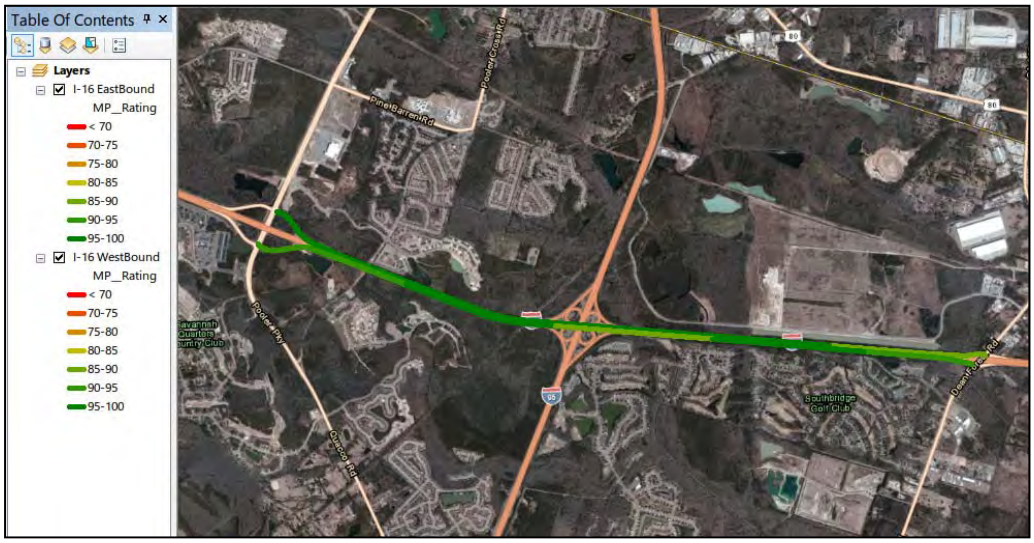

Figure 6-5 CPACES rating query result

In the map, each mile-long section is drawn in the same color. The legend for each color is shown in the left side panel. As all these sections have a score above 85, they are all in green, though it is still noticeable that some sections are in better condition than others.

If the user selected the “Query by Distress” option and further selected “All Distresses,” or “All Severities,” the map in Figure 6-6 will be generated.

Figure 6-6 Individual distress query result

The legend is also shown in the left side panel. It can be seen that the colored unit section is much smaller. In this demonstration, we only added cracking data; in the future, data of all the distress types will be supported. If the user wants to know all the detailed information about longitudinal cracks above Level 1 on I-16 Eastbound, the “Slab Distress” tab will help. As shown in Figure 6-7, the search results are listed in the left list-box with a section id number and the closet milepost numbers for each slab. By clicking a list item, the pavement image will show on the right side, and a label point indicating the slab location will show on the map instantly. The user could zoom in and out for the convenience of observation; the location of the label point will remain accurate.

4. Summary

4.1. Benefits

This application provides a customizable visualization function that creates an accurate, instant, and comprehensive impression of both overall roadway rating and the occurrences of a certain distress type. Unlike the traditional survey method, which only has a mile-level text records, this

application could locate every single distress accurately and provide slab-level, GPS-coordinated pavement distress images. These data provide all the necessary information to validate a maintenance decision that has already been made, eliminating the need for additional field trips and reducing the influence of subjectivity greatly. Different data collected from different survey times further provide an evolving image of the pavement condition, making effective examination of treatment much easier and more efficient. In addition, the powerful search function makes distress data management and utilization much more flexible and user-friendly.

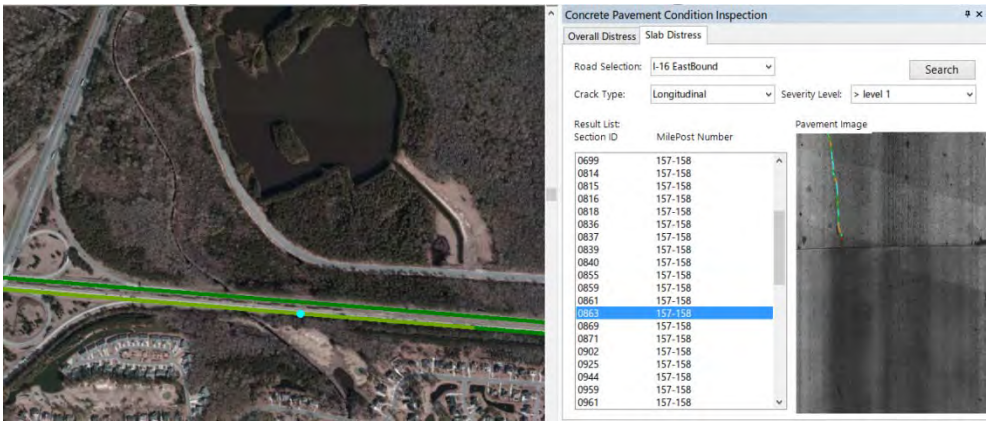

Figure 6-7 Slab distress search result

4.2. Next step

In the future, we will work with GDOT to identify a pavement section (like I-285 or I-75) that requires maintenance and rehabilitation (M&R) planning and programming and for which GIS can be used as a tool for better visualization and management. This will help implement and deploy the developed prototype GIS application. A slab-level condition trend graph function will be added to provide a more intuitive impression of the pavement condition history. In addition, other concrete distress protocols will be incorporated to support the use of agents from other states. A slab-level condition trend graph function will be added to provide a more intuitive impression of the pavement condition history.

Chapter 7 Roadway Horizontal Curve Safety Assessment – A Prototype GIS Application

1. Introduction

In this chapter, a prototype GIS-based roadway horizontal curve safety assessment application for the analysis of the adequacy of horizontal geometry design to prevent road departure is developed to demonstrate the capability of the spatial analysis using the derived sensing data. In addition, several potential applications are recommended for further development, including the adequacy of vertical geometry design and roadway drainage path control.

Section 2 introduces the developed GIS-based application. Section 3 presents a case study using the developed application and the actual data collected on I-285.

2. Development of the GIS-Based Application for Roadway Horizontal Curvature Safety Assessment

Motor vehicle accidents have brought about enormous human losses and property damages; more than one-third of crashes are related to the roadway and/or its environment. More than 25 percent of fatal crashes in the U.S. are associated with horizontal curves and an average crash rate three times higher than other types of highway segments; the vast majority of these crashes are roadway departures, so addressing the safety problem of horizontal curves is of significance (FHWA, 2010).

Traditionally, a design adequacy assessment is carried out manually; engineers take measurement using the chord length method for curvature and the digital level method for cross slope. Even so, no accuracy assessment can be conducted due to the nature of manual measurement: 1) limited number of measurements; 2) prone to measurement errors. Using the emerging LiDAR data, as validated in the previous quarter, both cross slope and curvature measurement can be conducted in a continuous manner, e.g. using an interval as small as 3 ft. In addition, because all the measurements are conducted using geo-referenced LiDAR point data, the measurements themselves are spatially ready to be integrated into a GIS application to facilitate different spatial analysis and simulations.

2.1. Roadway departure index definition

The roadway departure index (RDI) is defined as the tendency of a vehicle running out of road. It is essentially defined as the ratio between the external forces and the centripetal force. Figure 7-1 illustrates the idea of the external forces (i.e. part of the vehicle weight W and the side friction f) and the centripetal force (F_c).

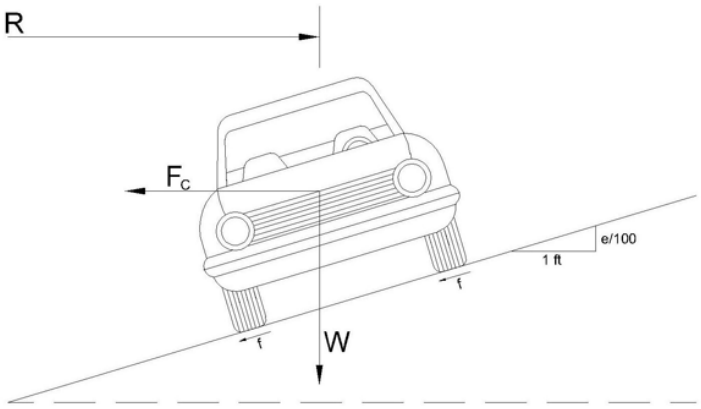

Figure 7-1 Illustration of the vehicle mechanics on sloped road section

From the laws of mechanics, the basic formula that guarantees the vehicle against side-sliding on a curve is [3]

$$\frac{e+f}{1-ef} > \frac{v^2}{gR} \qquad \text{Eq. 1}$$

where:

e = rate of roadway super-elevation, percent;

f = side friction (demand) factor;

v = vehicle speed, ft/s;

g = gravitational constant, 32.2 ft/s^2;

v = vehicle speed, mph;

R = radius of curve, ft.

Thus, the Safety Index for curves can be defined as

$$I = \frac{e+f}{1-ef} \cdot \left(\frac{gR}{v^2}\right) \qquad \text{Eq.2}$$

where the non-negative *I* is the RDI, describing the roadway departure risk for a curved segment. When *I* is greater than 1, Equation 1 is satisfied, and the curved segment can be assumed to be safe. When *I* ranges from 0 to 1, the curve is unsafe, with a high tendency of vehicle skidding. These unsafe segments with RDI much less than 1 are of most concerns for the analysts (AASHTO, 2011).

Since curve radius and cross slope (i.e. super-elevation at curved roadway) have been derived from LiDAR, as presented in the previous quarter of the project, these road geometry data can be acquired through road survey and then stored in the geo-database as static parameters. Accordingly, the variables that will affect roadway departure risks and function are the vehicle driving speed and the side friction factor. The side friction factor represents the vehicle's need for side friction, depending on the speed of the vehicle, the type and condition of the roadway surface, the type and condition of the vehicle tires, etc.

2.2. Key functions

2.2.1. Layer Selection

Layer selection in the application is designed to select the layers that correspond to the road sections for analysis. Figure 7-2 shows an illustration of the function for layer selection. When the road section for analysis is selected, the interactive map will automatically zoom-in to the scale of the selected road layer. With the visual-aid of the base map, the zoomed-in map provides users a good overview of the road section.

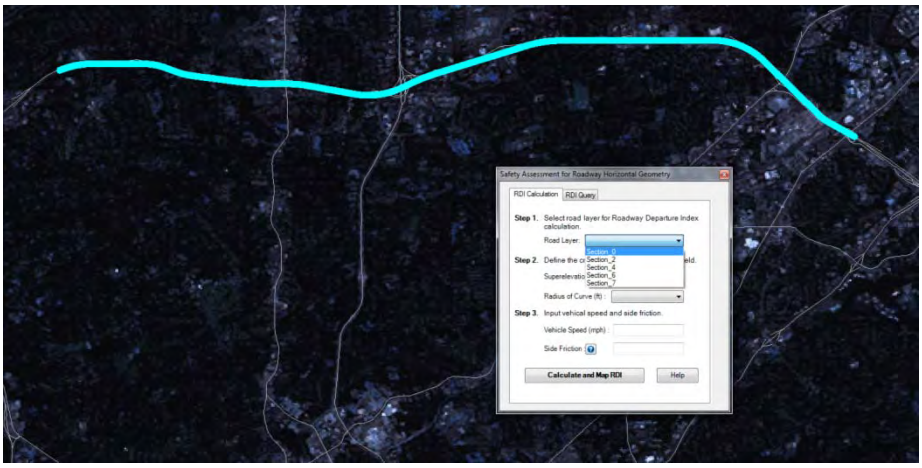

Figure 7-2 Illustration of the function for layer selection

2.2.2. RDI Computation and Mapping

After the road section is selected, the corresponding super-elevation and curve measurement derived from terrestrial LiDAR data can be retrieved from the corresponding database. To complete the RDI computation, the driving speed and side friction factor will be required to be input by the user. The user can either specify both of the values or just input one of the values, while the other value will be retrieved from the look-up table, as shown in Figure 7-3. Once all the parameters required in Equation 2 are designated, the RDI will be computed accordingly. The computation will be processed based on the minimum interval defined in the database. Figure 7-3 shows an example of the computation process. Once the computation is completed, the RDI will be visualized on the GIS map by overlapping a five-class color code on the road layer. The color-coded road layer gives a better representation of the RDI, which essentially indicates the "hotspots" that might require further investigation or even safety improvement.

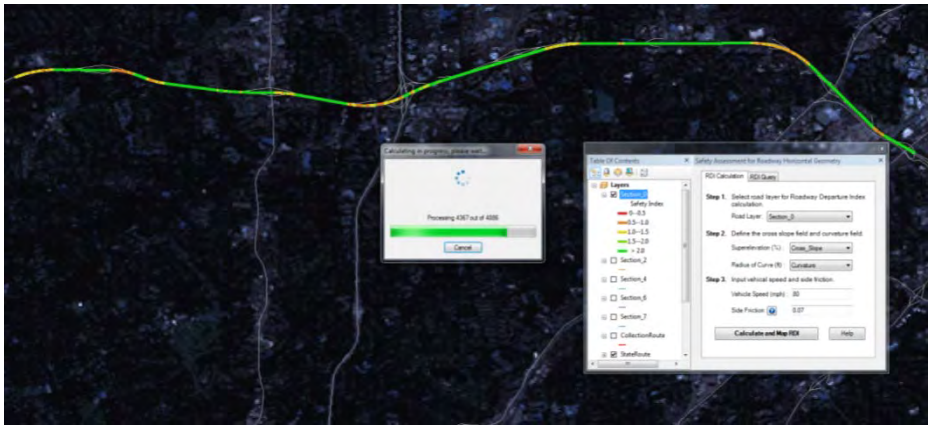

Figure 7-3 Illustration of the RDI computation and mapping function

2.2.3. RDI Query

To conduct detailed analysis and identify the actual geometry condition of the identified "hotspots," an RDI query function becomes essential. By defining the range of RDIs of interest, e.g. 0.8 to 1.2, which indicate the marginal locations with risk of roadway departure, the application will query out all the sections that meet the criteria. By further selecting the item in the list, the corresponding video log image can be retrieved for verification of the environment, e.g. pavement condition, curve, etc. Simultaneously, the selection will be displayed in the map view to indicate the spatial location of the section. Figure 7-4 shows an example of this function.

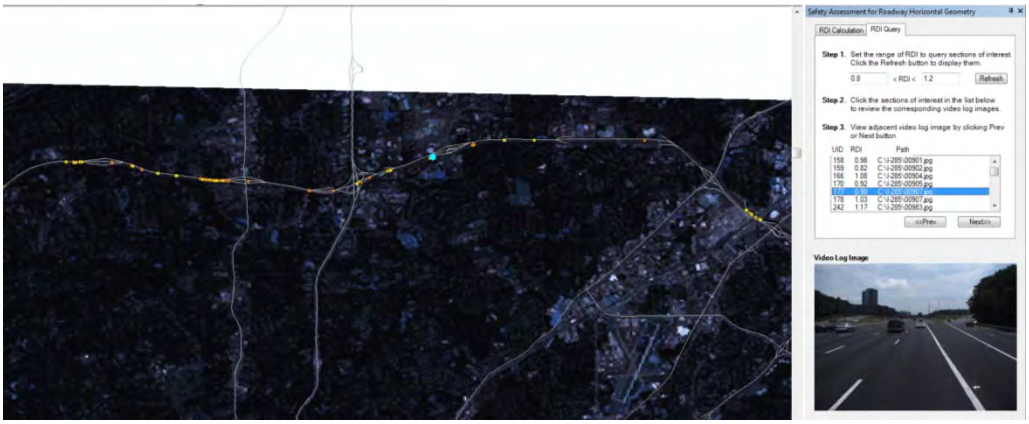

Figure 7-4 Illustration of the RDI query function with corresponding video log image

With the abovementioned key functions, the RDI can be computed, visualized, and queried according to the user's need. Besides, the functions provide necessary tools for the user to

conduct the safety analysis. The following section will use actual data collected on I-285 to demonstrate the capacity of this application

3. Case Study: I-285

Through communication with the GDOT maintenance department, it is identified that Milepost 10-10.6 on I-285 has had many road departure incidents during the past years. Figure 7-5 shows the scratches on broken concrete median caused by vehicles that ran off the road. It is important to evaluate the roadway conditions at this site to determine the causes of the accidents and to effectively take subsequent countermeasures.

Figure 7-5 Median scratches shown in the video log image

We created four scenarios for analyzing the potential factors that might lead to road departure using the developed application, including: 1) Regular case, 2) Over-speed case, 3) Wet-surface/worn tire case, and 4) Worst case.

Regular case: The average driving speed is around 65mph, while the corresponding typical surface side friction is 0.12 (AASHTO, 2004). With these input parameters and the measurements of super-elevation and curvature at this location, Figure 7-6 shows the computed RDIs and the corresponding GIS map. It is noticed that almost the entire section is green (i.e. an RDI that is greater than 2.0), which indicates a small risk in road departure.

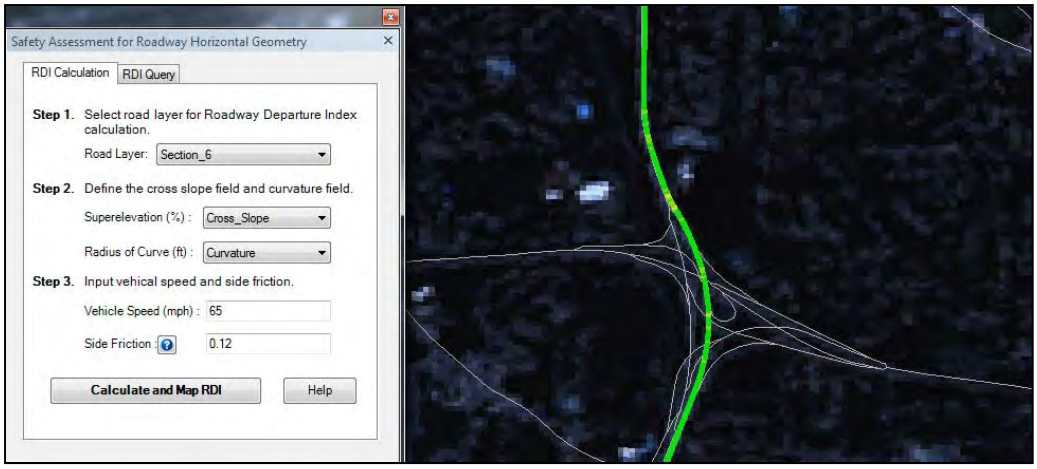

Figure 7-6 Illustration of the RDI distribution under regular case

Over-speed case: Assuming other than following the average driving speed 65mph in this section, some cars drive at extremely high speeds, e.g. 75 mph, while the surface side friction factor remains the same at 0.12. Figure 7-7 shows the computed RDIs and the corresponding GIS map. It is noticed that most of the section is green (i.e. an RDI that is greater than 2.0). However, some parts along the curve become yellow (i.e., an RDI that is between 1.0 and 1.5). This indicates that the risk of roadway departure increases as drivers unsafely accelerate, especially on curve. However, the geometry design and the side friction are still adequate to prevent road departure.

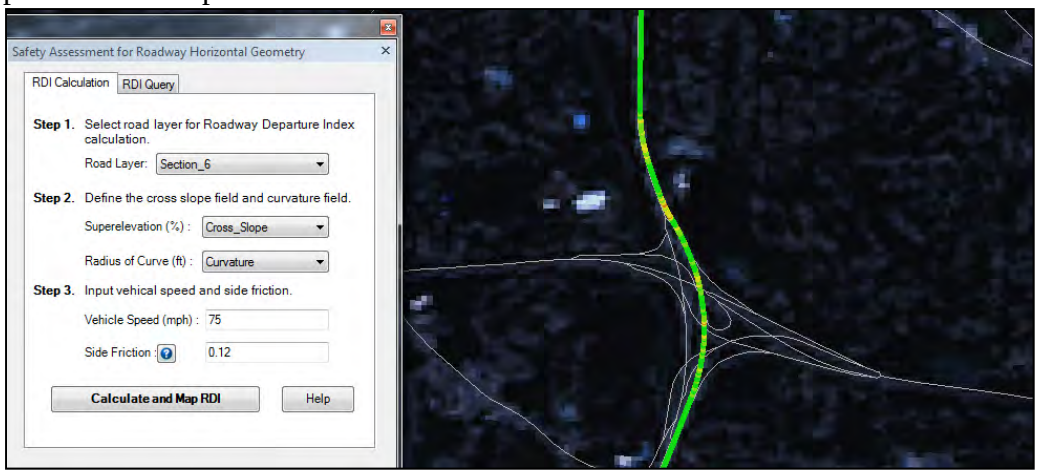

Figure 7-7 Illustration of the RDI distribution under over-speed case

Wet-surface/worn tire case: This assumes the driving speed is still 65mph in this section, but due to the rain and/or the vehicle's worn tires, the side friction factor becomes smaller, e.g. 0.09. Similar to the results as in the over-speed case, Figure 7-8 shows the computed RDIs and the

corresponding GIS map. It is noticed that most of the section is green (i.e., the RDI is greater than 2.0). However, some parts along the curve become yellow (i.e., the RDI is between 1.0 and 1.5). This indicates that the risk of roadway departure increases as the pavement surface becomes wet or the tires become worn, especially when on a curve. However, the geometry design and the side friction are still adequate to prevent road departure. In addition, by assuming different water film thicknesses and the degree of tire wearing, the detailed side friction factors can be derived more precisely so that additional scenarios can be created.

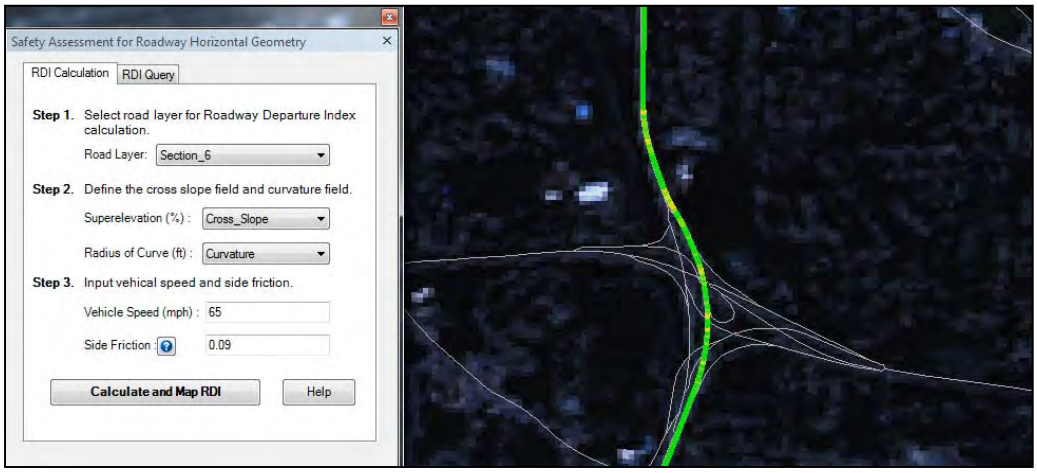

Figure 7-8 Illustration of the RDI distribution under Wet-surface/worn tire case

Worst case: This assumes a vehicle is driving at extremely high speed, e.g. 75mph, with a set of worn tires on a rainy day, so the surface side friction is 0.08. Unlike any other cases, the worst case shows several parts of the section are brown (i.e., the RDI is smaller than 1.0), as shown in Figure 7-9. This indicates that there are actually locations that might have the risk of road departure. Interestingly, one of the parts that have been identified in the map (brown in Figure 7-9) is the same location where the broken/scratched concrete medians are observed in Figure 7-9.

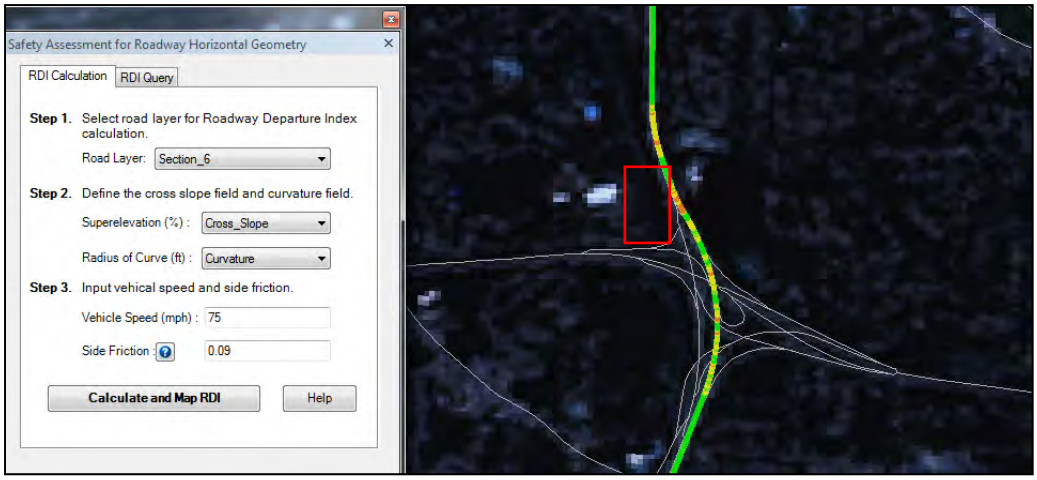

Figure 7-9 Illustration of the RDI distribution under worst case

Although this is only a simple case study to demonstrate the utility of the developed GIS-based application, it reveals the powerful capability and potential of analysis, especially with large scale spatial information and continuous geometry measurement. The developed application not only has the capability of conducting spatial analysis and what-if analysis, but it also has the capability of visualizing the "hotspots" and can potentially support maintenance planning and activities.

4. Summary

4.1.Benefits

The developed prototype GIS application for roadway horizontal curve safety assessment provides a convenient tool to help transportation agencies conduct safety analysis efficiently. The roadway geometry data derived from different emerging sensing technologies can be conveniently imported to the developed application. The operators can flexibly input parameter values based on engineering experience or official guidelines. More importantly, they can flexibly adjust the parameters under different scenarios. The whole application is developed upon the GIS framework that enables an immediate visualization of the analysis results. Additional GIS data, such as crash report data, can be seamlessly integrated with the developed application to generate more meaningful information for more in-depth safety analysis. In this study, horizontal curvature safety assessment is used to demonstrate the capability of the developed application. With additional pavement geometry data, e.g. vertical curvature, grade,

etc., the developed application can be immediately migrated to other safety elements that are important to different transportation agencies.

4.2. Next step

The High Friction Surface (HFS) program under FHWA's Every Day Count(s) (EDC) is highly interested in expanding the current prototype of this GIS application to identify and predict sites suitable for HFS treatments. Based on the current prototype GIS application, we will work with GDOT and the FHWA EDC program to develop a GIS application for "identification and prediction of sites suitable for HFS treatments" by analyzing, simulating, and visualizing roadway characteristics.

References

AASHTO. (2011). "A Policy on Geometric Design of Highways and Streets-2011 AASHTO Green Book." Washington D.C., American Association of State Highway and Transportation Officials.

FHWA. (2010). "RDs and Curves, in 2005-2008." Federal Highway Administration, Office of Safety.

Chapter 8 Standard File Exchange Format for Line Laser Imaging Data

The 3D line laser imaging technology has demonstrated its superior capability to detect cracks and other distresses because of its excellence in measuring elevation differences. Currently, many manufacturers and transportation agencies, including INO, Pavemetrics Systems Inc., WayLink Systems Corporation, Pathway Service Inc., and TxDOT, etc., have developed this type of device. In 2014, vendors, such as Fugro Roadware Inc, Mandli Communications Inc., Dynatest Consulting Inc, International Cybernetic Corporation, ARRB Group, etc., and transportation agencies, such as TxDOT, have used this pavement surface laser data to collect pavement distresses to support pavement management.

Though more and more vendors manufacture hardware and provide data services, with the growing interest from highway agencies, the data provided by most vendors is in their proprietary formats. Thus, a highway agency has to use one vendor for data collection, data processing, and information extraction. If a highway agency changes a vendor, the investment with the previous vendor has to be wasted because there is no data compatibility between the two vendors. This can adversely impact the utilization and adoption of pavement surface laser data and the line laser imaging technology because 1) a highway agency may hesitate to adopt this technology because of the potential risk of investment loss; and 2) third parties with strong data processing capabilities may have no interest to get into the market because there is no publically available data format for them to easily access the data. Thus, one of the urgent needs identified by the TAC is a standard File Exchange Format (FEF) for line laser imaging data (both 3D range and intensity data) to facilitate the utilization of line-laser imaging data. With FEF, all data providers will have the same data format and also, the ability to generate their own propriety data to protect their propriety data processing applications. Highway agencies will truly own the pavement surface laser data and have the flexibility to use different data providers and third parties for data processing. This will greatly promote the utilization of line-laser imaging data, and become a triple-win situation because highway agencies, data providers, and data processing companies can all benefit from the standard FEF. The major components of a standard FEF are proposed and presented below.

1. File Hierarchy

A line laser imaging device collects digitalized transverse profiles. These transverse profiles are stored in separate image files that are also called data frames. The size of a predefined data frame determines how many transverse profiles can be stored in one image. Thus, a survey is a continuous collection of data frames, as shown in **Error! Reference source not found.**.

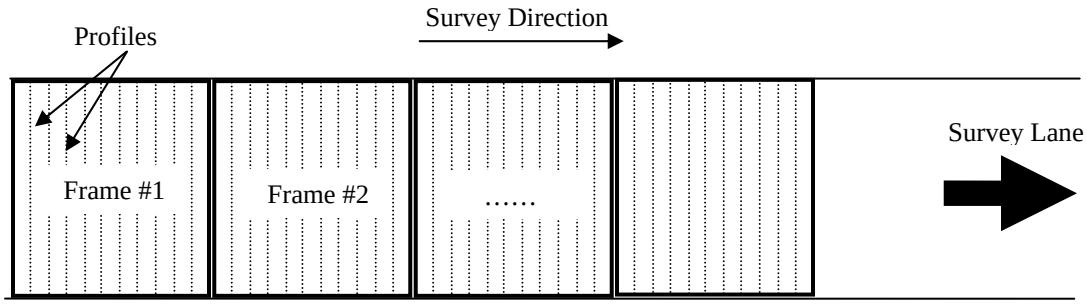

Figure 8-1 Line laser imaging data organization

In the standard FEF, each survey consists of two types of files: a single index file and many other data frame files. The index file is an XML file that describes the survey data. A data frame is a single image captured by the line laser camera. In the FEF, a data frame includes both range data and intensity data. Although the FEF can support both data types (range and intensity), the user can choose to collect and store only range data or intensity data. Within a single survey, all the files, including the index file and the data frame files should be kept within a single folder.

The most convenient layout is to have a subfolder for each individual camera in the system. If there is only one camera, the subfolder may be omitted and all the data stored in the survey folder. **Error! Reference source not found.** shows an example folder structure for a single camera. **Error! Reference source not found.** shows an example folder structure for two cameras, i.e. left and right ones at the back of sensing vehicle. Only one index file is stored in the survey folder. The subfolders for all cameras only store data frame files.

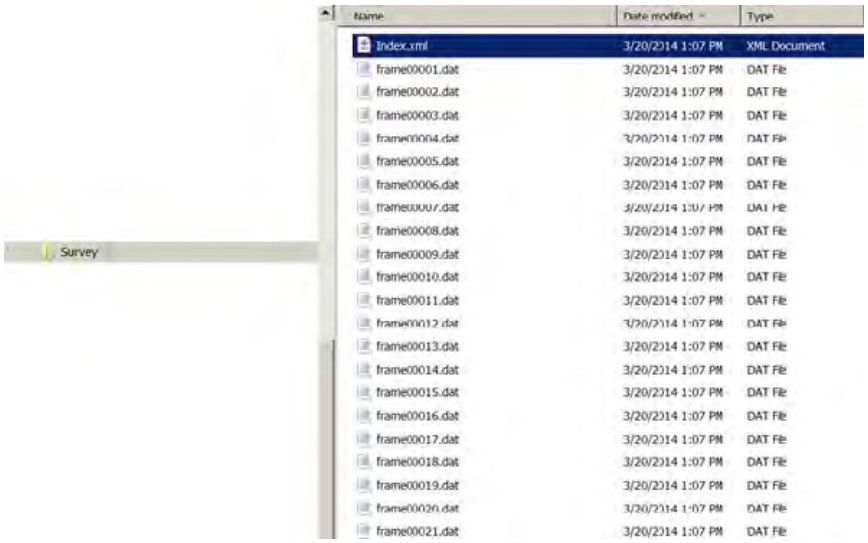

Figure 8-2 Single camera folder structure

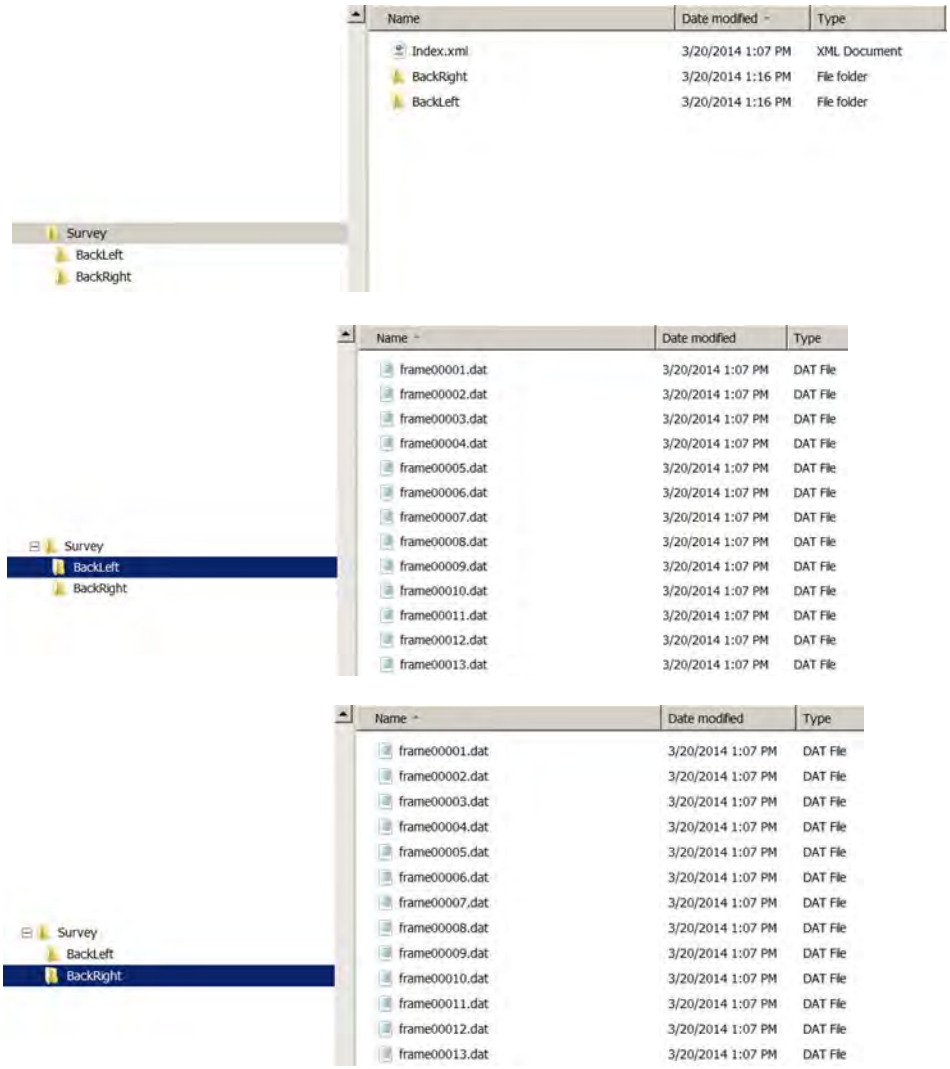

Figure 8-3 Two-camera folder structure

2. Index File

The index file consolidates all the header information from each data frame in one place that is easy to manage. It consists of three major components: general information about the survey, physical attributes of the cameras, and the location details of each data frame in the survey. The index file can be implemented as an XML file.

Error! Reference source not found. lists the major items for general survey information in the index file. Optionally, the camera information can contain the relative location of the camera to the GPS receiver.

Table 8-1 General Survey Information.

XML Tag	Type	Description
<LLCS version =“1.0”/>		XML root element name
LLCS attribute “version”	integer.integer	Format version number (Major.Minor)
<SurveyID/>	integer	A unique number that identifies a specific sequence
<SurveyDate/>	integer	Survey Date, format MMDDYYYY
<DataDepth/>	integer	Number of bytes per value
<FrameCount/>	integer	Total number of frames
<Description/>	string	User included text description
<DataFrames/>		Element to hold the collection of Data
<Cameras/>		Element to hold the collection of Camera Information

Error! Reference source not found. lists the major items for camera information in the index file. Optionally, the camera information can contain the relative location of the camera to the GPS receiver.

Table 8-2 Camera Information.

XML Tag	Type	Description
<Camera Information/>		Camera Information element name
<ID/>	integer	(Pseudo)-Unique Identifier
<Width/>	integer	Number of pixels in a row
<Height/>	integer	Number of pixels in a column
<PixelWidth/>	decimal	Physical width of pixel, in millimeters
<PixelHeight/>	decimal	Physical height of pixel, in millimeters
<RangeUnits/>	string	Unit information of range data (mm, cm, m, in, ft)
<CalibrationMethod/>	string	Calibration Method
<Description/>	string	Description

Error! Reference source not found. lists the major items for data frame information in the index file. The data frame can optionally include statistics, such as mean, min, and max, as additional fields. **Error! Reference source not found.** shows an example index file:

Table 8-3 Data Frame Information (Per Frame).

XML Tag	Type	Description
<Data>		Data Frame element name
<Path>	string	Relative path to data frame file
<Latitude>	decimal	Latitude
<Longitude>	decimal	Longitude
<Altitude>	decimal	Altitude
<Geodetic>	string	Geodetic System, e.g. (WGS-84)
<Time>	decimal	GPS Time
<Frame>	integer	Frame number within the survey
<CameraID>	integer	Camera's (Psuedo)-Unique Identifier
<HasIntensity>	True/False	Whether the data frame includes retro-intensity data
<HeaderSize>	integer	Header Size (bytes)

```
<LLCS version="1.0">
    <SurveyID>1234567890</SurveyID>
    <SurveyDate>20130729</SurveyDate>
    <FrameCount>4321</FrameCount>
    <DataDepth>1</DataDepth>
    …
    <Cameras>
        <CameraInformation>
            <ID>1234</ID>
            <Height>2048</Height>
            <Width>2048</Width>
            …
        </CameraInformation>
    </Cameras>
    <DataFrames>
        <Data>
            <Frame>1</Frame>
            <Name>data0001.dat</Name>
            <CameraID>1234</CameraID>
            …
        </Data>
    </DataFrames>
</LLCS>
```

Figure 8-4 An example index file

3. Data Frame

Each data frame is a structured binary file that includes some header information and all the data in a raster scan order. The data frame will also contain range data and may, also, contain intensity data. If a data frame contains intensity data, the range and intensity data is interleaved -

e.g. range 0, intensity 0, range1, intensity1, etc. **Error! Reference source not found.** lists the suggested header data items in a binary data frame.

Table 8-4 Data Items in Data Frame Header.

Byte Offset	Data Type	Description
0-3	char	“LLCS” Laser Line Camera System key
4	uint8	Version Major
5	uint8	Version Minor
6-13	double	Latitude
14-21	double	Longitude
22-29	double	Altitude
30-61	string	Geodetic System, e.g. (WGS-84). 32 characters
62-69	double	GPS Time
70-73	uint32	Frame number within the survey
74-77	uint32	Camera's (Psuedo)-Unique Identifier
78-79	uint16	Width of image
80-81	uint16	Height of image
82-85	single	Physical pixel size, width in mm
86-89	single	Physical pixel size, height in mm
90-93	uint32	Survey ID
94	uint8	Whether the data frame includes range and retro-intensity (1), or just range data (0)
95	uint8	Data Depth; number of bytes per value
96-103	double	Range minimum
104-111	double	Range maximum
112-113	uint16	Header Size in bytes. This value has to be at least 114.
114 - (HeaderSize-1)		Additional User Data
HeaderSize		End of File (EOF)

After the header, the data follows in row-major order. The range can be calculated as follows:

$$range = min + \left(\frac{value}{2^{DataDepth} - 1}\right) * (max - \min)$$

If there is intensity data, then the normalized intensity value is:

$$intensity = value/(2^{DataDepth} - 1)$$

4. Summary

This chapter suggested a standard File Exchange Format (FEF) for line laser imaging data, including both 3D range and intensity data. Currently, it is difficult for a highway agency, who owns the line laser imaging data, to extract useful decision-support information because of the lack of a standard FEF. The data in a proprietary format can only be processed by the vendor who provides the data collection service. This largely limits the use of line laser imaging data because third party algorithms cannot be used for data extraction. This study suggested a standard FEF that can be implemented by vendors who provides data collection services. Thus, a highway agency will have the flexibility to use a third party for data processing. Also, data collected by different vendors can be easily combined and reused. This will significantly save agencies' cost and minimize the risk of not being able to use the collected data. In addition, interested third parties can focus on developing algorithms and applications for data processing and extraction without the restrictions of having to use a specific proprietary data format or developing their own hardware and data format. Although an initial attempt has been made to develop a standard FEF in this study to address this urgent need, a follow-up study is recommended to refine and implement the FEF by working closely with transportation agencies, manufacturers, and service providers who are developing and using line laser imaging data. To make the data quality consistent and adequate for highway agencies' different applications, which is provided from different vendors and at different times, a standard calibration procedure is also needed. In addition, a suitable data compression method is required along with the suggested FEF, which needs further study.

Chapter 9 Potential Applications and Implementation

The objective of this research project is to scientifically validate the use of CRS&SI technologies for improving the inventory, condition assessment, and management of pavement assets and roadway geometric characteristics. The sensing devices chosen for the validation purposes do not imply any particular endorsement. With the rapid advancement of sensing technologies, end users should explore the most suitable devices and services in the market if they plan to apply such sensing technologies to pavement condition assessment and roadway geometric characteristics data collection. Some potential applications are recommended in this chapter. They can be implemented through the use of 3D line laser imaging, video log imaging, or mobile LiDAR technologies.

As a result of the comprehensive study of the six research focuses, the potential applications of 3D line laser imaging technologies, video log imaging, and mobile LiDAR are suggested below.

- **Standard File Exchange Format for Line Laser Imaging Data**

  Line laser imaging technology has been validated in this study and has demonstrated that it is promising for pavement crack detection and classification. In Chapter 8, a standard FEF was proposed for promoting the utilization of line laser imaging technology in highway agencies' practice. A follow-up research is needed to further refine and implement the proposed standard FEF by closely working with transportation agencies, hardware manufacturers, and service providers who are developing and using line laser imaging data so they can be used broadly. As an initiative, we will team up with several highway agencies and data providers 1) to address highway agencies' need; 2) to facilitate data providers' data conversion; and 3) to fine-tune the data format. It is hoped the proposed FEF can eventually become an ASTM or AASHTO standard that can be used by all data providers.

- **Automatic Asphalt Pavement Crack Classification**

  Chapter 2 validated the algorithms, previously developed by the PI, for automatic asphalt pavement crack classification using GDOT's pavement condition survey protocol. Two of the most occurring crack types, load cracking and block cracking, were evaluated. The algorithms can be further implemented in a software program and immediately used in

GDOT's pavement condition survey practice. This will significantly save the effort of manual field survey, improve workers' safety, and make it possible for conducting surveys on heavily trafficked highways, such as I-285 in Atlanta. An outreach effort is recommended to deploy the technologies, in a separate project, by working with GDOT to conduct a cost effective crack survey for statewide interstate highways (more than 2,500 survey miles), using the developed technology. The survey results will be directly fed into GDOT's current pavement management system.

The automatic crack classification algorithms will also be refined for GDOT's use and adapted to other state DOTs. We will first work with the Florida Department of Transportation (FDOT) to test the automatic crack classification application using FDOT's pavement condition survey protocol.

- **Automatic Concrete Pavement Distress Detection**

  In Chapter 3, extensive validation has been done for concrete pavement distress detection using pavement surface laser data. These distresses include faulting, cracking, spalling, and shoulder joint distress. Among these distresses, automatic faulting measurement shows very promising results, which can be further implemented.

  The Georgia Tech research team will work with GDOT to implement the automatic concrete pavement faulting measurements using pavement surface laser data. The measurements will be conducted on statewide interstate highways, and the results will be put into GDOT's current pavement management system.

- **Roadway Geometric Characteristics Data Collection using Sensing Technologies**

  Roadway geometric characteristics, such as pavement cross slopes, roadway curvatures, and pavement widths, are critical for roadway operational quality and safety. Chapter 5 validated the feasibility of collecting roadway geometry data using various sensing technologies, such as aerial photo, airborne LiDAR, mobile LiDAR, video log images, and GPS tracks. Based on the data collection efficiency and accuracy validated in this chapter 5, highway agencies can select the best method for them by considering both cost and application needs. A separate study to develop a performance matrix based on different data utilization purposes

(e.g. planning, design, construction, etc.) and input provided by transportation agencies is recommended. It is also recommended that automatic methods be developed to better collect roadway geometry data.

The PI has been invited to present the corresponding research findings in several national-level meetings and conferences, including FHWA Every Day Count (EDC), American Traffic Safety Services Association (ATSSA) High Friction Surfacing Council, and FHWA Safety Analyst. These agencies are showing great interest in the technologies we have tested and validated. An outreach effort is recommended by working with GDOT and/or FHWA, in a separate project, to utilize these emerging technologies to cost effectively extract roadway characteristics for roadway safety analysis and safety improvement (e.g. identifying the locations for High Friction Surface Treatments), for SafetyAnalyst, and for the Model Inventory of Roadway Elements (MIRE), using the validated emerging technologies**.**

- **GIS Applications for Concrete Pavement Condition Monitoring and Horizontal Curve Safety Assessment**

  A GIS platform is useful for integrating various spatial and non-spatial data sources and assisting in highway agencies' decision-making process. Chapters 6 and 7 present two prototype GIS-based applications for concrete pavement condition monitoring and roadway horizontal curve safety assessment. These two prototype applications were developed as ESRI ArcMap add-ins and can be easily used by highway agencies. By demonstrating these two prototype GIS applications, we will closely work with GDOT to collect their comments based on their practical applications. Then, refinement will be made to meet GDOT and other state DOTs' need. The applications will also to be extended to local agencies, such as county and city public works, to assist them in their decision-making processes.

  The High Friction Surface (HFS) program under FHWA's EDC is highly interested in expanding the current prototype of this GIS application to identify and predict sites suitable for HFS treatments. Based on the current prototype GIS application, we will work with GDOT and the FHWA EDC program to apply the GIS application for "identification and prediction of sites suitable for HFS treatments" by analyzing, simulating, and visualizing roadway characteristics.

Chapter 10 Conclusions and Recommendations

Through the study of six research focuses, this research project scientifically validated the use of CRS&SI technologies, including 3D line laser and mobile LiDAR, to improve the inventory, condition assessment, and management of pavement and roadway characteristics asset. The following summarize the major research findings and also recommend the future study.

1. Conclusions

The following conclusions are categorized in terms of seven research focuses.

- **Research Focus #1: Automatic asphalt pavement crack classification**

  This research focus validated the performance of an automatic crack classification algorithm developed by PI previously, using 3D line laser imaging data (for clarity's sake, called pavement surface laser data hereafter). The algorithm is based on a multi-scale Crack Fundamental Element (CFE) model and uses the crack detection results, i.e. crack maps, as inputs, which have been validated in RS-GAMS Phase 1. The classification of two most commonly occurring cracks, load cracking and block cracking defined in the Georgia Department of Transportation's (GDOT) pavement distress survey manual, Pavement Condition Evaluation System (PACES), were implemented, tested, and validated. The promising results demonstrated that the algorithm is capable of transforming the raw sensing data and the detected crack maps into useful decision-support information, including crack types, severity levels, and extents.

  In the first test set, the selected pavement surface laser data (the pavement surface laser data is stored and compressed in 1,069 images; each image covers about 5-meter long and 4-meter wide of the roadway section) was reviewed by GDOT pavement engineers to establish the ground truth. Then, the ground truth was compared with the automatically classified results. Based on GDOT's defined distresses, the algorithm showed an accuracy of 92.2% on classifying load cracking in four severity levels and 98.1% on classifying block cracking in three severity levels. In the second test set, ten 100-ft test sections were selected on State Route (SR) 236, SR 275, and SR 67 in Georgia. In each test section, GDOT pavement engineers visually identify the crack types, severity levels, and extents in field, which was

used as ground truth. Among ten test sections, four of them were surveyed by accurate measurements using a measuring wheel, while the other six sections were surveyed by visual estimation following GDOT's current survey practices. Then, comparison was made on deducts derived from the automatic crack classification and the field visual survey. For the wheel-measured sections, the average absolute difference of total deducts was 3.25 out of 100 (a pavement rating is between 0 and 100), and for the visually-estimated sections, the average absolute difference was 5 out of 100. Both differences were within the error tolerance based on GDOT's current practice (5 out of 100).

The validation results show that the use of pavement surface laser data and the corresponding algorithm could improve the productivity and efficiency of collecting decision-support information needed in existing pavement management system. Moreover, the fine-grained sensing data also opened the opportunity to improve existing pavement management by adding more detailed decision-support information that cannot be acquired before though further research is needed to develop new applications.

- **Research Focus #2: Concrete pavement distress detection**

  This research focus validated the detection and measurements of various concrete pavement distresses, including cracking, faulting, spalling, and shoulder joint distress using pavement surface laser data. The validation results demonstrate the potential of using pavement surface laser data for automatically detecting distresses in concrete pavements. The test sites were selected on interstate highways I-16 and I-516.

  The validation of concrete pavement cracking detection using pavement surface laser data showed acceptable performance. The automatic crack detection results were compared to the manually digitized ground truth using a buffered Hausdorff scoring method that was developed in RS-GAMS Phase 1. The results showed that detection of cracks on I-516 (mainly longitudinal cracks) is accurate and robust; however, the detection of cracks on I-16 (mainly transverse cracks) is not as good as the one on I-516. The larger data acquisition interval along the driving direction, which was about 5 mm, might be the reason that some transverse cracks cannot be captured by pavement surface laser data. In comparison, the transverse laser data resolution is about 1 mm, which can better capture the longitudinal

cracks. Limited to the laser data resolution, hairline cracks (thinner than 2 mm) were still challenging for automatic detection.

The validation of concrete joint faulting measurement showed that it is very feasible to use pavement surface laser data for collecting faulting data at highway speed. Using the regression-based method, the automatic faulting measurements were consistent with manually measured ground truth using the Georgia Faultmeter in both well-controlled lab test and the field test.

The accuracy of automatic spalling detection varied for different sizes of spalling. Spalling with widths greater than 90 mm can be successfully detected; the detection accuracy was reduced, but still acceptable for the ones between 50 and 90 mm wide, while it was hard to detect when the width was less than 50 mm. Though some small spallings were not successfully detected, they can be clearly observed on the laser data. Thus, the automatic detection algorithm could be further improved to handle such cases.

Since there is no dedicated application that is commercially available for shoulder joint distress detection, we explored the feasibility of using an automatic spalling detection algorithm to detect shoulder joint distress. The larger extent and depth of shoulder joint distress make them distinctive on laser range data and easier to detect. On the selected representative cases, the automatic detection results were visually consistent with field observation. However, it should be noted that due to the transverse coverage of the current pavement surface laser data (about 4 meters), the shoulder area might be missed when the vehicle wanders. In addition, a specific shoulder joint distress detection algorithm is needed to further ensure an accurate and robust detection.

- **Research Focus #3: Pavement marking condition assessment**

This research focus was to establish the correlation between the retroreflectivity measured by handheld retroreflectometer and the retro-intensity acquired from LiDAR point cloud. Establishing a reliable correlation is the key step for assessing pavement marking retroreflectivity conditions using a mobile LiDAR. In this preliminary study, thermoplastic and waterborne paint were selected, which are the most commonly used pavement marking

materials. Test sites were selected on Ferst Drive, Hemphill Avenue, and 17th Street on/near the Georgia Tech campus.

It was discovered that the retro-intensity values acquired from mobile LiDAR are not sensitive to ambient temperatures, with an average standard deviation less than 0.0041. The retro-intensity acquired from mobile LiDAR held good repeatability on the tested thermoplastic and waterborne materials with an average standard deviation of 0.0044.

There was an exponential correlation between retroreflectivity and retro-intensity with an R-square of 0.9525 for thermoplastic and 0.9267 for waterborne paint. The correlation between retroreflectivity and retro-intensity might be sensitive to different bead formulas of the pavement marking material. Separate correlation curves might be needed not only for different pavement marking material category, e.g. thermoplastic, waterborne, etc., but also for different bead formulas in the same material category. Based on the correlation results, a preliminary retro-intensity threshold corresponding to the minimum retroreflectivity (100 mcd/m^2/lux) defined in the MUTCD could be defined as 0.4263, with a 95% confidence interval ranging from 0.4035 to 0.4505 for thermoplastic and 0.3521, with a 95% confidence interval ranging from 0.2973 to 0.4264. Using the established correlations, a mobile LiDAR-based pavement marking retroreflectivity condition assessment method can be further developed.

- **Research Focus #4: Extraction of roadway geometric characteristics including cross slope, horizontal curvature, and pavement width**

  This research focus validated the accuracy, repeatability, and productivity of extracting roadway geometric characteristics, including pavement cross slopes, roadway horizontal curvatures, and pavement widths, using various sensing technologies, such as aerial photo, airborne LiDAR, mobile LiDAR, video log images, and GPS tracks. The measurement accuracy, repeatability, and productivity were evaluated for each pair of data type and technology.

1) Cross Slope

Mobile LiDAR is the only feasible technology for cross slope measurement. Using mobile LiDAR, the measurement achieved a desirable accuracy with a maximum difference of 0.28% cross slope (i.e. 0.17°) and an average difference less than 0.13% cross slope (i.e. 0.08°) on the tested sections with cross slopes between 1.9% and 7.2%. The acceptable accuracy is typically 0.2% (or 0.1°) during the construction quality control. Repeatability assessment results showed the proposed method can achieve a good repeatability with the standard deviations within 0.05% (i.e. 0.03°) at 15 different benchmarked locations in three different runs. The acceptable repeatability is typically 0.2% during the construction quality control. A case study conducted on I-285 showed that the continuous cross slope measurement on a 3-mile section of roadway can be derived in less than 2 man-hours using the collected raw mobile LiDAR data. In summary, mobile LiDAR demonstrated to be very promising for conducting pavement cross slope measurements.

2) Horizontal Curvature

Five technologies, including mobile LiDAR, GPS tracks, video log images, airborne LiDAR, and aerial photos, were evaluated for roadway horizontal curve measurements. Mobile LiDAR was found to be the most accurate (-0.35%) and precise (±6.65%) The dense LiDAR points also provide a better chance for measuring different curve and identifying and measuring the curve transitions. Aerial photo can be used for large-scale roadway curvature measurement because of the large area coverage. However, its 0.5 US-survey-feet resolution and the resultant aliasing error is an issue in delineating markings. Airborne LiDAR cannot achieve acceptable measurement accuracy because the LiDAR point spacing was about 1.87 feet and the majority of tested roadway curvature offsets were less than 2 ft, which makes it difficult to accurately measure curvature. The video log Image technology can also measure the roadway curvature fairly accurately (5.2%) with a relatively lower precision (±13.15%). GPS Track was identified as the most efficient and productive method in this study, and it took about 62.5% less time than the next quickest technology. It provided good accuracy (-3.63%) and a precision (±10.76%), which is only next to mobile LiDAR technology. However,

both the repeatability and the accuracy of the GPS track method relied on how close the data collection track is to the actual pavement lane. GPS data can be easily acquired, and the curve computation process is straightforward and can be fully automated. Thus, this method is very promising for highway agencies' practical use.

3) Pavement Width

Mobile LiDAR technology showed the best performance in pavement width measurement, in terms of accuracy (0.04% relative error), precision (±0.13%) and repeatability (0.1% variability). Mobile LiDAR technology, also, demonstrated good productivity in continuous pavement width measurement. Aerial photo and airborne LiDAR demonstrated relatively good accuracy and precision. However, the accuracy and precision were impacted by the difficulties in identifying the delineation of the road (i.e. starting and ending points for measurement) due to the limited data resolution, i.e. with an average density of 1.87 ft in the airborne LiDAR data used in this study and 0.5 US-survey-feet resolution in the aerial photo data used in this study. The effect of obstruction was also a factor that affects the measurement accuracy. Nevertheless, because both aerial photo and airborne LiDAR data have good area coverage in comparison to the limited roadway area captured by mobile LiDAR, they are feasible methods for conducting large-scale measurement with a less stringent accuracy requirement, e.g. for land use planning purposes. Video log image technology was fairly accurate (5.2%) and precise (±13.15%) for pavement width measurement. It also showed good repeatability (0.5% variability) in the repeatability assessment. Video log image technology also demonstrated the best productivity in measuring pavement width because it contains the best visual view to identify the measurement location and to conduct the measurement. However, the potential issue with this method is that the measurement accuracy relies on the accuracy of camera calibration, which requires rigorous computation and adjustment, which might be challenging for immediate use in transportation agencies. In addition, the coverage of the video log image is also limited. Therefore, multiple runs and multiple cameras will be needed for full coverage of different widths in both driving directions.

- **Research Focus #5: Two prototype GIS-based asset management and decision support systems for an concrete pavement condition evaluation and an roadway horizontal curve safety assessment**

  This research focus developed two prototype GIS-based applications to demonstrate the capabilities of using GIS as a platform to integrate different data sources and support various decision makings.

  The first prototype GIS application was to expedite concrete pavement condition evaluation. This application provided an adjustable visualization function that creates an accurate, instant, and comprehensive understanding of both overall roadway rating and the occurrences of a certain type of distress. Unlike the traditional survey method, which only has tabular data for project-level or segment-level pavement conditions, this application can accurately locate every single distress and provide slab-level spatial-referenced pavement distress images. These data provide all the detailed and necessary information to validate a maintenance decision, eliminating the need of additional field trips and greatly reducing the influence of subjectivity. Different data collected from different survey times (e.g. quarterly or annually) further provide an evolving image of the pavement condition, making effectiveness examination of treatment much easier and more efficient. In addition, the powerful search function makes distress data management and utilization much more flexible and user-friendly.

  The second prototype GIS application was to perform roadway horizontal curvature safety assessment. This application provides a convenient tool to help transportation agencies efficiently conduct roadway safety analysis. The roadway geometry data derived from different emerging sensing technologies can be conveniently imported to the developed application. The operators can flexibly input parameters based on engineering experience or official guidelines. More importantly, they can flexibly adjust the parameters under different analysis scenarios. The application was developed upon the GIS framework, which enables an immediate visualization of the analysis results. Additional GIS data, such as crash report data, can be seamlessly integrated with this application to generate more meaningful information for more in-depth safety analysis. In this study, horizontal curvature safety

assessment was used to demonstrate the capability of the developed application. With additional pavement geometry data, e.g. vertical curvature, grade, etc., the developed application can be immediately migrated to other safety elements that are important to different transportation agencies.

- **Research Focus #6: Standard file exchange format for line laser imaging data**

  This research focus suggested a standard File Exchange Format (FEF) for pavement surface laser data, including both 3D range and intensity data. Currently, it is difficult for a highway agency, who owns the line laser imaging data, to extract useful decision-support information because of the lack of a standard FEF. The data in a proprietary format can only be processed by the vendor who provides the data collection service. This largely limits the use of line laser imaging data because third party algorithms cannot be used for data extraction. This study suggested a standard FEF that can be implemented by vendors who provides data collection services. Thus, a highway agency will have the flexibility to use a third party for data processing. Also, data collected by different vendors can be easily combined and reused. This will significantly save agencies' cost and minimize the risk of not being able to use the collected data. In addition, interested third parties can focus on developing algorithms and applications for data processing and extraction without the restrictions of having to use a specific proprietary data format or developing their own hardware and data format. Although an initial attempt has been made to develop a standard FEF in this study to address this urgent need, a follow-up study is recommended to refine and implement the FEF by working closely with transportation agencies, manufacturers, and service providers who are developing and using line laser imaging data. To make the data quality consistent and adequate for highway agencies' different applications, which is provided from different vendors and at different times, a standard calibration procedure is also needed. In addition, a suitable data compression method is required along with the suggested FEF, which needs further study.

2. Recommendations

The performance of the above six research focuses aimed at bridging the gap between the state-of-the-practice CRS&SI technologies and the transportation agencies' practices; it also aimed at validating and promoting the use of technologies to improve the transportation asset data collection, condition assessment, and management. The following suggest the future research and implementation:

- With the promising results from the automatic asphalt pavement crack classification for load cracking and block cracking, it is recommended to extend the automatic classification to other types of distresses as defined in GDOT pavement distress manual. In addition, the algorithms can be easily extended to other crack survey protocols used by different state highway agencies because of the flexibility provided by the crack CFE model.

  The validated results of automatic cracking classification for load cracking and block cracking can be implemented in GDOT's pavement condition survey practice. Since these are the two major crack types in Georgia, it can dramatically save the field survey effort and improve the data quality and coverage. The Georgia Tech research team will work with GDOT to select large-scale roadways for testing. The results will be fed into GDOT's current pavement management system.

- The validation results for automatic concrete pavement faulting measurements showed very good consistency with manual measurements using a Georgia Faultmeter. A large-scale pilot study with a state DOT, e.g. GDOT, is suggested to automate the network-level faulting measurements. This can significantly improve the productivity, data accuracy, and data coverage.
- The concrete pavement crack detection shows promising results. However, it is difficult to detect hairline, transverse cracks due to the relatively coarser data resolution at the driving direction using the current line laser imaging device. Thus, to capture hairline cracks, the data capture frequency and resolution of a line laser imaging device needs to be further improved. In addition, to automate the crack evaluation for concrete pavements, automatic crack classification algorithms need to be developed, which can be based on the work we have done for asphalt pavements.

- New algorithms need to be developed because the automatic detection for concrete spalling doesn't work well on those with width less than 50 mm. In addition, new algorithms are needed for automatic shoulder joint distress detection.
- The pavement marking validation results indicate that pavement marking retroreflectivity conditions could be measured and evaluated using mobile LiDAR that can be operated at highway speed. However, the testing samples in this research project are limited. It is suggested that large-scale testing on more marking materials be conducted before it can be implemented.
- The validation results for roadway geometric characteristics data extraction can be used by state DOTs to select proper sensing technologies in considering data accuracy requirements and measurement productivity. Since horizontal curvatures and pavement cross slopes are important factors for roadway safety, a large-scale pilot study with a state DOT, e.g. GDOT, is suggested to automate the data collection procedures.
- A pilot study with a state DOT, e.g. GDOT, is suggested as a way to implement the two prototype GIS applications for concrete pavement condition evaluation and roadway horizontal curve safety assessment by integrating various large-scale data sources to support state highway agencies' decision making. The developed prototype GIS applications can also be useful for local transportation agencies (counties and cities) because of their limited resources to manage pavement condition data and conduct roadway safety analysis.
- With the urgent need of fully utilizing line laser imaging data for extracting useful decision-support information, a follow-up study is recommended to refine and implement the suggested standard FEF by closely working with selected transportation agencies, hardware manufacturers, and data collection service providers.

Appendix I: Specifications for 3D Line Laser Imaging System

Laser Profiler (2 Per System)

Feature/Specification	Value	Notes
Laser class	3B (IEC) IIIb (FDA)	IEC60825-1:2001 21CFR 1040.10 and 1040.11
Wavelength	808 nm ± 3nm	Continuous, infrared (invisible)
Enclosure	IP-65 NEMA 4	IEC 60529:2001-02
Sampling rate	5600 Hz	configurable
Depth range of operation	250 mm	configurable
Transversal resolution	4160 points	2080 point per sensor
Vehicle speed	0-100 km/h	
Transversal field-of-view	4 m	at nominal height
Nominal depth precision	± 0.5 mm	
Transversal accuracy	± 1 mm	
Dimensions	137mm x 421mm x 261 mm	25.4mm = 1inch
Weight	10 kg	
Electrical interface		
Input voltage	12 VCC	
Operation Current (AC)	1.2A	
Environnemental conditions		
Operation	+0 / +40 degrees C	
Storage	-20 / +50 degrees C	
Altitude	2000 m.	Maximum altitude for which the system has been designed.

LCMS Controller

Feature/Specification	Value	Notes
Dimensions	400mm x 480mm x 90 mm	Standard 19-inch 2U rack-mount unit
Weight	3.6 kg	
Electrical interface		
Input voltage	100-240 VAC	
Frequency	60/50Hz	
Power consumption	150W	
Operation Current (AC)	0.8A	
Power cord	3 x 18 AWG	3 conductors, conductor size = 18 AWG

Appendix II: Specifications for Mobile LiDAR System

Mobile LiDAR

A mobile LiDAR is an optical remote sensing device that can measure distance and other properties of a target, e.g. the reflectance. The LiDAR sensor used in this project is a 2-D point scanning system that can measure the distance of each target point and the corresponding reflectance (represented by retro-intensity). The basic information of the LiDAR is listed below:

- Model: RIEGL LMS-Q120i
- Max. Measurement Range: up to 150m
- Min. Measurement Range: 2m
- Distance Accuracy: 20mm
- Distance Precision: 15mm
- Effective Measurement Rate: 10,000 measurement/sec
- Scanning Rate: 5 to 100Hz
- Angle Step Width: 0.04°

APPLANIX POS LV

The positioning devices used in this project, including the GPS receiver and antenna, IMU, and DMI, are incorporated as an integrated sub-system by Applanix. The model for this integrated sub-system used in the project is Applanix POS LV 210 IARTK. The accuracy for Applanix POS LV 210 IARTK is specified below:

- X, Y position (m): 0.035
- Z Position (m): 0.050
- Roll and Pitch (°): 0.020
- True Heading (°): 0.100

GPS (x1): GPS is a space-based global navigation satellite system (GNSS) that provides location and time information. The basic information of the GPS used in this project is listed below:

- Model: GPS-16
- Signal: GPS L1/L2/L2C, GLONASS L1/L2, OMNISTAR L Band

- Acquisition Frequency: 5Hz

IMU (x1): IMU is an electronic device that measures and reports on a craft's velocity, orientation, and gravitational forces, using a combination of accelerometers and gyroscopes. An IMU contains three accelerometers and three gyroscopes. The accelerometers are placed in such a position that each pair is orthogonal for measuring the inertial accelerations in the three directions. The gyroscopes are placed in the similar orthogonal pattern as the accelerometer to measure the rotational position in reference to an arbitrarily chosen coordinate system, e.g. the GPS coordinate system.

- Model: IMU-17
- Acquisition Frequency: 100Hz

DMI (x1): A DMI is an instrument that measures a wheel's traveling distance. The DMI used in this project is a rotary encoder based DMI that converts the angular position of the wheel into pulses and translates the pulse count into the traveling distance after calibration. The basic information of the DMI used in this project is listed below:

- Model: BEI H25
- Pulse per resolution (PPR): 1024

Video Camera

A video camera is a camera that can acquire a continuous motion picture. The video camera used in this project is only used to capture discretized images at certain intervals controlled by a DMI to create a video log image sequence. The basic information of the video camera is listed below:

- Model: Point Grey GRAS-50S5C-C
- Resolution: 2,448 x 2,048
- Max Frame Rate: 15fps

Appendix III: Literature Review on Automatic Crack Classification Algorithms

1. Overview of Industry Techniques

For the past two decades, many researchers have been developing pavement distress detection and recognition algorithms using a 2D intensity-based imaging system and improved artificial and laser lighting. The National Cooperative Highway Research Program (NCHRP) synthesis document (McGhee, 2004) contains a comprehensive summary of highway practices, research, and development efforts in the automated collection and processing of pavement condition data typically used in network-level pavement management. It is in fully automated methods of distress data segmentation from images that the greatest amount of research and development work seems to have occurred over the past decade. The most widely reported automated method is that known as WiseCrax. The vendor, Roadware Group, Inc., has noted several limitations of the WiseCrax technology (McGhee, 2004). First, all digital image analysis is limited by the quality and resolution of the images. WiseCrax can detect cracks approximately 3mm or wider. Second, crack visibility on certain types of pavement surface, e.g. chip seal, is not good. To detect this type of crack, human intervention is required. At present, no method has achieved completely satisfactory results. Different pavement distress data acquisition systems are briefly reviewed and their corresponding issues summarized below.

Wang (2000) and Wang and Gong (2002) introduced a new automated system capable of collecting and analyzing pavement surface distress, primarily cracks, in real-time through the use of a high-resolution digital camera, efficient image-processing algorithms, and multi-computer and multi-CPU based parallel computing. E1-Korchi et al. (1991) point out the importance of lighting in determining the fraction of distress that went undetected. Nazef et al. (2006) does a comprehensive evaluation of pavement distress systems looking into different factors, including spatial resolution, brightness resolution, optical distortion, and signal-to-noise ratio. Xu (2005), as part of a Texas Department of Transportation (TxDOT) team, uses artificial lighting as the ultimate solution for eliminating all shadows in an image and for improving data uniformity across different weather conditions. The TxDOT team designed a Halogen light with a special reflector to accomplish this objective. Hou et al. (2007) assesses the possibility of using 3D

pavement stereo images for the automated crack analysis. The preliminary test shows that the accuracy of the system is about 5 mm in the vertical direction. Ahmed and Haas (2010) use a low-cost photogrammetric system to reconstruct a detailed model of a pavement surface and demonstrate its capability. In summary, a 2D intensity-based imaging system is the main data acquisition system that has been used for the past two decades. It is used by most state departments of transportation to collect data. Its intensity-based data acquisition method makes it sensitive to lighting effects.

With the advances in sensor technology, a 3D line laser imaging system that can collect high-resolution 3D continuous pavement profiles for constructing pavement surfaces has become available. This 3D laser system is different from the current 2D intensity-based imaging system. First, the 3D laser system is not sensitive to lighting effects when measuring the range (i.e. elevation) like other laser and Light Detection and Ranging (LiDAR) devices. Noises, like oil stains and poor intensity contrast, will not interfere with the segmentation algorithms using the acquired range data. As long as there is a distinguishable elevation difference between a crack and its surrounding background, the segmentation algorithm is able to capture the crack. Increased attention has been drawn to the development of this 3D laser-based data acquisition system and its potential application. The Laser Crack Measurement System (LCMS) (Laurent et al., 2008) can achieve 0.5 mm crack depth resolution, collect 5,600 profiles per second and operate at highway speed (100km/hr for collecting transverse profiles at an interval less than 5mm). This system can produce data with much better granularity, and, thus, it has a great potential to better detect pavement distress.

Compared to the traditional 2D digital image technique for crack detection, the most significant advantage of 3D laser technique is that it is not sensitive to different lighting conditions or noises such as oil stains. For crack classification, the 3D laser technique can provide a more accurate width measurement (common and important crack classification factor in most DOT's protocols) and, also, additional crack depth information (not considered in the past practice due to measurement limitations, but that can be used as useful factors in the future). For the past two decades, the crack classification research has mostly focused on using 2D digital images as the input. In the following several sections, different approaches for automatic crack classification will be discussed.

2. Statistics Based Approaches

In this type of crack classification method, statistical indicators are calculated based on pavement data and crack map (detection results). Different from graphics-based methods, graphic information of crack lines (such as orientation) is not necessary; instead, related information can be obtained by analyzing statistical indicators of pavement data and used for classification. By using different indicators, the following papers presented different solutions for the classification objective.

Orientation is crucial information during pavement crack analysis, and almost all the protocols use orientation as a fundamental factor for crack type definition. Cheng et al. (1999) proposed a crack detection and analysis algorithm based on fuzzy set theory. The focus of this paper is originally the detection stage; however, it provided a typical solution for using statistical indicators to determine crack orientation and, also, simple block pattern. After the crack map was generated, the resulting binary image is projected into four directions: horizontal, vertical, and both diagonal directions (see Figure 1). Since there is no unique crack pattern template, it becomes difficult to recognize crack type by 2D matching. So, it is a feasible solution to reduce the image into a 1D projection and analyze the trends. In this way, the cracks are classified into four types: transverse, longitudinal, diagonal, and alligator cracking. Transverse cracking will be presented as an obvious peak in the vertical projection, as longitudinal cracking in the horizontal projection. For diagonal cracking, peaks will appear in the diagonal direction (45 degrees or 135 degrees). For alligator cracking, peaks will appear in more than one direction (usually in all four projections). The focus of the paper is the crack detection part. However, it doesn't provide an effective way to validate the crack detection results. The only judgment standard is whether the image is detected with a crack or not without considering the accuracy of crack locations. For crack classification, the algorithm claimed to have almost 100% accuracy for transverse, longitudinal, and diagonal cracks; since the sample size of alligator cracking is limited, no results are provided.

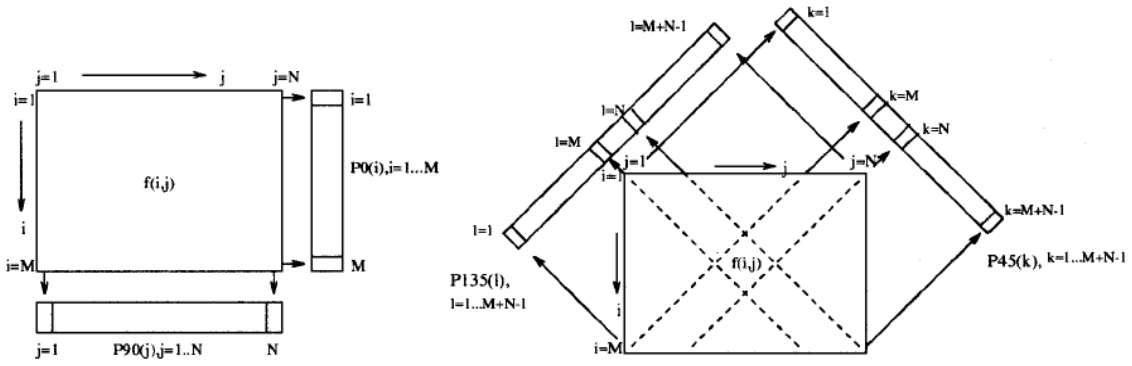

Figure 1 Project the crack map into four directions by Cheng, et al. 1999

The potential issues of this method are obvious: 1) from the algorithm itself, it is difficult to set up a threshold to define a peak in the histogram; 2) the results of alligator cracking are not presented. Even if the algorithm works well on several simple cases (transverse, longitudinal, or diagonal), its performance on cracks with complicated patterns is not ensured. Furthermore, in many real cases, the data appears to have not one type of crack but the combination of several different types, and this will introduce challenges to the classification task; 3) the output provided by this method is too limited, and transportation agencies usually have far more complicated definitions for crack types. Transportation agencies usually consider some other information, such as location and width; different severity levels are also defined for crack types, which introduce more challenges into the automatic classification. Some of them are, also, common issues for crack classification methods.

Instead of focusing on orientation, Cheng and Miyojim (1998) proposed different statistical indicators to classify cracks. The classification algorithm builds a data structure storing the geometry of the skeleton obtained from a crack map. This data structure is pruned, simplified, and aligned, yielding a set of features for distress classification: number of distress objects (connected pavement distress, e.g. crack), number of branch intersections, number of loops (complete polygon pattern), relative sizes of branches in each direction, etc. The first advantage of this skeleton analysis algorithm is that, these two-dimensional geometrical parameters are understandable by both developers and users and have reasonable indications, unlike some methods that deal with abstract quantities not readily understood by ordinary users. For example, a number of distress objects can reflect the density of the crack; if this pavement image sample has more distress objects, it usually indicates that it has a high density of crack distribution. The

number of branch intersections can indicate the polygon pattern, which, under most situations, is difficult to accurately detect**.** Another advantage of this method is that it can quickly accept new classification rules for classification. As long as these parameters are proved to be correlated with crack types and severity levels, they are easily implemented under different protocols. The parameters just need to be trained using the specific data set and protocols from different transportation agencies. This paper classifies cracks into simple cracks (transverse, longitudinal, and diagonal) and complex ones (block, alligator). The classification algorithm uses, experimentally, the following general rules: (1) if there only are a few independent significant PVDUs (pavement distress units) with no loops, the distress is composed of a simple crack, longitudinal, transverse, or diagonal, depending on global orientation. For example, an image having a high proportion of branches in the longitudinal direction is classified as a longitudinal crack, even if there are a few other shorter branches or PVDUs with other orientations.(2) If there are no loops, but numerous PVDUs, then the distress is an alligator crack. (3) If there are one or more large loops, then the distress is also an alligator crack. (4) If there are no loops, but the PVDUs intersect each other at two or more points, then the distress is a block crack. (5) If there are no loops, and there is a single intersection or there are both a longitudinal and a transverse component with significant lengths (more than 35% each of the total length of skeletons in the image), then the distress is a combination crack. The test sample is small (less than 10 samples for each type), and the algorithm shows good performance (100%) for classification. The major issues of this paper are 1) these indicators highly depended on pre-stage crack graphic analysis. Currently, crack detection algorithms may not be able to provide results with the demanded accuracy, so some of the indicators, such as loop number, will be hard to be computed using computer graphic techniques. 2) The paper did not provide a very clear solution for using these indicators to make rules to classify pavement cracks.

Georgopoulos, et al. (1995) provided another solution using vertorizing distances. The input pavement image is first converted into numerical vectors by a given procedure. Image interpretation is based on the vectorization of the distress. The distress may be represented by a set of vectors which approximate the cracks composing the distress. In this way, a geometric model of the cracking, including elements of interest, is obtained, capable of describing its shape. Then, with the property and differences between vector tiles, the data is then interpreted into

different crack types. The paper provides a complete flowchart to interpret the vector information and categorize the cracks into four types: longitudinal, transverse, block, and alligator. The paper did provide a numerical severity level result (score from 0 to 100) for each type; however, this kind of definition is not related to DOT's protocols. As mentioned previously, the vector expression is not directly related to crack characteristics, and, also, the classification flowchart is quite fixed. In that way, for other crack protocols or complicated crack type definition, it would become difficult to set up corresponding rules and implement this method.

Salari and Bao (2010) recently proposed a combination of pavement crack detection and classification. After the pavement images are captured by a digital camera, regions corresponding to cracks are detected over the acquired images by local segmentation and then represented by a matrix of square tiles. Since the crack pattern can be represented by the distribution of the crack tiles, standard deviations for both vertical and horizontal histograms are calculated to map the cracks onto a 2D feature space. A couple of simple rules were set to use both deviations to classify cracks into different types. Similarly, four types of cracks are tested in the experimental test, including longitudinal, transverse, block, and alligator cracking, and for each type, 50 pavement image samples are employed for the test. The algorithm shows high accuracy (average 98.5%) for all cases.

From the review, some statistical indicators have been proved highly related with crack types and severity levels and can be used for crack classification. However, the problem still remains about how to interpret these indicators and set up related rules or procedures for classification. The most representative solution to solve this problem is a neural network.

3. Neural Network Based Approaches

Artificial neural network (ANN or NN) is originally designed to mimic human neural networking to solve computation problems. Figure 2 illustrates a simple ANN. Between the input layer and output layer, one or several hidden layers are designed. After a proper selection of a training dataset, the structure of the neural network, including the weight of each node, will be automatically calculated. The neural network performs well in the machine learning field, especially for classification tasks.

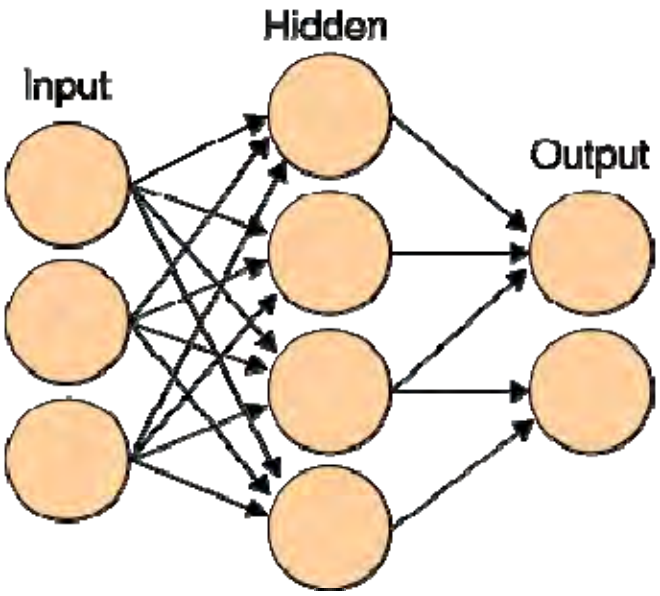

Figure 2 A simple neural network

Neural networks provide a possible way to solve the problem that exists in most statistical crack classification approaches as mentioned above. The neural network can automatically determine its own parameters based on the training set. When implementing a pavement crack classification, the input layer will be the pavement data or several indicators (which can be provided by statistical approaches), and the output layer will be different crack types and severity levels. A fair number of studies on crack classification have been done based on neural networks. Since the structure of a neural network is relatively fixed, the main difference between the studies mainly lies in the input layer.

One of the most representative neural network solutions is provided by Lee ((Lee and Lee, 2003; Lee & Lee, 2004; Lee & Kim, 2005). The input crack map was first divided into tiles (40x40 pixels) to 1) reduce the computational complexity; 2) reduce background noise. Three different types of neural networks were designed and tested: image-based, histogram-based, and proximity-based. Figure 3 shows the computation procedure of the different inputs for the three models. The input for the image-based neural network is all the divided crack tiles. For example, for an image of 19x26 tiles, as shown in the figure, the input layer for image-based model will contains 19x26 = 494 nodes. The input for the histogram-based model is very similar with Cheng et al.'s (1999) previous study, which projects the crack tiles into horizontal and vertical

directions. This also shows that the input of a neural network can usually be statistical indicators, as mentioned above. This also provides a solution to automatically interpret the statistical indicators to different crack types and severity levels. In this way, the input for the histogram-based model will be a horizontal and vertical sum of crack tiles, as shown in the figure, containing 19+26 = 45 nodes. The most significant finding of this study is the introduction of a proximity value. By calculating proximity, the difference between horizontal sums or vertical sums is first calculated. Then, difference vectors of horizontal sums and vertical sums are summed up separately to get two proximity values. The proximity values represent for the total change in the horizontal or vertical direction. Intuitively, if the proximity is large in horizontal direction, there are supposed to be transverse cracks; if the proximity is large in vertical there are supposed to be longitudinal cracks. The only three input nodes of the proximity model are total horizontal proximity, total vertical proximity, and total crack tiles number. The proximity-based neural network showed the best performance with the simplest structure and highest computation efficiency. To classify cracks into longitudinal, transverse, block, and alligator cracking, this neural network can achieve an accurate classification rate of over 90% using these three input nodes, which shows that proximity has a strong correlation with crack orientation and can be used as representative indicator during the crack classification.

In early research, Kaseko et al. (1994) presented a comparative evaluation of traditional and neural network classifiers to detect cracks in video images of asphalt-concrete pavement surfaces. The traditional classifiers used are the Bayes classifier and the k-nearest neighbor (k-NN) decision rule. The neural classifiers are the multilayer feed-forward (MLF) neural-network classifier and a two-stage piecewise linear neural network classifier. Though the NN-based classifier is shown to be slightly better than traditional classifiers, there is a lot of subjectivity in the interpretation of the results from the paper.

Later on, Bray et al. (2006) also conducted a comparative study on crack detection and classification. To demonstrate the performance of neural network, experiments with local thresholding and wavelets are also conducted. The wavelet method is based on Zhou et al.’s (2006) study which will be discussed later. The focus of the research is both detection and classification. In the experimental results, the algorithm demonstrated a good detection rate

(around 80%); however, the classification results are poor (only around 50%, corresponding to four types: longitudinal, transverse, block, and alligator).

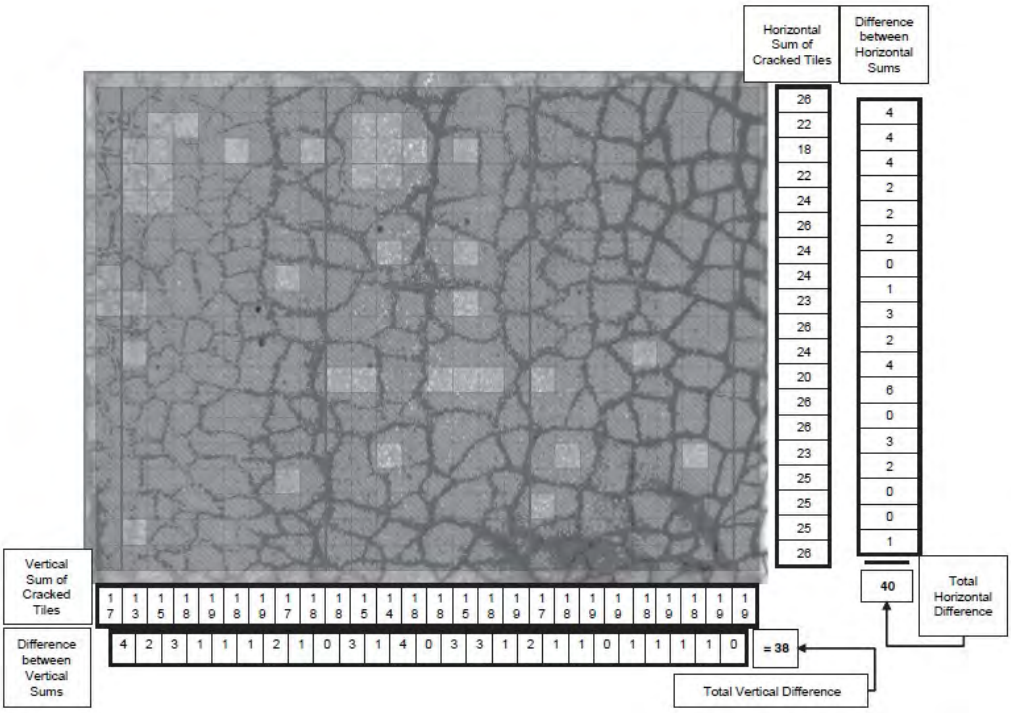

Figure 3 Illustration of input layer calculation (Lee and Kim 2005)

As mentioned above, since the structure of a neural network is relatively fixed, the main difference between different studies is the input of ANN. As early as 1994, Chou, J. and Cheng, H. (1994) used feature vectors as inputs of the neural network. Three kinds of moments (Hu's, Bamieh's, and Zernike's) represent the following information of cracks: center of mass, orientation, bounding box, best-fit ellipse, and eccentricity. Xiao et al. (2006) proposed a revised neural network structure based on pavement image density. Distress Density Factor (DDF) is used to search the patterns of variously irregular crack types in all directions while maintaining its position invariance. The algorithm is claimed to have 97% classification accuracy. However, the definition and significance of DDF is not presented clearly. Saar and Talvik (2010) used a very similar neural network with the histogram mentioned above, and the only improvement was that horizontal and transverse convolution was introduced as additional inputs to preserve cracks of corresponding directions and remove noise. Salari and Bao (2011) used the same histogram plus a neural network framework, but they have a unique input for detection –

chromatic digital image. Recently, Li et al. (2011) chose spatial distribution features as the input of neural network. The D-coding method was used to extract direction information, and Delaunay triangulation was used to extract density information.

As a brief summary, the neural network method is an efficient tool to utilize pavement data (e.g. pixel values of digital pavement image) and statistical indicators to classify pavement cracks. The major issues of this method are 1) the performance of the neural network is highly related to the input selection; the neural network itself doesn't contribute too much to the classification results; 2) similar to the method mentioned above, the existing studies only focus on simple types of cracks: longitudinal, transverse, block, and alligator. Whether a neural network can deal with the complicated crack type definition and fit well in DOT's protocols still needs to be tested.

4. Wavelet based approaches

Wavelet-based techniques have proven to be useful tools for extracting image features in many past studies. The applications of wavelet transform on pavement distress evaluation have been developed recently. The literature review shows that the wavelet transform has the capability of pavement data de-noising and rough automatic evaluation of several representative types of pavement distresses, including cracking, raveling, and rutting.

For any automated distress inspection system, typically a huge number of pavement images are collected. Use of an appropriate image compression algorithm can save disk space, reduce the saving time, increase the inspection distance, and increase the processing speed. The embedded Zero-tree Wavelet (EZW) coding method is a widely used image compression method. In Zhou's previous research (2005), a modified EZW coding method was proposed for both pavement image compression and noise reduction. The advantage of the proposed method was that it used only one pass to encode both the coordinates and magnitudes of wavelet coefficients. An adaptive arithmetic encoding method was implemented to encode four symbols P, N, Z and I for all wavelet coefficients. An image compressor and noise-reducer was proposed based on the modified EZW coding method. The study proved the capability of wavelet on pavement image compression and de-noising; however, the paper did not present an evaluation of compression results on different types of pavement distresses.

Zhou et al. (2005; 2006) proposed a representative solution to utilize wavelet transform for crack detection and evaluation. Figure 4 shows a demonstration for pavement image wavelet transform. After a pavement image is decomposed into different frequency sub-bands by the wavelet transform, distresses are transformed into high-amplitude wavelet coefficients, and noise is transformed into low-amplitude wavelet coefficients, both in the high-frequency sub-bands, referred to as details. Background is transformed into wavelet coefficients in a low-frequency sub-band, referred to as approximation. First, several statistical criteria are developed for distress detection and isolation, which include the high-amplitude wavelet coefficient percentage HAWCP, the high-frequency energy percentage HEFP, and the standard deviation STD. These criteria are tested on hundreds of pavement images differing by type, severity, and extent of distress. No classification results are presented in this paper.

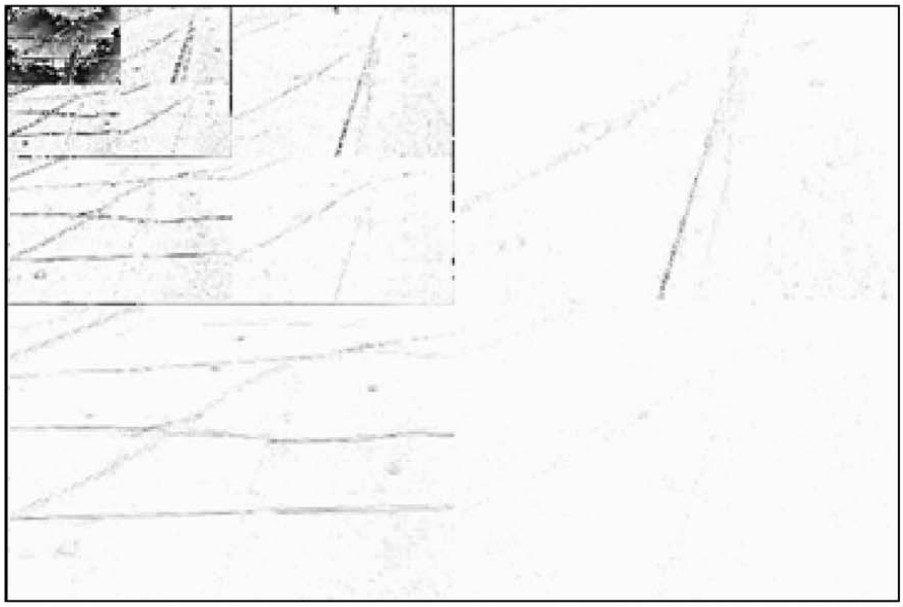

Figure 4 Wavelet transform of pavement image with distress (Zhou, Huang et al. 2006)

The HAWCP, HEFP and STD indicators may work for crack detection, but are not sensitive enough for the classification task. To solve this problem, the Radon transform is introduced to further represent crack properties. In previous research, projection to certain directions is usually used to determine crack orientation information. For example, after projecting the crack map into the horizontal and vertical directions, longitudinal or transverse cracks can be obtained by analyzing the histogram. The Radon transform is a similar idea but with further development. The Radon transform is applied to the wavelet modulus to transform cracks into peaks in the

Radon domain. The patterns and parameters of the peaks are finally used for distress classification. The relationship between the patterns of peaks and properties of cracks is shown in Table 1. The cracks are classified into longitudinal, transverse, diagonal, alligator, and block cracking. The classification accuracy for alligator cracking is 70%, with all other types over

Table 1 Relationship between the Patterns of Peaks and Properties of Cracks

Pattern of Peaks	Position Number	Position	Area	Peak Value or Area
Properties of cracks	Longitudinal Transverse Diagonal Block Alligator	Left lane edge Right lane edge Lane center Left wheelpath Right wheelpath	Crack width Low Medium High	Crack length or crack area Occasional Frequent Extensive
Classification	Type	Location	Severity	Extent

Wang (2007) used wavelets as an edge detection tool for pavement distress detection. Pavement surface images frequently have various details at different scales. Therefore, a wavelet-based multi scale technique can be a candidate to extract edge information from pavement surface images. This paper adopts the à trous-based wavelet algorithm to detect pavement distress image edges. In comparison with other edge-detection methods, the à trous algorithm is a good tool and provides stable performance in pavement distress edge detection.

Later on, Nejad and Zakeri(2011) improved the wavelet-based crack detection method. The major framework was similar to Zhou's study based on Wavelet-Radon transform. Compared to the previous study, a more comprehensive criteria set was proposed in this paper. After the criteria were extracted from wavelet and Radon domains, a dynamic neural network was implemented. A neural network gave a more accurate and robust performance for the decision rule stage than simple thresholding, and a dynamic neural network allowed the system to work under online real-time conditions. They also conducted a comparison study between different multi-resolution pavement image analysis methods, including wavelet transform, ridgelet transform, and curvelet-based texture descriptor (Nejad & Zakeri 2011).

Besides pavement cracking, a wavelet tool has also been used to evaluate road roughness (which is related to raveling issues) in past research. Summary roughness statistics are commonly used by highway agencies to characterize road roughness profiles to provide convenient numerical indices for pavement performance monitoring and management planning. Many different roughness indices have been used by different highway agencies worldwide, including the International Roughness Index (IRI), root-mean-square vertical acceleration (RMSVA), mean absolute vertical acceleration (MAVA), and slope variance (SV), etc. However, since different indices are computed with different considerations and mathematical procedures, they often do not correlate well with one another. This presents a practical problem for the exchange of information and experience among practitioners or highway agencies. Wei and Fwa (2004) proved that the detailed pavement roughness features of different wavelengths quantitatively in terms of wavelet energy have high correlations with each of the commonly used indices. Therefore, wavelet energy statistics can be a useful common basis to relate different forms of pavement roughness measures. In further study, Wei, Fwa et al. (2005) presented a wavelet analysis procedure to offer supplementary information to pavement roughness indices (such as the IRI and RMSVA) to provide further insight into the characteristics of the roughness profile of interest. The summary pavement indices suffer from a common limitation in that the detailed contents of pavement surface roughness of the pavement section concerned are lost. Such detailed contents could provide valuable information for pavement maintenance management and planning. The experimental results showed that the wavelet energy statistics have the capability of differentiating these detailed information.

The following briefly summarizes this section of literature review:

First, wavelet transform has been proved a useful tool for pavement distress identification. However, as shown in the existing studies, wavelet transform usually cannot provide the detailed pavement distress information; instead of distress position and shape, the wavelet energy statistics only provide the overall condition evaluation of the data sample. This makes it fit better to the large-scale distress analysis stage. Utilizing wavelet transform, the pavement regions of interest (which most probably contain distress) can be extracted after a rough large-scale detection; additional tools, such as ridgelet and curvelet transform, can also be incorporated into this stage. A large-scale analysis will provide a better data management solution and input for

data compression. In further steps, a small-scale analysis is still needed to detailed evaluate and classify different distresses.

Second, pavement surface condition evaluation deals with different types of pavement distresses, and the existing studies usually focus on one certain type of distress. Different types of pavement distresses have very different characteristics, no matter in space domain or in frequency domain. The distress types cover most frequency bands of data analysis: rutting is, generally, low-frequency information, while crack and raveling deal with texture. Also, for detailed applications, one type of distress itself may be the noise for other distresses. This introduces the challenge to utilize wavelet transform to cover multiple distress types.

5. Graphics based approaches

By analyzing the graphic information of detected crack lines or patterns, the graphics-based crack classification approach is in nature closest to conventional visual and manual crack survey. However, the accuracy of current crack detection algorithms usually limits the input of crack classification algorithms. For instance, even though whether or not a complete crack polygon pattern has formed is used as important judgment factor for most DOTs in their pavement survey protocol, the current crack detection algorithms can hardly preserve complete polygon information as their detection output. Also, because of immature computer image processing techniques in current research of this field, it is hard for computers to give the same accurate graphics information as humans do, especially for pattern types. Therefore, in previous research, the type of approach has been rarely touched. This section will present two recent studies using graphics method on crack classification.

Salari et al. (2009) presented a new attempt for graphics based crack classification. A self-adaptive image processing method is proposed for the extraction and connection of break points of cracks in pavement images. The algorithm first finds the initial point of a crack and then determines the crack's classification into transverse, longitudinal, and alligator types. Different search algorithms are used for different types of cracks. Then, the algorithm traces along the crack pixels to find the break point and then connect the identified crack point to the nearest break point in the particular search area. The nearest point then becomes the new initial point, and the algorithm continues the process until reaching the end of the crack. Different search

strategies correspond to different crack types. A longitudinal crack is an example: the three prioritized search directions will be as follows. . The downward direction is crucial for longitudinal cracks, so it will be the first direction with high priority to search for continuity. The second and the third directions are the right and left directions, respectively. Note that, the order of priority is very important and should be observed during the search process. We cannot use the same search method for both transversal and longitudinal cracks because the tendency for transversal cracks is in the right direction, and the tendency of longitudinal crack is in the downward direction. Currently, only the results of transverse and longitudinal cracks have been presented, and no quantitative evaluation was provided. However, this is still a good starting point and provides another direction for crack analysis.

Ying (2009) proposed another approach using beamlet transforms. To extract the linear features, such as surface cracks from the pavement images, the image is partitioned into small windows, and a beamlet transform is applied. The output of the beamlet transform is very similar to the idea of fundamental crack elements. The crack segments are then linked together. Angles and branches are used to classify cracks into vertical, horizontal, transverse, and block cracking.

References

Ahmed, M. F. M., and Haas. C. T. (2010). “The Potential of Low Cost Close Range Photogrammetry Towards Unified Automatic Pavement Distress Surveying.” Transportation Research Board Annual Meeting 2010 (CD-ROM).

Albitres, C. M. C., R. E. Smith, et al. (2007). "Comparison of automated pavement distress data collection procedures for local agencies in San Francisco Bay Area, California." Transportation Research Record(1990): 119-126.

Bray, J., B. Verma, et al. (2006). A neural network based technique for automatic classification of road cracks. International Joint Conference on Neural Networks, IEEE: 907-912.

Capuruço, R. A. C., S. L. Tighe, et al. (2006). "Performance evaluation of sensor- And image-based technologies for automated pavement condition surveys." Transportation Research Record(1968): 47-52.

Cheng, H. D., J.-R. Chen, et al. (1999). "Novel approach to pavement cracking detection based on fuzzy set theory." Journal of Computing in Civil Engineering 13(4): 270-280.

Cheng, H. D. and M. Miyojim (1998). "Automatic pavement distress detection system." Information sciences 108(1-4): 219-240.

Chi-Ho, C. and G. Pang (1999). Fabric defect detection by Fourier analysis. Industry Applications Conference, 1999. Thirty-Fourth IAS Annual Meeting. Conference Record of the 1999 IEEE

Chou, J. and H. D. Cheng (1994). Pavement distress classification using neural networks. Systems Man and Cybernetics (SMC), 2010 IEEE International Conference on.

Fu, P., J. Harvey, et al. (2011). California's Experience in Evaluating Automated Pavement Condition Survey Service Providers' Technical Competence. Transportation Research Board Annual Meeting.

Fu, P., J. Harvey, et al. (2011). New Method for Classifying and Quantifying Flexible Pavement Cracking in Automated Pavement Condition Survey. Transportation Research Board Annual Meeting.

Georgopoulos, A., A. Loizos, et al. (1995). "Digital image processing as a tool for pavement distress evaluation." ISPRS Journal of Photogrammetry and Remote Sensing 50(1): 23.

Iivarinen, J. and A. Visa (1998). An adaptive texture and shape based defect classification. Pattern Recognition, 1998. Proceedings. Fourteenth International Conference on

Kaseko, M. S., Z.-P. Lo, et al. (1994). "Comparison of traditional and neural classifiers for pavement-crack detection." Journal of Transportation Engineering 120(4): 552-569.

Kim, S. C. and T. J. Kang (2005). Texture classification and segmentation using incomplete tree structured wavelet packet frame and gaussian mixture model. Proceedings of the 2005 IEEE International Workshop on Imaging Systems and Techniques.

Lee, B. J. and H. Lee (2003). A Robust Position Invariant Artificial Neural Network for Digital Pavement. Transportation Research Board Annual Meeting.

Lee, B. J. and H. D. Lee (2004). "Position-invariant neural network for digital pavement crack analysis." Computer-Aided Civil and Infrastructure Engineering 19(2): 105-118.

Lee, H. and J. Kim (2005). "Development of a crack type index." Transportation Research Record(1940): 99-109.

Li, Q., Q. Zou, et al. (2011). "Pavement Crack Classification via Spatial Distribution Features." EURASIP Journal on Advances in Signal Processing 2011.

Lucas, R., A. Rowlands, et al. (2007). "Rule-based classification of multi-temporal satellite imagery for habitat and agricultural land cover mapping." ISPRS Journal of Photogrammetry and Remote Sensing 62(3): 165-185.

Mcqueen, J. M. and D. H. Timm (2005). "Statistical analysis of automated versus manual pavement condition surveys." Transportation Research Record(1940): 55-62.

Nejad, F. M. and H. Zakeri (2011). "A comparison of multi-resolution methods for detection and isolation of pavement distress." Expert Systems with Applications 38(3): 2857-2872.

Nejad, F. M. and H. Zakeri (2011). "An expert system based on wavelet transform and radon neural network for pavement distress classification." Expert Systems with Applications 38(6): 7088-7101.

Nejad, F. M. and H. Zakeri (2011). "An optimum feature extraction method based on Wavelet-Radon Transform and Dynamic Neural Network for pavement distress classification." Expert Systems with Applications 38(8): 9442-9460.

Obaidat, M. T. and S. A. Al-kheder (2006). "Integration of geographic information systems and computer vision systems for pavement distress classification." Construction & Building Materials 20(9): 657-672.

Rahman, M. K. A., R. Arora, et al. (1998). Classification of partial discharge transient patterns using texture analysis algorithms. Electrical Insulating Materials, 1998. Proceedings of 1998 International Symposium on

Saar, T. and O. Talvik (2010). Automatic asphalt pavement crack detection and classification using neural networks. Proceedings of the 12th Biennial Baltic Electronics Conference.

Salari, E. and G. Bao (2010). Pavement distress detection and classification using feature mapping. IEEE International Conference on Electro/Information Technology.

Salari, E. and G. Bao (2011). Pavement distress detection and severity analysis. Proceedings of SPIE - The International Society for Optical Engineering.

Sang, H. L., I. K. Hong, et al. (2005). Automatic defect classification using boosting. Proceedings - ICMLA 2005: Fourth International Conference on Machine Learning and Applications.

Sinha, S. K. and P. W. Fieguth (2006). "Morphological segmentation and classification of underground pipe images." Machine Vision and Applications 17(1): 21-31.

Sun, Y., E. Salari, et al. (2009). Automated pavement distress detection using advanced image processing techniques. Proceedings of 2009 IEEE International Conference on Electro/Information Technology.

Tighe, S. L., L. Ningyuan, et al. (2008). "Evaluation of semiautomated and automated pavement distress collection for network-level pavement management." Transportation Research Record(2084): 11-17.

Wang, K. C. P., Q. Li, et al. (2007). "Wavelet-based pavement distress image edge detection with a trous algorithm." Transportation Research Record(2024): 73-81.

Wei, L. and T. F. Fwa (2004). "Characterizing road roughness by wavelet transform." Transportation Research Record(1869): 152-158.

Wei, L., T. F. Fwa, et al. (2005). "Wavelet analysis and interpretation of road roughness." Journal of Transportation Engineering 131(2): 120-130.

Wong, B. K., M. P. Elliot, et al. (1995). Automatic casting surface defect recognition and classification. Proceedings of SPIE - The International Society for Optical Engineering.

Xiao, W., X. Yan, et al. (2006). Pavement Distress Image Automatic Classification Based on DENSITY-Based Neural Network. Proceedings of RSKT'2006.

Yang, X., J. Gao, et al. (2005). Textile defect classification using discriminative wavelet frames. Proceedings of 2005 International Conference on Information Acquisition.

Ying, L. (2009). Beamlet Transform Based Technique for Pavement Image Processing and Classification. Master, The University of Toledo.

Zhou, J., P. Huang, et al. (2005). "Wavelet-based pavement distress classification." (1940): 89-98.

Zhou, J., P. S. Huang, et al. (2005). Wavelet-based pavement distress image compression and noise reduction. Proceedings of the SPIE - The International Society for Optical Engineering.

Zhou, J., P. S. Huang, et al. (2006). "Wavelet-based pavement distress detection and evaluation." Optical Engineering 45(2).

Appendix IV: Literature Review on Current Crack Survey Protocols

Different types of cracks can occur on the road, and each type has different impact on the ride quality. To deduce useful information on the ride quality and the pavement treatment analysis, each state DOT uses its particular protocol to classify cracks after dividing the highway into standard sections of constant length. Cracks are generally classified according to different protocols of different states, and guidelines given by agencies like FHWA and AASHTO. The challenge in the process of crack classification is compounded by the differences in crack protocols in every state and the subjectivity in the crack classification process. In this summary, we will cover some prominent protocols and assess the differences between them. We cover the following protocols:

1) FHWA standard
2) SHRP standard
3) AASHTO PP00 standard
4) AASHTO PP01 standard for automatic classification
5) State Protocols
    (i) Louisiana Department of Transportation (LaDOT) protocol
    (ii) Texas Department of Transportation (TxDOT) protocol
    (iii) Georgia Department of Transportation (GDOT) protocol

1. FHWA Standard

The FHWA, Road Inventory Program (RIP), collects roadway condition data on paved asphalt surfaces, including roads, parkways, and parking areas in national parks nationwide. The road surface condition data is collected using an automated data collection vehicle called ARAN. The classification and measurement of all surface condition data is done in intervals of 0.02 miles (105.6 ft) along the route. The cracks are classified into three types: transverse crack, longitudinal crack, and alligator crack. Each of these three types is divided into three severity levels. Table 1 gives the overview of the different types, and Figure 1 shows pavement images corresponding to these types. Transverse cracking occurs predominantly perpendicular to the

pavement centerline. The severity levels, low, medium and high, are assigned according to the mean width of the transverse crack. Figure 2 illustrates the width measurement process. Longitudinal cracking occurs predominantly parallel to the pavement centerline. The severity levels are assigned in a similar manner to transverse cracks. Alligator cracking may be considered a combination of fatigue and block cracking. It is a series of interconnected cracks in various stages of development. Alligator cracking develops into a many-sided pattern that resembles chicken wire or alligator skin. It can occur anywhere in the road lane. Alligator cracking must have a quantifiable area. A combination of observed crack width and crack pattern is used to determine overall severity of alligator cracking. Based on above description of each severity, the highest level of crack width and crack pattern determines overall severity, illustrated in Table 2.

Table 1: Different Distress Types in FWHA protocol (FHWA 2006)

ASPHALT-SURFACED PAVEMENT DISTRESS TYPES with RUTTING and ROUGHNESS				
DISTRESS TYPE	UNIT OF MEASURE…	…CONVERTED TO	DEFINED SEVERITY LEVELS?	MEASURED BY
Alligator Cracking	Square Feet	Percent of Lane Per 0.02 Mile	Yes	Contractor (Video Analysis)
Transverse Cracking	Linear Feet	Number of Cracks Per 0.02 Mile	Yes	Contractor (Video Analysis)
Longitudinal Cracking	Linear feet	Percent of Lane Length Per 0.02 Mile	Yes	Contractor (Video Analysis)

(a)

(b)

(c)

Figure 1 (a) Transverse Crack (b) Longitudinal Crack (c) Alligator Crack (FHWA 2006)

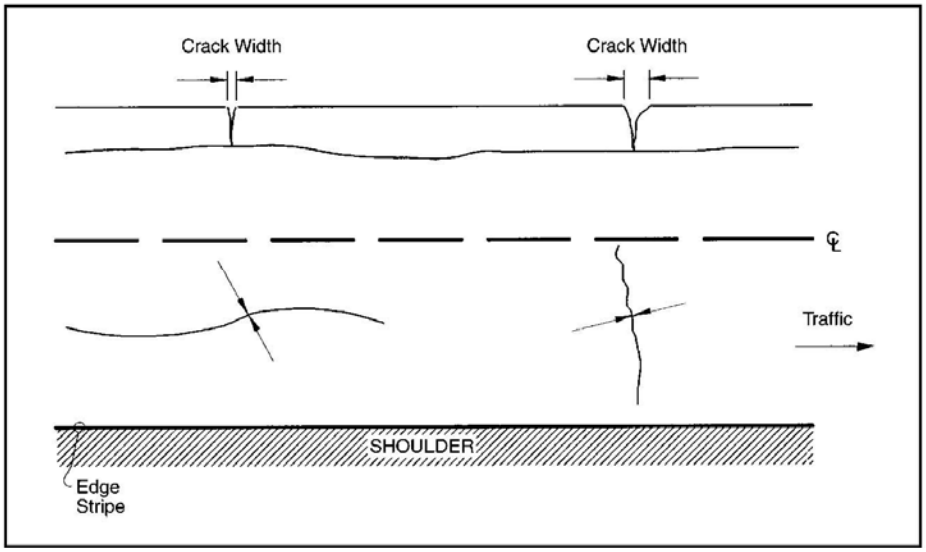

Figure 2 Width Measurement process in FHWA protocol (FHWA 2006)

Table 2: Alligator Crack Severity Level

ALLIGATOR CRACKING SEVERITY LEVELS		Crack Pattern		
		LOW	MED	HIGH
Crack Width	LOW	L	M	H
	MED	M	M	H
	HI	H	H	H

The FHWA protocol combines cracking, potholes, and rutting information to come up with a Pavement Condition Index (PCI) to quantify the overall pavement condition of each pavement section.

2. SHRP LTPP Protocol

In 1987, the Strategic Highway Research Program (SHRP) began the largest and most comprehensive pavement performance test in history called the Long-Term Pavement Performance (LTPP) program. The SHRP is the most detailed protocol among all protocols. First of all, the protocol considers the classification of three types of pavements independently: asphalt concrete surfaces, jointed Portland cement concrete surfaces, and pavement with continuously

reinforced concrete surfaces. Tables 3, 4 and 5 illustrate the crack classification types for these three surfaces.

Table 3 Classification for asphalt concrete surfaces

DISTRESS TYPE	UNIT OF MEASURE	DEFINED SEVERITY LEVELS?
A. Cracking / page 7		
1. Fatigue Cracking	Square Meters	Yes
2. Block Cracking	Square Meters	Yes
3. Edge Cracking	Meters	Yes
4a. Wheel Path Longitudinal Cracking	Meters	Yes
4b. Non-Wheel Path Longitudinal Cracking	Meters	Yes
5. Reflection Cracking at Joints		
Transverse Reflection Cracking	Number, Meters	Yes
Longitudinal Reflection Cracking	Meters	Yes
6. Transverse Cracking	Number, Meters	Yes

Table 4 Classification for jointed portland cement concrete surfaces

DISTRESS TYPE	UNIT OF MEASURE	DEFINED SEVERITY LEVELS?
A. Cracking / page 39		
1. Corner Breaks	Number	Yes
2. Durability Cracking ("D" Cracking)	Number of Slabs, Square Meters	Yes
3. Longitudinal Cracking	Meters	Yes
4. Transverse Cracking	Number, Meters	Yes

Table 5 Classification for continuously reinforced concrete surfaces

DISTRESS TYPE	UNIT OF MEASURE	DEFINED SEVERITY LEVELS?
A. Cracking / page 65		
1. Durability Cracking ("D" Cracking)	Number, Square Meters	Yes
2. Longitudinal Cracking	Meters	Yes
3. Transverse Cracking	Number, Meters	Yes

We just briefly describe the classification procedure for asphalt concrete surfaces.

There are six different types of cracking: Fatigue Cracking, Block Cracking, Edge Cracking, Longitudinal Cracking - Wheel Path, Longitudinal Cracking - Non-Wheel Path, Reflection Cracking at Joints, and Transverse Cracking. Figure 3 illustrates these cracking types. Each of the above are classified into three severity levels. SHRP protocol's classification procedure classifies crack according to the cause of cracking. That information is primarily obtained by analyzing whether the crack lies in the wheel path. Fatigue cracking and block cracking extent is measured in area (square metres), while the extent of other cracking types is measured by length (metres). Only crack pattern is used to estimate severity of fatigue cracking. Edge cracking

severity is determined by the percentage of break-up of pavement material near the edge. For all other cracking types, severity is estimated using classification procedure for SHRP are different from FWHA.

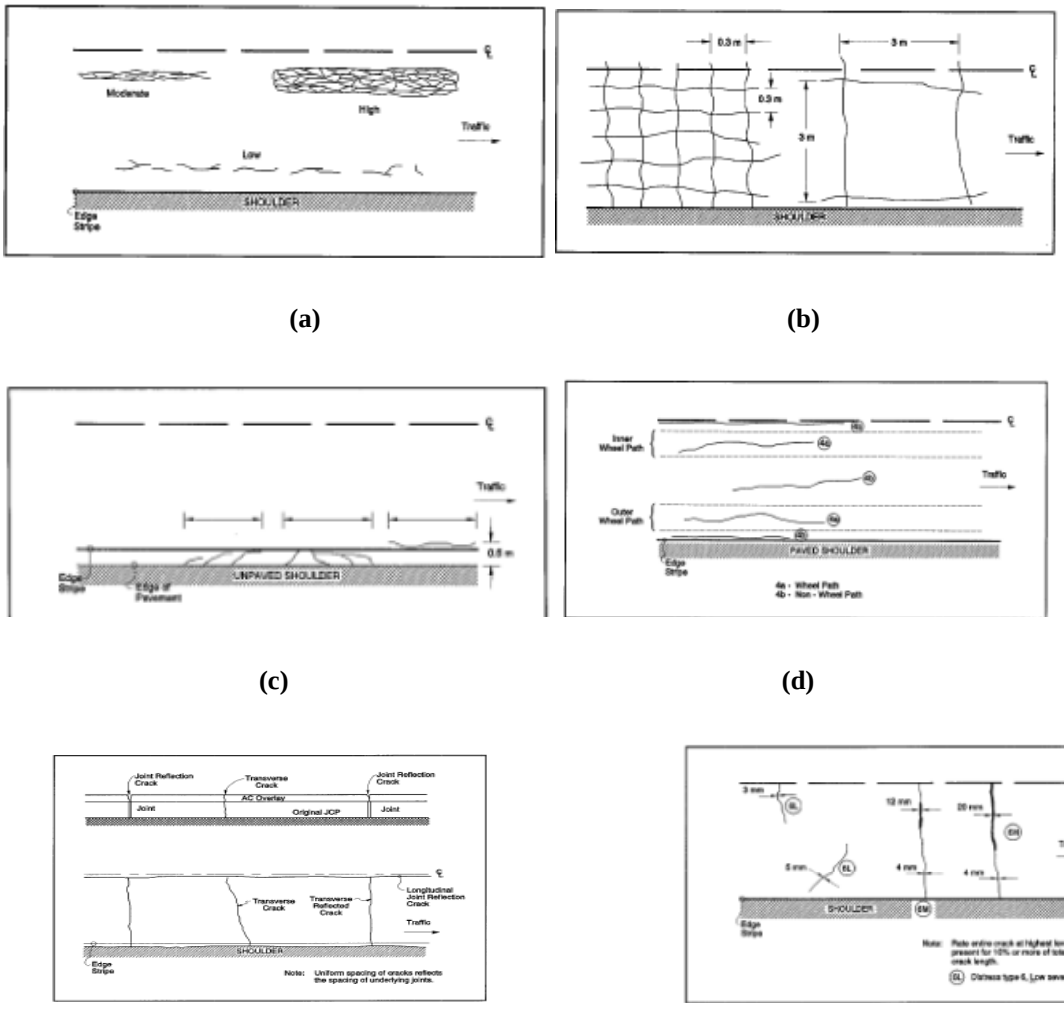

(a) **(b)**

(c) **(d)**

(e) **(f)**

Figure 3 (a) Fatigue cracking (b) Block Cracking (c) Edge Cracking (d) Longitudinal Cracking (e) Reflection Cracking (f) Transverse Cracking

3. AASHTO PP00 Standard

A crack is defined as a discontinuity in the pavement surface with minimum dimensions of 3 mm (1/8 in) width and 25 mm (1 in) length. Cracks may include longitudinal cracks, transverse cracks, and pattern cracks. The intent of this practice is to quantify and differentiate between load associated (fatigue) and non-load associated (environmental, reflective, etc.) pavement

cracking and joints. For this practice, increased cracking intensity in the wheel path, as compared to the non-wheel path areas, is assumed to quantify load associated cracking. Non-load associated cracking is quantified by the cracking measured in the non-wheel path areas. There are three severity levels for both load and non-load associated cracking, and crack-width information is used to characterize this information. The severity of each cracking level is quantified as the total length of cracking per unit area (m/m^2) for each defined survey strip.

4) AASHTO PP01 standard: In 2001, AASHTO came up with a new provisional standard for automatic crack classification, which is current to this date. According to the new standard, a crack is defined as a fissure of the pavement with a minimum dimension of 3cm by 1mm. Maximum length of the crack is 367cm. The standard defines crack width as the average width of the crack when measured at different points that are 3mm apart. Apart from that, the definitions of crack termination, crack orientation, crack length, and crack position are provided in the standard. The Inside Wheel Path is defined as a longitudinal stripe of the road 750cm wide and centered at 875cm from the centre line of the lane towards the adjacent lane. The Outside Wheel Path is defined by a longitudinal stripe of the road 750cm wide and centered at 875cm from the centre line of the lane towards the shoulder. The area between inside and outside wheel path is divided into five measurement zones where cracking is measured. Cracking of three types: longitudinal, transverse, and pattern cracking is measured. Longitudinal and transverse cracking types are defined according to crack orientation in a particular measurement zone. Interconnected cracks or cracks that cannot be classified into the other two types are classified as pattern cracks. Crack width and crack length information in each measurement zone is also retained, but no severity levels are assigned. This protocol is suited for automatic crack classification because the difficulties associated with assigning 3 or 4 severity levels is avoided, while all information of about the crack is preserved using the crack length, crack width, and crack type information in each measurement zone.

4. State DOTs' Protocols

Many states follow their own particular protocols. We will just briefly describe the protocols of two states:

1) TxDOT Protocol

Cracks according to this protocol are divided into four types: block cracking, alligator cracking, longitudinal cracking, and transverse cracking. Alligator cracking is identified by block pattern near the wheel path, and it corresponds to load-associated cracks. All the other types correspond to non-load associated cracks caused by movement below the surface and are identified outside the wheel path. Block cracking and alligator cracking are identified by area, while longitudinal and transverse cracking are identified using length. However, the data for each type is converted to an index between 0 and 99, which uses the area or the length information. Therefore, TxDOT has a very different way of classifying cracks that does not use any crack width information for classification. There are some ambiguities associated with some patterns: for example, longitudinal cracks that lie on the wheel path but don't enclose any area cannot be classified as either alligator cracks or longitudinal cracks (supposed to lie outside the wheel path).

2) LaDOT Protocol

The LaDOT protocol divides cracks only into two types: fatigue cracking and random (non-fatigue cracking). Fatigue cracking consists of longitudinal, transverse, or block cracks occurring around either wheel path. Random cracking is identified by the presence of cracks outside the wheel path. The region around a wheel path is taken with a transverse width of 3 feet centered at the middle of wheel path. Each cracking type is divided into three severity levels. Both crack width and crack pattern are used to classify cracking into severity levels. Crack width is used to identify severity levels of longitudinal and transverse cracks, while crack area is used to identify block cracking severity levels.

The above survey indicates the complexity of the crack classification procedure and the lack of standardization in crack classification. The differences in different protocols make automatic crack classification even more difficult because the data processing algorithms need to be fine tuned for each particular protocol separately.